A&A manuscript no.
(will be inserted by hand later)
Your thesaurus codes are:
06(08.02.3; 08.12.2; 08.12.3)

To Martha, many thanks for your comments, Christoph

ASTRONOMY AND ASTROPHYSICS
2.8.1997

The 1997 reference of diffuse night sky brightness *

Ch. Leinert[1], S. Bowyer[2], L.K. Haikala[3], M.S. Hanner[4], M.G. Hauser[5], A.-Ch. Levasseur-Regourd[6], I. Mann[7], K. Mattila[3], W.T. Reach[8], W. Schlosser[9], H.J. Staude[1], G.N. Toller[10], J.L. Weiland[11], J.L. Weinberg[12], and A.N. Witt[13]

[1] Max-Planck-Institut für Astronomie, Königstuhl 17, D-69117 Heidelberg, Germany
[2] Astronomy Dept., University of California, 601 Campbell Hall, Berkeley CA 94720, USA
[3] Observatory, P.O. Box 14, FIN-00014 University of Helsinki, Finland
[4] Jet Propulsion Laboratory, 4800 Oak Grove Drive, Pasadena CA 91109, USA*
[5] Space Telescope Science Institute, 3700 San Martin Drive, Baltimore MD 21218, USA
[6] Service d'Aéronomie BP3, F-91371 Verrières le Buisson, France
[7] Max-Planck-Institut fur Aeronomie, Max-Planck-Straße 2, D-37191 Katlenburg-Lindau, Germany
[8] Institut d'Astrophysique Spatiale, Université Paris XI, 91405 Orsay Cedex, France
[9] Astronomisches Institut, Ruhr-Universitat Bochum, D-44780 Bochum, Germany
[10] General Sciences Corporation, 6100 Chevy Chase Drive, Laurel, MD 20707, USA
[11] Hughes STX, NASA/Goddard Space Flight Center Code 685.9, Greenbelt, MD 20771, USA
[12] MK Industries, 2137E Flintstone Drive, Tucker, Georgia 30084, USA
[13] Ritter Astrophys. Res. Center, University of Toledo, Toledo, OH 43606, USA

Received date; accepted date

Abstract. In the following we present material in tabular and graphical form, with the aim to allow the non-specialist to obtain a realistic estimate of the diffuse night sky brightness over a wide range of wavelengths from the far UV longward of Lyα to the far-infrared. At the same time the data are to provide a reference for cases in which background brightness has to be discussed, including the planning for space observations and the issue of protection of observatory sites. We try to give a critical presentation of the status at the beginning of 1997.

Key words: night sky brightness; airglow; zodiacal light; integrated starlight; diffuse galactic light; extragalactic background light,; photometry

Contents

Send offprint requests to: Ch Leinert

* Prepared by members of Commission 21 "Light of the night sky" of the IAU, including most of the recent (vice-)presidents.

Table 1. Conversion factors for ultraviolet brightness units

Wavelength (11111)	1 photon/cm² s sr Å corresponds to I_λ [W/m² sr μm]	I_λ [erg/cm² s sr Å]	I_ν [Jy/sr]	R/Å	Conversion factor I_ν + [,
30	$6.62 \cdot 10^{-10}$	$6.62 \cdot 10^{-11}$	0.199	12610-5	333110-''
60	$3.31 \cdot 10^{-10}$	$331 \cdot 10^{-11}$	0.398	1.2610-'5	8.32$,10''
100	$1.99 \cdot 10^{-10}$	1.9910-"	0.663	$1.26 \cdot 10^{-5}$	299810- 'o
121.6[a]	$1.63 \cdot 10^{-10}$	$1.63 \cdot 10^{-11}$	0.856	1.2610-5	202710- 'o
150	$1.32 \cdot 10^{-10}$	$1.32 \cdot 10^{-11}$	0.994	1.2610-5	1.33210 10
200	9.9310-"	9.9310-'2	1.325	1.2610-5	7.49510"[
250	$7.95 \cdot 10^{-11}$	$7.95 \cdot 10^{-12}$	1.657	1.2610-5	4.79710-"'
300	$6.62 \cdot 10^{-11}$	6.6210-12	1.988	1.2610-5	$3.331 \cdot 10^{-11}$
350	$5.68 \cdot 10^{-11}$	$5.68 \cdot 10^{-12}$	2.319	$1.26 \cdot 10^{-5}$	$2.447 \cdot 10^{-11}$
400	4.97 .10-"	$4.97 \cdot 10^{-12}$	2.650	$1.26 \cdot 10^{-5}$	$1.874 \cdot 10^{-11}$
500	3.9710-11	3.9710-12	2.120	1.2610-3	1.19910-"'
656.3[b]	$3.03 \cdot 10^{-11}$	$3.03 \cdot 10^{-12}$	4.349	$1.26 \cdot 10^{-5}$	$6.960 \cdot 10^{-12}$
1 μm	1.9910-1'	1.9910-'2	6.628	1.2610-5	$2.998 \cdot 10^{-12}$
2 μm	$9.93 \cdot 10^{-12}$	9.9310-13	.13.25	1.2610-5	7.495 .10-"13
4 μm	4.9710-12	4.9710-'3	26.50	1.2610-5	1.87410 13

[a] Lyα [b] Hα

Table 2. Conversion factors for visual brightness units

Wavelength (μm)	1 MJy/sr corresponds to I_λ [W/m² sr μm]	R/Å	F_ν[Jy][a] for 0 mag	1 S_{10} unit[b] corresponds to I_λ [W/m² sr μm]	I_ν [Jy/sr]	1 $S10_\odot$ unit corresponds to I_λ [W/m² sr μm]	S_{10} units	I_ν[Jy/sr]
0.36 (U)	2.31.10-5	5.27	1810	$1.37 \cdot 10^{-8}$	590	6.70.10-9	0.488	290
0.44 (B)	1.55.10–5	4.31	4260	2.1710-8	1400	$1.19 \cdot 10^{-8}$	0.550	770
0.502 ±12nm	1.19.10-5	3.78	3960	$1.55 \cdot 10^{-8}$	1300	1.28.10-8	0.825	1070
0.5.30 ± 3.5 nm	107-10-5	3.58	3790	1.3310-8	1240	$1.24 \cdot 10^{-8}$	0.935	1160
0.55 (v)	9.91.10-6	3.45	3640	1.1810-s	1200	1.18.10-8	1.0	1200
0.64 (R_C)	7.3210-6	2.96	3080	7.40.10–9	1010	$1.05 \cdot 10^{-8}$	1.42	1440
0.70 (R,)	6.12.10-6	2.71	2840	5.7010-9	930	9.21.10-9	1.61	1510
0.79 (It)	4.80.10-6	2.34	2550	$4.02 \cdot 10^{-9}$	840	7.80.10-9	1.94	1620
0.90 (I_J)	3.70.10 -'3	2.11	2250	2.7310-9	740	5.76.10-9	2.11	1560
1.25 (J)	1.92.10-6	1.52	1570	9.89 10-10	515	2.93.10–9	2.97	1530
1.65 (H)	$1.10 \cdot 10^{-6}$	1.15	1020	3.69 10-10	335	1.41.10–9	3.84	1290
2.2 (K)	$6\,19 \cdot 10^{-7}$	0.86'2	636	$1.29 \cdot 10^{-10}$	210	5.2410-10	4.06	850

"References: for U. B, V, R_C, I_C Bessell (1979); for R_J, I_J Allen (1985); for J, H, K Bessell and Brett (1988); for 502 nm and 530 nm Hayes (1985). The references give F. or F_λ for a star of magnitude zero, with uncertainties of about 2% - 5'% They are transformed to S_{10} units by: 1 zeroth magnitude star/sr = 3.046 S_{10} units.

[b] By definition 1 S_{10} unit corresponds to 27.78 mag/□", while 22 mag/□" = 205 S_{10}.

"The definition of this unit depends on the solar UBVRIJHK values, which are uncertain by several % beyond 1.0 μm. and below 400 nm. References: for U, B, V, R_J, I_J Allen (1985); for R_C, I_C Bessell and Brett (1988), Taylor (1992); for J, H, K Alonso et al. 1995; for 502 nm and 530 rrrn Neckel and Labs (1984).

ingly mom important, the light pollution due to the ever-growing man-made lighting.

For space observations atmospheric extinction and scattering are irrelevant, but other complexities like instrumental stray light of lunar, terrestrial or solar radiation may arise. For low orbits, spacecraft-induced glow phenomena may be present.

Quite understandably then, extracting accurate brightness values from Equ. (1) is a difficult task, and the past has seen a measure of disagreement between individual determinations, In the following we want to summarise what consensus has been obtained in this field during the last years, in order to provide a basis for easier reference and comparability.

The aim of this article is to provide the reader with comparatively easy access to agreed-upon or at least recommended values of night sky brightness. Inevitably this requires smoothing and interpolating of data. Therefore we want to give at the same time sufficient information on original publications to give an impression on the grade of agreement or disagreement of the available data and to allow the reader who wants to do so to draw his own conclusions.

We will go through the components basically in the order in which they appear in Equ. (1), and for each component try to provide information on the visual, infrared and ultraviolet wavelength ranges.

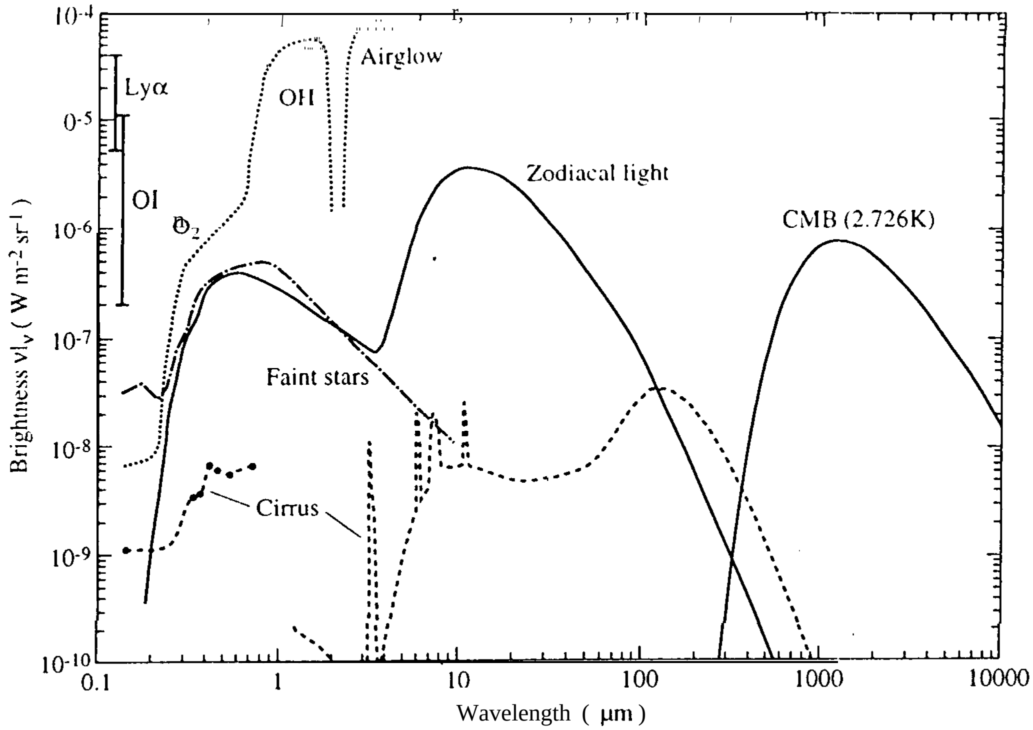

Fig. 1. Overview on the brightness of the sky outside the lower terrestrial atmosphere and at high ecliptic and galactic latitudes. The zodiacal emission and scattering as well as the integrated light of stars are given for the South Ecliptic Pole (l = 276°, b =-300). The bright magnitude cut-off for the stellar component is V = 6.0 mag for 0.3 – 1 pm. In the infrared, stars brighter than 15 Jy between 1.25 and 4.85 μm and brighter than 85 Jy at 12 μm are excluded, corresponding to the COBE/DIRBE beam. No cut-off was applied to the UV data, $\lambda \leq 0.3\,\mu m$. The interstellar cirrus component is normalized for a column density of 10^{20} H-atoms cm^{-2} corresponding to a visual extinction of 0.053 msg. This is close to the values at the darkest patches in the sky. Source for the long-wavelength data, $\lambda \geq$ 1.25 μm, are COBE DIRBE and FIRAS measurements as presented by Désert et al. (1996). The IR cirrus spectrum is according to the model of Désert et al. (1990) fitted to IRAS photometry. The short-wavelength data, $\lambda \leq$ 1.0 pm, are from the following sources: zodiacal light: Leinert and Grün (1990); integrated starlight: $\lambda \leq$ 0.3 pm, Gondhalekar (1990), $\lambda \geq 0.3 \mu$m, Mattila (1980); cirrus: λ = 0.15 μm, Haikala et al. (1995), λ = 0.35-0.75 μm, Mattila and Schnur (1990), Mattila (1979). The geocoronal Lyman α(121.6 nm) and the 01(130.4, 135.6 nm) line intensities were as measured with the Faint Object Camera of the Hubble Space Telescope at a height of 610 km (Caulet et al. 1994). The various references for the airglow emission can be found in section 6.

1. Overview

This paper is concerned with the night sky brightness from the far UV (≈ 100 nm) to the far infrared (≈ 200 #m).

Quite a few sources contribute to the diffuse brightness of the moonless sky ($I_{night\ sky}$) in this wavelength range:
– *airglow* from the upper atmosphere (1,4)
– *zodiacal light*, both as scattered sunlight and thermal emission of interplanetary dust particles, from interplanetary space (I_{ZL}). (In the far UV interplanetary Lyα emission is important.)
– *integrated starlight* (I_{ISL}) of the stars not individually accounted for
– *diffuse galactic light* (I_{DGL}), in the UV and visual mainly reflections off interstellar dust particles. Their infrared thermal emission is known as "cirrus" since the pioneering IRAS observations. It dominates the sky brightness in the far-infrared. Interstellar gas contributes line emissions over all of our wavelength range.
– *extragalactic background light* (I_{EBL}) in addition to the radiation of individually detected galaxies.

The combined light of these radiations is attenuated by *atmospheric extinction,* while *tropospheric scattering* of the infalling flux adds a non-negligible brightness component (I_{sca}).

Formally, the above statements may be expressed as

$$I_{night\ sky} = (I_A + I_{ZL} + I_{ISL} + I_{DGL} + I_{EBL}) \cdot e^{-\tau} + I_{sca} \quad (1)$$

It should be noted that the "extinction coefficient" τ (which depends on wavelength λ, zenith distance z, height of the observer and change of the atmospheric conditions with time) for diffuse sources has a value different from that determined for stars. The scattered light I_{sca} not only contains additional contributions due to stars and galaxies otherwise accounted for individually, but, increas-

Table 3. Conversion factors for infrared brightness units

Wavelength (μm)	1 MJy/sr corresponds to I_λ [W/m^2 sr μm]	I_λ [cgs^a]	F_ν [Jy] for star of 0 mag	Ref	1 S_{10} unit corresponds to I_λ [W/m^2 sr μm]	I_λ [cgs^a]	I_ν [Jy/sr]
1.25 (J)	1.92 10-6	1.9210-7	1570	1	9.89.10-'"	$9.89 \cdot 10^{-11}$	515
1.65 (H)	1.1010-6	1.1010-7	1020	1	3.6910 -'0	$3.69 \cdot 10^{-11}$	335
2.2 (K)	6.1910-7	$6.19 \cdot 10^{-8}$	636	1	1.29.10-'"	1.2910-"	209
3.5 (L)	$2.45 \cdot 10^{-7}$	2.4510-8	281	1	2,26.10-"	2.2610-12	92.3
3.8 (L')	2.0810-7	$2.08 \cdot 10^{-8}$	235	1	1.60.10-"	1.6010 -'2	77.2
4.8 (M)	1.30 .10-7	1.3010-8	152	1	$6.50 \cdot 10^{-12}$	6.5010-13	49.9
8.4	$4.25 \cdot 10^{-8}$	4.25 .10-9	58	2	8.0910-13	8.0910-14	19.0
10	3.0010-8	3.0010-9	40	3	3.9410 -'3	3.9410-14	13.1
10.6 (N)	2.67 .10-8	2.6710-9	36	3	3.1510 -'3	3.1510-14	11.8
12	2.0810-8	2.08 .10-9	28	4	2.19.10 -'3	$2.19 \cdot 10^{-14}$	10.5
20	7.50 .10-9	7.5010-10	10,4	3	2.5610 -'4	2.5610-15	3.41
21 (Q)	6.80 .10-9	6.80.10-10	9.4	3	2.10.10 -'4	2.1010-'5	3.09
25	4.80 .10-9	4.80.10-'0	6.7	4	$9.76 \cdot 10^{-15}$	$9.76 \cdot 10^{-16}$	2.04
60	8.33.10-10	8.33 .10-"	1.19	4			
90	3.7010-10	3.7010-11					
100	3.00.10-10	3.00.10-'1					
135	1.64.10-10	$1.64 \cdot 10^{-11}$					
175	9.7911-10	9.7910-12					
200	7.50.10-11	$7.50 \cdot 10^{-12}$					
240	$5.21 \cdot 10^{-11}$	5.2110-12					

[a] unit is [erg/cm^2 s sr Å]
[1] Bessell and Brett 1988 [2] Gillett and Stein 1971 [3] Rieke et al. 1985 [4] Neugebauer et al. 1988
The above references give F_ν or F_λ for a star of magnitude zero, with uncertainties of about 2% - 5%.
These values are transformed to S_{10} units by: 1 zeroth magnitude star/sr = 3.046 S_{10} units.

2. Brightness units

There are a number of different brightness units in use in the different fields of night sky brightness with their individual traditions and advantages. Rather than trying the Sisiphus work of standardising the use of brightness units, we give here conversion tables. These should help to transform whatever was given in an original reference to the desired physical units and allow intercomparison between different sources. As a rule, we will in the quantitative information on night sky brightness stay with the units of the original papers.

The units come in two groups:

(1) *physical units*:
- photons/cm^2 s sr Å
- Rayleigh/Å [R/Å]. Originally a measure of the emission in a column through the atmosphere, it also may be understood as a sky brightness of $10^6/4\pi$ photons/cm^2 s sr A
- F_λ in W/m^2 sr μ as well as in W/cm^2 sr μ and - in the cgs system - in erg/cm^{2}s sr Å, where
1 W/m^2 sr p = 10^{-4}W/cm^2 sr μ = 0.10 erg/cm^2 s sr Å
- F_ν in MJy/sr or Jy/sr, where 1 Jy = 10^{-26} W m^{-2}Hz^{-1}.
Note that νF_ν [W/m^2 sr Hz] = λF_λ [W/m^2 sr μm] and F_λ[W/m^2 sr pm] = c/λ^2[Hz/m]$\cdot 10^{-6} \cdot F_\nu$[W/m^2 sr Hz].

(2) traditional *units*:
- S_{10} units [tenth magnitude star per degree squared]. This is the brightness equivalent to the flux of a star of magnitude 10 (tenth magnitude in the wavelength range under consideration) distributed over one degree squared. Basically it refers to AO stars, which by definition have the same magnitude in all wavelength bands. The S_{10} unit was convenient in terms of calibration by stars and in that by its use most values of the night sky brightness in the visual fall in the range 100-1000.
- $B/\bar{B}_\odot$ (units of the mean brightness of the solar disk, mainly used in observations of the solar corona).
- $S10_\odot$ [solar type stars of tenth magnitude per degree squared]. The unit has also been called S1O or S_{10}(vis). This unit is a convenient measure of the zodiacal light in the visual, where its spectral energy distribution would be equal to the solar one for neutral scattering. With $V_\odot$ = -26.74 and the mean solid angle of the Sun of 6.80$\cdot$ 10^{-5} sr (.Allen 1985), we have, denoting the solar irradiance at 1 AU as $F_\odot$,

$$1\ S10_\odot = 6.6110\text{-}12\ F_\odot/\mathrm{sr} = 4.50.10\text{-}16\ B/\bar{B}_\odot.$$

As representation of the solar radiation we use the solar spectral irradiance data of Neckel and Labs (1984). This understanding of the $S10_\odot$ unit almost exactly agrees with the definition given by Sparrow and Weinberg (1976).

Because of the different traditions we give the conversion tables separately for the ultraviolet, the visual and the infrared. Note that the conversion factors to physical units may be slightly different for a narrow-band filter and a broad-band filter at the same wavelength. A useful quantity to remember when working with the conversion tables is the energy of a 1 μm photon: $h\nu$ = 1.986.10-19 Ws.

3. Coordinate transformations

Object coordinates are usually given in the equatorial α,δ sytem.
The zodiacal light is given in terms of ecliptic coordinates $\lambda - \lambda_\odot, \beta$ with the zero point of λ in the Sun. Description of a line of sight by elongation ϵ and inclination i also is common. For the relation between these two sets of coordinates see Figure 7 and section 3.5 below.
Integrated starlight is naturally presented in galactic coordinates 1, b.
For estimates of the diffuse background brightness at a given position, transformation between these three systems is necessary. Figures 2-6 provide a simple way to do so graphically with about one-degree accuracy, which is sufficient for many applications. The underlying transformation equations are summarised below for ease of access.

Airglow, extinction and scattering are best described in the local horizontal system A,z (azimuth, zenith distance). The transformation to the other systems depends on time and on the observer's geographic coordinates. For the horizontal system, only the equations for the transformation to the equatorial system are given.

3.1. *Ecliptic and equatorial coordinates*

The obliquity of the ecliptic is essentially constant, ϵ = 23.446° for equinox 1950, respectively ϵ = 23.439° for equinox 2000. The precession of the vernal equinox along the ecliptic is p. = 50.3 "/year. Hence

$$\lambda_{2000} = \lambda_{1950} + 0.698°. \quad (2)$$

The north ecliptic pole is at α = 18 h, δ = 90°- ϵ.
The north celestial pole is at λ = 90°, β = 90°- ϵ.
Both α and λ are counted eastward from the vernal equinox. Apart from the minimal change in ϵ, the transformation equations then are the same for 1950 and 2000:

3.1.1. Transformation $\alpha,\delta \rightarrow \lambda,\beta$

$$\begin{aligned}
\sin\beta &= \sin\delta\cos\epsilon - \cos\delta\sin\epsilon\sin\alpha \\
\cos\lambda &= \cos\alpha\cos\delta/\cos\beta \\
\sin\lambda &= [\sin\delta\sin\epsilon + \cos\delta\cos\epsilon\sin\alpha]/\cos\beta
\end{aligned} \quad (3)$$

3.1.2. Transformation $\lambda,\beta \rightarrow \alpha,\delta$

$$\begin{aligned}
\sin\delta &= \sin\beta\cos\epsilon + \cos\beta\sin\epsilon\sin\lambda \\
\cos\alpha &= \cos\lambda \operatorname{Cos}\beta/\operatorname{Cos}\delta \\
\sin\alpha &= [-\sin\beta\sin\epsilon + \cos\beta\cos\epsilon\sin\lambda]/\cos\delta
\end{aligned} \quad (4)$$

3.2. *Galactic and equatorial coordinates*

By IAU decision, for equinox 1950 the north galactic pole (NGP) is at α = 12 h 49.0 m, δ = 27.4° and the celestial pole at 1 = 123.0°, b = 27°24.0'. Hence the ascending node of the galactic equator is at α_0 = 18 h 49.0 m = 282.25°, l_0 = 33.0°. For equinox 2000, the coordinates of the north galactic pole are α = 12 h 51.42 m, δ = 27° 07.8', and we have α_0 = 282.86°, l_0 = 32.93°. The inclination of the galactic equator with respect to the ecliptic is 90°- δ_{NGP}. .4s α and λ, l is also counted eastwards.

With these parameters, the transformations are as follows:

3.2.1. Transformation $\alpha,\delta \rightarrow l,b$

$$\begin{aligned}
\sin b &= \sin\delta \ \sin\delta_{NGP} - \cos\delta\cos\delta_{NGP}\sin(\alpha - \alpha_0) \\
\cos(l - l_0) &= \cos(\alpha - \alpha_0)\cos\delta/\cos b \\
\sin(l - l_0) &= [\sin\delta\cos\delta_{NGP} + \\
&\quad \cos\delta\sin\delta_{NGP}\sin(\alpha - \alpha_0)]/\ \cos b
\end{aligned} \quad (5)$$

3.2.2. Transformation $l,b \rightarrow \alpha,\delta$

$$\begin{aligned}
\sin\delta &= \sin b\sin\delta_{NGP} + \cos b\cos\delta_{NGP}\sin(l - l_0) \\
\cos(\alpha - \alpha_0) &= \cos(l - l_0)\operatorname{COS} b/\cos\delta \\
\sin(\alpha - \alpha_0) &= [-\sin b\cos\delta_{NGP} + \\
&\quad \cos b\sin\delta_{NGP}\sin(l - l_0)]/\cos\delta
\end{aligned} \quad (6)$$

3.3. *Galactic and ecliptic coordinates*

In ecliptic coordinates, for equinox 1950 the north galactic pole is at $\lambda = 179.32°, \beta$ = 29.81°, and the ascending node of the galactic equator at λ_0 = 269.32°, l_1 = 6.38°. For equinox 2000, the coordinates of the north galactic pole are λ = 190.02°, β = 29.81°, and we have λ_0 = 270.02°, l_1 = 6.38°. The inclination of the galactic equator with respect to the ecliptic is 90° - β_{NGP}. As already mentioned, l is counted eastwards. With these parameters, the transformations are as follows:

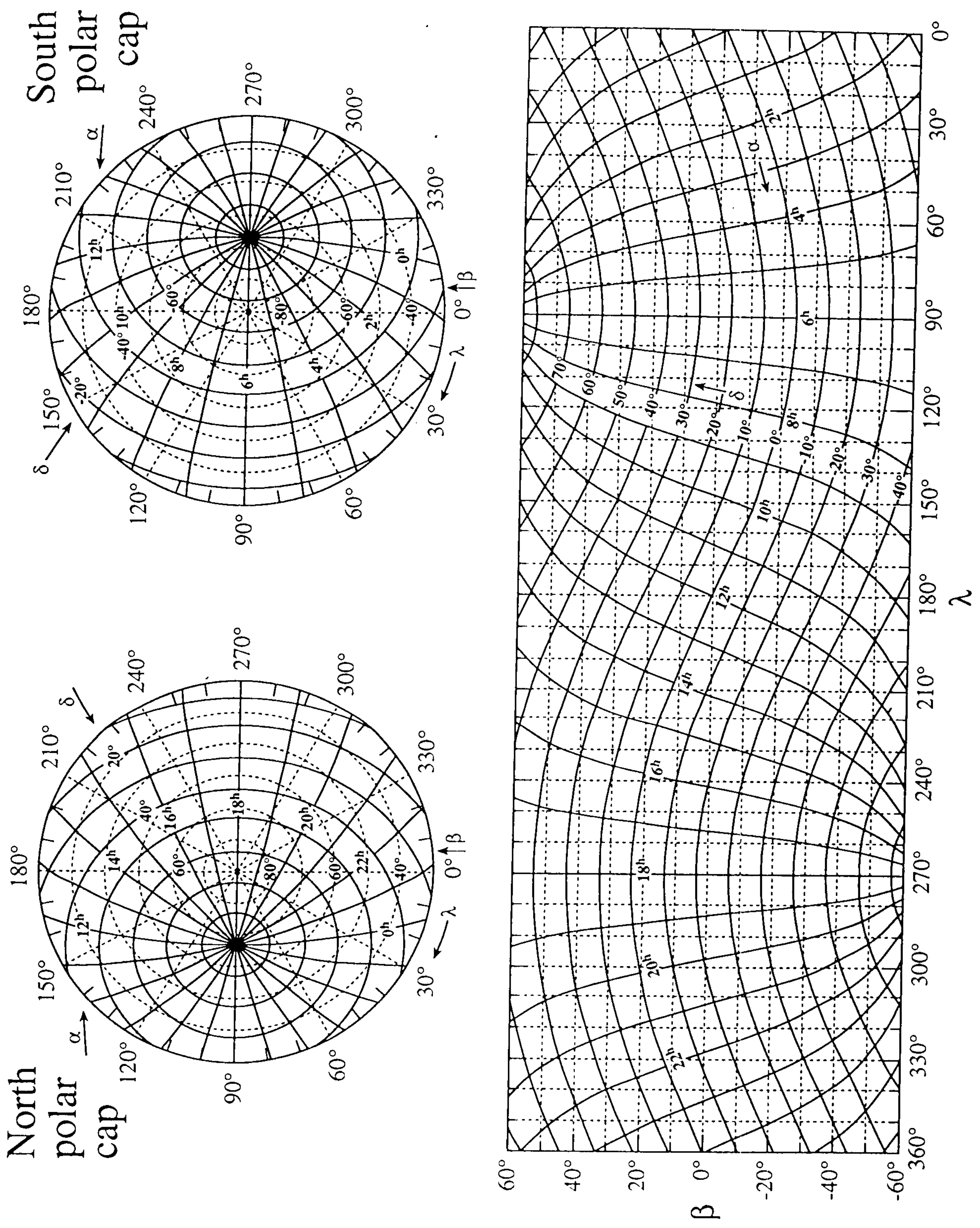

Fig. 2. Relation between coordinates α, δ (lines) and λ, β (underlying dotted grid) for equinox 2000

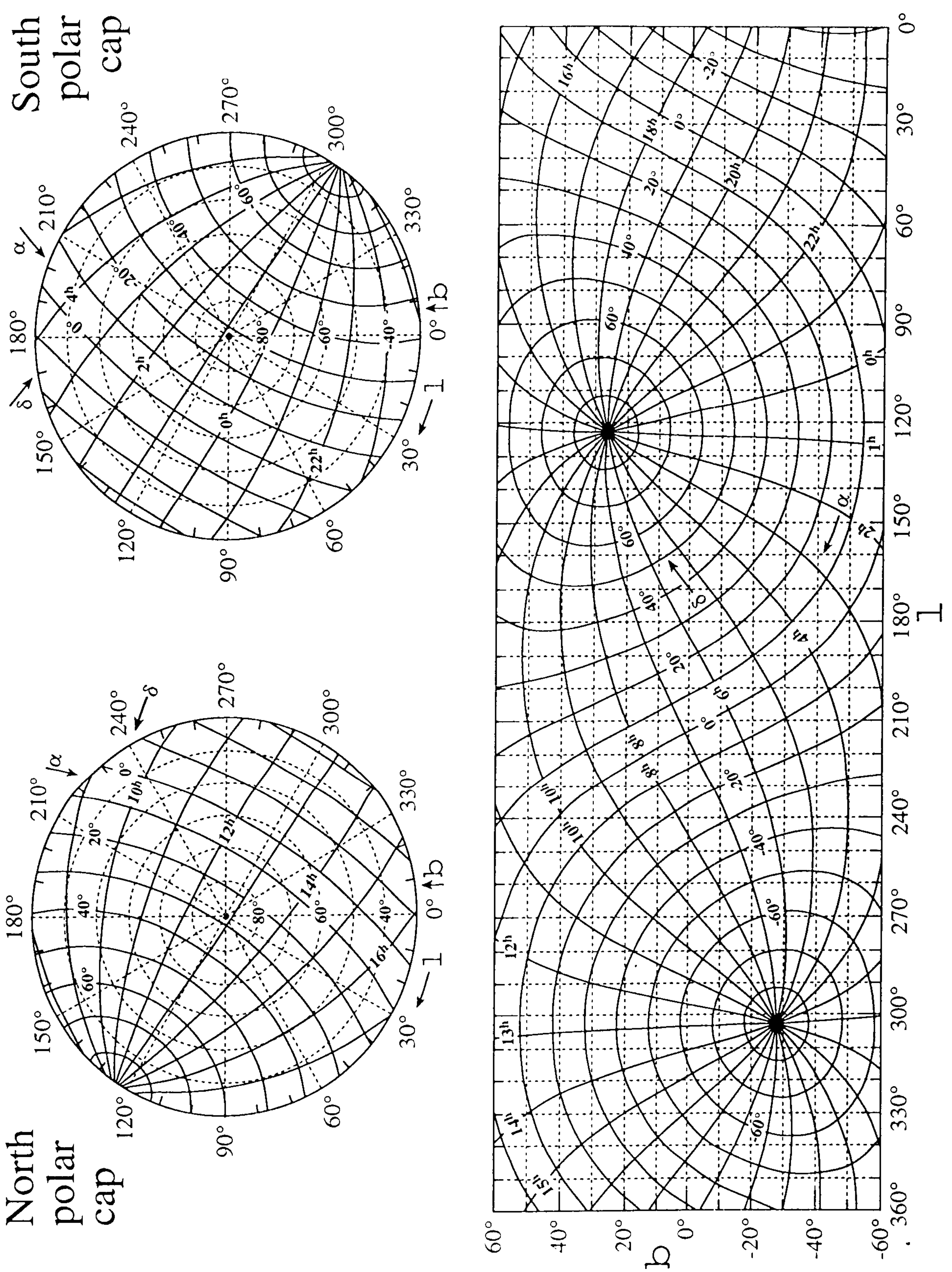

Fig. 3. Relation between coordinates α, δ (lines) and l, b (underlying dotted grid) for equinox 2000

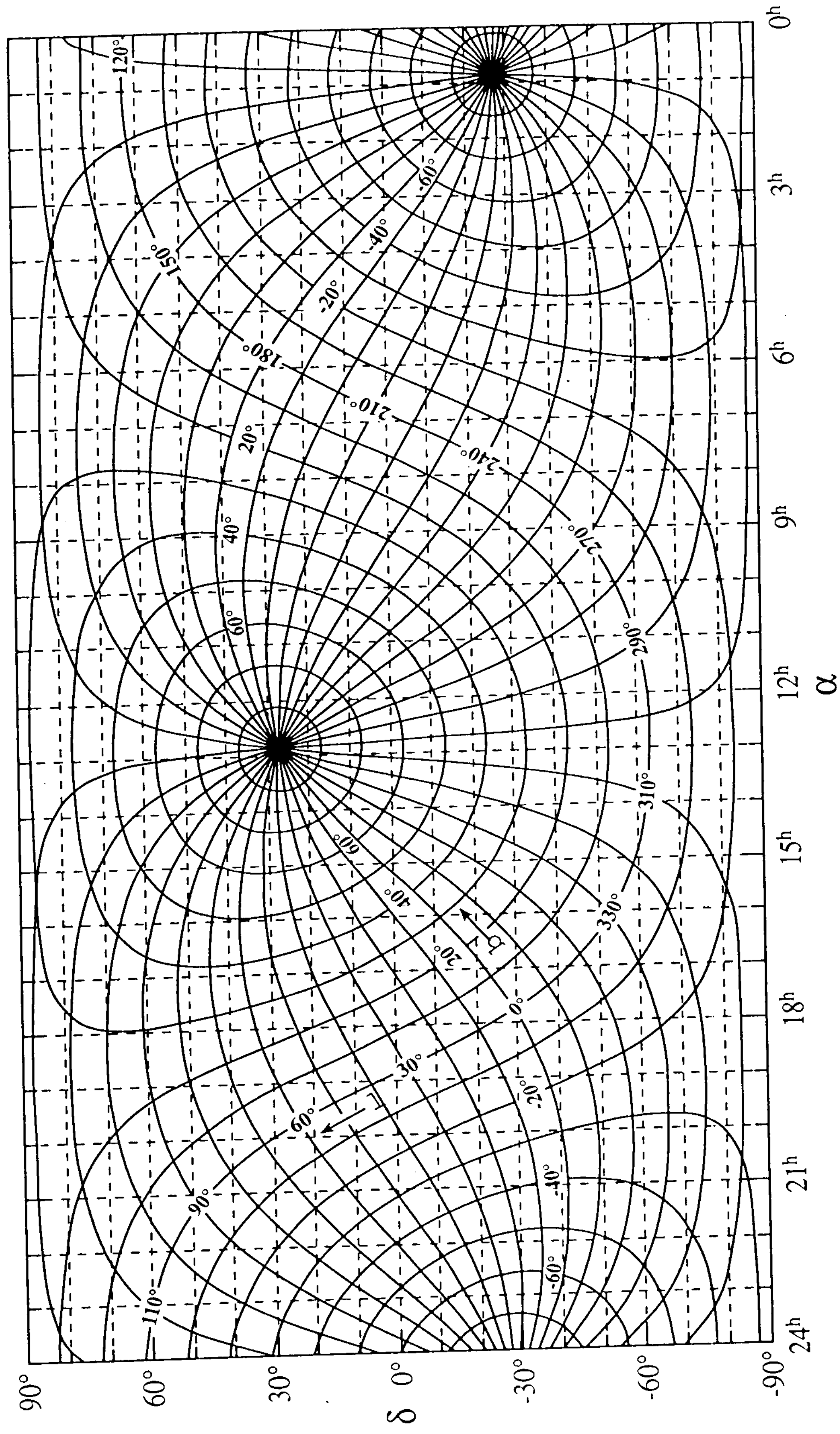

Fig. 4. Relation between coordinates l, b (lines) and α, δ (underlying dotted grid) for equinox 2000 - alternative projection.

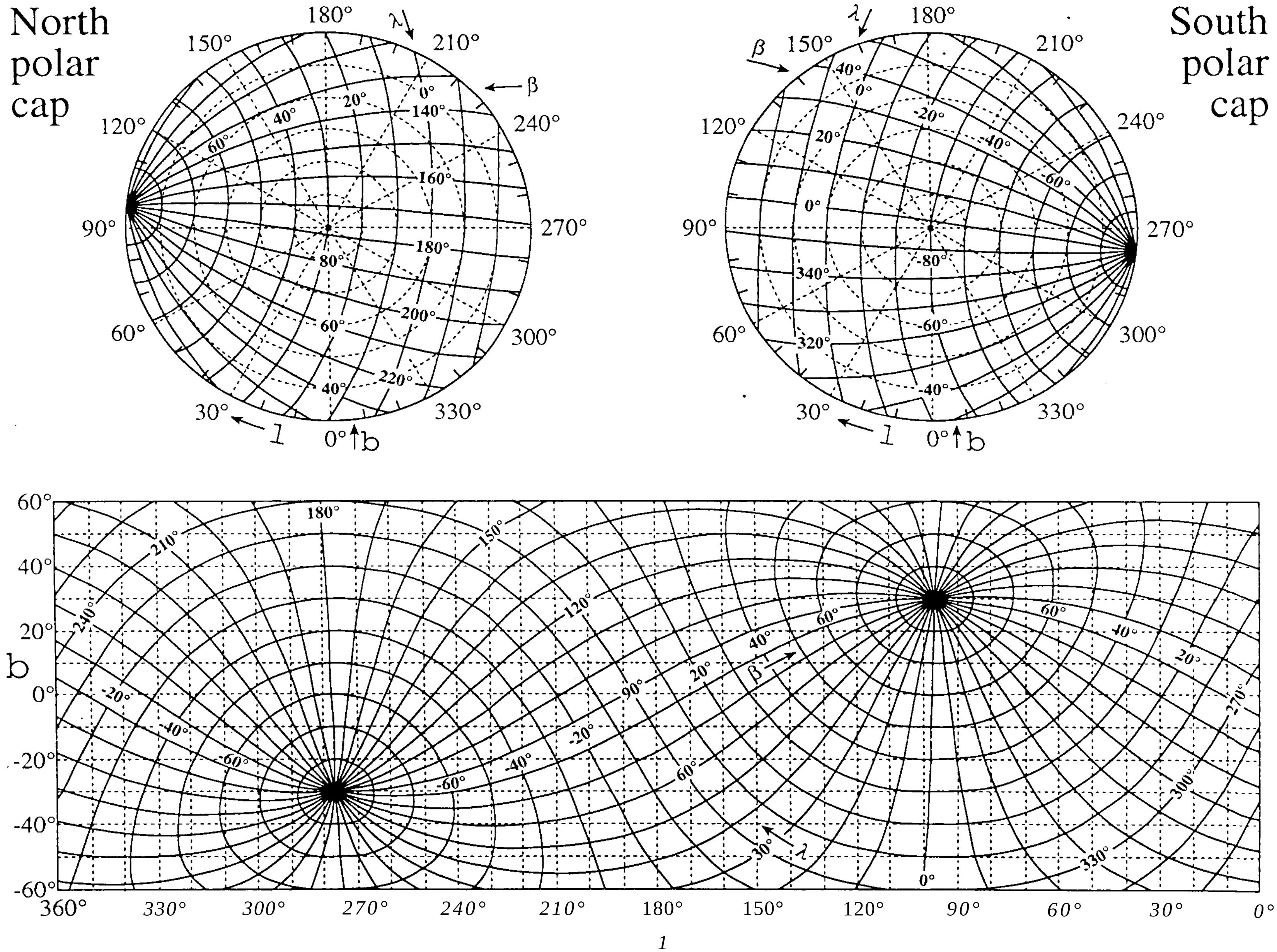

Fig. 5. Relation between coordinates λ, β (lines) and l, b (underlying dotted grid) for equinox 2000

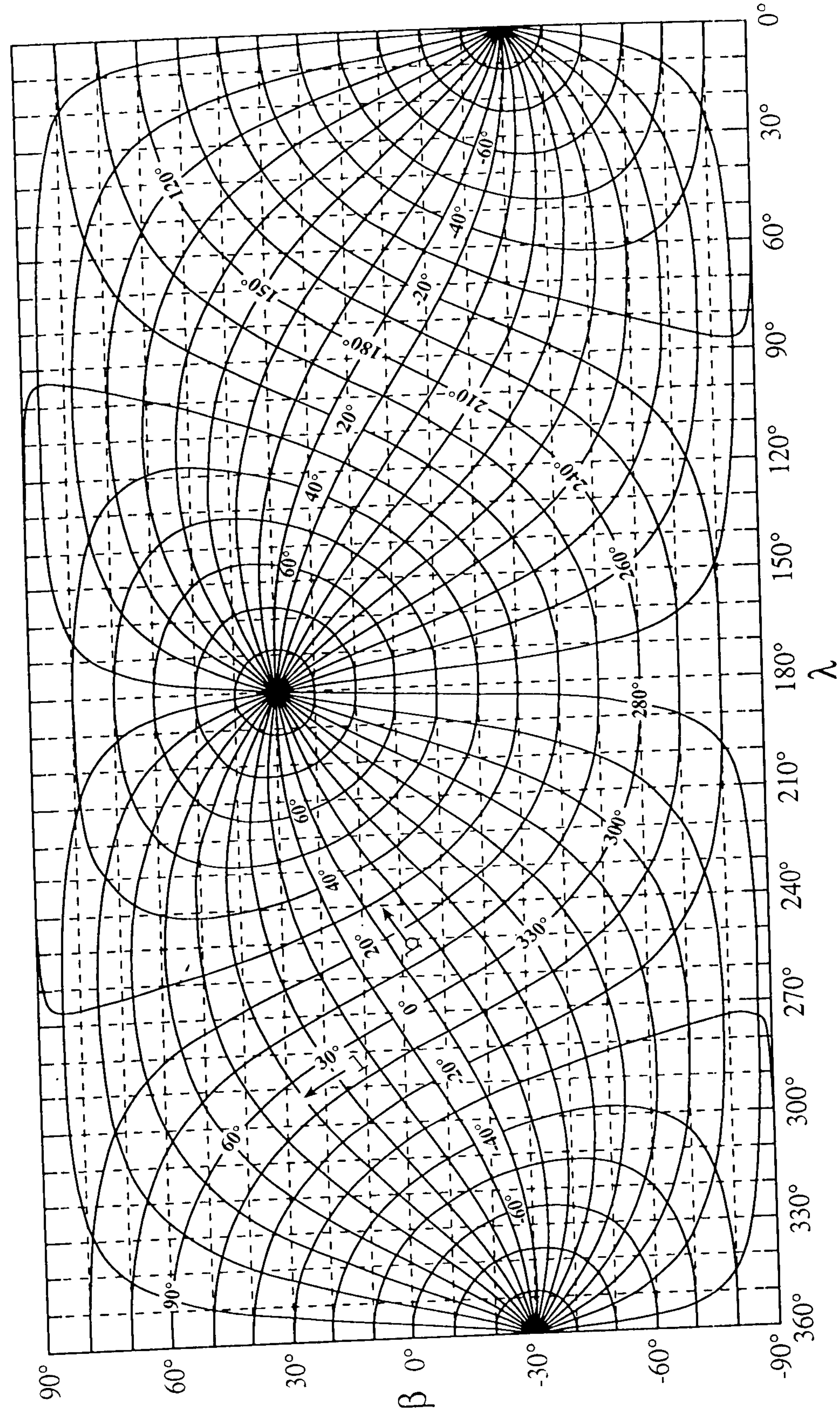

Fig. 6. Relation between coordinates l, b (lines) and λ,β (underlying dotted grid) for equinox 2000 – alternative projection.

3.3.1. Transformation $\lambda,\beta \rightarrow l, b$

$$\begin{aligned} \sin b &= \sin\beta\sin\beta_{NGP} - \cos\beta\cos\beta_{NGP}\sin(\lambda-\lambda_0) \\ \cos(l-l_1) &= \cos(\lambda-\lambda_0)\cos\beta/\cos b \qquad (7) \\ \sin(l-l_1) &= [\sin\beta\cos\beta_{NGP} + \\ &\quad \cos\beta\sin\beta_{NGP}\sin(\lambda-\lambda_0)]/\cos b \end{aligned}$$

3.3.2. Transformation $l, b \rightarrow \lambda,\beta$

$$\begin{aligned} \sin\beta &= \sin b\sin\beta_{NGP} + \cos b\cos\beta_{NGP}\sin(l-l_1) \\ \cos(\lambda-\lambda_0) &= \cos(l-l_1)\cos b/\cos\beta \qquad (8) \\ \sin(\lambda-\lambda_0) &= [-\sin b\cos\beta_{NGP} + \\ &\quad \cos b\sin\beta_{NGP}\sin(l-l_1)]/\cos\beta \end{aligned}$$

3.4. *Altazimuth and equatorial coordinates*

The transformation depends on local sidereal time Θ and on geographical latitude ϕ. Instead of elevation, zenith distance z = will be used. The zenith distance of the celestial pole is 90°- ϕ. Both, azimuth A and hour angle $t = \Theta - \alpha$ are counted from the meridian through west.

3.4.1. Transformation $\alpha,\delta \rightarrow A, z$

$$\begin{aligned} \cos z &= \sin\delta\sin\phi + \cos\delta\cos\phi\cos(\Theta-\alpha) \\ \cos A &= [-\sin\delta\cos\phi + \cos\delta\sin\phi\cos(\Theta-\alpha)]/\sin z \qquad (9) \\ \sin A &= \sin(\Theta-\alpha)\cos\delta/\sin z \end{aligned}$$

3.4.2. Transformation $A, z \rightarrow \alpha,\delta$

$$\begin{aligned} \sin\delta &= \cos z\sin\phi - \sin z\cos\phi\cos A \\ \cos(\Theta-\alpha) &= [\cos z\cos\phi + \sin z\sin\phi\cos A]/\cos\delta \qquad (10) \\ \sin(\Theta-\alpha) &= \sin A\sin z/\cos\delta \end{aligned}$$

3.5. *Alternate ecliptic coordinates*

Instead of $\lambda - \lambda_\odot, \beta$ also a sun-centered polar coordinate system is used. Its coordinates are the angular distance from the sun, called elongation ϵ, and a position angle i, counted from the ecliptic counterclockwise, called inclination. The relation between the two sets of coordinates, when describing the position of a field-of-view with respect to the sun, is shown in Figure 7.
It is unfortunate that the obliquity of the ecliptic, used in equations (3) and (4), and the angular distance from the sun, used in equations (11) and (12), both are designated by the. same letter ϵ. However we did not want to change the commonly used notations. In practice this dual meaning rarely should lead to confusion.

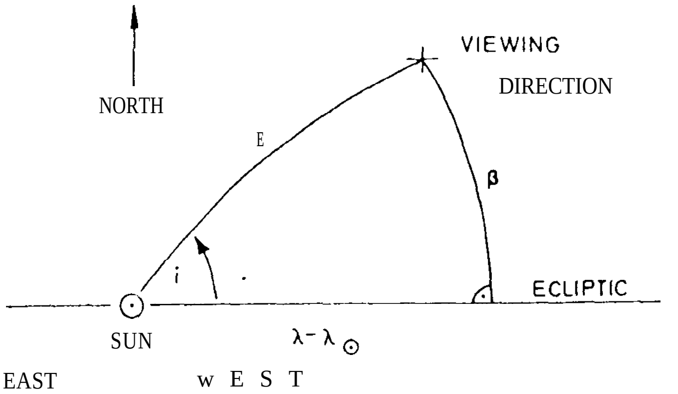

Fig. 7. Relation between the coordinates used for presenting zodiacal light measurements. λ is counted positive towards east, i is counted positive counterclockwise from the ecliptic west of the Sun

3.5.1. Transformation $\lambda-\lambda_\odot,\beta \rightarrow \epsilon, i$

$$\begin{aligned} \cos\epsilon &= \cos(\lambda-\lambda_\odot)\cos\beta \\ \cos i &= \cos\beta\sin(\lambda-\lambda_\odot)/\sin\epsilon \qquad (11) \\ \sin i &= \sin\beta/\sin\epsilon \end{aligned}$$

3.5.2. Transformation $\epsilon, i \rightarrow \lambda-\lambda_\odot,\beta$

$$\begin{aligned} \sin\beta &= \sin i\sin\epsilon \\ \cos(\lambda-\lambda_\odot) &= \cos\epsilon/\cos\beta \qquad (12) \\ \sin(\lambda-\lambda_\odot) &= \cos i\sin\epsilon/\cos\beta \end{aligned}$$

The reader is cautioned that in some papers the differential helioecliptic longitude $\lambda - \lambda_\odot$ may be called 'elongation' or may be designated as 'ϵ', contrary to our definition of elongation ϵ as the angular distance from the sun to the field-of-view.

Table 4. Comparison of B and V zenith sky brightnesses at different sites in units of mag/□″. The minimum /maximum values given are averages of the three smallest/largest sky brightness values (nightly averages) given for each site. In the case of ESO and Calar Alto, the numbers in boldface refer to actual B,V measurements, while the numbers in parentheses have been transformed from medium band filter measurements. The given solar 10.7 cm flux value (in units of 10^4 Jy) is the average of the three nights in question.

Site	I_B(max)	I_B(min)	I_V(max)	I_V(min)	Solar flux	Corresponding dates	ref.
ESO	[illegible]		**21.69**		164	**78-02-05**	1.
	(22.20)		(20.85)		168	80-12-06; 80-06-08; 88-12-05	
		22.97			161	**78-02-08**	
		(22.94)			116	78-02-08; 87–12–16; 87–12–19;	
	2 2 7 4			**21.91**	162	**78-02-07**	
				(22.02)	94	87-12-15; 87-12-16; 87-12-19;	
Calar Alto	22.51(22.30)				61	**95–05–26,27,28**	2.
		23.05(22.98)			176	89-05-06; 90-06-26; 93-06-21	
			21.16		206	89-05-04; 91-06-11; 91-06-16	
				21.79	61	95–05–27,28,29	
San Benito hit.	22.37		21.32		233	80-04-11; 81-07-28; 82-06-22	3.
		23.08			78	76-04-30; 87-04-25; 87-06-29	
				22.07	76	76-04-30; 87-04-28; 87-06-29	
Kitt Peak	22.65				114	88-01-21; 88-03-17; 88-06-14	4.
		22.98			75	86-12-02; 86-12-30; 87-06-22	
			21.60		114	87-11-20; 88-03-17; 88-06-14	
				22.01	75	86-12--02; 86-12-31; 87-06-22	
Crimea	21.91		21.10		122	68-04--28; 71-04-25; 70-08-09	5.
		23.05		22.05	136	68-03--29; 68-04-06; 68-04-28	
Hawaii	22.27				210	88--11--13; 89-03-28; 89-09-12	6.
		23.03			142	87-08--26; 87-11-13; 89-06-10	
			21.21		166	85-12-13; 88-11-13; 89-03-28	
				22.05	102	86-06-02; 87-08-26; 88-07-18	
McDonald Observatory	22.54		21.54		138	60-02-04; 72-12-30; 73-01-12	7.
		23.01			156	60-01-27; 72-01-11; 72-01-15	
				21.92	159	60-01-27:72-01-15: 73-01-08	

1. Mattila et al. (1996)
2. Leinert et al. (1995), Leinert et. al. (1996, unpublished)
3. Walker (1988)
4. Pilachowski et al. (1989)
5. Lyutyi and Sharov (1982)
6. Krisciunas (1990)
7. Kalinowski, Roosen, and Brandt (1975)

4. Total sky brightness

In this section we give the minimum diffuse sky brightness to be expected (values for an arbitrary field-of-view have to beestimaterl as a sum of the components of the night sky brightness). For the ultraviolet and the infrared, extraterrestrial values are given. For the visual spectral region we give the values as seen from ground. Here, the extraterrestrial values would closely correspond to the minimum brightness of the zodiacal light, stars being resolved by optical space telescopes like the HST. For the near-infrared, sky brightness as seen from ground is also included.

In the infrared, total brightnesses as observed by the DIRBE experiment onboard COBE are conveniently available in the form of weekly averages of the brightness seen in different viewing directions from the heliocentric position taken by COBE during the respective week. The data, covering the 10 photometric DIRBE bands from 1.25 μm to 240 μm (see section 8.5), including Stokes Parameters Q and U for the 1.25 μm, 2.2 μm and 3.5 μm bands, are available on CD-ROM or tape. Under http://www.gsfc.nasa.gov/astro/cobe/cobe_home.html on the World Wide Web one finds the information necessary to actually receive those data.

4.1. *Ultraviolet*

4.1.1. Far UV (91.2 nm - 180 nm)

The sky brightness over most of this band is the sum of starlight and starlight scattered by interstellar dust. The

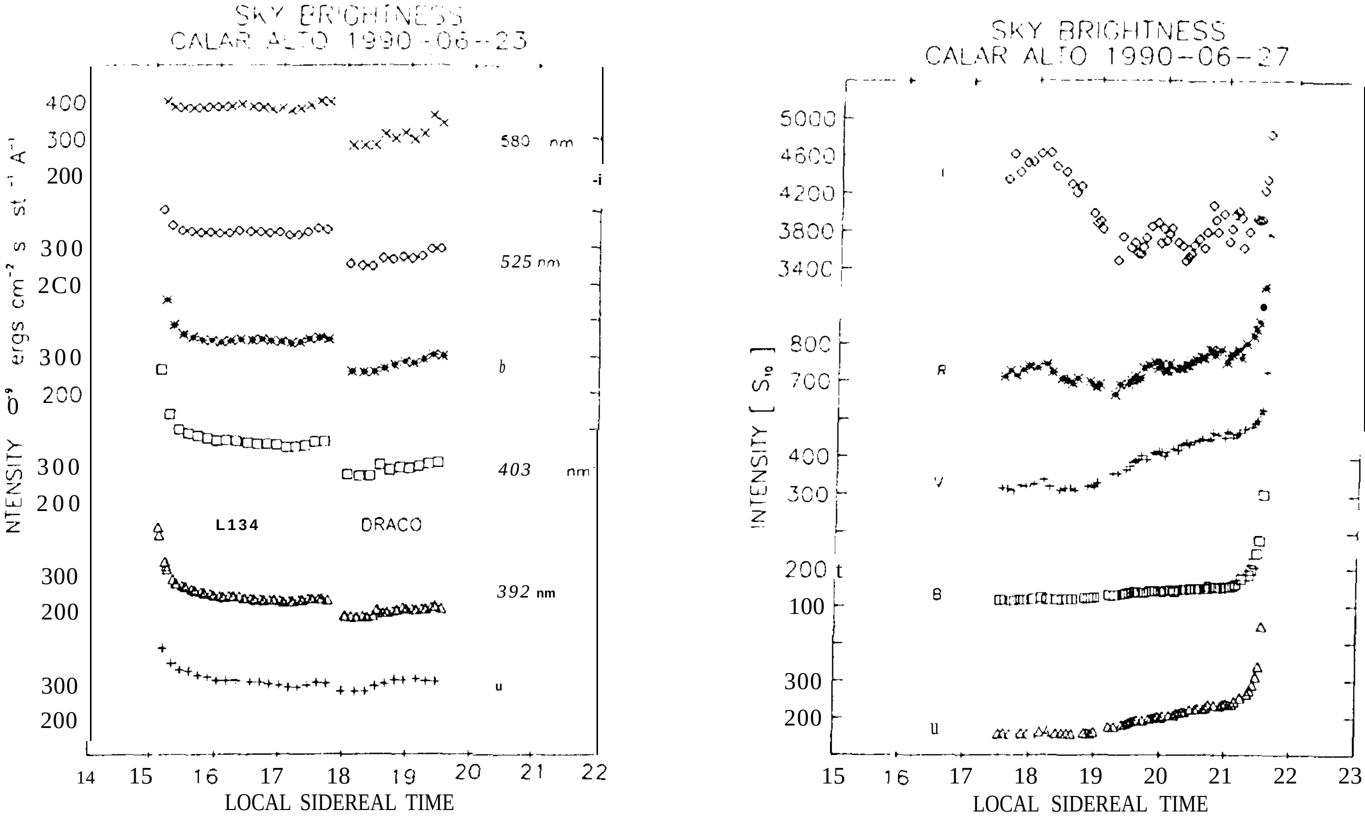

Fig. 8. Variation of the night sky brightness at Calar Alto during the course of one night. Left: Observations in medium band filters, including Strömgren *u* and *b* on June 23, 1990. L134 is a dark cloud in Ophiuchus at ecliptic latitude 15°, the Draco field is at high ecliptic latitude, hence the lower brightness level. Right: Observations in broad band filters on June 27, 1990 near the ecliptic pole. -- The effect of dawn and dusk can be seen in the data around 15 h and 21 h siderial time.

Sun's flux is sufficiently low that zodiacal light is virtually non-existent. An intense diffuse emission in this band is emission from hydrogen Lyman-alpha at 121.6 nm. This flux is produced by scattering of solar radiation by neutral hydrogen in the Earth's geocorona, and by scattering from neutral interstellar hydrogen entering the heliosphere. The geocoronal flux varies by more than a factor of 10 between day and night; typical fluxes range from 3 kR (night) to 34 kR (day). This flux varies with distance from the Earth's geocorona. An excellent exposition of the variation of this flux as a function of these variables is given by Raurden et al. (1986). See also section 6.

4.1.2. Near UV (180 nm -300 nm)

The sky brightness in this range is primarily the sum of zodiacal light, starlight, and starlight scattered by interstellar dust. The zodiacal light in this range has not yet been well characterized, the presently available information is shown in sections 8.4 and 8.6. The integrated starlight is discussed in Section 10.2. Scattering by dust *near* early type stars is a major contributor to the diffuse flux in this range, and is highly variable from place to place in the Galaxy (see also section 11.5).

4.2. *Visual*

Table 4, adapted from a recent paper (Leinert et al. 1995), gives minimum and maximum values of broadband sky brightness as observed in moonless nights at several observatories in suitable "dark regions" of the sky. The main constituents of this diffuse brightness are airglow, zodiacal light and tropospherically scattered light, in this order, but in roughly comparable quantities. The variation between minimum and maximum is mostly due to solar activity, which leads to increased airglow emission. The individual entries in Table 4 are not stricly comparable. Some of the measurements were performed with small telescopes and excluded stars only down to about 10 mag (San Benito Mt.), about 13 mag (Kitt Peak, 90 cm telescope, diaphragm 50") and about 12 mag (Hawaii, 15 cm telescope, 6.5 □ '). The residual contributions of individual stars to their observed zenith brightnesses then can be estimated (Roach and Megill 1961) to be still 0.05-0.22 mag, 0.03-0.11 mag, and 0.05-0.15 mag, respectively, both at B and V. In clear nights therefore the sky appears to be more or less equally dark at all major observatories.

Figure 8 shows the observed variation of sky brightness in a starless spot for a typical night. both for inter med Ateband and broad-band observations. The central wavelengths of the intermediate bands have been selected to coincide with minima of the night sky spectrum. Figure 9 indicates what emission *may* be expected outside those bands. Brightness variations usually are well correlated between different wavelength bands (see Leinert et al. 1995 and Figure 29 in section 6.3). An example for the variation of sky brightness with solar activity is given in Figure 10.

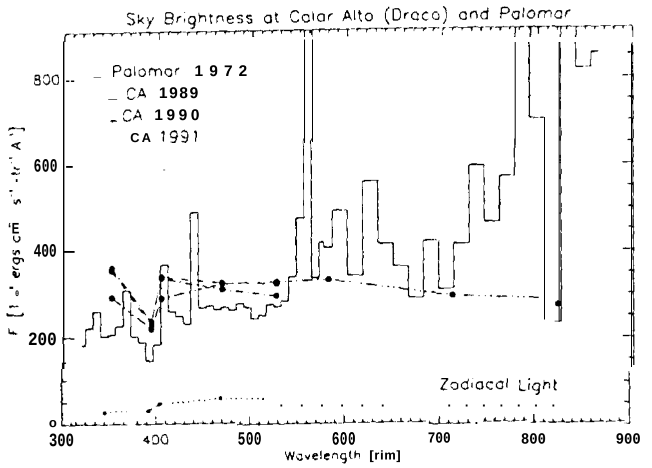

Fig. 9. A low resolution night sky spectrum at Palomar Observat–ory, taken on November 28, 1972 (Turnrose 1974), compared to medium band measurements on Calar Alto (CA).

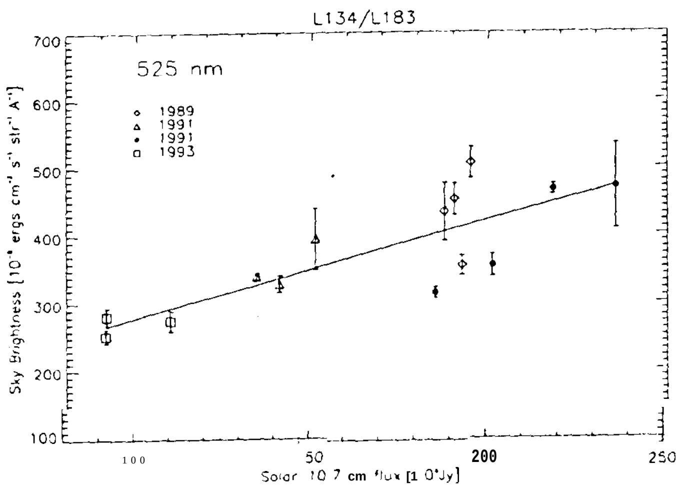

Fig. 10. Correlation between the night sky brightness observed at Calar Alto at 525 nm with the solar activity, measured by the 10.7 cm radio flux density (in units of 10' Jy).

4.3 Near-infrared from the ground

The near-infrared sky brightness seen from ground at a typical observing site is shown in Figure 11. Below $2\,\mu m$ the night sky emission is dominated by OH airglow emission (see also section 6). Above $2\,\mu m$ thermal emission by the atmosphere is dominating. Between 2 μm and 4 μm emission from the telescope also adds a considerable fraction to the total radiation.

The situation is quite different for observations from Antarctica. The much reduced thermal emission in an environment with winter temperatures below -60° C leads to a substantial reduction of sky background particularly in the K photometric band (Ashley et al. 1996, Nguyen et al. 1996, see Figure 12 and Table 5). Because of the absence of strong airglow emission between $2.3\,\mu m$ and $2.5\,\mu m$ (see Figure 27', section 6. 1.c), in this spectral region values of zenith sky brightness as low as $50\,\mu$Jy arcsec^{-2} (K = 17.7 mag arcsec^{-2}) have been measured. The dependence on zenith distance is normal: proportional to sec z down to $z \approx 50°$. In the L band, between 2.9 μm and 4.1 μm, still an improvement by a factor of 40- 20 was found.

Table 5. Comparison of K band sky brightnesses[a]

Site	λ (μm)	$\Delta\lambda$ (pm)	I (μJy/□″)	I (mag/□″)	Ref.
Mauna Kea	2.22	0.39	≈4000	≈13	1
Mauna Kea	2.11	0.35	≈2700	≈13.4	1
Balloon	2.4	0.1	< 26	< 18.4	2
Balloon	2.38	0.08	130±19	16.7	3
South Pole	2.36	0.14	162±67	16.5	4
South Pole	2.40	0.04	50	17.7	5

[a] adapted from Nguyen et al. (1996)

References: [1] Wainscoat and Cowie 1992, [2] Hofmann et al. 1974, [3] Matsumoto et al. 1994, [4] Nguyen et al. 1996, [5] Ashley et al. 1996.

4.4. Infrared

Table 6 shows the darkest spots on the sky from $1\,\mu m$ to $240\,\mu m$ as measured by the infrared photometric experiment DIRBE on the COBE satellite in an 0.7 °s0.7 °wide field-of-view (adapted from Hauser 1995). These are conservative upper limits to the cosmic infrared background light. For wavelengths of $\lambda \leq 60\mu m$, where the zodiacal light (thermal emission) dominates, the darkest fields are close to the ecliptic poles. For longer wavelengths, the thermal emission of interstellar dust is dominating, and the darkest fields are found in regions around the galactic poles with particularly low HI 21cm emission (Lockman et al. 1986).

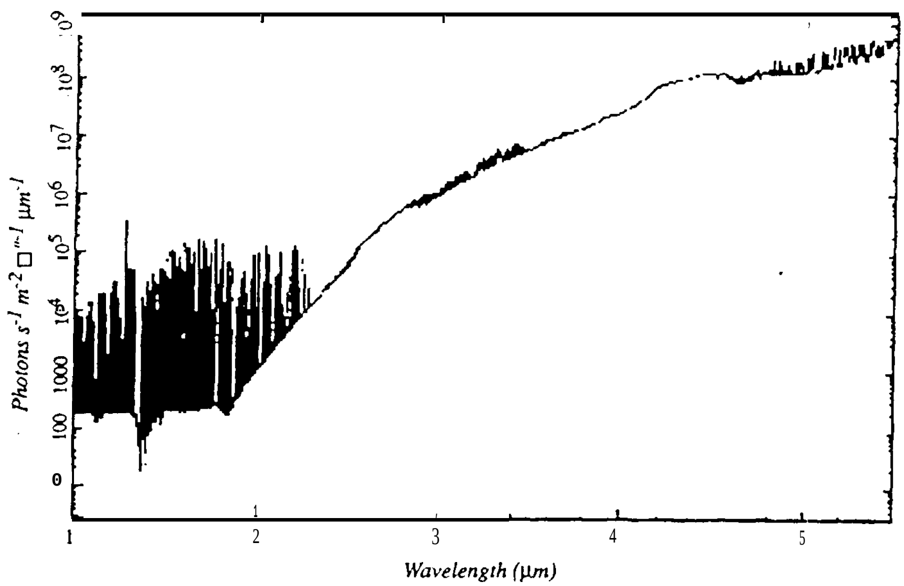

Fig. 11. Near-infrared spectrum of the night sky brightness, measured just inside the cryostat window of the UKIRT IRCAM camera (McCaughrean 1988). Note that 10^4 photons $m^{-2}s^{-1}\square''^{-1}\mu m^{-1}$ correspond *to* 4.23 $Wm^{-2}sr^{-1}\mu m^{-1}$. *From* Beckwith 1994.

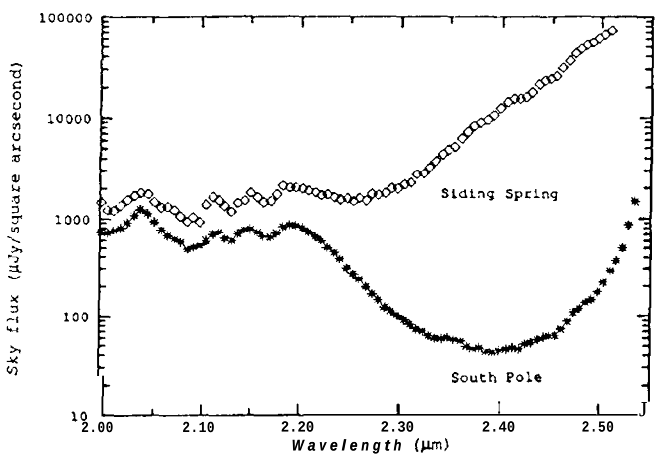

Fig. 12. Near-infrared sky brightness around 2.3 μm as observed in Antarctica on May 31, 1994 with an ambient temperature of -62”. The dip around 2.4 μm is due to the lack of airglow emission in this region. The South Pole data are compared to observations obtained at the Siding Spring observatory (.Australia) with an ambient temperature of +10°. From Ashley *et* al. (1996).

Table 6. Minimum observed sky bright nesses found in the DIRBE weekly averaged sky maps

λ (μm)	$\nu I_\nu = \lambda I_\lambda$ (nW m^{-2} sr^{-1})	I_ν (MJy/sr)	Reference
1.25	393 ± 13	0.16 ±0.005	1
2.2	150 ± 5	0.11 ±0.004	1
3.5	63± 3	0.074 ±0.004	1
4.9	192 ±7	0.31 ±0.01	1
12	2660 ± 310	10.7 ± 1.2	1
25	2160 ± 330	18 ±3	1
60	261 ± 22	5.2 ±0.4	1
100	74± 10	2.5 * 0.3	1
140	57 ± 6	2.7± 0.3	1
240	. 22 ± 2	1.8± 0.2	1

[1] Hauser 1995

5. Tropospheric scattering

From earthbound measurements of the night sky brightness the contribution due to tropospheric scattering (see Equ. 1) has to be subtracted in order to determine its uncontaminated extraterrestrial intensity and polarization, The strongest contributions to scattered light come from airglow, zodiacal light (ZL) and integrated starlight (ISL) - that is, the correction to be applied is in part determined by the brightness distribution of the sources under study themselves. The correction is of the order of 10- 100 S_{10}, which corresponds to 15% or more of the Zodiacal light, and to typically 10- 30% of the ISL. Due to the limited accuracy to which the correction can be determined, it can be applied explicitly only to measurements aimed at the determination of ZL and ISL. The weaker components of the night sky brightness, DGL and EBL, must be determined by differential methods.

Detailed calculations on first order Rayleigh- and Mie-scattering (including linear and circular polarization) in the (spherical) Earth's atmosphere illuminated by a uniform, unpolarized source, by the Milky Way and by the Zodiacal light were performed by Staude (1975) for various values of the optical thickness of the Rayleigh and Mie components of the atmosphere, and assuming two different values for the refractive index m of atmospheric aerosols (m = 1.33, as for water vapour, and $m = 1.5 - 0.1i$, as for aerosols in dry air). The position and orientation of Milky Way and Zodiacal Light cone were varied independently over the whole range occurring in practice. Some results from this study are reported in the following.

5.1. *A uniform unpolarized source of unit brightness*

The brightness of tropospherically scattered airglow can be estimated using the results obtained for an uniform unpolarized source of unit brightness (extending over the entire visible sky) in the single scattering approximation, which are given in Figures 13 and 14. They give the intensity of the scattered light and its polarization as a function of zenith distance of the observing direction z_0, for different values of the zenith extinction τ_0 of the Rayleigh and Mie component.

Table 7. The correction factors for multiple scattering in a Rayleigh atmosphere for different values of the zenith extinction τ_R^o. See text for details.

τ_R^o	F_{MS}	f_{MS}
0.05	1.12 ± 0.04	0.95 ± 0.05
0.10	1.22 ± 0.06	0.90 ± 0.05
0.15	1.33 ± 0.06	0.85 ± 0.05
0.20	1.44 ± 0.07	0.80 ± 0.05

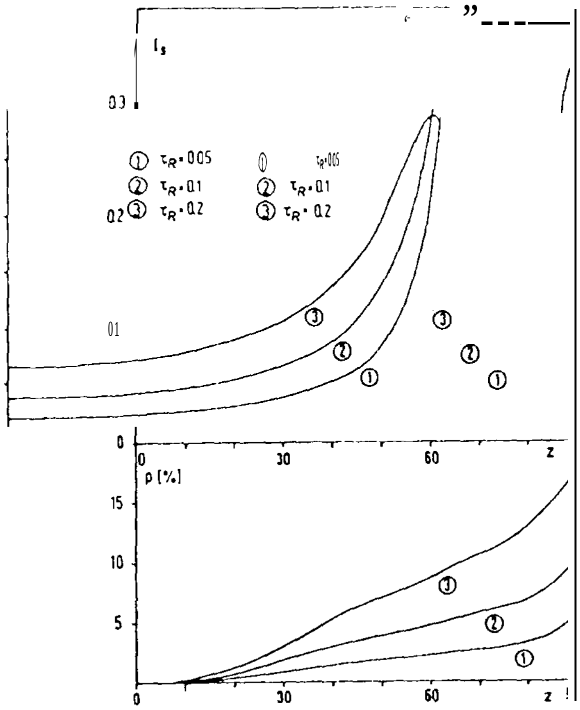

Fig. 13. Intensity and polarization of the atmospheric scattered light in a pure Rayleigh atmosphere, for a source of unit brightness and various values of the zenith extinction τ_R, as a function of zenith distance z.

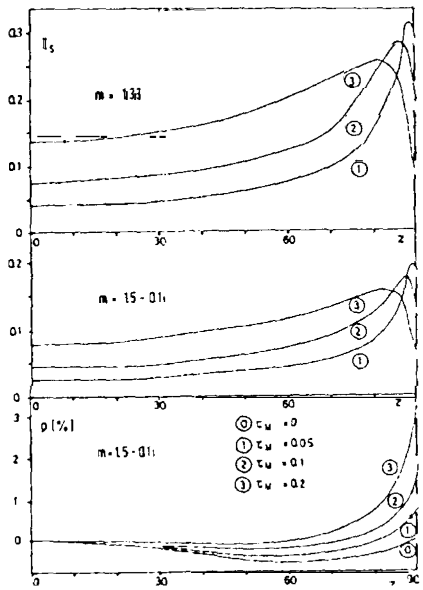

Fig. 14. Same as Figure 13 for two pure Mie atmospheres

Table 8. Intensity in S_{10} and polarization of scattered integrated starlight for two pure Rayleigh and two pure Mie atmospheres with the given values of zenith extinction τ_R and τ_M. The galactic center is assumed at the zenith (z = 0), the galactic equator crosses the horizon at A = 90, 270; l and b are galactic coordinates

l	b	A	z	I_1	I_2	I_s	p_s	ϕ	I_2	I_s	p_s	ϕ
					τ_R = .10				τ_R = 0.20			
0	0	0	0	260.0	235.3	4.0	10.4	90	213.0	8.2	8.7	90
330	0	90	30	220.8	196.8	4.5	12.9	90	175.4	9.0	11.4	90
333	14	120	30	112.5	100.3	4.4	11.6	69	89.4	8.9	10.2	69
344	26	150	30	57.3	51.1	4.4	8.3	41	45.5	8.8	6.9	43
360	30	180	30	52.3	46.6	4.3	6.0	0	41.6	8.7	4.4	0
300	0	90	60	151.9	124.5	7.0	18.3	90	102.0	13.4	17.4	90
304	26	120	60	54.1	44.3	6.8	15.9	82	36.3	13.1	15.4	82
319	49	150	60	36.3	29.7	6.5	9.9	74	24.4	12.5	10.1	77
360	60	180	60	29.4	24.1	6.4	4.7	90	19.7	12.2	6.1	90
					τ_M = .05				τ_M = 0.15			
360	0	0	0	260.0	247.4	5.9	0.6	90	223.9	15.8	0.5	90
330	0	90	30	220.8	208.4	5.8	0.7	90	185.7	15.4	0.6	90
333	14	120	30	112.5	106.2	4.9	0.7	67	94.7	13.0	0.7	68
344	26	150	30	57.3	54.1	3.9	0.6	40	48.2	10.2	0.6	42
360	30	180	30	52.3	49.4	3.5	0.5	0	44.0	9.4	0.4	0
300	0	90	60	151.9	137.5	7.2	1.0	90	112.7	17.4	1.1	90
304	26	120	60	54.1	48.9	5.1	1.1	86	40.1	12.3	1.3	87
319	49	150	60	36.3	32.8	3.5	0.9	86	26.9	8.6	1.1	88
360	60	180	60	29.4	26.6	3.0	0.7	90	21.8	7.4	1.0	90

Table 9. Same as for Table 8, but with the Galactic center at A=0, z=180

l	b	A	z	I_1	I_2	I_s	p_s	ϕ	I_2	I_s	p_s	ϕ
					$\tau_R = 0.10$				$\tau_R = 0.20$			
180	0	0	0	100.0	90.5	2.8	9.9	90	81.9	5.6	8.1	90
180	30	0	30	50.6	45.1	3.1	7.0	180	40.2	6.1	5.2	180
196	26	30	30	51.9	46.2	3.1	8.0	144	41.2	6.2	6.5	142
207	14	60	30	67.6	60.2	3.1	9.8	115	53.7	6.2	8.5	114
210	0	90	30	100.1	89.2	3.2	10.6	90	79.5	6.3	9.3	90
180	60	0	60	29.0	23.8	4.7	0.6	180	19.5	8.9	1.5	90
221	49	30	60	35.8	29.3	4.8	5.4	120	24.1	9.1	5.8	111
236	26	60	60	51.9	42.5	5.0	10.2	103	34.9	9.5	10.2	101
240	0	90	60	101.8	83.4	5.1	12.1	90	68.4	9.7	12.0	90
					$\tau_M = 0.05$				$\tau_M = 0.15$			
180	0	0	0	100.0	95.1	3.0	0.7	90	86.1	8.0	0.6	90
180	30	0	30	50.6	47.7	2.5	0.7	180	42.5	6.5	0.6	180
196	26	30	30	51.9	49.0	2.6	0.7	148	43.6	6.9	0.6	146
207	14	60	30	67.6	63.8	3.0	0.6	118	56.8	7.9	0.6	116
210	0	90	30	100.1	94.5	3.3	0.6	90	84.3	8.7	0.6	90
180	60	0	60	29.0	26.2	2.6	0.2	180	21.5	6.3	0	90
221	49	30	60	35.8	32.4	3.0	0.2	129	26.6	7.2	0.3	107
236	26	60	60	51.9	47.0	1.0	0.5	101	38.5	9.6	0.6	98
240	0	90	60	.01. s	92.1	5.1	0.6	90	75.5	1'2.3	0.6	90

Table 10. Intensity in S_{10} and polarization of tropospherically scattered Zodiacal light. The Sun is located at $A = 90$, $z = 105$, the ecliptic is perpendicular to the horizon

ϵ	β	A	z	I_1	I_2	I_s	p_s	ϕ	I_2	I_s	p_s	ϕ
						$\tau_R =$	10			$\tau_R =$	20	
105	0	0	0	158.2	143.2	9.5	32.5	90	129.6	18.5	27.6	90
85	0	90	20	220.3	198.1	10.6	26.5	90	178.2.	20.5	22.6	90
89	13	130	20	173.1	155.7	10.3	27.8	48	140.0	20.0	23.5	48
105	20	180	20	133.6	120.1	9.9	31.6	178	108.0	19.1	26.5	177
125	o	270	20	138.6	124.7	10.0	33.2	90	112.1	19.3	28.6	90
65	0	90	40	351.6	308.7	13.7	18.7	90	271.0	25.9	16.6	69
72	24	130	40	170.2	149.5	12.9	20.2	46	131.2	24.3	17.1	47
105	40	180	40	102.4	89.9	11.4	29.0	175	78.9	21.6	23.8	174
145	o	270	40	146.8	128.9	12.7	27.9	90	113.2	23.9	25.1	90
45	0	90	60	865.6	709.4	21.4	13.0	90	581.4	38.5	12.5	90
52	34	130	60	186.8	153.1	19.2	10.8	44	125.5	34.6	9.1	48
105	60	180	60	90.5	74.2	15.8	25.9	171	60.8	28.6	20.5	170
165	0	270	60	164.4	134.8	20.0	20.1	90	110.4	35.9	19.2	90
30	0	90	75	2200.0	1504.5	37.8	11.3	90	1028.9	61.6	11.7	90
34	38	130	75	201.4	137.7	33.1	3.0	45	94.2	54.1	3.1	66
105	75	180	75	78.8	53.9	26.4	23.9	169	36.9	43.3	18.2	166
180	0	270	75	180.0	123.1	36.4	15.2	90	84.2	59.3	15.4	90
						$\tau_M =$	05			$\tau_M =$	5	
105	0	0	0	158,2	150.5	6.5	17.6	90	136.2	17.3	17.3	90
85	o	90	20	220.3	208.9	8.9	18.9	90	187.9	23.4	18.8	90
89	13	130	20	173.1	164.2	7.9	18.8	52	147.6	20.8	18.7	52
105	20	180	20	133.6	126.7	6.3	17.4	4	113.9	16.7	17.2	4
125	o	270	20	138.6	131.5	5.9	12.8	90	118.2	15.6	12.7	90
65	0	90	40	351.6	329.4	16.0	17.5	90	289.2	40.4	17.6	90
72	24	130	10	170.2	159.5	10.9	17.9	52	140.0	27.6	18.0	52
105	40	180	40	102.4	95.9	6..5	17.1	7	84.2	16.6	16.9	7
145	0	270	10	146.8	137.6	6.8	6.7	90	120.8	17.6	6.7	90
45	0	90	60	865.6	783.6	38.4	14.8	90	642.2	88.6	15.1	90
52	34	130	60	186.8	169.1	17.5	15.3	50	138.6	40.7	15.6	51
105	60	180	60	90.5	81.9	7.9	16.6	10	67.1	18.8	16.3	10
165	o	270	60	164.4	148.9	9.9	9.0	90	122.0	23.6	3.1	90
30	0	90	75	2200.0	1819.3	32.3	12.7	90	1244.2	178.9	13.2	90
34	38	.39	75	201.4	166.5	29.8	12.7	49	113.9	59.1	13.0	50
105	75	80	75	78.8	65.2	11.5	16.0	12	44.6	23.7	15.5	12
180	0	270	75	180.0	148.9	.6.1	2.1	90	101.8	32.7	2.5	90

The influence of multiple Rayleigh scattering was estimated using the work of Dave (1964) and of de Bary and Bullrich (1964), who determined the higher order contributions to the scattered light from a point source in a plane-parallel atmosphere. The derived correction factors $F_{MS} = I_{MS}/I_{SS}$ for the intensity, and $f_{MS} = p_{MS}/p_{SS}$ for the depolarization of scattered light are given in Table 7. All results for Rayleigh scattering given in the following are corrected for multiple scattering. For Mie scattering, de Bary (1964) concludes that higher order contributions are negligible for scattering angles $\theta < 30°$. Therefore, since the main contribution by atmospheric aerosols to the scattered light comes from regions with $\theta < 30°$, no corrections were applied to the first order results for Mie scattering.

5.2. *The integrated starlight*

The integrated starlight scattered in the troposphere was calculated using an analytical model for the extraterrestrial brightness of the LSL: a two dimensional Gauss distribution was fitted to the blue isophotes given by Elsässer and Haug (1960). The constants were adjusted to give a model intensity $I_1(l = 0, b = 0) = 260\ S_{10}$, $I_1(l = 120, b = 0) = I_1(l = 240, b = 0) = 100\ S_{10}$, and $I_1(l, b = \pm 30) = 50\ S_{10}$. At higher galactic latitudes an exponential decrease was assumed, with $I_1(l, b = \pm 80) = 20\ S_{10}$, following the

Table 11. Same as Table 10, with the Sun at $A = 90$, $z = 135$

ϵ	β	A	z	I_1	I_2	I_s	p_s	ϕ	I_2	I_s	p_s	ϕ
						$\tau_R =$	10			$\tau_R =$	20	
135	0	0	0	141.1	127.7	6.6	16.9	90	115.6	13.1	14.3	90
115	0	90	20	143.2	128.8	7.0	17.8	90	115.9	13.7	15.3	90
119	13	130	20	128.4	115.5	6.9	17.1	53	103.9	13.6	14.5	53
135	20	180	20	120.2	108.1	6.9	15.2	3	97.3	13.6	12.6	3
155	0	270	20	153.6	138.1	7.2	14.7	90	124.2	14.1	12.6	90
95	0	90	40	183.5	161.1	8.4	17.8	90	141.4	16.2	16.0	90
102	24	130	40	129.7	113.9	8.2	16.1	57	100.0	15.8	14.1	59
135	40	180	40	92.9	81.6	8.0	11.8	7	71.6	15.4	9.1	8
175	0	270	40	176.6	155.0	8.8	13.1	90	136.1	17.0	11.9	90
75	0	90	60	273.4	224.1	12.6	16.6	90	183.6	23.1	15.8	90
82	34	130	60	128.5	105.3	11.9	13.6	63	86.3	21.9	12.8	66
135	60	180	60	90.0	73.8	11.1	7.7	16	60.4	20.5	5.2	22
195	0	270	60	164.4	134.8	13.1	12.5	90	110.4	24.0	12.1	90
60	0	90	75	420.0	287.2	22.1	15.3	90	196.4	37.0	15.3	90
64	36	130	75	137.9	94.3	20.6	11.1	70	64.5	34.5	11.4	74
135	75	180	75	78.9	53.9	18.5	5.8	27	36.9	31.2	4.1	42
210	0	270	75	150.0	102.6	22.7	12.9	90	70.2	37.9	13.1	90
						$\tau_M =$	05			$\tau_M =$	15	
135	0	0	0	141.1	134.2	5.4	8.2	90	121.5	14.4	8.1	90
115	0	90	20	143.2	135.8	5.9	13.8	90	122.2	15.6	13.6	90
119	13	130	20	128.4	121.8	5.6	12.8	57	109.5	14.8	12.6	57
135	20	180	20	120.2	114.0	5.2	8.8	15	102.6	13.9	8.7	15
155	0	270	20	153.6	145.6	5.7	3.1	90	131.0	15.1	3.0	90
95	0	90	40	183.5	171.9	8.3	17.3	90	151.0	21.1	17.3	90
102	24	130	40	129.7	121.5	6.9	16.1	61	106.7	17.6	19.0	62
135	40	180	40	92.9	87.1	5.5	10.4	28	76.5	14.1	10.3	28
175	0	270	40	176.6	165.4	7.0	0.9	90	145.2	18.1	0.9	90
75	0	90	60	273.4	247.5	14.9	18.5	90	202.9	34.8	18.6	90
82	34	130	60	128.5	116.3	10.0	17.6	64	95.4	23.6	17.6	64
135	60	180	60	90.0	81.5	6.9	12.5	38	66.8	16.5	12.3	38
195	0	270	60	164.4	148.9	9.6	0.7	90	122.0	23.0	0.7	90
60	0	90	75	420.0	347.3	29.3	18.4	90	237.5	57.6	18.5	90
64	38	130	75	137.9	114.0	16.4	17.5	65	78.0	32.9	17.6	65
135	75	180	75	78.9	65.2	10.1	13.7	42	44.6	20.8	13.5	42
210	0	270	75	150.0	124.0	14.4	1.7	90	84.8	29.6	1.7	90

star counts of Roach and Megill (1961). The assumption of such a smooth brightness distribution is safe even for Mie scattering, since also in this case scattering angles up to $\theta = 30°$ contribute substantially to the integrated scattered light. Figure 15 shows the intensity of the scattered ISL as a function of zenith distance for the case that the galactic centre is at the zenith. In Table 8 the scattered intensity I_s, and its degree and orientation of polarization, (in percent) and ϕ are tabulated for this situation together with the assumed source brightness I_1 in the viewing direction and the transmitted brightness I_2 weakened by atmospheric extinction. In Table 9 the same values are given for the galactic anticentre at the zenith. The refractive index of the Mie particles is assumed to be $m = 1.33$.

5.3. *The Zodiacal light*

Intensity and polarization of Zodiacal light scattered in the troposphere were calculated assuming the brightness distribution given by Dumont (1965) at $\lambda = 5000$ Å. For the linear polarization the values measured by Weinberg (1964) at the ecliptic were used, assuming that over the whole sky the polarization is a function of angular distance to the *Sun* (elongation ϵ, see section 3.5) alone (Dumont and Sanchez Martinez 1966). The polarization was assumed to be perpendicular to the direction of the Sun.

Table 12. Same as Tables 10 and 11, with the Sun at $A = 90$, $z = 180$

ϵ	β	A	z	I_1	I_2	I_s	p_s	ϕ	I_2	I_s	p_s	ϕ
					$\tau_R = 0.10$				$\tau_R = 0.20$			
180	0	0	0	180.0	162.9	6.0	5.9	90	147.4	12.0	4.8	90
160	0	90	20	158.0	142.1	6.3	7.0	90	127.8	12.5	6.0	90
104	13	130	20	144.5	129.3	6.3	6.0	57	116.9	12.5	5.0	58
180	20	180	20	130.0	116.9	6.2	4.2	0	105.1	12.4	3.2	0
140	0	90	40	144.0	126.4	7.4	10.1	90	111.0	14.4	9.2	90
147	24	130	40	117.4	103.1	7.3	7.7	71	90.5	14.2	7.1	74
180	40	180	40	90.0	79.0	7.2	0.3	87	69.4	14.0	1.3	89
120	0	90	60	140.0	114.7	10.5	13.8	90	94.0	19.6	13.2	90
127	34	130	60	101.9	83.5	10.3	11.2	82	68.4	19.2	11.1	83
180	60	180	60	90.0	73.8	9.9	6.2	90	60.4	18.6	7.1	90
105	0	90	75	158.2	108.2	17,9	16.0	90	74.0	30.4	15.8	90
109	36	130	75	102.3	70.0	17.4	13.7	86	47.9	29.6	13.9	87
180	75	180	75	78.9	53.9	16.7	9.9	90	36.9	28.4	10.9	90
					$\tau_M = 05$				$\tau_M = 15$			
180	0	0	0	180.0	171.2	5.7	0.7	90	155.0	15.2	0.6	90
160	0	90	20	158.0	149.8	5.7	1.6	90	134.7	15.1	1.5	90
164	13	130	20	144.5	137.0	5.5	1.2	72	123.2	14.7	1.2	73
180	20	180	20	130.0	123.3	5.3	0.1	88	110.9	14.1	0.2	88
140	0	90	40	144.0	134.9	6.5	5.5	90	118.5	16.7	5.3	90
147	24	130	40	117.4	110.0	5.9	4.8	85	96.6	15.2	4.7	85
180	40	180	40	90.0	84.3	5.3	3.8	90	74.0	13.7	3.8	30
120	0	90	60	140.0	126.7	8.9	10.7	90	103.9	21.3	10.5	90
127	34	130	60	101.9	92.2	7.6	10.0	88	75.6	18.2	9.9	88
180	60	180	60	90.0	81.5	6.6	9.2	90	66.8	15,9	9.1	90
105	0	90	75	158.2	130.8	14.4	13.9	90	89.5	29.2	13.7	90
109	38	130	75	102.3	84.6	11.7	13.2	89	57.9	23.9	13.0	89
180	75	180	75	78.9	65.2	9.7	12.4	90	44.6	20.0	12.3	90

Figures 16 and 17 show the results for two cases, pure Rayleigh- and pure Mie-scattering (water vapor), respectively. In Tables 10, 11 and 12 the results are collected for three different positions of the Sun below the horizon. The ecliptic is assumed to be perpendicular to the horizon. All other quantities as in Tables 8 and 9.

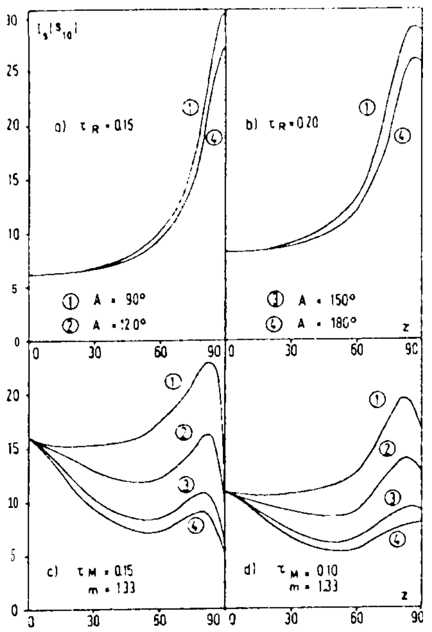

Fig. 15. The intensity of the scattered IS as a function of zenith distance, for different azimuths and zenith extincion values of the Rayleigh resp. Mie components of the atmosphere. The galactic centre is assumed at the zenith, the galactic equator crosses the horizon at A = 90°,270°.

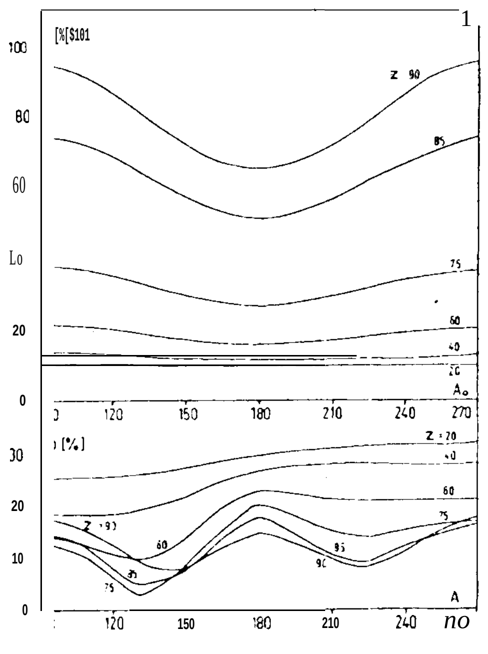

Fig. 16. The intensity of the scattered ZL for a pure Rayleigh atmosphere with optical thickness τ_R=0. 1. Positron of the sun at azimuth $A_\odot$=90°, zenith distance $z_\odot$=105°, the ecliptic is perpendicular to the horizon

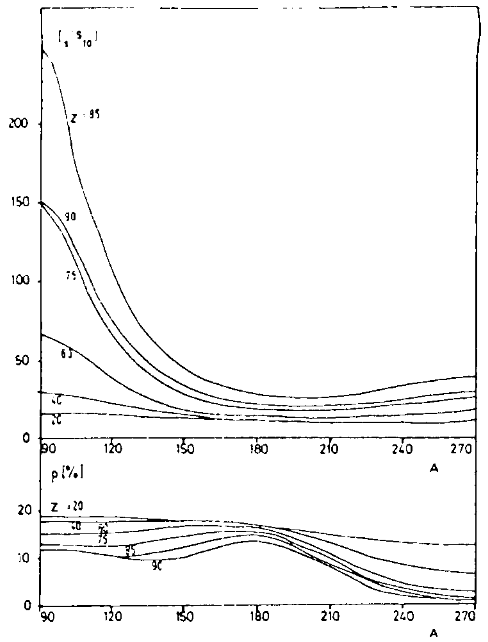

Fig. 17. The intensity of the scattered ZL for pure Mie scattering with optical thickness τ_M=0.1, for particles with refractive index m=1.33. Otherwise same as for Figure 16.

6. Airglow

The airglow emissions vary considerably with time, on snort. (minutes) and long timescales, mainly due to changes in the atmosphere and irr solar activity. They also depend on geomagnetic latitude, with a distinctive tropical brightness enhancement. The brightness values given below therefore are only indicative of the typical intensities. Many of the airglow emissions arise in the ionospheric E layer at ≈ 90 km, some in the F region above 150 km (see Figure 18), some, like Lyα and Hα in the Geocorona. The phenomenological side of airglow, which is the part of interest for the night sky brightness, has for the visual region in large part been studied in the sixties and seventies, which reflects in the list of references. Typical brightness values of main airglow lines are summarised in Table 13.

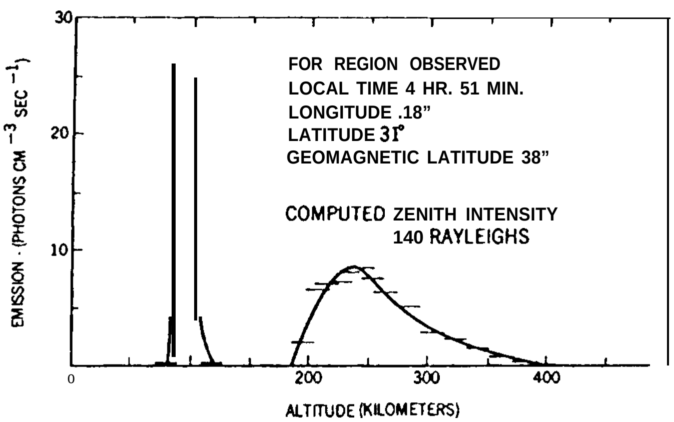

Fig. 18. A typical height profile of airglow volume emission, as measureed from the satellite OGO II. The peak near 90 km is due to OH emission, the extended peak at higher altitudes to [01] emission at 630 nm. From Reed and Blamont (1967).

6.1. *A irglow spectrum*

a) Visual

Broadfoot and Kendall (1968) give the spectrum of the airglow from 300 nm to 1 μm (see Figure 20). It is based on photoelectric observations at Kitt Peak near zenith and within 30° of the galactic pole. The spectral resolution is 5Å, the scan step four times smaller. The [01] lines at 630 nm and 636.4 nm and also Hα are weaker than average in these observations.

b) Ultraviolet

Ultraviolet astronomical observations mostly are taken from above the atmosphere by rockets or satellites. In this context it is relevant to know the airglow as seen from such spacecraft positions. Results obtained at typical altitudes are shown in Figures 19 and 21. The strength of the main emission lines is also summarised in Table 13. For the 01 130.4 nm and 135.6 nrn lines enhanced values observed in the tropical airglow (Barth and Schaffner 1976) are given. At mid latitudes they are less intense by about one order of magnitude. Apart from the main emission lines shown in Figure 19, the ultraviolet region between 850 Å and 1400 Å is thought to be free of nightglow emission.

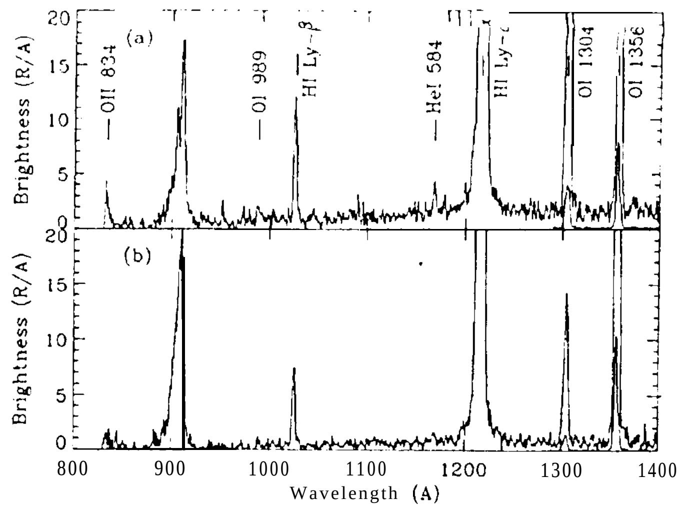

Fig. 19. Spectra of the nightglow from 800 Å to 1400.$ at 3.$ resolution. The data were obtained from the space shuttle at an altitude of 358 krn on December 5, 1990. Two spectra are shown, of which the upper one was taken closer to the dusk terminator. It therefore also shows 011834 and HeI 584, which are features belonging to the dayglow. The zenith distance was ≈ 85° and ≈ 90° for the upper and lower spectrum, respectively. Lyα is a geocoronal line. The continuum at 911 Å is due to 0^{+}recombination to the ground state. From Feldman et al. (1992).

The viewing line of spacecraft on the night side of the atmosphere may cross the terminator and continue through the sunlit parts of the atmosphere. Under these twilight conditions, dayglow features become important. E.g. the NO γ bands then are excited by resonance fluorescence and then are much stronger, the N_2 Lyman-Birge-Hopfield bands are clearly visible, and the forbidden [011] emission at 247 nm is strong. Figure 22 shows ultraviolet airglow emission observed under such conditions. An excellent review on observations and modelling of both dayglow and nightglow ultraviolet emissions has been given by Meier (1991).

c) Near infrared

From 1 μm to 3 μm, OH in a layer around 90 krn height dominates the airglow emission. There is a gap in the OH

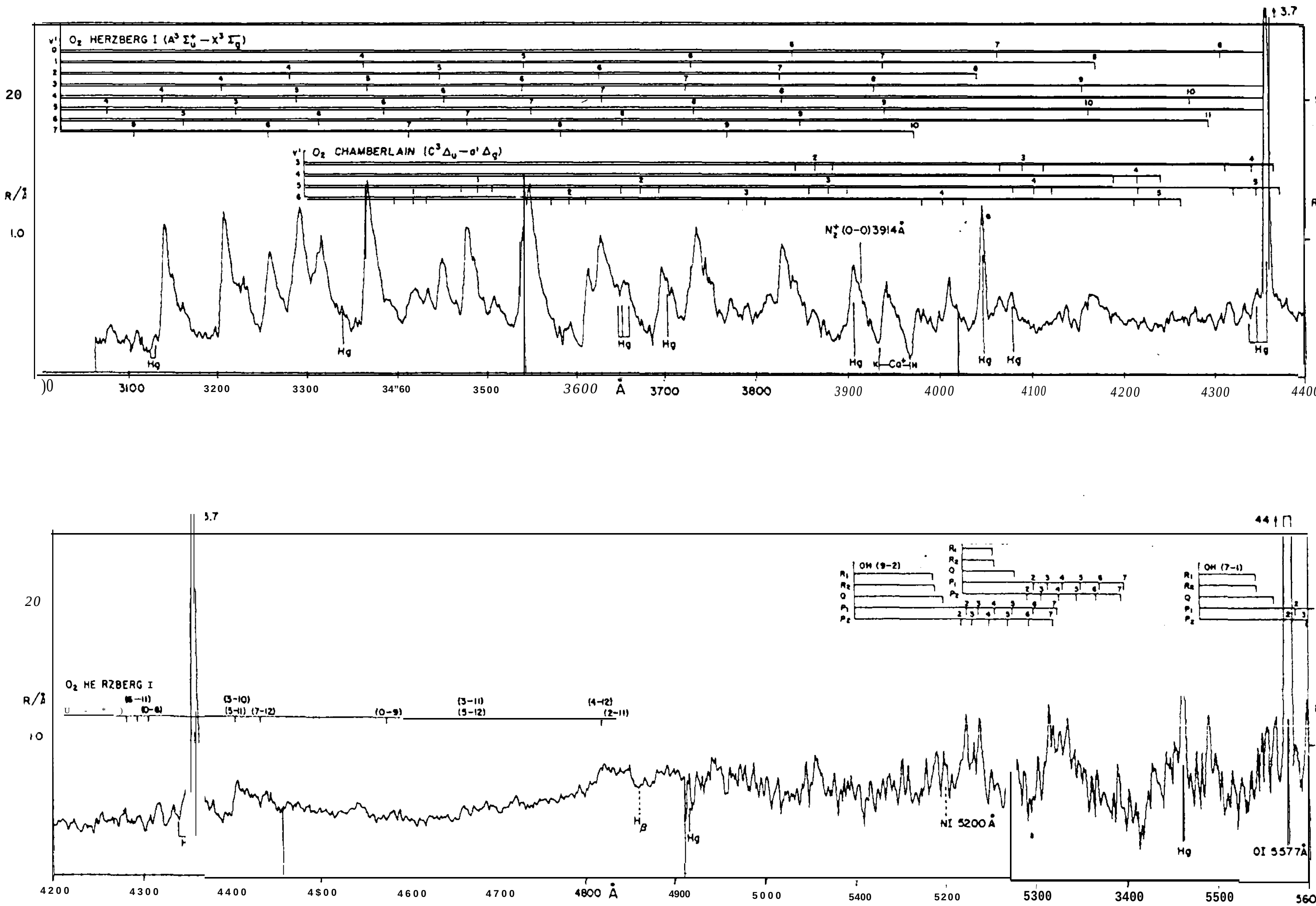

Fig. 20. Spectrum of the airglow from 300 nm to 1 μm (from Broadfoot and Kendall 1968)

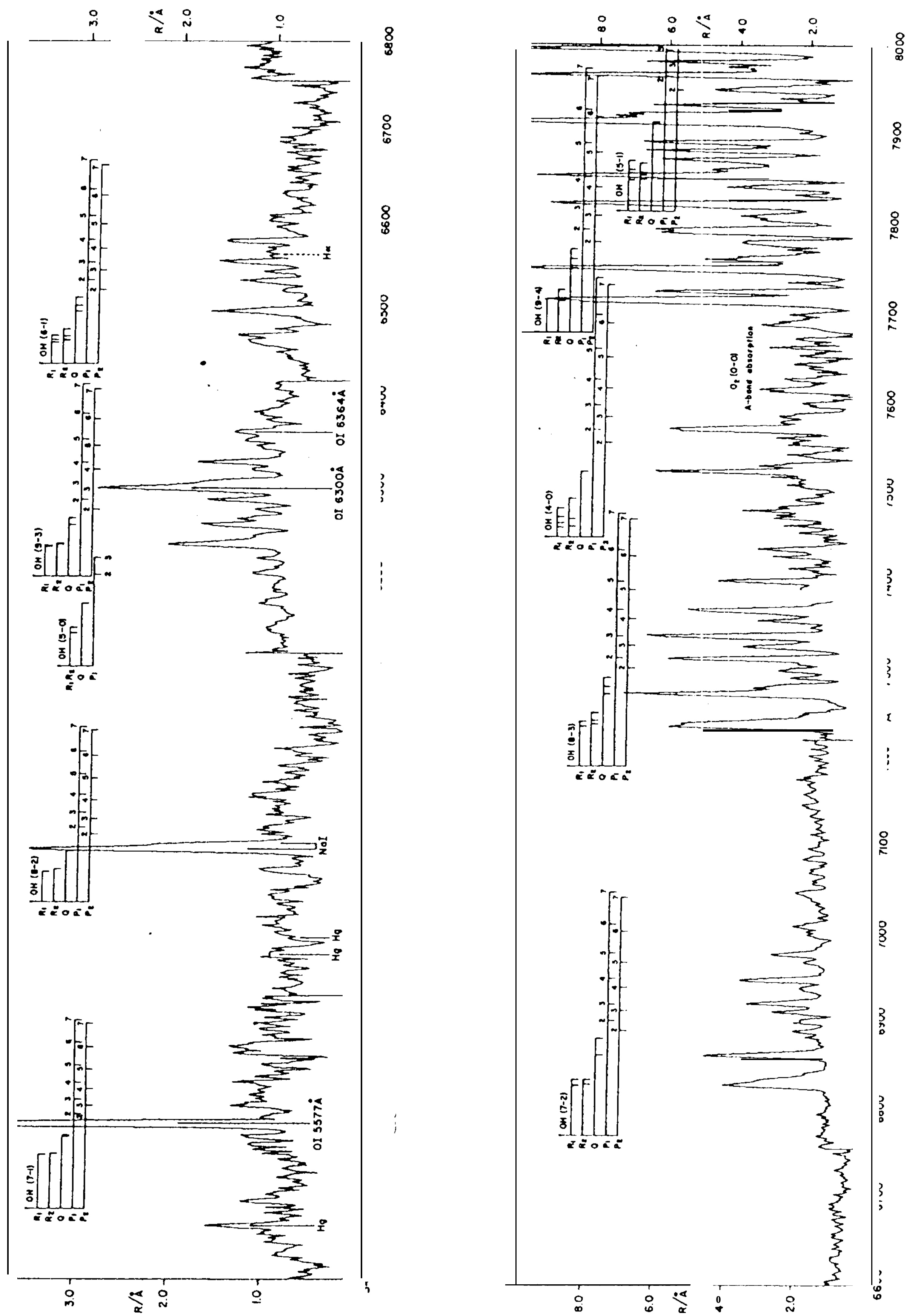

Figure 20 continued

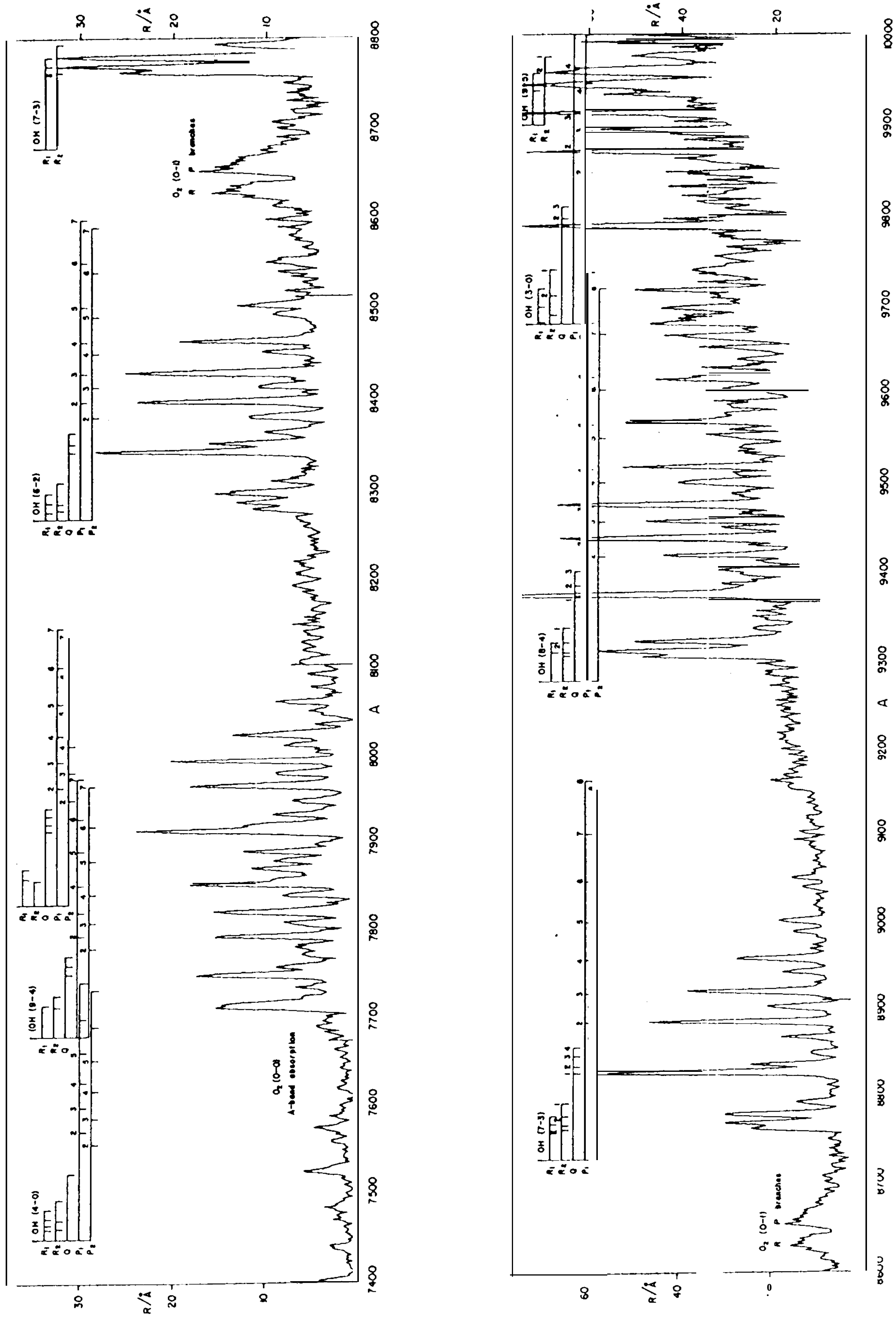

Figure 20 continued

Table 13. Typical zenith brightness of nightglow emissions[a]

Source	Wavelength	Height of emitting layer	Intensity[b]
Lyβ	102.6 nm	geocorona	$\approx$10 R
Lyα	121.6 nm	geocorona	3 kR(night) -34 kR(day)
01	130.4 nm	250-300 krn	$\approx$40 R (in tropical airglow)
01	135.6 nm	250-300 km	$\approx$30 R (in tropical airglow)
O_2(Herzberg bands)	300 nrn -400 nm	90 km	0.8 R/Å
[01]	557.7 nm	90 km	250 R
Na D	589.0 nm, 589.6 nm	$\approx$92 km	30 R (summer) to 100 R (winter)
[01]	630.0 nm	250-300 km	60 R
[01]	636.4 nm	250-300 km	20 R
Hα	656.3 nm	geocorona	4-6 R (night)
pseudocontinuum	400 nm -700 nm	90 km	0.3 R/i
O_2	864.5 nm	$\approx$80 km	1 kR
OH	600 nm -4.5 μm	85 km	4.5 MR(all bands)

[a] after Chamberlain (1961), Roach (1964), Roach and Gordon (1973), Meier (1991); see also the references in the sections on geocorona and ultraviolet airglow.
[b] transformed to zenith, where necessary

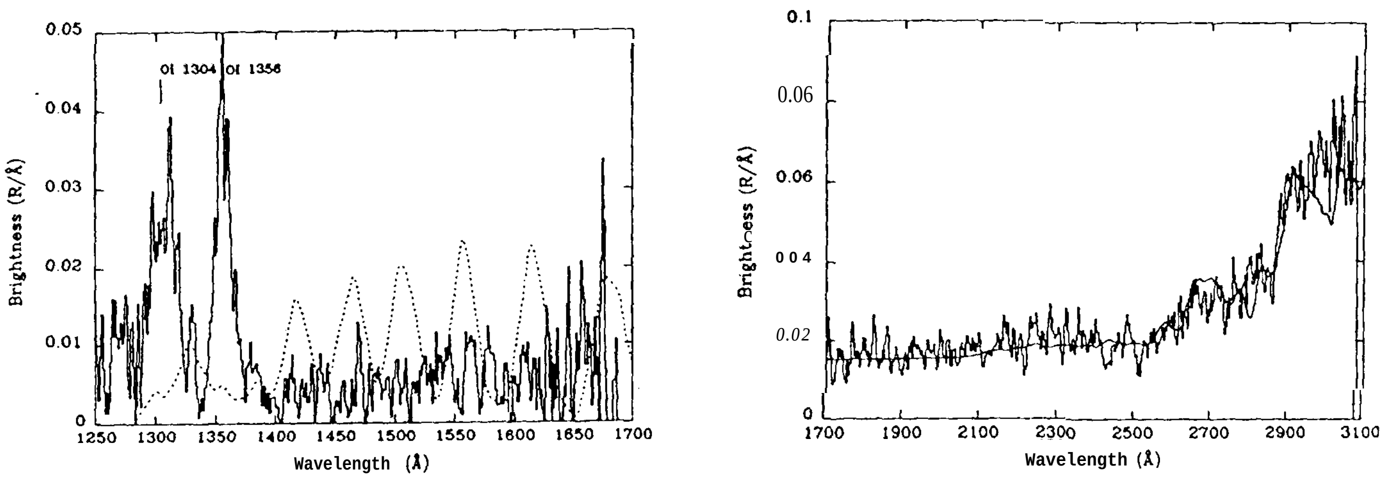

Fig. 21. Left: Spectrum of the nightglow from 1250 Å to 1700 Å at 17 Å resolution. The data were obtained" from the space shuttle at a height of 330 km in January 1986 at minimum solar activity. The oxygen OI lines at 1304 Å and 1356 Å are the brightest features. For the weakly visible Lyman-Birge-Hopfield bands the dashed curve shows a predicted spectrum. Right: Spectrum of the ultraviolet nightglow from 170 nm to 310 nm at 29 Å resolution obtained on the same flight. The solid line shows an appropriately scaled solar spectrum and is assumed to show the contribution to zodiacal light. From Morrison et al. (1992)

spectrum around 2.4 μm (see Figure 27) which is important for balloon observations and also for the low background observations possible from Antarctica (see section 4.3). Seen from the ground, longward of 2.5 μ airglow is only a small addition to the thermal emission from the troposphere (compare Figure 11 in section 4 above). Figures 25 and 26 show the near-infrared OH spectrum at two resolutions, once with a low spectral resolution of $\Delta\lambda$ = 160 Å, and once with a higher resolution of $\lambda/\Delta\lambda$ = 250 - 800. Wavelength lists and intensities for the individual OH bands can be found in Ramsay et al. (1992) and Oliva and Origlia (1992). Obviously, the near-infrared airglow is dominated by the OH bands. They primarily also determine the night sky brightness in the J (1.2 μm) and H (1.6 pm) bands (Figure 11, section 4.3).

6.2. Dependence on zenith distance

In absence of atmospheric extinction, a thin homogeneously emitting layer at height h above the Earth's surface shows a brightness increase towards the horizon,

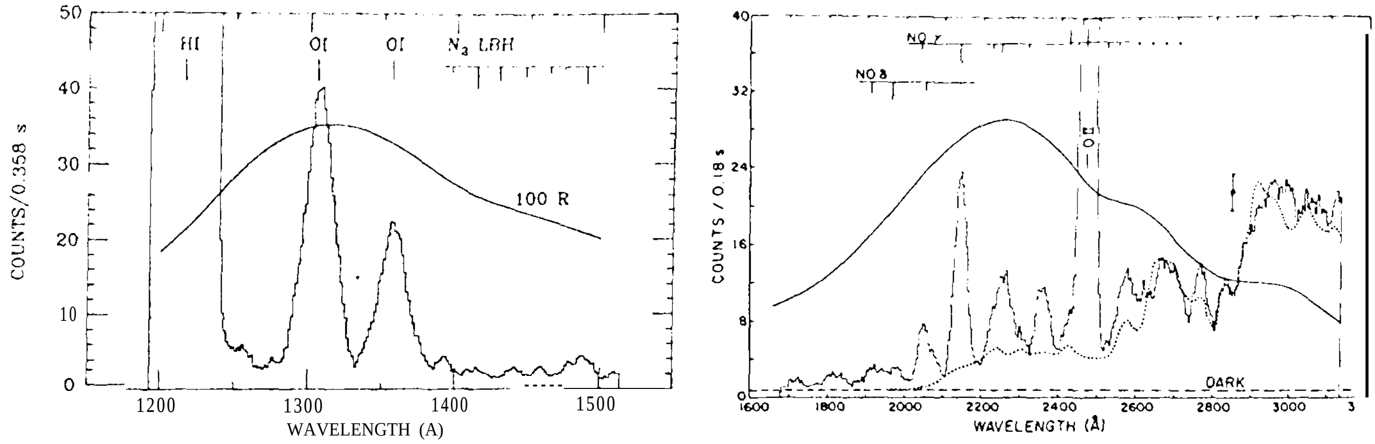

Fig. 22. Ultraviolet twilight airglow spectrum, as observed during a rocket flight on September 24, 1979. Left: from 1200 Å to 1500 Å at 20 Å resolution. Lyα is at left. 'LBH' refers to the Lyman-Birge-Hopfield bands. These Observations were done in the height range 100 km -200 km. - Right: From 170 nm to 310 nm at 25 Å resolution. The dotted line shows the zodiacal light contribution. These observations refer to rocket heights of 170 km - 246 km. – The field of view of the experiment was oriented 23° from the sun and essentially in the horizontal plane (0.2° elevation). For conversion to absolute fluxes, a solid line is given with both parts of the figure. It indicates which signal would be poduced at each wavelength by a monochromatic source of a given brightness (100 R for the short-wavelength part, 18 R for the longer wavelengths). For continuum emission this would correspond to 5.0 R/Å and 0.72 R/Å, respectively. From Cebula and Feldman (1982, 1984).

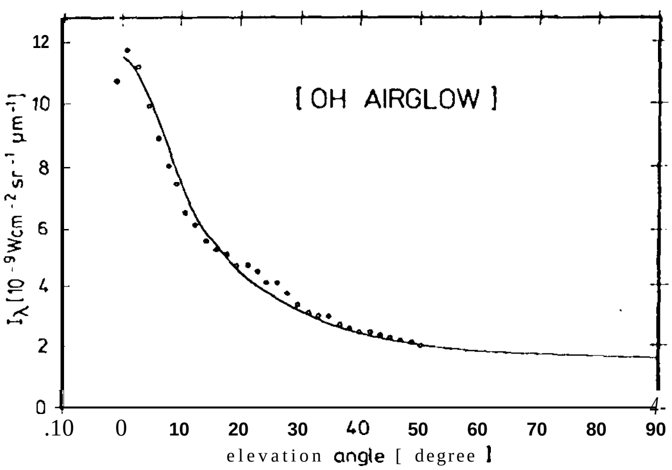

Fig. 23. *Increase* of airglow brightness at 2.1 μm towards the horizon observed from a balloon at 30 km altitude on October 23, 1972. Dots represent the measurements, the line gives the van Rhijn function for a height of the emitting layer of 92 km. From Hofrnann et al. (1977).

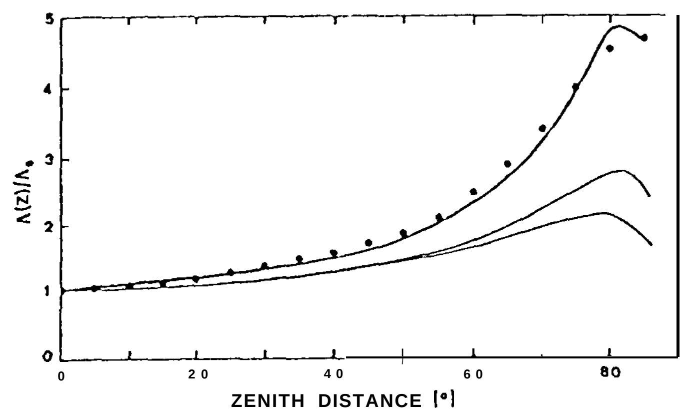

Fig. 24. **Zenith** angle **dependence** of sky brightness observed at 530 nm from Haleakala (Kwon et al. 1991). The points represent an average normalised profile. The thin lines are the curves predicted by Barbier in 1944 for heights of the airglow emitting layer of 50 krn (higher maximum) and 200 km, respectively. The solid line fitting the data is an ad-hoc modification of Bar bier's formula.

which is given by the so-called *van Rhijn function*

$$I(z)/I(zenith) = \frac{1}{\sqrt{1-[R/(R+h)]^2\sin^2 z}}, \qquad (13)$$

where R = 6378 km is the radius of the earth. E.g., for h = 100 km $[I(z)/I(0)]_{max}$ = 5.7 results (Roach and Meinel 1955). This situation typically applies for balloon experiments. Figure 23 shows an example. For observations from the ground, extinction and scattering change the behaviour in particular for zenith distances > 40°. Around λ = 500 nm - 600 nm a maximum airglow increase by about a factor of about four may be expected at z = 75° - 80°, with the brightness decreasing again towards the horizon .(see Figure 24 for an observation and Roach and Meinel (19.55) for a selection of predicted profiles). For shorter wavelengths, with stronger scattering and extinction, this de-

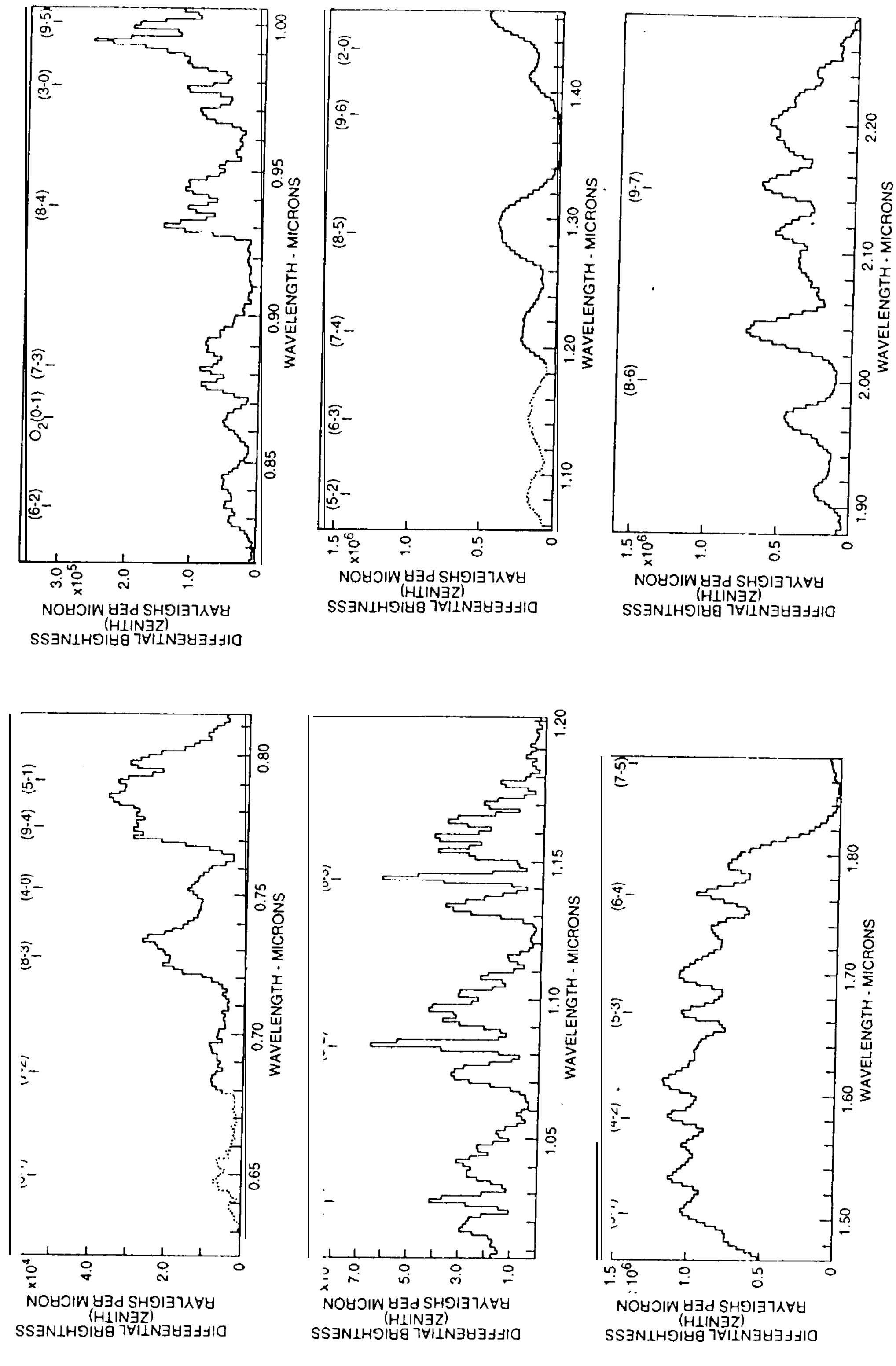

Fig. 25. Near-infrared airglow spectrum as seen from the round at 160 Å resolution (for $\lambda > 1.2\ \mu m$). The OH bands mainly contributing to the emission have been identified in the figure. "differential" simply means "per micron". From Harrison and Kendall (1992).

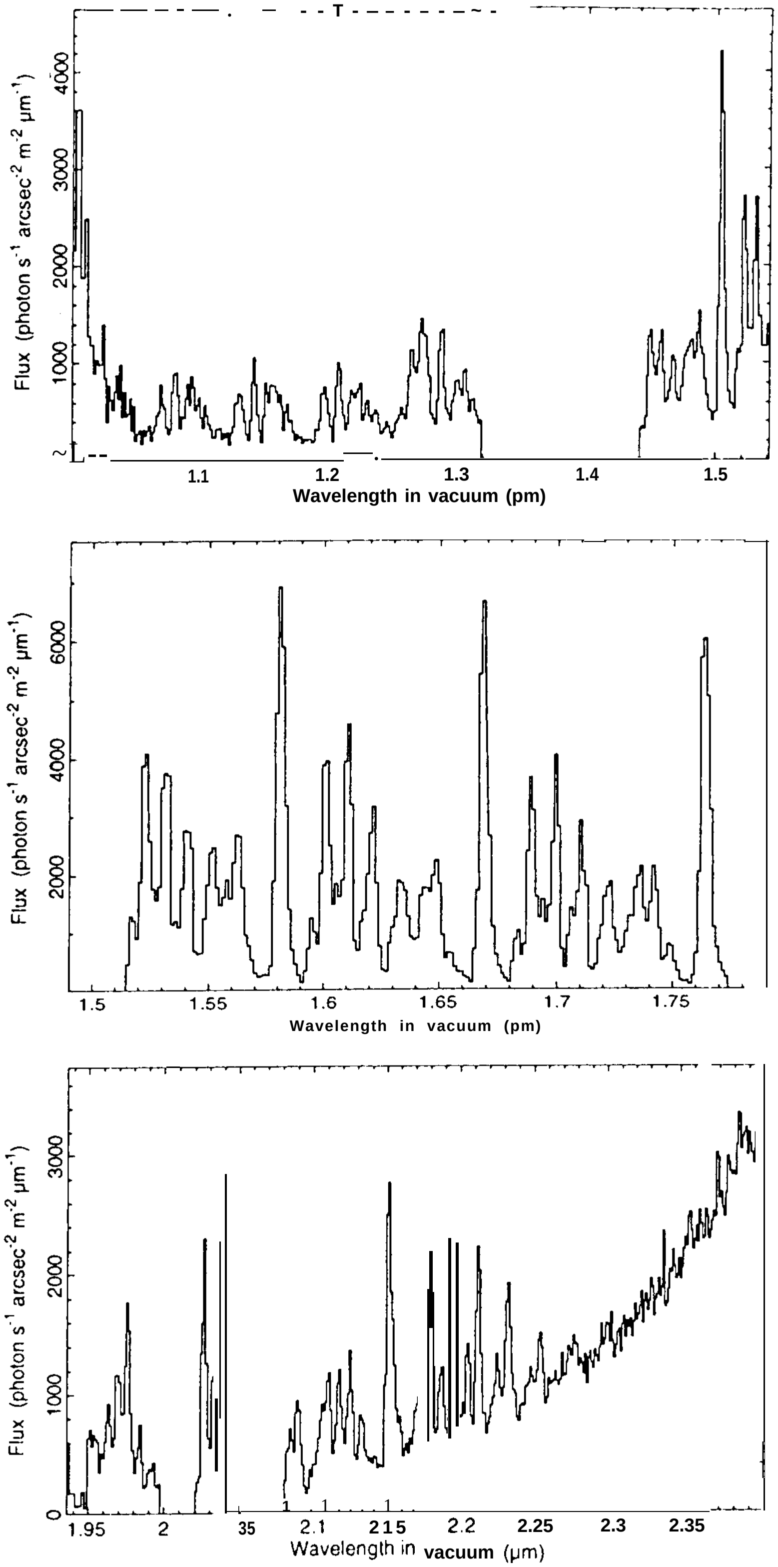

Fig. 26. Near-infrared airglow spectrum as observed from Mauna Kea at spectral resolution $\lambda/\Delta\lambda$ = 250-800. In regions with atmospheric transmission ≤ 0.75 the flux has been arbitrarily set to zero. Longward of '2.1 μm thermal atmospheric emission takes over. Note that 1000 of the units used correspond to 6.77×10^{-6}, 5.11 x10^{-6}, and 3.84×10^{-6} W/m^2 sr μm at 1.25 pm, 1.65 pm and 2.2 μm, respectively. From Ramsay et al. (1992).

crease starts already at higher elevations. However, appropriate models (based on realistic assumptions, including multiple scattering in a spherical atmosphere and going down to the horizon) to account for the observed brightness profiles from the zenith to the horizon have not yet been calculated. The results given in section 5 do not claim to be accurate near the horizon.

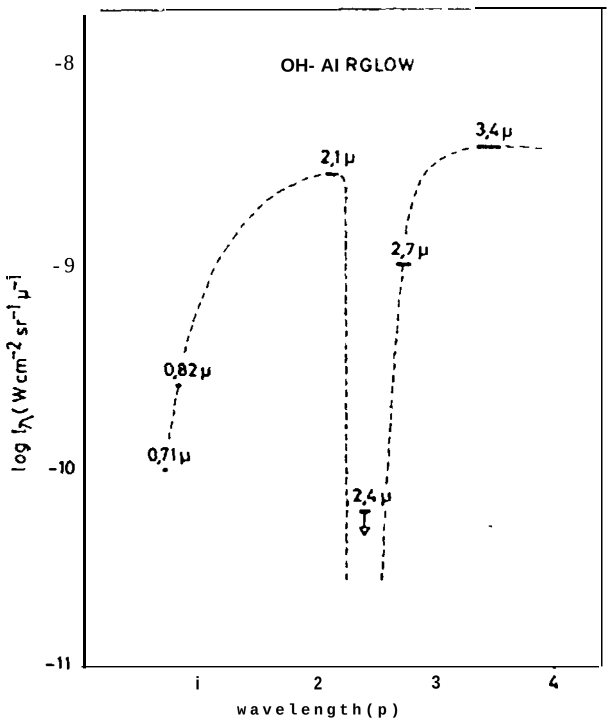

Fig. 27. Spectral distribution of near-infrared zenith airglow showing the gap in airglow emission around 2.4 μm. The airglow measurement shavebeen performed from a balloon at 30 km altitude during flights in 1972 and 1974. Variations from flight to flight and during one night were less than a factor of two. From Hofmann et al. (1977).

6.3. *Variations*

Airglow emission is often patchy and varying in brightness and spatial distribution with time. Roach and Gordon (1973) demonstrate this by showing airglow maps in time steps of 15 minutes on the right upper corner of odd pages, thus enabling a " thumb-cinema" look at these spatio-temporal variations. Quantitative examples for variation during one night or variation with solar cycle can be seen in Figures 8 and 10 in section 4. Often a systematic decrease of airglow emission during the course of the night is observed, explained as result of the energy stored during day in the respective atmospheric layers. Figure 29 shows this for the OH emissions and also gives an example for the wavelike structures often apparent in

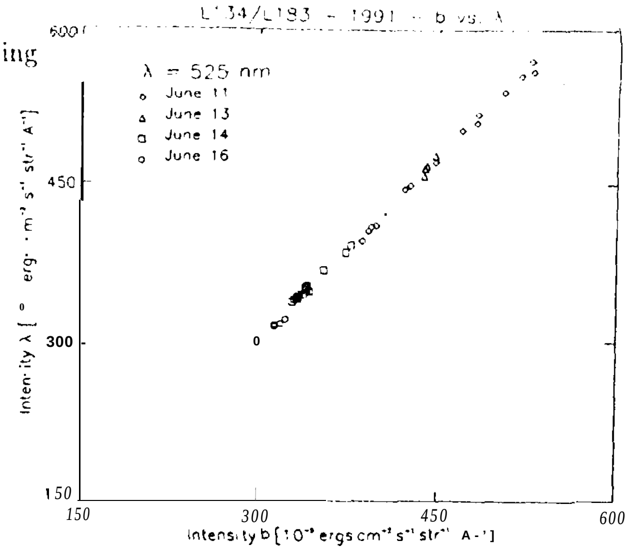

Fig. 28. Correlation between' the diffuse sky emission at 467 nrn (Strömgren b) and at $\lambda =$ 525 nm. The brightness variations in both bands mainly are due to airglow. From Leinert et al. (1995).

these emissions. These examples do not give at all a full overview on airglow variability but just demonstrate that it is a typical property of this source of night sky brightness.

In the visual spectral region, correlations between the prominent [01] and NaD airglow emission lines and "pseudocontinuurn" bands at 367 nm, 440 nm, 526 nm, 558 nm, 634 nrn and 670 nrn have been studied by Barbier (1956) who established three " covariance groups". E.g., the correlation between the 557.7 nm line and the "pseudocontinuum" at 502 nm has been used by Dumont (1965) to eliminate the airglow contribution from his zodiacal light meastrrernents. Sometimes such correlations can be quite tight (see Figure 28).

6.4. *Geocorona*

Above 1000 km, the earths atmosphere changes to a composition of mainly neutral hydrogen with some ionised helium, the density falling off gradually over a few earth radii. Two telling images of the geocorona in Lyα, including the globe of the earth, are shown by Frank et al. (1985, see p.63). This geocorona is optically thick to the solar Lyman lines. Typical intensities of the emissions observed from ground (in the visual) or from earth orbit are given in Table 13, with the data taken from Caulet et al. (1994) and Raurden et al. 1986 for Lyα, Meier et al. (1977) for Lyβ, Levasseur et al. (1976) for Hα.

6.5. *Interplanetary emissions*

Solar radiation is scattered by neutral interstellar gas atoms which are coming from the solar apex direction and

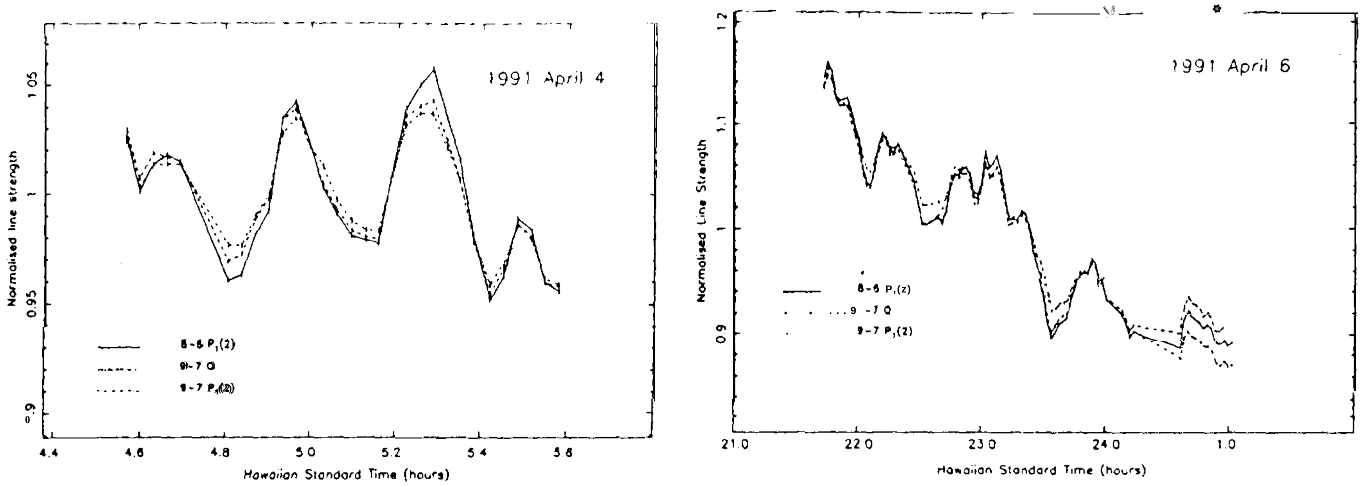

Fig. 29. Variation of OH airglow, observed from Mauna Kea. Left: Short term variations (minutes) caused by the passage of wavelike structures. Right: Decrease of OH airglow during the course of a night, shown for several bands separately. From Rarnsay et al. 1992.

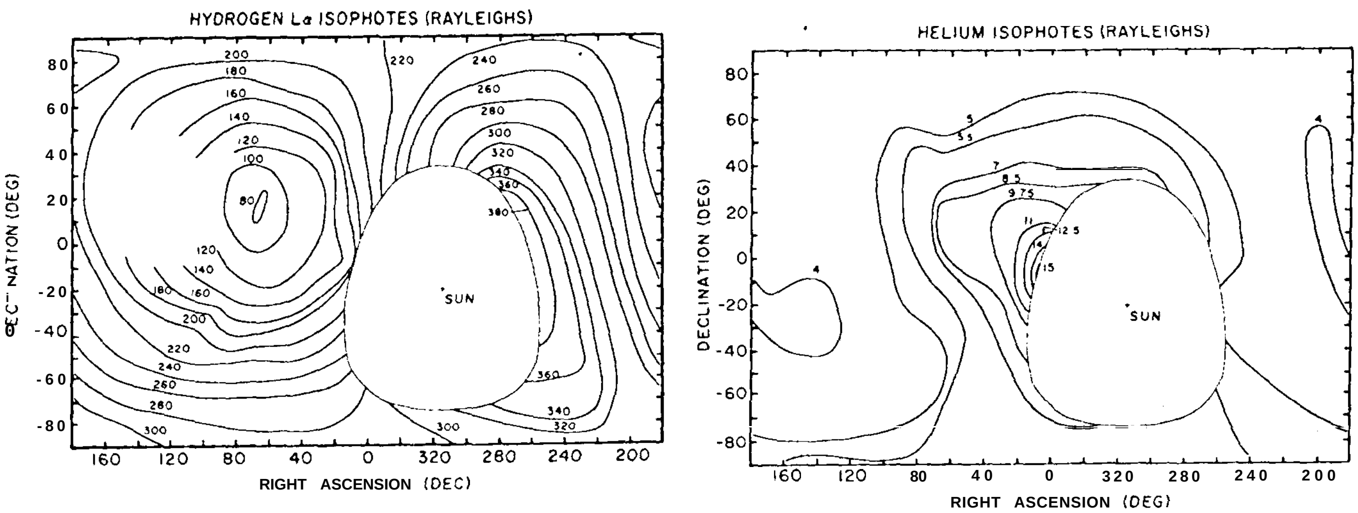

Fig. 30. Interplanetary emission in the Lyα (left) and He 584 Å lines (right) observed by the Mariner 10 UV spectrometer (Broadfoot and Kumar 1978). The observations were performed on January 28, 1974, while the spacecraft was at a heliocentric distance of 0.76 AU and $\approx 60°$ from the apex-Sun axis. The brightness units are Rayleighs. From Thomas (1978).

are pervading the solar system until ionized. The emitting region is a sort of cone around the apex-Sun line. The observed emission depends on the position of a spacecraft with respect to this cone (see, e.g. the review by Thomas (1978)). Typical patterns observed for the Lyα and He 584 Å lines are shown in Figure 30.

6.6. Shuttle glow

Depending on altitude and solar activity, satellites produce additional light emissions by interaction with the upper atmosphere (*Shuttle glow*). Photometric measurements thus may be affected. These light phenomena are relatively strong in the reel and near-infrared spectral regions, but are noticeable towards the ultraviolet as well.

For instance, during the Spacelab 1 mission the emissions of the N_2 Lyman-Birge-Hop field bands were found to be in the range of 10-50 R/Å (Torr et al. 1985). These observations at 250 km altitude were performed under conditions of moderate solar activity. During minimum solar activity and at 330 km, Morrison et al. (1992) observed no such emissions. The GAUSS camera onboard the German Spacelab mission D2 (296 km, moderate solar activity) observed a patchy glow with $\approx$ O-3x $10^{-9}\,\mathrm{W\,m^{-2}sr^{-1}nm^{-1}}$ at 210 nm (Schmidt tobreick 1997). Taking into account the appropriate conversion factor, the observed glow intensity amounts to about 0.4 R/Å in its brightest parts. Although these three observations were made at somewhat different wavelengths, the overall increase of emission intensity I with surrounding air density ρ is in agreement with an I $\sim \rho^3$ law.

7. Light pollution

Artificial lighting at earth contributes via tropospheric scattering to the night sky brightness over a large area around the source of light. Both a continuous component as well as distinct emission lines are present in the light pollution spectrum. A recent review of sky pollution is given in McNally (1994).

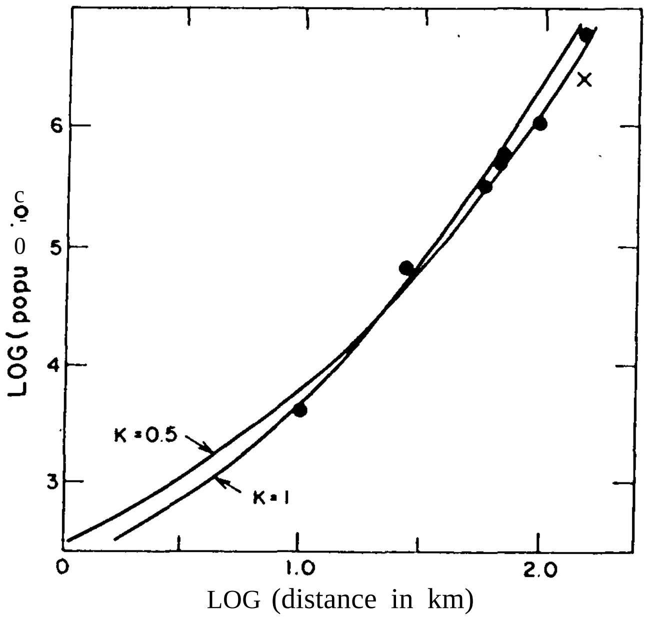

Fig. 31. Variation with city population of the distance at which the lights of a city produce an artificial increase of the night sky brightness at 45 deg altitude toward the city by 0.20 msg. This increase refers to an assumed natural sky brightness of V = 21.9 mag/□″. Observations by Walker (1977) are indicated by dots. Two models by Garstang (1986) are shown as solid lines. K is a measure for the relative importance of aerosols for scattering light. The uppermost dot refers to Los Angeles County, the cross below it to Los Angeles City. From Garstang (1986).

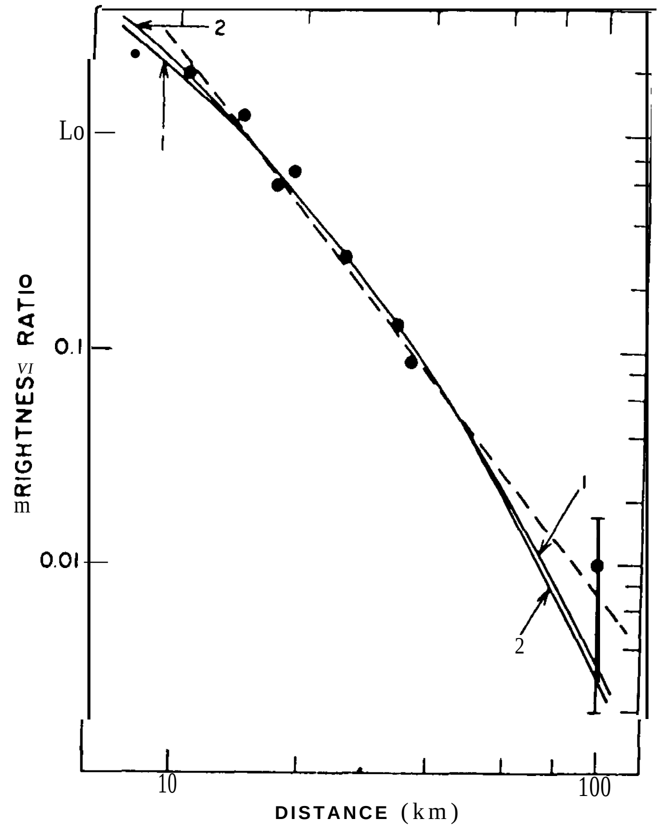

Fig. 32. Variation with distance from the city of the sky brightness at 45 deg altitude in the direction of the city. The dots indicate observations in V band by Walker(1977) near the city of Salina. The solid curves are according to models by Garstang (1986). The brightness ratio is defined as $\frac{b(\text{Salinas at } +45^\circ) - b(\text{Salinas at } -45^\circ)}{b(\text{sky background only at } +45^\circ)}$, where b = sky brightness, Zenith distance +45° 'is towards and -45° away from the city. The solid curves are according to models by Garstang (1986), Curve 1: L_0= 986 lumens per head, K = 0.43, F = 11 %. Curve 2: L_0= 1000 lumens per head, K = 0.5, F = 10 %. L_0 is the artificial lighting in lumens produced per head of the population. K is a measure for the relative importance of aerosols for scattering light. F: a fraction F of the light produced by the city is radiated directly into the sky at angles above the horizontal plane, and the remainder (l-F) is radiated toward the ground. The dashed line is the relation $\sim D^{-2.5}$. From Garstang (1986).

7. 1. Observations of sky pollution

Systematic broad-band observations of the sky pollution light near cities have been carried out by Bertiau et al. (1973) in Italy, Berry (1976) in Canada and Walker (1973, 1977) in California. Berry showed that there is a relationship between the population of a city and the zenith sky brightness as observed in or near to the city. Walker interpreted his extensive observations by deriving the following relationships: (1) between the population and luminosity of a city; (2) the sky brightness as a function of distance from the city; and (3) between the population and the distance from a city for a given sky pollution light contribution. The last two relationships are shown in Figures 31 and 32. These figures can be utilized to derive an estimate for the sky pollution at 45 deg altitude caused by a city with 2000 – 4 million population and with a similar street lighting power per head as California, Starting with the city population Fig. 31 gives the distance at which the artificial lighting contribution increases the natural sky brightness by 20 % (0.2 mag/□″). With this distance one can enter Fig.32 and obtain a scaling for the (arbitrary) intensity axis of this figure. Thus the artificially caused

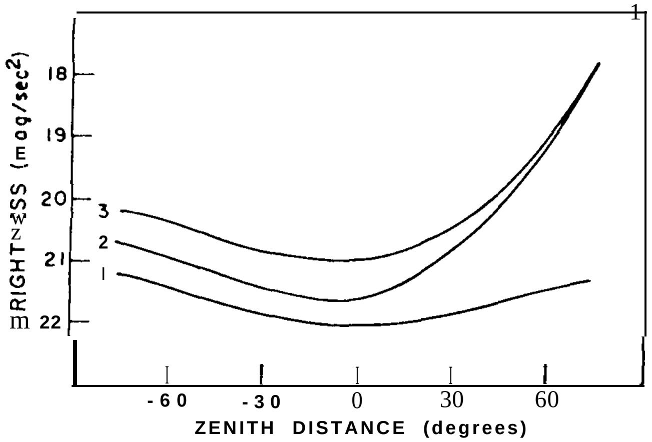

Fig. 33. Zenith distance dependence of sky pollution light according to the model calculations of Garstang (1986). Results are for sky pollution due to Denver as seen from a distance of 40 km in the vertical plane containing the observer and the center of Denver. Curve 1: sky background; Curve 2: Denver only; Curve 3: Denver and sky background. Negative zenith distances are away from Denver. From Garstang (1986)."

sky brightness at 45 deg altitude at 6- 200 km distance from the city can be estimated from this figure.

7.2. Modelling of sky pollution

Treanor (1973) and Bertiau et al. (1973) have used an empirical formula, based on a simplified model of the tropospheric scattering, to fit the sky pollution observations near cities. Garstang (1986, 1989a, 1989b, 1991) has used radiative transfer models including 1st and 2nd order Rayleigh and aerosole scattering, effects of ground albedo and curvature of the earth's surface, and the areal distribution of the light source to calculate the sky pollution light intensity. He has compared and scaled his model results against the above mentioned observational results. Garstang's fitted models are shown in Figures 31 and 32. superimposed on the observational points of Walker (1977). Garstang (1986, 1989a, 1989b) gives also the calculated zenith distance dependence of the sky pollution light intensity both towards and away from the source of light. These results are reproduced in Fig. 33.

7.3. Spectrum of the sky pollution light

The emission line spectra of the different types of street lamps are visible in the night sky light even at good observatory sites, such as Kitt Peak in Arizona. While the most commonly used street lamps until the 1970's were filled with Hg there has been since then a general change over to sodium lamps, both of the high pressure (HPS) and low pressure sodium (LPS) types. The most important sky pollution lines are given in Table 14 according to Osterbrock et al. (1976), Osterbrock and Martel (1992) and Massey et al. (1990). At good sites (e.g. Kitt Peak), the strongest pollution lines are about a factor of two weaker than the strongest airglow lines. The opposite is true for strongly contaminated sites (e.g. Mt Hamilton). Whereas the pollution lines are normally restricted to a relatively narrow wavelenth range the Na D line wings produced by the HPS lamps are extremely broad, extending over 5700 – 6100 Å. Thus the LPS lamps are highly preferable over the HPS ones from the astronorner's point of view.

Other studies of the night sky spectrum, including the artificial pollution lines, have been presented by Broadfoot and Kendall (1968) for Kitt Peak, Turnrose (1974) for Mt. Palomar and hit. Wilson, and Louistisserand et al. (1987) for Pic du Midi.

Table 14. The strongest artficial emission lines in the night sky spectrum between 3600 – 8200 Å. The most intense features are shown in boldface

Line	Sources
Hg I 3650	'Hg lighting
Hg I 3663	Hg lighting
Hg I 4047	Hg lighting
Hg I 4078	Hg lighting
Hg I 4358	Hg lighting
Na I 4665, 4669	HPS
Na I 4748, 4752	HPS
Na I 4978, 4983	HPS
Na I 5149, 5153	HPS
Hg I 5461	Hg lighting
Na I 5683, 5688	HPS, LPS
Hg I 5770	Hg lighting
Hg I 5791	Hg lighting
Na I 5890, 5896	HPS, LPS, airg
Na I 5700-6100 (wings)	HPS
Na I 6154, 6161	HPS, LPS
K I 7665	HPS, LPS
K I 7699	HPS, LPS
Na I 8183	HPS, LPS
Na I 8195	HPS, LPS

8. Zodiacal light

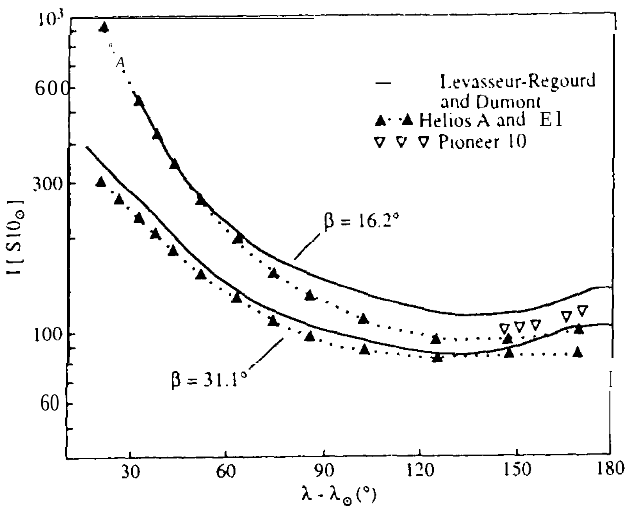

Fig. 34. Comparison of zodiacal light measurements along the bands of constant ecliptic latitude β = 16.2° and/3 = 31.0° observed by Helios A and B. The ground-based measurements of Levasseur-Regourd and Dumont (1980) at λ_{eff} = 502 nm have been linearly interpolated to these latitude values. The Helios measurements at B and V (Leinert et al. 1981) have been linearly interpolated to λ_{eff} = 502 nm. The Pioneer measurements (Toiler and Weinberg 1985) have been extrapolated from blue to 502 nm with the values applicable for Helios and from/3 = 10° to β = 16° according to the table of Levasseur-Regourd and Dumont (1980). For definition of the SIO_0 unit see section 2.

8.1. Overview and general remarks

The zodiacal light in the ultraviolet, visual and near-infrared region is due to sunlight scattered by the interplanetary dust particles. In the mid- and far-infrared it is dominated by the thermal emission of those particles. Zodiacal light brightness is a function of viewing direction ($\lambda - \lambda_\odot, \beta$), wavelength, heliocentric distance (R) and position of the observer relative to the symmetry plane of interplanetary dust. Its brightness does not vary with solar cycle to within 1 % or at most a few percent (Dumont and Levasseur-Regourd 1978, Leinert and Pitz 1989), except for subtle effects associated with the scattering of sunlight on the electrons of the interplanetary plasma (Richter et al. 1982). However, seasonal variations occur because of the motion of the observer in heliocentric distance and with respect to the symmetry plane of interplanetary dust cloud (by the annual motion of the earth or the orbital motion of the space probe). The colour of the zodiacal light is similar to solar colour from 0.2 μm to 2 μm, with a moderate amount of reddening with respect to the sun (see Figure 3S). Beyond these wavelengths, the thermal emission of interplanetary dust gradually takes over, the emission being about equal to the scattering part at 3..5 μm (Berriman et al. 1994). In general the zodiacal light is smoothly distributed, small-scale structures appearing only at the level of a few percent.

At present, the overall brightness distribution and polarisation of zodiacal light have been most completely, with the largest sky coverage determined in the visual. The infrared maps obtained by the DIRBE experiment on satellite COBE (see section 8.5) from 1.25 μm to 240 μm provide excellent data, with relative accuracies of 1% to 2% at least for the wavelengths between 1.25 μm and 100 pm. Their absolute accuracy is estimated to $\approx$5% for wavelengths $\leq 12\mu$m and $\approx$10% for the longer wavelengths. But these maps are limited to the range in solar elongations of ϵ = 94° ± 30°. An impression of the accuracy achieved in the visual is obtained by comparing the best available ground-based map (Levasseur-Regourd and Dumont 19S0) with space probe results from Pioneer 10 (Toiler and Weinberg 1985) and Helios k/B (Leinert et al. 1985) in Figure 34. Among these, e.g. the calibration of the Helios zodiacal light photometers was extensive enough to predict *before launch* the count rates for bright stars observed in flight to within a few percent, and to propose the same correction to solar U-B and B-V colours (Leinert et al. 19S1) as the cledicated solar measurements of Tüg and Schmidt-Kaler (19S2). However the deviation between the three zodiacal light data sets is larger than suggested by this precision, typically 10 %, and up to 20 %. The deviation appears to be more systematic than statistical in nature. We conclude that the zodiacal light in the visual is known to an accuracy of 10 % at best, about half of which uncertainty is due to multiplicative errors like calibration (including the definition of what a V = 10 mag solar analog G2V star exactly looks like).

In the ultraviolet, the maps of zodiacal light brightness and polarisation are less complete than in the visual, and the calibration is more difficult. In lack of convincingly better information, we assume the overall distribution of zodiacal light brightness at these wavelengths to be the same as in the visual. This, of course, is only a convenient approximation to hardly better than $\approx$20%. Figures 35 and 36 show that this assumption nevertheless gives a reasonable description of the IRAS zodiacal light measurements at elongation ϵ = 90° (Vrtilek and Hauser 1995) and an acceptable approximation to the 10.9 μm and 20.9 μm rocket measurements of Murdock and Price (1985) along the ecliptic over most of the elongation range. Therefore, in the infrared, it also may be used in those areas where direct infrared measurements are not available.

In this spirit, we now want to give the reader the information necessary to get the mentioned estimates of zodiacal light brightness on the basis of the brightness table for visual wavelengths. To this end we write the observed zodiacal light brightness I_{ZL} for a given viewing direction, position of the observer and wavelength of observation

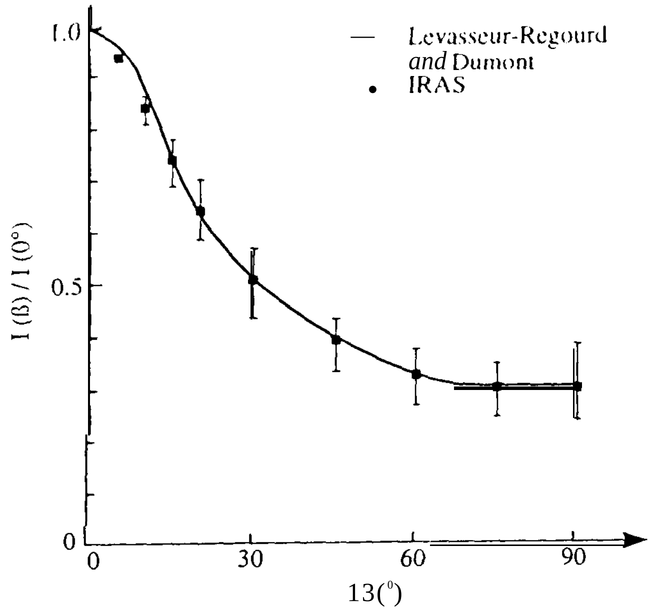

Fig. 35. Comparison of the out-of-ecliptic decrease of zodiacal light brightness at elongation 90° as measured from ground at 502 nm (Leva-sseur-Regourd and Dumont (1980)) and by IRAS (Vrtilek and Hauser 1995). The IRAS measurements are represented here by their annual average. The squares give the average of the profiles at 12 μm, 25 pm and 60 μm, the bars given with the IRAS measurements show the range covered by the profiles at the different wavelengths, with the measurements at 60 μm delineating the lower and the measurements at 12 μm the upper envelope.

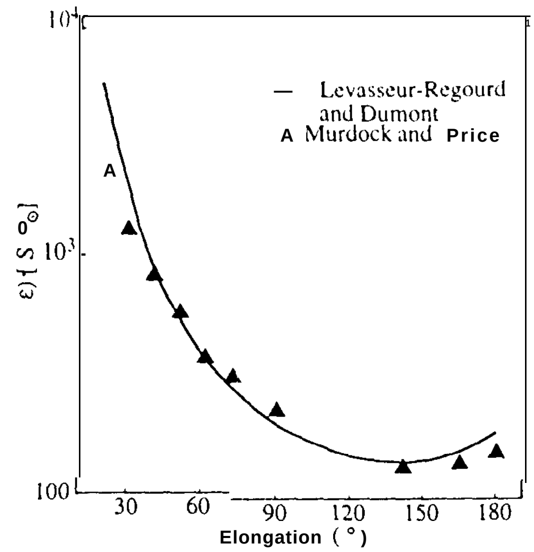

Fig. 36. Comparison of zodiacal light brightness profile along the ecliptic as measured by Levasseur-Regourd and Dumont (1980) at 502 nm and by a rocket flight (Murdock and Price 1985) at 10.9 μm and 20.9 pm. The rocket data for the two wavelength bands have been averaged and normalised to the ground-based measurements at an elongation of 60°. For definition of the $S10_\odot$ unit see section 2.

in acceptable approximation (i.e. more or less compatible with the uncertainties of the results) as a product

$$I_{ZL} = f_R \cdot I(\lambda - \lambda_\odot, \beta) \cdot f_{abs} \cdot f_{co} \cdot f_{SP} \quad (14)$$
$$[S10_\odot, respectively W m^{-2} sr^{-1} \mu m^{-1} or MJy/sr]$$

where

- $I(\lambda - \lambda_\odot, \beta)$ is the map of zodiacal light brightness in the visual for a position in the symmetry plane at 1 AU (Table 16 ,resp. Table 17),
- f_{abs} transforms from 500 nmto the wavelength dependent absolute brightness level of the map
- f_{co} gives the differential wavelength dependence (i.e. the colour with respect to a solar spectrum), including a colour dependent correction of the map. This factor is applicable from 0.25 μm to 2.5 μm when the brightness is wanted in $S10_\odot$ units, starting from the value at 500 nrn (Table 16).
- f_{SP} describes the influence of the position of the observer with respect to the Symmetry Plane of interplanetary dust on the observed brightness. This effect is discussed at length in section 8.7.
- f_R gives the dependence on heliocentric distance R.

In the following sections 8.2 -8.7 we provide the quantitative information needed to use the unifying approximate equation (14) but also present present individual original results and topics not directly related to it. Section 8.8 discusses the structures present in the zodiacal light on the level of several percent, and section 8.9 indicates how the observed zodiacal light brightness depends on the position of the observer in the solar system.

8.2. *Heliocentric dependence*

This section gives information which allows us to estimate the factor f_R.

In the inner solar system, for 0.3 AU < R < 1.0 AU, the Helios experiment (Leinert et al. 1980) found the visual brightness to increase with decreasing heliocentric distance for all elongations between 16° and 160° as

$$\frac{I(R)}{I(1.0 AU)} = R^{-2.3 \pm 0.1} \quad (15)$$

In this same range the Helios experiment (Leinert et al. 1982) observed the degree of polarisation to increase with increasing heliocentric distance as

$$\frac{p(R)}{p(1AU)} \cdot R^{+0.3\pm0.05} \quad (16)$$

In the outer solar sytem, for 1.0 AU < R <3.3 AU, Pioneer 10 (Toiler and Weinberg 1985, see also Hanner et al. 1976) found a decrease with heliocentric distance which can be summarised as

$$\frac{I(R)}{I(1AU)} \cdot R^{-2.5\pm0.2}, \quad (17)$$

neglecting the correction for Pioneer 10's changing distance from the symmetry plane (compare Table 29). Such a steepening is expected to result if there is less interplanetary dust outside the asteroid belt than extrapolated from the inner solar system (van Dijk et al. 1988, Hovenier and Bosma 1991).

Similarly simple expressions for the thermal infrared cannot be given, since the thermal emission of interplanetary dust

- depends on the temperature T(R) of the dust grains via Planck's function, which is highly nonlinear and therefore
- critically depends on wavelength.

Infrared observations from positions in the inner or outer solar system are not yet available. Estimates therefore have to be based on model predictions (see section 8.9). Examples for such, to varying degrees physical or simply parameterising models are to be found, e.g. in Röser and Staude (1978), Murdock and Price (1985), Deul and Wolstencroft (1988), Rowan-Robinson et al. (19'30), Reach (1988,1991), Reach et al. (1996a), Dermott et al. (1996); see also the discussion of several of these models by Hanner (1991). Present knowledge on the most important physical input parameters is summarised in Table 15, mostly taken from Levasseur-Regourd (1996). Note that "local" polarisation does not mean the zodiacal light polarisation observed locally at the Earth, but the polarisation produced by scattering under 90° in a unit volume near the Earth's orbit. The gradients (power law exponents in heliocentric distance R) have been derived from brightness measurements at 1 AU using an inversion method called "nodes of lesser uncertainty" (Dumont and Levasseur-Regourd 1985). The one directly observed physically relevant quantity in the infrared is the colour temperature of the zodiacal light. At elongation ϵ = 104° the colour temperature has been measured between 5 pm and 16.5 μm from the infrared satellite 1S0 to be 261.5±1.5 K (Reach et al. 1996b). In this wavelength range, the spectrum of the zodiacal light closely followed blackbody emission. See also *the* discussion of an infrared zodiacal light model in section S.5.

Table 15. Heliocentric gradient of physical properties of interplanetary dust (scattering properties are given for a scattering angle of 90°).

	Value at 1 AU	Gradient (power law)	Range (in AU)
Density	10^{-19} kg/m^3	-0.93 ± 0.07	1.1 -1.4
Temperature	26O*1O K	-0.36 ± 0.03	1.1-1.4"
Albedo	0.08±0.02 (from IRAS)	-0.32 ± 0.05	1.1 -1.4
Polarisation (0.5μm, local)	0.30±0.03	+0.5 * 0.1	0.5 -1.4

8.3. *Zodiacal light at 1 A U* in *the visual*

First we give here the values for the zodiacal light at 500 nm (the possible minute difference to 502 nm, to which the data of Levasseur-Regourd and Dumont (1980) refer, is neglected). Brightnesses are expressed in $S10_\odot$ units. At 500 nrn ($\Delta\lambda$ = 10 nm) we have

$$1S10_\odot = 1.28 \ .10\text{-}8 \ [Wm^{-2}sr^{-1}\mu^{-1}]$$
or (18)
$$1S10_\odot = 1.28 \ .10\text{-}9 \ [erg\ cm^{-2}s^{-1}sr^{-1}\text{Å}^{-1}].$$

8.3.1. Pole of the ecliptic

The annually averaged brightness and degree of polarisation and the polarised intensity I_{pol} *at the ecliptic* poles *at* 500 nrn result as (Levasseur-Regourd and Dumont 1980, Leinert et al. 1982)

$$I_{ZL}(\beta = 90°) = 60 \pm 3S10_\odot$$

$$p_{ZL}(\beta = 90°) = 0.19 \pm 0.01 \quad (19)$$

$$I_{pol\,ZL}(\beta = 90°) = 11.3+: 0.3s10(3 .$$

For completeness we note that the polarized intensity appears to be very much agreed upon, while many of the space experiments (Sparrow and Ney 1968, Sparrow and Ney 1972, Levasseur and Blamont 1973, Frey et al. 1974, Weinberg and Hahn 1980) tend to find I_{ZL} lower by about 10 % and p_{ZL} correspondingly higher. But for uniformity of reference within the zodiacal light map below we recommend use of the numbers given above.

8.3.2. Maps

Because of the approximate symmetry of the zodiacal light with respect to the ecliptic (resp. symmetry plane) and also with respect to the helioecliptic meridian (sun-ecliptic poles-antisolar point) only one quarter of the celestial sphere has to be shown. We present the groundbased brightness map for 500 nm in three ways:

$\beta°$ / $\lambda - \lambda_\odot$	0	5	10	15	20	25	30	45	60	75
0				2450	1260	770	500	215	117	78
5				2300	1200	740	490	212	117	78
10			3700	1930	1070	675	460	206	116	78
15	9000	5300	2690	1450	870	590	410	196	114	78
20	5000	3500	1880	1100	710	495	355	185	110	77
25	3000	2210	1350	860	585	425	320	174	106	76
30	1940	1460	95.5	660	480	365	285	162	102	74
35	1290	990	710	530	400	310	250	151	98	73
40	925	735	545	415	325	264	220	140	94	72
45	710	570	435	345	278	228	195	130	91	70
60	395	345	275	228	190	163	143	105	81	67
75	264	248	210	177	153	134	118	91	73	64
90	202	196	176	151	130	115	103	81	67	62
105	166	164	154	133	117	104	93	75	64	60
120	147	145	138	120	108	98	88	70	60	58
135	140	139	130	115	105	95	86	70	60	57
150	140	139	129	116	107	99	91	75	62	56
165	153	150	140	129	118	110	102	81	64	56
180	180	166	152	139	127	116	105	82	65	56

Table 16. Zodiacal light brightness observed from the Earth (in $S10_{\odot}$) at 500 nm. Towards the ecliptic pole, the brightness as given above is 60 ± 3 $SIO_{\odot}$. The table is an update of the previous work by Levasseur-Regourd and Dumont (1980). The values remain the same but for a slight relative increase, both for the region relatively close to the Sun, and for.. high ecliptic latitudes. The previous table is completed in the solar vicinity, up to 15° solar elongation. Intermediate values rnaybeobtained by smooth interpolations, although small scale irregularities (e.g. cometary trails) cannot be taken into account.

$\beta°$ / $\lambda - \lambda_\odot$	0	5	10	15	20	25	30	45	60	75
0				3140	1610	985	640	275	150	100
5				2940	1540	945	625	271	150	100
10			4740	2470	1370	865	590	264	148	100
15	11500	6780	3440	1860	1110	755	525	251	146	100
20	6400	4480	2410	1410	910	635	4.54	237	141	99
25	3840	2830	1730	1100	749	545	410	223	136	97
30	2480	1870	1220	845	615	467	365	207	131	95
35	1650	1270	910	680	510	397	320	193	125	93
40	1180	940	700	530	416	338	282	179	120	92
45	910	730	555	442	356	292	250	166	116	90
60	505	442	352	292	243	209	183	134	10-1	86
75	338	317	269	227	196	172	151	116	93	82
90	259	251	225	193	166	147	132	104	86	79
105	212	210	197	170	150	133	119	96	82	77
120	188	186	177	154	138	125	113	90	77	7-1
135	179	178	166	147	134	122	110	90	77	73
150	179	178	165	148	137	127	116	96	79	72
165	196	192	179	165	151	141	131	104	82	72
180	230	212	195	178	163	148	134	105	83	72

Table 17. **Zodiacal light brightness** observed from the Earth (in S1 units). This table is identical to the previous one, but for the unit: the values are given in 10^{-8} W m^{-2} sr^{-1} μm^{-1}, for a wavelength of 0.50 μm. The multiplication factor is 1.28× IO-S W m^{-2} sr' μm^{-1} (see Table 2 in section 2). Towards the ecliptic pole, the brightness as given above is 77± ×10^{-8} W m^{-2} sr-' μm^{-1}. This table (adapted from Levasseur-Regourd 1996) still needs to be multiplied by a corrective factor F_{co} for use at other wavelengths, in order to take into account the solar spectrum. This table has been added for direct use by those who are not familiar with magnitude related units.

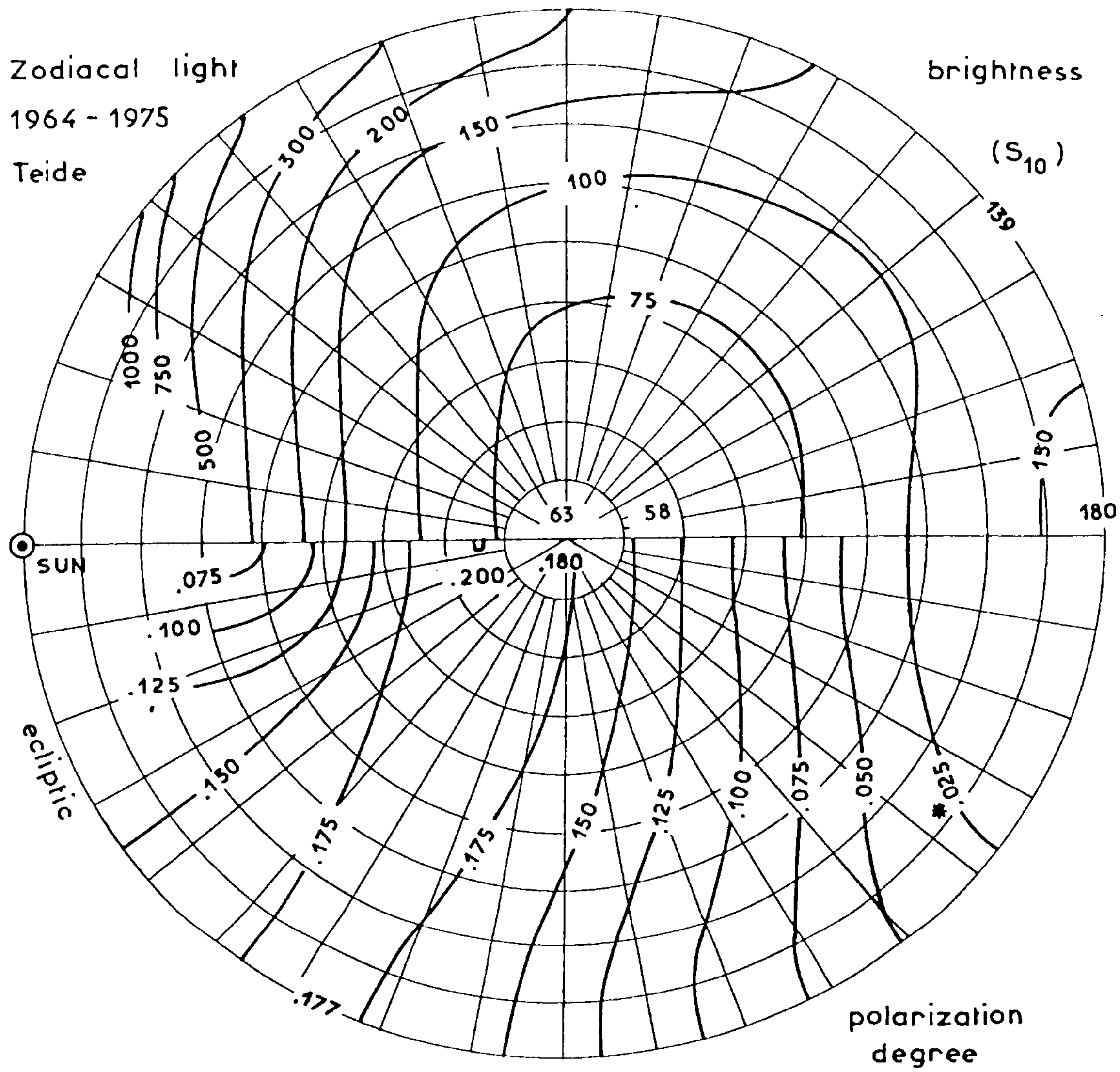

Fig. 37. Annually averaged distribution of the zodiacal light over the sky in differential ecliptic coordinates. Upper half: zodiacal light brightness I_{ZL} (SIO.), lower half degree of polarisation of zodiacal light. The circumference represents the ecliptic, the ecliptic pole is in the center, and the coordinates $\lambda - \lambda_{\odot}$ and β are drawn in intervals of 10°. The '*' indicates a line of lower reliability. From Dumont and Sanchéz 1976.

1. Figure 37, taken from Dumont and Sanchéz (1976) gives the original data in graphical form and allows quick orientation.
2. Table 16, based on the results of Levasseur-Regourd and Dumont (1980) contains a smoothed tabulation of these (basically same) data in steps of 5° to 15° in $\lambda - \lambda_{\odot}$ and 3.
3. Table 17 is identical to Table 16, except that the brightness now is given in physical units.

The zodiacal light tables given here deviate somewhat from the original earthbound data sets, which were limited to elongation > 30°, because they were subject to additional smoothing, and because they also give a smooth connection to two measurements closer to the sun: the results obtained by Helios A/B (Leinert et al. 1982) and those of a precursor rocket flight (Leinert et al. 1976) for small elongations (ϵ < 300). For interpolation, if the smaller 5° spacing is needed, still the table in Levasseur-Regourd and Dumont (1980) can be used. In addition, Table 18 gives a map of zodiacal light polarisation, structured in the same way as Tables 16 and 17.

For these maps, the errors in polarisation are about 1%. The errors in brightness are 10-15 SIO_z for low values and 5% - 10 % for the higher bright nesses.

β° / $\lambda - \lambda_\odot$	0	5	10	15	20	25	30	45	60	75
0				8	10	11	12	16	19	20
5				9	10	11	12	16	19	20
10			11	11	12	13	14	17	19	20
15	13	13	13	13	13	14	15	17	19	20
20	14	14	14	15	15	1.5	15	17	19	20
25	15	15	16	16	16	16	16	18	19	20
30	16	16	16	16	16	17	17	18	19	20
35	17	17	17	17	17	17	17	18	20	20
40	17	17	17	17	18	18	18	19	20	20
45	18	18	18	18	18	18	18	19	20	20
60	19	19	19	19	19	20	20	20	20	20
75	18	18	18	18	18	19	19	19	19	19
90	16	16	16	16	16	16	17	18	18	19
105	12	12	12	12	13	13	14	15	17	19
120	8	8	9	9	9	10	11	13	15	18
135	5	5	5	6	6	7	8	11	14	17
150	2	2	2	3	3	4	5	8	12	16
16.5	-2	-2	-1	-1	0	2	3	7	11	16
180	0	-2	-3	-2	-1	0	2	6	11	16

Table 18. Zodiacal light polarization observed from the Earth (in percent) The table provides the values for linear polarisation (Levasseur-Regourd 1996). Circular polarisation of zodiacal light is negligible. Positive values correspond to a direction of polarisation (E vector) perpendicular to the scattering plane (Sun-Earth-scattering particles), negative values correspond to a direction of the polarisation in the scattering plane. Towards the ecliptic pole, the degree of polarisation as given above is 19 ± 1 percent. The negative values noticed in the Gegenschein region correspond to a parallel component greater than the perpendicular component, as expected for the scattering by irregular particles at small phase angles.

8.4. Wavelength dependence and colour with respect to the sun

The wavelength dependence of the zodiacal light generally follows the solar spectrum from 0.2 μm to $\approx 2 \mu$m. However, detailed study shows a reddening of the zodiacal light with respect to the sun. The thermal emission longward of 3 pm, as mentioned already in section 8.1, can be approximated by a diluted blackbody radiation, as discussed in section *8.5*. A recent determination of the temperature of this radiation gives a value of 261.5 ± 1.5 K (Reach et al. 1996).

Figure 38 gives an impression of the spectral flux distribution of the zodiacal light at elongation ϵ = 80 °in the ecliptic. It emphasises the closeness to the solar spectrum from 0.2 μm to 2 pm. Note that at wavelengths $\lambda <$ 200 nm the intensity levels expected for a solar-type zodiacal light spectrum are quite 10W, therefore difficult to establish (see section 8.6).

8.4.1. Wavelength dependence - absolute level

This section gives information which allows us to estimate the factor f_{abs}.

From the ultraviolet to near-infrared, if zodiacal light brightness is given in $S10_\odot$ units and the zodiacal light spectrum were solar-like, then we would have simply f_{abs} = 1.0.

If the zodiacal light brightness again is expressed in $S10_\odot$ units but its reddening is taken into account, we still take f_{abs} = 1.0 and put the reddening into the colour correction factor f_{co} (see the following section).

If the zodiacal light brightness is given in physical units, f_{abs} gives the factor by which the absolute level of brightness changes from λ = 500 nrn to a given wavelength. Because best defined observationally at an elongation of ϵ = 900 in the ecliptic, the factors f_{abs} should be used for that viewing direction. Table 19 already implicitly contains these factors, since it gives the wavelength dependent brightnesses $I_{ZL}(\lambda) = I_{ZL}(500 \text{ nm}) \times f_{abs}$, for the 90° points in the ecliptic. (Where appropriate, the factor f_{co} has also been included). For the infrared emission this brightness is taken from the COBE measurements (see section 8.5) and added here for completeness and easy comparability.

8.4.2. Colour effects - elongation-dependent reddening

This section gives information which allows us to estimate the factor f_{co}. This factor applies to the ultraviolet to near-infrared part of the spectrum only. Since it deviates from

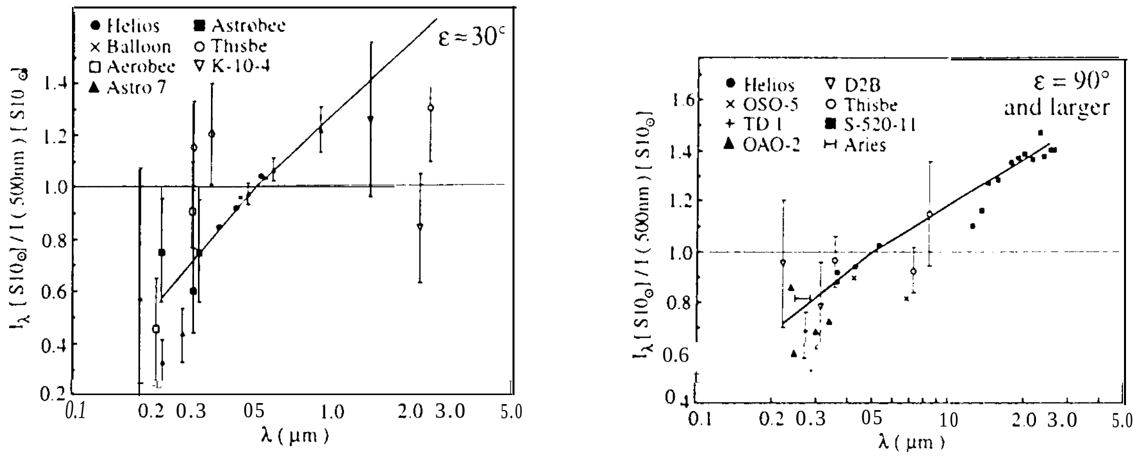

Fig. 39. Reddeningof the zodiacal light according to colour measurements by various space-borne and balloon experiments. Left: at small elongations; right: at large elongations. The quantity plotted is the ratio of zodiacal light brightness at wavelength λ to zodiacal light brightness at wavelength 500 nm, normalised by the same ratio for the sun (i.e. we plot the colour ratio C(A, 500 rim). Reddening corresponds to a value of this ratio of < 1.0 for λ <500 nm and > 1.0 for λ > 500 nm. The thick solid line represents the adopted reddening (equ. 22). The references to the data points are: Leinert et al. 1981 (Helios), Vande Noord 1970 (Balloon). Feldman 1977 (Aerobee rocket), Pitz et al. 1979 (Astro 7 rocket), Cebula and Feldman 1982 (Astrobee rocket), Frey et al. 1977 (Balloon Thisbe), Nishimura 1973 (rocket K-10-4), Sparrow and Ney 1972 (OSO-5), Morgan et al. 1976 (TD-1), Lillie 1972 (0.40 -2), Maucherat-Joubert et al. 1979 (D2B), Matsuura et al. 1995 (rocket S-520-11), Tennyson et al. 1988 (Aries rocket).

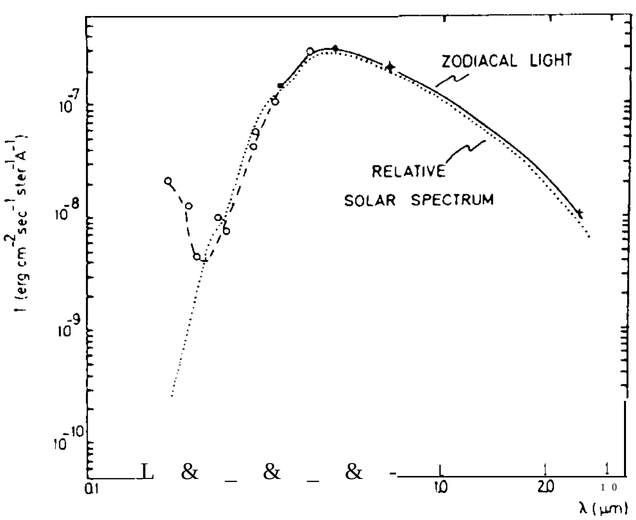

Fig. 38. Broadband spectrum of the zodiacal light. The shown observations are by Frey et al. (1974, ●), Hofmannet al. (1973, +), Nishimura et al. (1973, ∇) and Lillie (1972, o). From Leinert (1'375).

Table 19. Zodiacal light at ϵ = 90" in the ecliptic

$\lambda(\mu m)$	S10$_\odot$	W m^{-2} sr^{-1} μm^{-1}	MJy/sr
0.2		$2.5\ 10^{-8}$	
0.3	162	$5.3\ 10^{-7}$	
0.4	184	$2.2\ 10^{-6}$	
0.5	202	$2.6.\ 10^{-6}$	
0.7 (R_J)	220	$2.0\ 10^{-6}$	
0.9 (I_J)	233	$1.3\ 10^{-6}$	
1.0	238	$1.2\ 10^{-6}$	
1.2 (J)		$8.1\ 10^{-7}$	0.42
2.2 (K)		$1.7\ 10^{-7}$	0.28
3.5 (L)		$5.2\ 10^{-8}$	0.21
4.8 (M)		$1.2\ 10^{-7}$	0.90
12		$7.5\ 10^{-7}$	36
25		$3.2\ 10^{-7}$	67
60		1.8 10-s	22
100		$3.2.\ 10^{-9}$	10.5
140		$6.9\ 10^{-10}$	4.5

unity by less than 20% from 350 nm to 800 nm, neglecting it (i.e. assuming a strictly solar spectrum) may be acceptable in many <applications. Otherwise one has to go

through the somewhat clumsy colour correction detailed below.

It is convenient to express the colour of zodiacal light as a colour ratio which linearly measures the deviation of zodiacal light from the the solar spectrum:

$$C(\lambda_1,\lambda_2) = \frac{I_{ZL}(\lambda_1)/I_\odot(\lambda_1)}{I_{ZL}(\lambda_2)/I_\odot(\lambda_2)} \tag{20}$$

and which, for $\lambda_1 < \lambda_2$, is related to the colour indices (CI) by

$$CI_{ZL} - CI_\odot = -2.5\log C(\lambda_1,\lambda_2) \tag{21}$$

We compile in Figure 39 measurements of the colour of the zodiacal light with respect to the solar spectrum. There is quite some disagreement in detail, but also a trend for a general reddening which is stronger at small elongations ($\epsilon \approx 30°$). To be specific, we decide on the basis of Figure 39, on the following reddening relations (straight lines in this log-linear presentation and giving particular weight to the Helios measurements):

$$\begin{aligned}
\epsilon < 30° :\ & f_{co} = f_{co-30} \\
\epsilon = 30° :\ & f_{co-30} = 1.0 + 1.2 \times \log(\frac{\lambda}{500nm}) \\
& \quad 220nm \le \lambda \le 500nm \\
& \quad = 1.0 + 0.8 \times \log(\frac{\lambda}{500nm}) \\
& \quad 500nm \le \lambda \le 2.5\mu m \\
\epsilon = 90° :\ & f_{co-90} = 1.0 + 0.9 \times \log(\frac{\lambda}{500nm}) \\
& \quad 220nm \le \lambda \le 500nm \\
& \quad = 1.0 + 0.6 \times \log(\frac{\lambda}{500nm}) \\
& \quad 500nm \le \lambda \le 2.5\mu m \\
\epsilon > 90° :\ & f_{co} = f_{co-90}
\end{aligned} \tag{22}$$

Here, $f_{co} = 1.0$ corresponds to solar colour, while a reddening results in $f_{co} < 1.0$ for $\lambda < 500$ nm and in $f_{co} > 1.0$ for $\lambda > 500$ nm.

For intermediate values of ϵ, f_{co} can be interpolated. The curves for the assumed colour in Figure 39 are made to closely fit the Helios data, where the UBV (363 nm, 425 nm, 529 nm) colours (Leinert et al. 1982), again expressed as colour ratios, were

$$\frac{I_V}{I_B} = 1.14 - 5.5 \cdot 10^{-4} \cdot \epsilon(°) \tag{23}$$

$$\frac{I_B}{I_U} = 1.11 - 5.0 \cdot 10^{-4} \cdot \epsilon(°)$$

Obviously the colour ratio factor f_{co} cannot be very accurate in the ultraviolet (where measurements don't agree to well) nor beyond 1 μm (where partly extrapolation is involved). The situation for $\lambda \le 220$ nm in the ultraviolet and for the emission part of the zodiacal light are described below in separate sections.

8.4.3. Wavelength dependence of polarisation

The available zodiacal light polarisation measurements between 0.25 μm and 3.5 μm fall in two groups (Figure 40): Most observations in the visual can be represented within their errors by a polarisation constant over this wavelength range. Two quite reliable measurements, on the other hand (by Helios in the visible and by COBE in the near-infrared), show a definite decrease of observed degree of polarisation with wavelength.

In the limited wavelength range from 0.45 μm to 0.80 μm it is still an acceptable approximation to assume the polarisation of the zodiacal light as independent of wavelength. But overall, the wavelength dependence of polarisation summarised in Figure 40 has to be taken into account. For an elongation of 90°, to which most of the data in Figure 40 refer, it can be reasonably represented by the relation (solid line in the Figure)

$$p(\lambda) = 0.17 + 0.10 \cdot \log(\lambda/0.5\mu m)\,, \tag{24}$$

i.e. by a decrease of $\approx$ 3% per factor of two in wavelength. With $p(0.5\,\mu m) = 0.17$, this can also be written in the form

$$p(\lambda) = p(0.5\mu m)[1 + 0.59 \log(\lambda/0.5\mu m)]\,, \tag{25}$$

which may be applied tentatively also to other viewing directions.

At longer wavelengths, with the transition region occuring between $\approx$2.5 μm and 5 μm, the zodiacal light is dominated by thermal emission and therefore unpolarised. At shorter wavelengths the zodiacal light brightness is very low, and the polarisation is not known (although it may be similar to what we see in the visual spectral range).

Maps of the zodiacal light polarisation at present are available with large spatial coverage for the visual spectral range only. For other wavelength ranges, it is a *first* approximation to use the same spatial distribution.

8.5. *Zodiacal light in the thermal infrared*

Extensive space-based measurements, of the diffuse infrared sky brightness in the infrared have become available over the past 13 years (e.g., Neugebauer et al. 1984 (IRAS); see Beichman 1987 for a review of IRAS results; Murdock and Price 1985 (ZIP); Boggess et al. 1992 (COBE); Murakami et al. 1996 (IRTS); Kessler et al. 1996 (ISO)). In general, some form of modeling is required to separate the scattered or thermally emitted zodiacal light from other contributions to the measured brightness, though at some wavelengths and in some directions the zodiacal light is dominant. Because the COBE/DIRBE measurements have the most extensive combination of sky, temporal) and wavelength coverage in the infrared, and have been carefully modeled to extract the zodiacal light signal (Reach et al. 1996a; COBE/DIRBE Explanatory Supplement), we largely rely on these results.

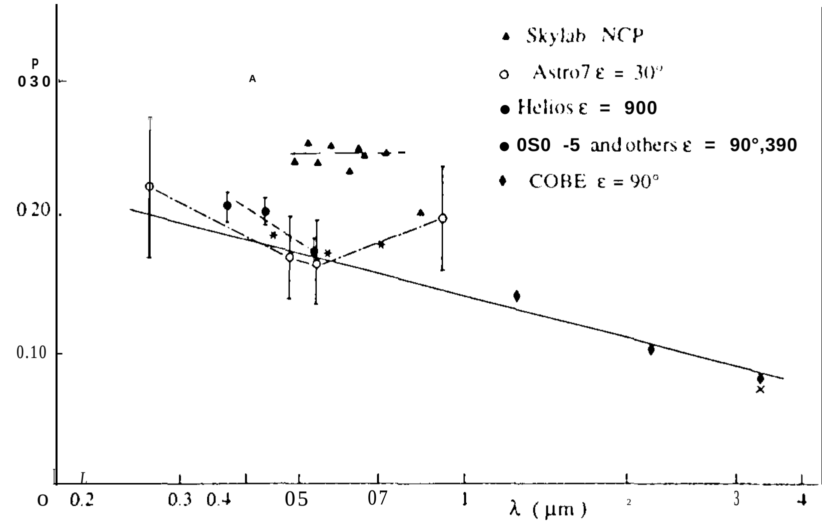

Fig. 40. Wavelength dependence of polarisation observed at different positions in the zodiacal light. Filled triangles - Skylab at the north celestial pole (Weinberg and Hahn 1979); open circles: rocket Astro 7 at elongation ϵ = 30 °(Pitz et al. 1979); dots: Helios at β = 16°, ϵ = 90° (Leinert et al. 1982); diamonds: COBE measurements (Berriman et al. 1994); stars: an average of three similar results (0 S0-5, ϵ = 90°, Sparrow and Ney 1972; balloon at ϵ = 30°, Vande Noord 1970; ground-based at ϵ = 39°, Wolstencroft and Brandt 1967). Note: it is the wavelength dependence within each group which matters. The solid line shows the approximation (24) to the wavelength dependence of p.

The spectral energy distribution of the zodiacal light indicates that the contributions from scattered and thermally emitted radiation from interplanetary dust are about equal near 3.5 μm (Spiesman et al 1995; Matsumoto et al 1996), where the interplanetary dust (IPD) contribution to the infrared sky brightness is at a local minimum. This turnover is most clearly seen in the data of the near-infrared spectrometer onboard the satellite IRTS (Matsumoto et al. 1996, see Figure 41). Observations in the range 3-5 μm are expected to be neither purely scattering not purely thermal. The thermal spectrum peaks near 12 μm, and the observed spectral shape for λ < 100 μm approximates that of a blackbody (for a power law emissivity proportional to v–n, spectral index n= O) with a temperature in the range 250 - 290 K (Murdock and Price 1985, Hauser et al. 1984, Spiesman et al. 1995), depending in part on the direction of observation. As already mentioned, recent results from 1S0 (Reach et al 1996b) fit the 5 - 16.5 μm wavelength range with a blackbody of T = 261.5 ± 1.5 K. Using COB E/ DIRBE data, Reach et al. (1996a) find a slow roll-off of the emissivity in the far-infrared (spectral index n $\approx$ 0.5 for λ > 100 pm).

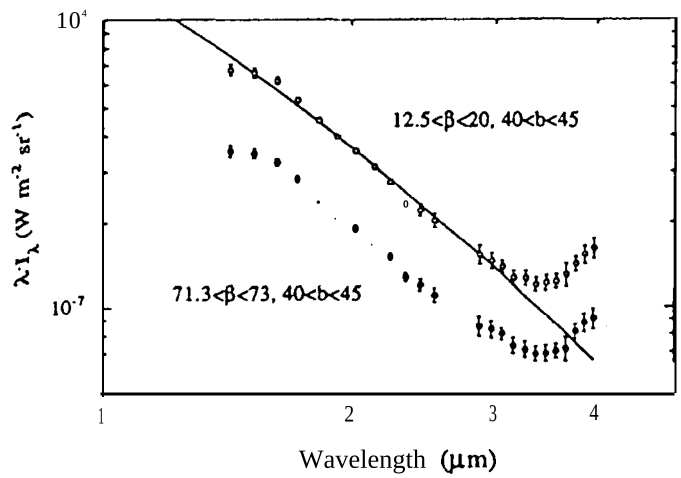

Fig. 41. Near-infrared spectra of the sky brightness measured with the satellite IRTS at low and at high ecliptic latitudes β. The solid line gives a solar spectrum, normalised to the measurements at low β at 1.83 μm. From Matsumoto et al. (1996).

Except near the Galactic plane, the signal due to interplanetary dust dominates the observed diffuse sky brightness at all infrared wavelengths shortward of $\approx$ 100 μm. This is illustrated in Figure 42, which presents COBE/DIRBE observations (0.7 deg resolution) of a strip of sky at elongation 90 deg in 10 photometric bands ranging from 1μm - 240 pm. The estimated contribution from zodiacal light (based upon the DIRBE model, see below) is also shown at each wavelength in Figure 42. Even in the far infrared, the contribution from zodiacal light is not necessarily negligible: Reach et al (1996a) estimated the fraction of total sky brightness due to zodiacal light at the NGP as roughly 25% at 240 μm. Examination of Figure 42 shows that, although the signal due to interplanetary dust peaks near the ecliptic plane at all wavelengths, the detailed shape of the signal is wavelength-dependent. An analytic empirical relation for the brightness in the thermal infrared at 90° elongation (based upon IRAS data) has been described by Vrtilek and Hauser (1995). As already mentioned, the brightness distribution in visual can serve as a first approximation to the brightness distribution in the thermal infrared, if the respective infrared data are not available.

Although the shape of the underlying zodiacal 'lower envelope' is clearly visible in the data of Figure 42, the determination of the absolute zero-level of the zodiacal light in the infrared is difficult. In addition to absolute calibration uncertainties in the sky brightness measurements themselves, contributions from Galactic sources and possibly extragalactic background make this a challenging problem.

A summary of several techniques which have been used to isolate the zodiacal light from other sky signals is documented by Hauser (1988): many involve filtering the data in either the angular or angular frequency domain, leaving the absolute signal level uncertain. Others accomplish removal of the Galactic component via models, e.g. by using the statistical discrete source model of Wainscoat et al (1992), or by use of correlations with measurements at other wavelengths (e.g., HI; Boulanger and Perrault 1988). We choose here to quote zodiacal light levels as derived from the DIRBE zodiacal light model, which is based upon a pararneterized physical model of the interplanetary dust cloud similar to that used for IRAS (Wheelock et al. 1994, Appendix G). Rather than determining the model parameters by fitting the observed sky brightness, the DIRBE model was derived from a fit to the seasonally-varying component of the brightness in the DIRBE data, since that is a unique signature of the part of the measured brightness arising in the interplanetary dust cloud (Reach et al. 1996a). The model explicitly includes several spatial components (see Section 8.8): a large-scale smooth cloud, the dust bands attributed to asteroidal collisions, and the resonantly-trapped dust ring near 1 A.U. Zodiacal light levels given here are estimated to be accurate to ≈10% for wavelengths of 25 μm and shortward, and ≈20% for longer wavelengths. Note that for all DIRBE spectral intensities presented here, the standard DIRBE (and IRAS) convention is used: the calibration is done for a spectrum with νI_ν = constant, which means in particular that the effective bandwidth of each DIRBE wavelength band is calculated assuming a source spectrum with this shape. In general, arid for accurate work, then a colour correction based upon the actual source spectral shape must be applied (see DIRBE Explanatory Supplement for details).

Figure 43 presents contours of 'average' zodiacal light isophotes in geocentric ecliptic coordinates for one quarter of the sky (other quadrants are given by symmetry), as computed from the DIRBE *model.* Although this average serves as a guideline for the contribution of zodiacal light to the night sky brightness at infrared wavelengths, at no point in time will an Earth-based observer see a zodiacal light foreground exactly resembling these contours. The detailed DIRBE measurements indicate that the individual spatial components of the interplanetary dust cloud possess their own geometry, their own 'symmetry plane' and their own temporal variation pattern.

Figure 44 illustrates, again on the basis of the COBE zodiacal light model, the variation in isophotes at 25 pm at four different times during the year, corresponding roughly to the times when the Earth is in the approximate symmetry plane of the main dust cloud [days 89336 and 90162] and when it is 90° further along its orbit [days 90060 and 90250].

Detailed quantitative maps of the DIRBE measurements and zodiacal light model are available from the NASA National Space Science Data Center in the DIRBE Sky and Zodiacal Atlas (DSZA). The COBE/DIRBE Explanatory Supplement and information on how to access the COBE/DIRBE data products are available through the COBE Home Page at http::/ /www.gsfc.nasa.gov/astro/cobe/cobe_home.html on the World Wide Web.

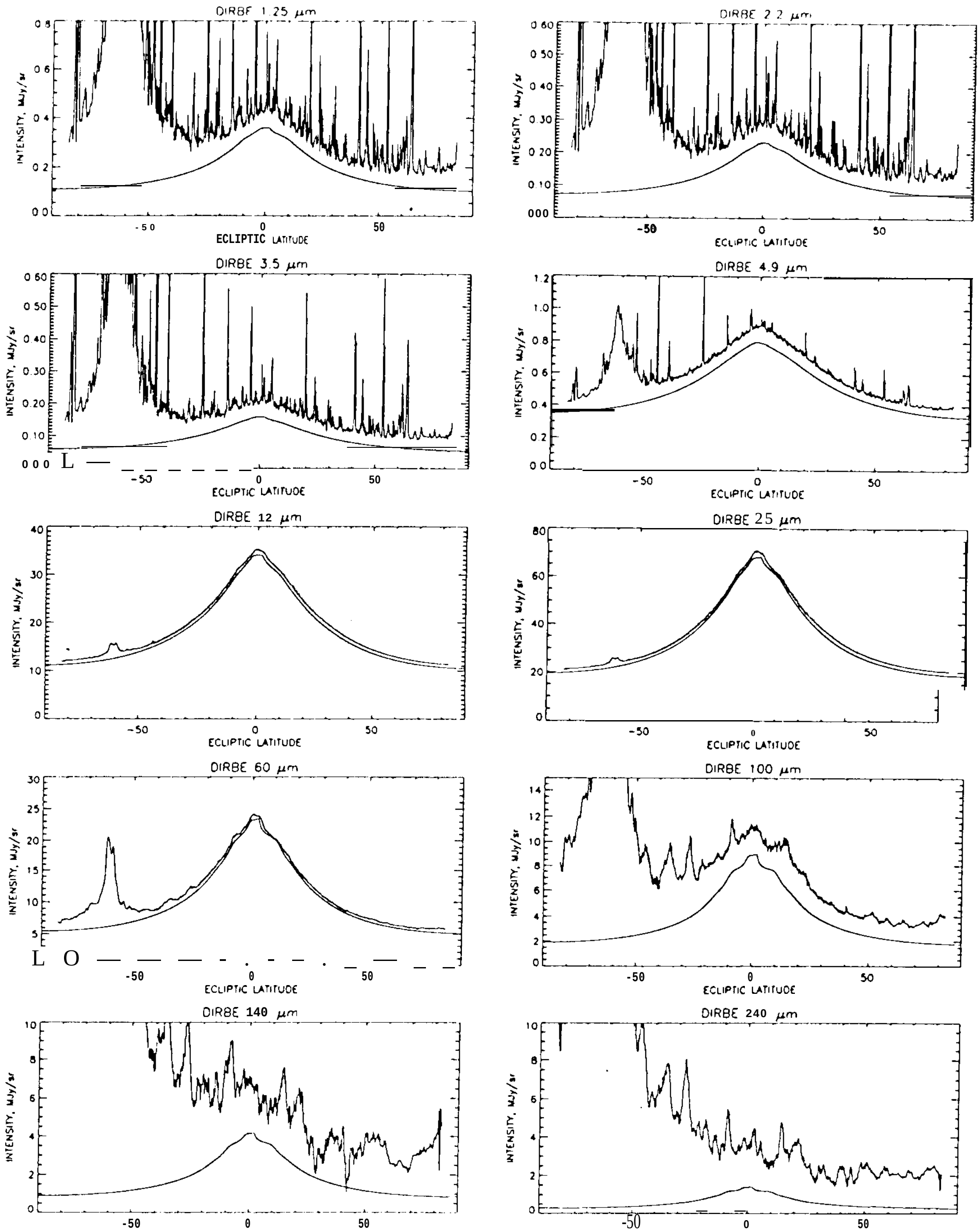

Fig. **42. Example of total** IR **sky brightness** measured by **the** COBE/DIRBE **instrument and brightness contributed** by **zodiacal light at 10 infrared wavelengths.** At **each wavelength, the upper** curve shows the sky brightness measured by DIRBE on 1990 Jun 19 at solar elongation 90°, ecliptic longitude 179°, as a function of geocentric ecliptic latitude. Because of low, signal-to-noise ratio at the longest wavelengths, the 140μm **and** 240μm data have been averaged and smoothed. The lower curve in each plot is the zodiacal light brightness for this epoch obtained from the DIRBE zodiacal light model. DIRBE is a broad-band photometer: flux densities are given in MJy/sr at the nominal wavelengths of the DIRBE bands, assuming an input energy distribution of the form $\nu I_\nu =$ constant.

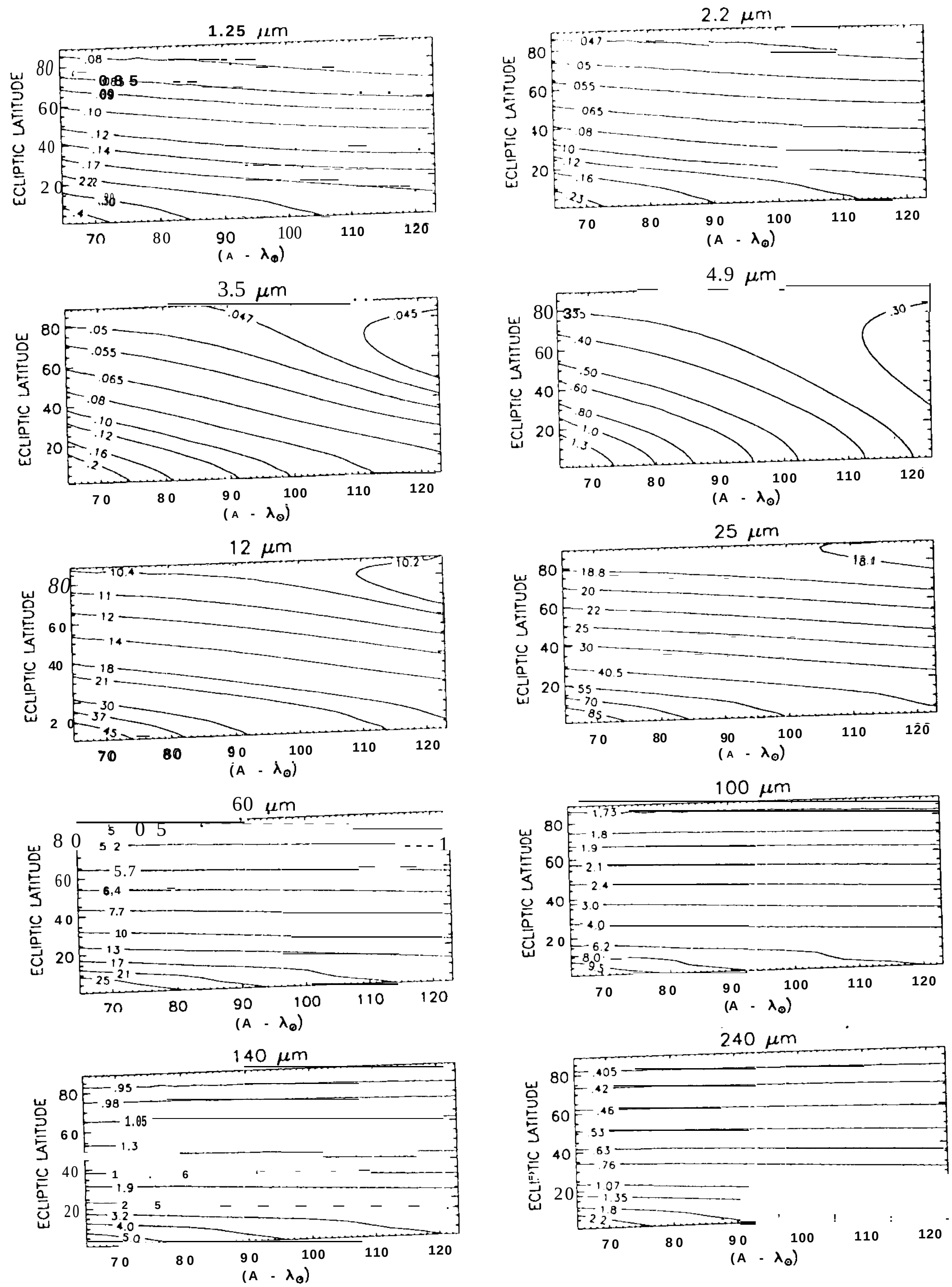

Fig. 43. Contour maps of average zodiacal light brightness in the 10 DIRBE wavebands, as derived from the DIRBE zodiacal light model. Contours are labelled in units of MJy/sr. No color corrections for the broad DIRBE bandwidths have been applied (see DIRBE Explanatory Supplement, Section 5.5, for details).

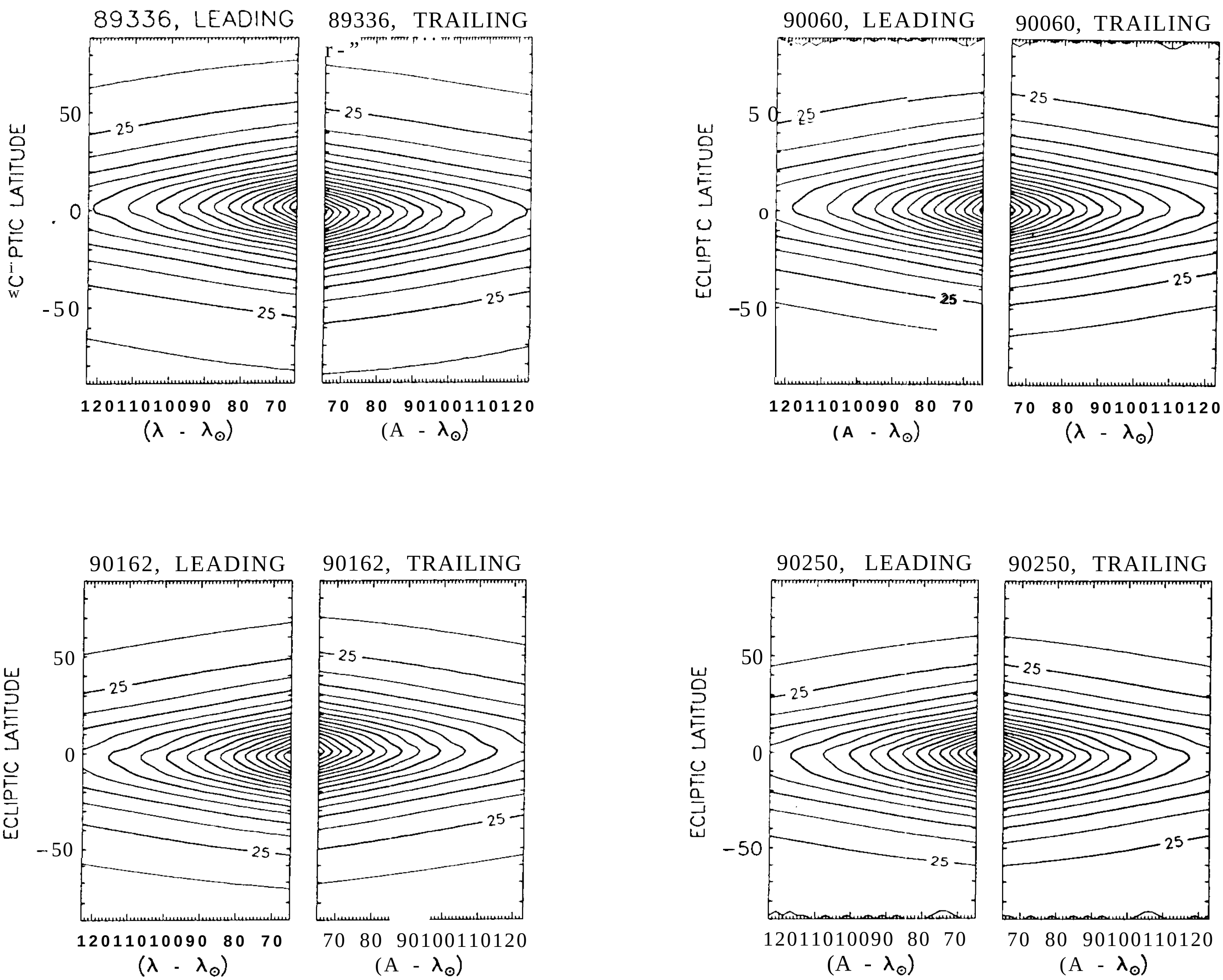

Fig. 44. Contour maps of the zodiacal light brightness at 25 μm for four different times of the year, based on the DIRBE zodiacal light model. Contours are given in increments of 5 MJy/sr, with the 25 MJy/sr level labelled. Each pair of maps shows contours for both the leading side and trailing side of the Earth's orbit. The epoch for each pair is indicated above the map, in the format yyddd, e.g., 89336 is day 336 (Dec. 2) of 1989. Asymmetries between the two sides, as well as changes with epoch, can be seen in these maps. Again, flux densities are given in MJy/sr at the nominal wavelengths of the DIRBE bands, assuming an input energy distribution of the form νI_ν = constant. $(\lambda - \lambda_\odot)$ is given from 70° to 120° in steps of 10°.

8.6. Zodiacal *light in the ultraviolet ($\lambda <$ 300 nm)*

The difficulty with this wavelength range is that here the zodiacal light contribution appears only as a small fraction of the observed background. Available measurements therefore have large error bars or only give upper limits. In addition there is a sharp drop of solar irradiance below 220 nm, by three orders of magnitude until 150 nm. This can be seen in Figure 45 which summarises available results. The scatter between the observations is very large. Whatever the reason for Lillie's (1972) high values (variation, galactic component, instrumental effects), his results shortward of λ = 220 nm no longer are accepted as originally given. In view of the obvious discrepancies we suggest to accept the following:

$$I_{ZL}(\lambda) = \text{negligible}, < 1 \cdot 10^{-8}\ W m^{-2} sr^{-1} \mu m^{-1}$$
$$(for\ \lambda < 160 nm)$$
$$I_{ZL}(\lambda) = 2.5 \cdot 10^{-8} \frac{I[(\lambda - \lambda_\odot, \beta) + I(6,0^\circ)]/2}{I(90^\circ,0^\circ)} \qquad (26)$$
$$W m^{-2} sr^{-1} \mu m^{-1}$$

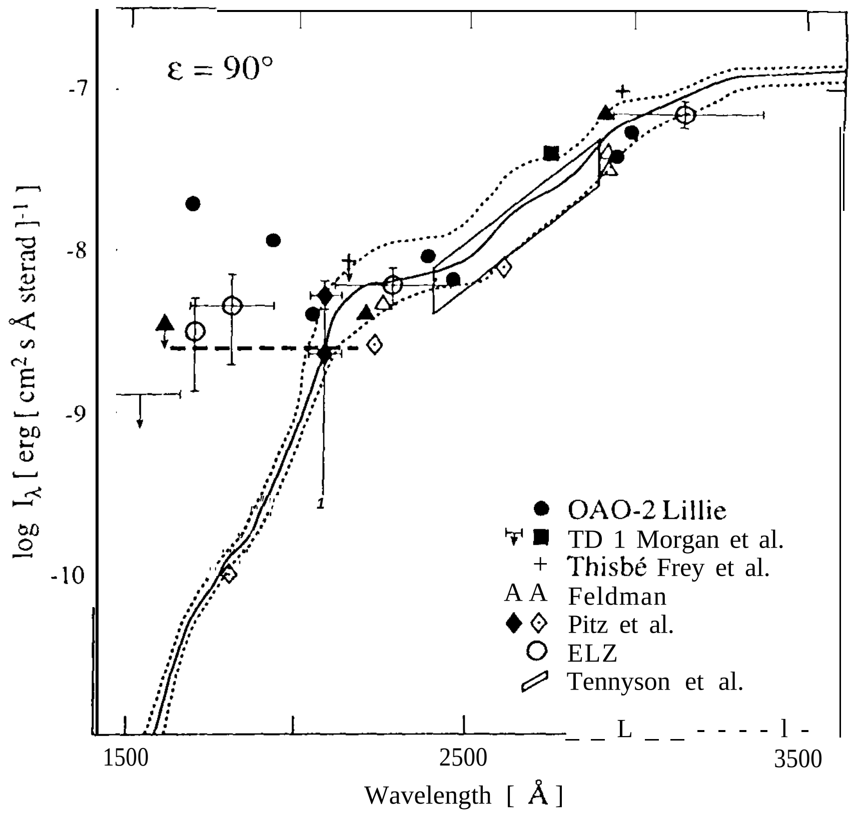

Fig. 45. Ultraviolet zodiacal light measurements at 90" elongation in the ecliptic in absolute fluxes, compared to the solar spectrum. Measurements from smaller elongations have been transformed to the intensity scale of the figure by assuming the same distribution of zodiacal light brightness over the sky as in the visual. The chosen average zodiacal light brightness for 160 nm $\leq \lambda \leq$ 220 nm is shown as thick broken line. Differences with respect to Fig. 38 result from what is used as solar spectrum in the ultraviolet and from the way in which visual data are compared to ultraviolet measurements. The references to the data points are: Lillie (1972), Morgan (1978), Morgan et al. (1976), Frey et al. (1977), Feldman (1977), Cebula and Feldman (1982), Pitz et al. (1979) and a reanalysis by Maucherat-Joubert et al. (1979), Maucherat-Joubert et al. (ELZ, 1979), Tennyson et al. (1988). Adapted from Maucherat-Joubert et al. (1979).

$$
\begin{aligned}
& (for\ \ 160nm \leq \lambda < 220nm) \\
I_{ZL}(\lambda) = \ & \text{of solar spectrum, with reddening} \\
& \text{as given in section 8.4.2 above} \\
& (for\ \ 220nm \leq \lambda < 300nm) \,.
\end{aligned}
$$

Here, $I(\lambda - \lambda^{\odot}, \beta)$ refers to the map of the zodiacal light at 500 nm given above in Table 16.

Murthy et al. (1990) from their Space Shuttle experiment found that the colour of the zodiacal light gets bluer with increasing ecliptic latitude between 165 nm and 310 nm. This would mean, that the zodiacal light is less flattened and more symmetrically distributed around the sun at these wavelengths, as also found from 0.40-2 (Lillie 1972). This is an important result which should systematically be confirmed. In equation 26 we take such an effect qualitatively into account and approximate it by halving the out-of ecliptic decrease with respect to the visible wavelengths (this is what the lengthy fraction does).

At 220 nm there are now two expressions for the brightness of zodiacal light in Equ. 26, with different out-of ecliptic decrease of brightness. They agree at an intermediate latitude (resp. inclination) of 30° - 45°. The discontinuity at the other ecliptic latitudes is accepted, given the large uncertainties of the determination of zodiacal light brightness at these wavelengths.

8.7. Seasonal *variations*

The effects to be discussed in this section have been summarised as factor f_{SP} in equation 14 above.

Seasonal variations of zodiacal light brightness occur for an observer moving with the earth, on the level of $\approx$ 10%. They result from the orbital motion of the earth through the interplanetary dust cloud, which changes the heliocentric distance (by 2e = 3.3%) and the position of the observer with respect to the symmetry plane of the interplanetary dust distribution (see Figure 46). (The symmetry plane is a useful concept for describing the interplanetary dust distribution, although in detail it is too simplified: the symmetry properties appear to change with heliocentric distance, see Table 20). The change in heliocentric distance of the observer translates into a brightness increase of about 8% from aphelion in July to perihelion in January. Otherwise, the effects are different for high and for low ecliptic latitudes. Since the effects are very similar in the visual spectral range and in the infrared, examples from both wavelength ranges will be used to show the effects.

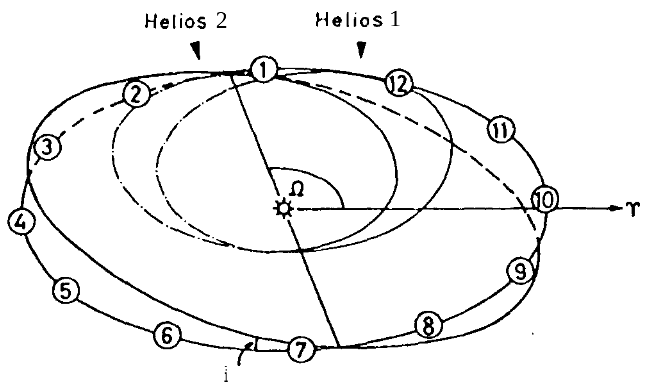

Fig. 46. Geometry of the earth orbit and the symmetry plane of interplanetary dust (with ascending node Ω and inclination i). Numbers give the position of the earth at the beginning of the respective month. Also shown are the orbits of the Helios spaceprobes and the direction to the vernal equinox.

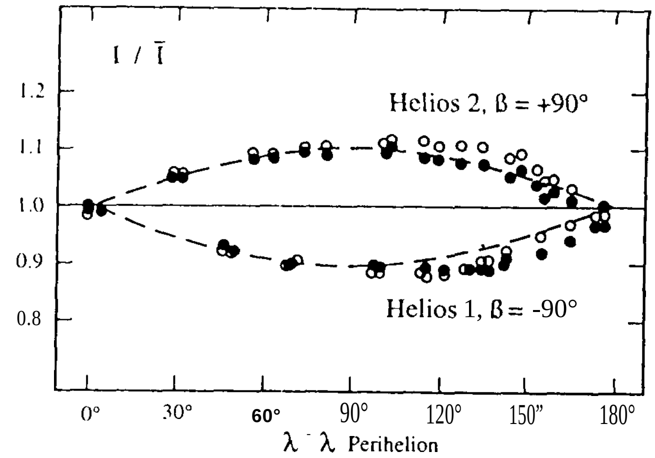

Fig. 47. Change of brightness with ecliptic longitude observed by Helios at the ecliptic poles. The dashed line gives a sinusoidal fit to the data. These observations refer to the inner solar system, from 0.3 AU to 1.0 AU. The perihelia of the Helios space probes are at $\lambda \approx$ 100°. From Leinert et al. 1980b.

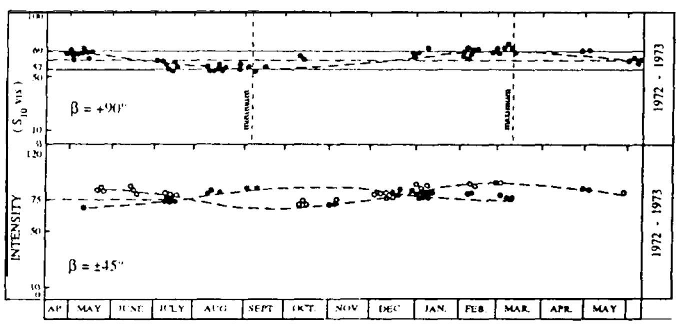

Fig. 48. Yearly variation of zodiacal light brightness at the north ecliptic pole and at ± 45° ecliptic latitude, observed at 653 nm by the satellite D2A. The dashed line is a prediction for a plane of symmetry coinciding with the invariable plane of the solar system (i = 1.6°, Ω = 1070), including the effect of changing heliocentric distance. Adapted from Levasseur and Blamont 1975.

8.7.1. High ecliptic latitudes

At high ecliptic latitudes, the main effect is a yearly sinusoidal variation of the brightness with an amplitude of $\approx \pm 10\%$. This is due to the motion of the earth south and north of the midplane of dust depending on its orbital position. The extrema occur when the earth (the observer) is at maximum elevation above or below the symmetry plane, while the average value is obtained when crossing the nodes. The effect is clearly visible in the broadband optical Helios measurements in the inner solar system (Fig. 47), in the D2A satellite observations at 653 nrn along the earth's orbit (Fig. 48) and in the COBE infrared measurements (Fig. 49). Of these, the Helios measurements have been corrected for the changing heliocentric distance of the instrument, while in the other data the modulation still contains the $\approx 8\%$ effect due to the eccentricity of the earth's orbit. The effect of the tilted symmetry plane gradually decreases towards low ecliptic latitudes to $\lesssim 1\%$. The brightness changes in low ecliptic latitude observations from the earth or from earthbound satellites then arc dominated by the effect of changing heliocentric distance.

S.7.2. Low ecliptic latitudes

At low ecliptic latitudes, the motion of the earth with respect to the symmetry plane of interplanetary dust mainly leads to a sinusoidal variation in the ecliptic latitude of the peak brightness of the zodiacal light by a few degrees. Fig. 50 shows this variation as observed at 25 μm from COBE. In these measurements, the remaining yearly peak flux variation of 5-10% is almost exclusively due to the change in heliocentric distance. Misconi (1977) has used an approximate method to predict the expected position of the brightness maxima in the visible zodiacal light for elongations of ϵ = 2° - 1SO°(typically, the positions vary by

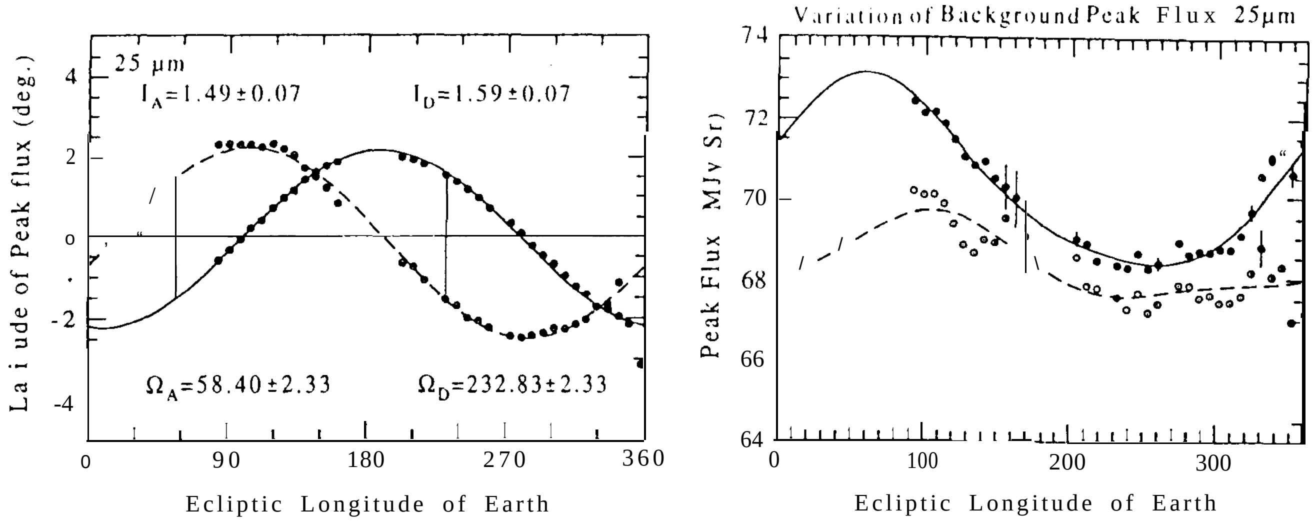

Fig. 50. Yearly variation of the ecliptic latitude of zodiacal light peak brightness (left) and yearly variation of peak brightness (right) observed at 25 μm at elongation ϵ = 900 By the DIRBE experiment on infrared satellite COBE. Open circles refer to the leading (apex), filled circles to the trailing (antapex) direction. From Dermott et al. 1996a,b.

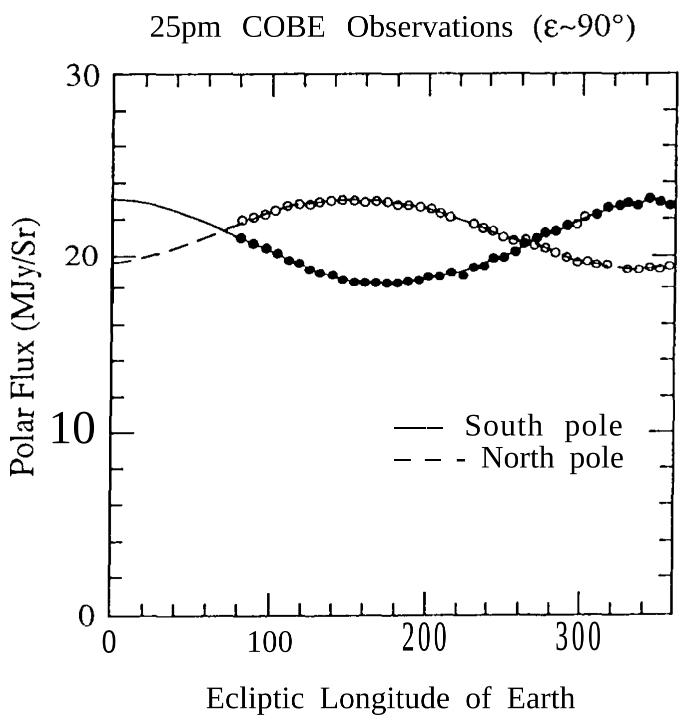

Fig. 49. Yearly brightness variations in the zodiacal light at the ecliptic poles, observed at 25 pm by the DIRBE experiment on infrared satellite COBE. The variation is dominated by the effect of the tilt of the symmetry plane but also includes the variation due to the changing heliocentric distance of the earth. From Dermott et al. 1996b.

a couple or a few degrees; at elongations ≥ 150° the approximation he uses gets unreliable).

8.7.3. Plane of symmetry of interplanetary dust

Table 20. Plane of symmetry of interplanetary dust

Range (AU)	Ω (“)	i(°)	Ref.	Remarks
0.3 -1.0	87±4	3.0±0.3	1	optical
≈1.0	96±15	1.5±0.4	2	optical
	79±3	1.7±0.2	3	infrared at poles
≈1.3	55±4	1.4±0.1	4	infrared in ecliptic
≈3	≈96	≈1.1	5	asteroidal bands

References: 1) Leinert et al. 1980b 2) Durnont and Levasseur-Regourd 1978 3) Reach 1991 4) Hauser 1988 5) Sykes 1985

The seasonal variations discussed above have repeatedly been used to determine the plane of symmetry of interplanetary dust. This midplane of the interplanetary dust distribution appears to vary with heliocentric distance, as summarised in Table 20, compiled from Reach (1991). For comparison, we give here also inclinations and ascending nodes for Venus, Mars and the invariable plane of the solar system (i = 3.4”, Ω = 76°, i = 1.8°, Ω = 49°, i = 1.6°, Ω = 1070).

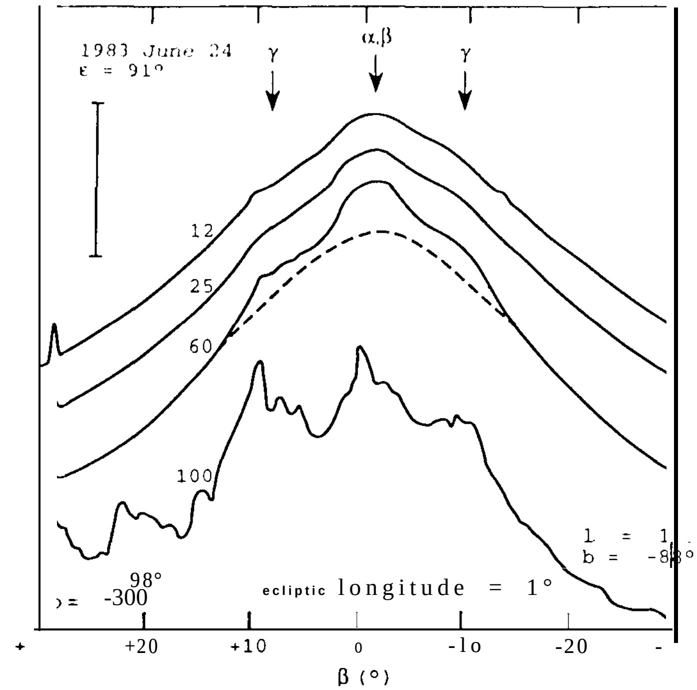

Fig. 51. Scans through the ecliptic at ecliptic longitude λ = 1° on June 24, 1983. The approximate galactic coordinates for the point at ±30° ecliptic latitude are given. The curves are labelled by the wavelength of measurement in pm. A rough calibration is given by the bar at upper left, the length of which corresponds to 12,30, 10 and 6 MJy/sr in the wavelength bands from 12 μm to 100 μm. The dashed curve illustrates how a completely smooth zodiacal light distribution might have looked. The arrows indicate the positions of the asteroidal bands. The 100 μm profile is strongly distorted by thermal emission from interstellar dust ("cirrus"). Adapted from Low et al. 1984.

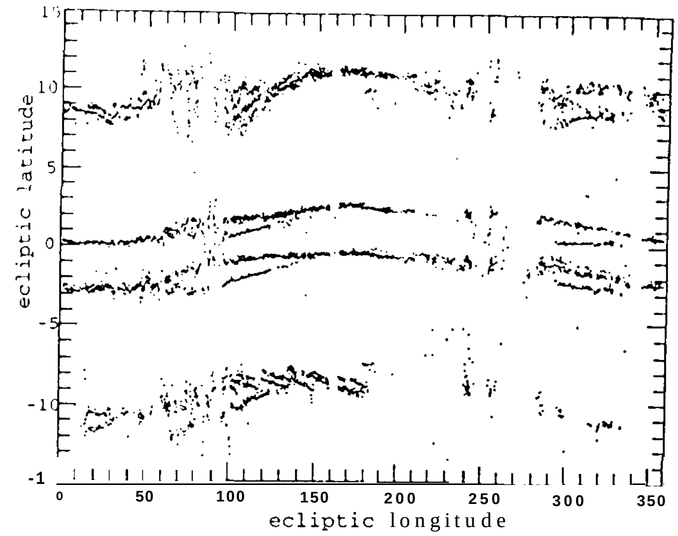

Fig. 52. Observed ecliptic latitude of the peak brightness of the asteroidal bands as function of the ecliptic longitude of the viewing direction (basically as function of the orbital motion of the earth). The expected sinusoidal variation is evident but distorted, since the elongation of the viewing direction was modulated on an approximately monthly timescale, and because observations both east and west of the sun were contained in the data set. Taken from Reach (1992).

8.8. *Structures in the zodiacal light*

Notwithstanding the variety of sources contributing to the interplanetary dust population, the zodiacal light in general is quite smooth, and it was found to be stable to $\approx 1\%$ over more than a decade (Leinert and Pitz 1989). However, there are fine structures on the brightness' level of a few percent, most of which have been detected by the IRAS infrared sky survey: asteroidal bands, cometary trails, and a resonant dust ring just outside the Earth's orbit. They are included here because of their physical importance; they also represent upper limits in brightness to any other structures which still might be hidden in the general zodiacal light distribution. The rrns brightness fluctuations of the zodiacal light at 25 μm have been found by observations from the satellite 1S0 in a few half-degree fields to be at most $\pm 0.2\%$ (Ábráham et al. 1997).

Asteroidal bands

They were seen in the IRAS infrared scans across the ecliptic as bumps in the profile near ecliptic latitude $\beta = 0°$ and as shoulders at $\beta \approx 10°$ (Low et al. 1984, see Figure 51). The bands near the ecliptic plane have been called α ancl β (counted from ecliptic latitude β=0° outwards), the ones around β=10° have been called γ bands. Their peak brightness is 1% - 3% of the in-ecliptic zodiacal light brightness, their width at half maximum ≈ 2-3° (Reach 1992, but the detailed values depend on the method actually used to fit the bumps, in this case by Gaussian). They are thought to be the result of major collisions in the asteroid belt, in the Themis and Koronis families for the α and β bands, in the Eos family for the higher latitude γ bands (Derrnott et al. 1984). The collisional debris then is expected to be mainly distributed along the walls of widely opened, slightly tilted, sun-centered cones. Therefore the ecliptic latitudes at which these bands occur vary both with the annual motion of the observer (the earth in most cases) and, at a given elate, with the elongation from the sun. Formulae to predict the position of the maximum with help of a simplified geometrical model are given by Reach (1992). Figure 52, resulting from an analysis of the IRAS data, gives a good impression of the resulting yearly sinusoidal latitude variation. Table 21 (taken again from Reach 1992) summarises the average observed properties of the asteroidal dust bands in the case Gaussian fitting is used to measure the bumps in the general distribution of zodiacal light. 'I'here must be in addition an underlying (Distribution of asteroidal debris particles of about 10% of the zodiacal light brightness, which cannot be seen sep-

Table 22. Photometry of cometary trails

Comet	R(AU)	Δ(AU)	ΔΘ(°)[a]	F_ν(12 μm) (MJy/sr)	F_ν (23 pm) (MJy/sr)	F_ν(60 pm) (MJy/sr)	F_ν(100 μm) (MJy/sr)
Encke	3.926	3.779	52.8		0.07±0.01	0.06±0.01	
Gunn	2.681	2.473	0.82	0.22±0.06	0.97±0.08	0.55±0.03	-
Kopff	1.577	0.953	0.53	1.04*0.14	1.19*0,20		
S-W 1	6.287	6.281	0.96	-	0.11±0.02	0.15±0.02	0.10±0.02
Tempel 2	1.460	1.149	0.37	2.44±0.09	3.93±0.14	1.54±0.035	-

a) ΔΘ(°) isangular distance behind comet in mean anomaly

Table 21. Properties of dust bands from Gaussian fits

Band	12 μm	25 μm	60 μm
Peak surface brightness (MJy sr^{-1})			
γ northern	0.4±0.2	1.1±0.5	0.8*0.4
cr, β northern	1.1*0.5	3.0±1.0	1.5±0.5
α, β southern	1.4*0.3	2.9±1.2	1.6*0.6
γ southern	0.6±0.3	0.8±0.3	0.7±0.4
Average geocentric latitude of peak (°)			
γ northern	9.7±0.1	9.6±0.1	9.6±0.2
α, β northern	1.4±0.1	1.4±0.1	1.4±0.1
α, β southern	-1.4± 0.1	-1.4±0.1	-1.4* 0.1
γ southern	-9.7±0.1	-9.6± 0.1	-9.6± 0.1
Full width at half maximum brightness (°)			
γ northern	3.3*1.3	3.7±1.1	3.2±1.5
α, β northern	3.3±1.1	3.3±1.2	3.2±1.2
α, β southern	3.7±1.3	3.3±1.2	3.4*1.4
γ southern	2.8±1.1	3.1±0.8	3.0±1.4

arately from the general zodiacal light. Note that Sykes (1988) resolved the α and β bands also into band pairs, with a FWHM of ≈ 0.5° for each of the components. The claim for eight additional, though weaker bands between β = -22° and β = +21° (Sykes 1988) should be taken with reservation and can be neglected here.

Cometary trails

These trails have been seen in the IRAS infrared sky survey stretching along the orbit of a few periodic comets, which were in the perihelion part of their orbit (Sykes et al.1986). These were the comets Tempel 2, Encke, Kopff, Tempel 1, Gunn, Schwassrnann-Wachmanrr 1, Churyumov-Gerasimenko and Pens- Winnecke, but also nine faint orphan trails without associated comet were found (Sykes and Walker 1992). The trails typically extend 10° behind and 1° ahead of the comet, their brightness decreasing with increasing distance from the comet. They are thought to consist of roughly mm-sized particles ejected from the comet during times of activity over many years (Sykes et al. 1990). The trails are bright enough to be seen above the zodiacal light only when the comets arc near perihelion and the dust in the trails is warm. The width of the trails is about one arcminute, for comet Tempel 2 it has been determined to 45″±2″(≈30000 km). Trail brightnesses are of the order of 1% of the zodiacal light brightness near the ecliptic. Examples are given in Table 22, taken in shortened form from Sykes and Walker (1992). Other periodic comets in the perihelion part of their orbit are expected to behave similarly. A new observation of the cornet Kopff trail from ISO (Davies et al. 1997) has shown chnages in the trail since the observations by IRAS, and measured a trail width of ≈ 50”.

The somewhat related brightness enhancements along some meteor streams, seen in the visible from the satellite D2A-Tournesol, have not been confirmed, neither by the photometric experiment on the Helios space probes (Richter et al. 1982) nor from IRAS. They probably are fainter than originally thought and certainly of lower surface brightness in the infrared than cometary trails or asteroidal bands.

The resonant dust ring outside the Earth's orbit

A leading/trailing asymmetry, with the zodiacal light at elongation 90° being brighter in the trailing (antapex) direction, has been found in the IRAS observations (Dermott et al. 1988, 1994) and has been confirmed by measurements of the DIRBE experiment on board the COBE spacecraft (Reach et al. 1995 b). From the COBE measurements, the excess in the trailing direction in January 1990 was 0.05±0.01 MJy/sr or 4.8±1.0 % at 4.9 μm, 1.1±0.2 MJy/sr or 2.8±0.5% at 12 μm and 1.7±0.1 MJy/sr or 2.4±0.15 % at 25 μm. The region of enhanced brightness in the trailing direction is at ≈90° from the sun, extending 30° (FWHM) in latitude and 15° (FWHM) in longitude (see Figure 53, taken from Reach et al. 1995). In the leading direction there is a smaller enhancement around elongation SO°.

These are quite extended structures (see Figure 53). They are explained by resonant interaction of the orbiting earth with interplanetary particles drifting closer to

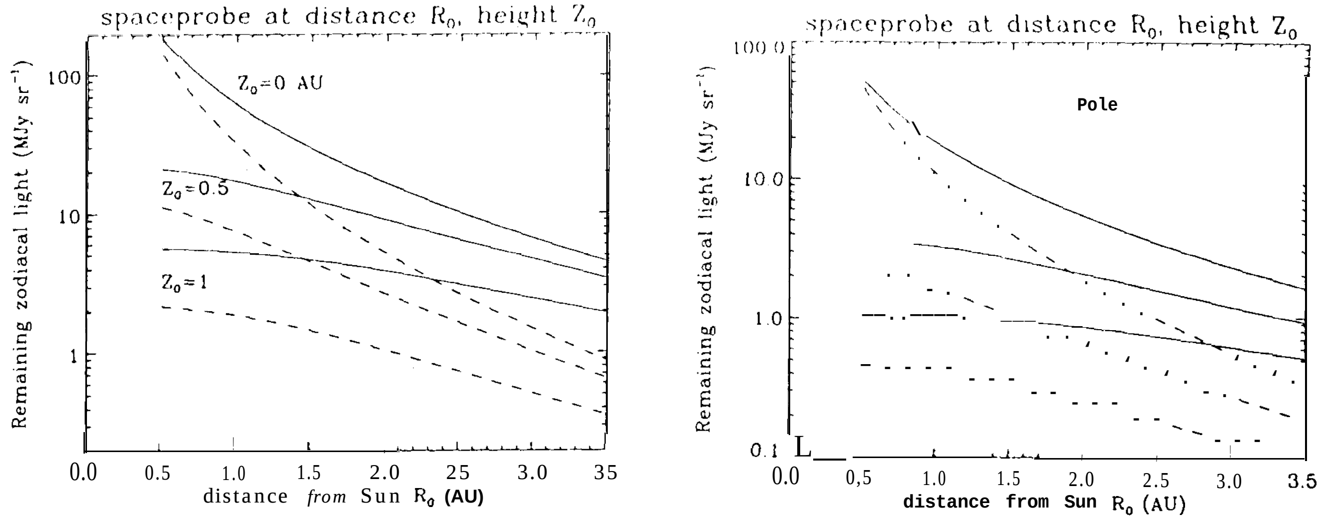

Fig. 54. Decrease of infrared zodiacal light brightness when moving out of the ecliptic plane. Left: for a viewing direction parallel to the ecliptic plane at elongation ϵ = 90°. Right: for a viewing direction towards the ecliptic pole. The calculations have been done for a position of the observer in the ecliptic (Z_0 = O AU) and heights above of the ecliptic of 0.5 AU and 1.0 AU, as indicated in the figure. R_0 is the heliocentric distance of the observer, projected into the ecliptic plane. The solid and broken lines give the predicted run of brightness with heliocentric distance for a wavelength of 25 μm and 12 μm, respectively. The calculations have assumed grey emission of the interplanetary particles, and radial decreases of spatial density $\sim r^{-1.4}$ and of particle temperature $\sim r^{-0.44}$ (W. Reach, private communication).

the sun under the action of the Poynting-Robertson effect. This interaction leads to an inhomogeneous torus of enhanced dust density just outside the earth's orbit, with the earth sitting in a gap of this torus and the largest enhancement following it at a few tenths of an AU. The resonant ring structure therefore is expected to be a persistent feature of the zodiacal light.

8.9. *The zodiacal light seen from other places*

8.9.1. Inside the solar system

The decrease of zodiacal light brightness seen in a given viewing direction, occuring when the observer moves to larger heliocentric distances, has been measured along the ecliptic in the visual out to 3 AU (Pioneer 10, Toiler and Weinberg 1985) and can be reasonably predicted also for the infrared. The change to be expected when moving out of the ecliptic plane is less well known, but can be predicted from models fitting the out-of-ecliptic observations obtained from in-ecliptic positions at earth orbit.

For the infrared, Figure 54 shows the predicted brightnesses in viewing directions parallel to the ecliptic and towards the ecliptic pole for an observer moving from 1 AU to 3 AU in planes of different height above the ecliptic. The outward decrease is stronger for 12 pm than for 25 pm. This is because the thermal emission of interplanetary dust is close to black-body radiation, and for black-body radiation with decreasing temperature the shorter wavelengths first enter into the exponential decrease of the Wien part of the emission curve.

For the visual, Figure 55 shows the corresponding decrease for the visual zodiacal light brightness when the observer moves from 1 AU to 3 AU in planes of different height above the ecliptic. Only one curve is shown, since any colour dependence is expected to be small.

The careful reader will note that the visual in-ecliptic brightness decreases a little slower with increasing distance than given in section 8.2. This is because Giese (1979) used a slightly different heliocentric radial brightness gradient, $I(R) \sim R^{-2.2}$. The decrease as function of height above the ecliptic Z_0 is typical for the models of three-dimensional dust distribution being discussed to explain the distribution of zodiacal light brightness (Giese et al. 1986). Since the three-dimensional dust distribution is not very well known, the decreases shown in Figures 54 and 55 cannot be very accurate either.

8.9.2. Surface brightness seen from outside the solar system

Since the interplanetary dust cloud is optically very thin, the pole-on surface brightness at 1 AU is just twice the polar surface brightness observed from the earth, and the edge-on surface brightness just twice the brightness observed at elongation 90° in the ecliptic. The same type of relations hold for other heliocentric distances.

The brightness in an annulus extending over a range of heliocentric distances has to be obtained by integration.

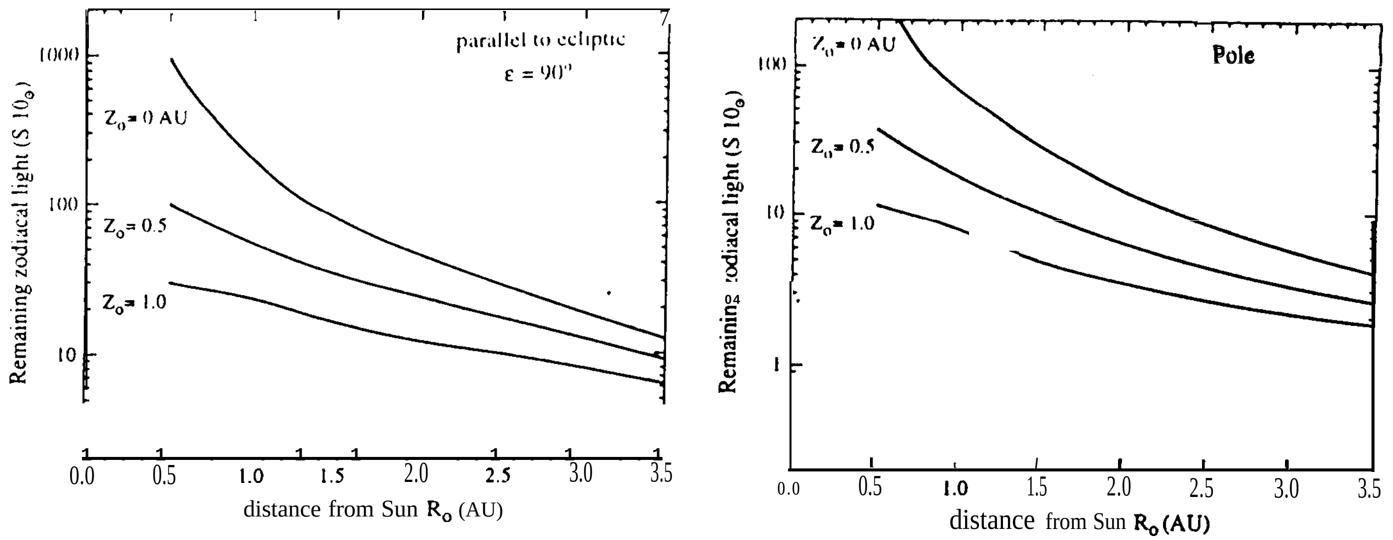

Fig. 5s. Decrease of the visual brightness of the zodiacal light when the observer moves out of the ecliptic. Left: for a viewing direction parallel to the ecliptic plane at elongation $\epsilon = 90°$. Right: for a viewing direction towards the ecliptic **pole.The curves** show how the brightness changes with projected heliocentric distance **Ro (measured** in the ecliptic) for **different heights** Zo above the ecliptic plane (interpolated from Giese 1979).

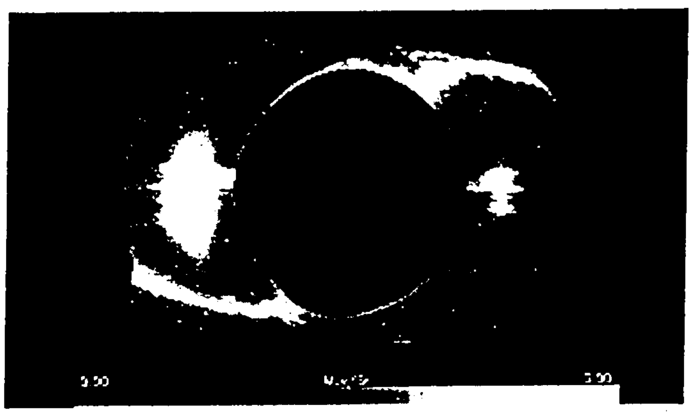

Fig. 53. Distribution of excess zodiacal light brightness due to the resonant dust ring outside the earth's orbit according to COBE measurements (Reach et af. 1995 b). In this presentation, the position of the sun is at the center, the ecliptic runs horizontally through it, the ecliptic north pole is at top, the black central circle is the region inaccessible to COBE within 60° elongation from the sun, and the two bright spots at 90° from the sun on the ecliptic are at left the trailing (antapex) enhancement due to this dust ring, with a peak brightness of 1.7 MJy/sr at 25 μm, and at right the corresponding but weaker enhancement in leading (apex) direction. The S-shaped bright strip crossing the image is due to the Milky Way.

The total brightness as seen from outside very much depends on the distribution of interplanetary dust near the sun, and therefore is strongly model dependent. E.g., at least in the optical wavelength range an annulus of width dr [AU] has a brightness $\sim r^{-1.3}dr$ over a large region of the inner solar system, making the integrated brightness contribution strongly peaked towards the solar corona. In discussions of future planet-searching spacecraft (called DARWIN (Léger et al. 1996) and Terrestrial Planet Finder (Angel and Woolf 1997)) a value of integrated zodiacal light brightness at 10 μm, when seen from a distance of 10 PC, of 70 μJy, 300 to 400 times brighter than the Earth, is assumed (3.5 .10-5 of the solar brightness).

9. Coronal brightness and polarisation

9.1. Overview

The brightness of the corona surrounding the solar disk is composed of three main components: i) Thomson-scattered light from free electrons in the solar environment (K-corona) which is highly variable in space and time, ii) emission from coronal ions, especially in highly ionised states, and iii) contributions due to interplanetary dust (F-corona): solar radiation scattered on the dust particles in the visual, as well as thermal emission of these dust particles in the near and middle infrared regime. The F-corona dominates the visible coronal brightness from about 3 $R_\odot$ distance from the center of the Sun outward and has an increasing contribution to the total coronal brightness at longer wavelengths.

For measurements in the corona, the elongation ϵ is often expressed in units of $R_\odot$, i.e. in terms of the minimum projected distance r of the line of sight from the center of the Sun. Because the solar radius is $R_\odot$ = 1 AU/214.94 (Allen 1985), 1° in elongation corresponds to 3.75 $R_\odot$ (and $1R_\odot$ to 16.0'), while more generally for an observer at the earth

$$\sin\epsilon = r[R_\odot] \cdot \frac{1R_\odot}{1AU} \qquad (27)$$

As mentioned in section 2, coronal brightnesses often are expressed in terms of the average brightness of the 'solar disk as $B/\bar{B}_\odot$, where $1B/\bar{B}_\odot$ = 2.22" 101%100 = $1.47.10^4 F_\odot/sr$.

9.2. *K-corona separation*

The main uncertainty in determination of the inner F-corona is the separation from the K-coronal brightness. A common method of separation is based on the assumption that the F-coronal brightness is produced by diffraction of dust near the observer and hence unpolarized. This approach may be suitable for distances, respectively elongations of < 5 $R_\odot$, the increasing polarization of the F-corona at larger elongations (Blackwell et al. 1967) however leads to errors of this subtraction method. A further method of K-coronal separation uses the depth of Fraunhoferlines in the Solar spectrum. Both methods are described in Blackwell et al. (1967).

9.3. *Atmospheric and instrumental stray light*

Ground-based coronal observations generally are made during solar eclipses, with the local sky brightness constituting the main disturbance to be corrected for. The eclipse sky background on the ground may vary considerably with daily conditions as well as eclipse site. An early work by Blackwell et al. (1967) cites values of (1.9 - 19) $10^{-10}\,\bar{B}_\odot$ for the eclipse sky background in the visible light, i.e. at wavelengths from 500 to 830 nm.

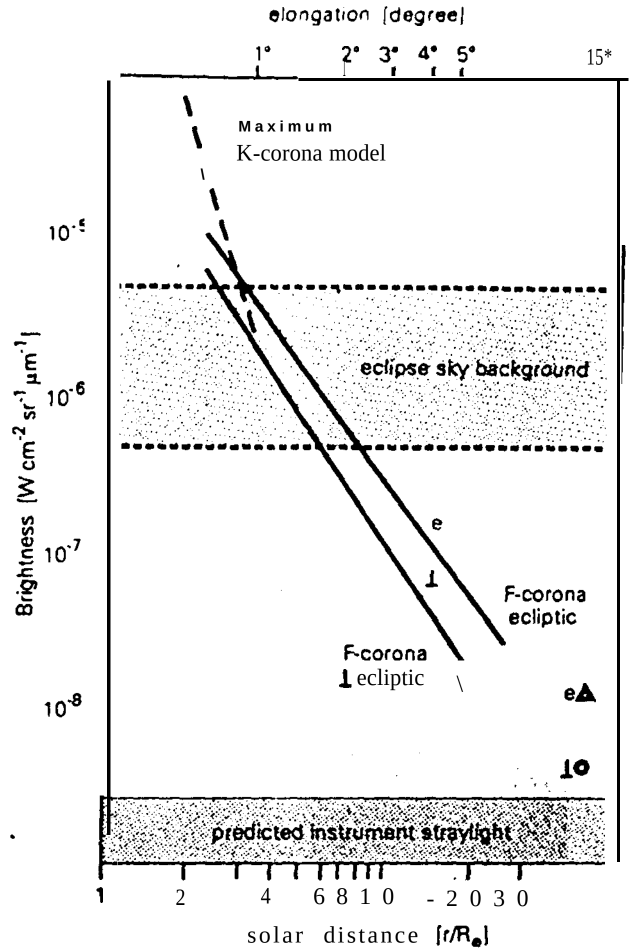

Fig. 56. The visible equatorial and polar F-corona brightnesses in comparison to typical values for K corona, the aureole (circumsolar sky brightness enhancement) and instrumental straylight levels. At 150, the brightnesses measured in the zodiacal light (see sect ion 8) are included.

For 2.12 μm, MacQueen and Greeley report a value of $10^{-10}\bar{B}_\odot$ during the 1991 eclipse sky from Hawaii. However, these measurements suffered from thin clouds and the presence of high altitude aerosols from the Pinatubo eruption. The enhanced circumsolar sky brightness caused by diffraction on aerosols is called solar aureole. It may vary with elongation, and may be described as a function A(r). Dürst (1982) derives values of about 10^{-11} to $10^{-9}\bar{B}_\odot$ and a radial gradient according to $r^{-1.37}$ at 600 nm wavelength. Infrared results differ at the 1991 eclipse, but MacQueen and Greeley (1995) find a description $A(r) \sim r^{-1.54}$ for the region from 3 to 9 $R_\odot$ and a constant value of $2 \cdot 10^{-8}\,W\,cm^{-2}\,\mu m^{-1}\,sr^{-1}$ (i.e. $10^{-10}\,\bar{B}_\odot$) beyond for the infrared aureole during the 1991 eclipse. Instrumental straylight for externally occulted systems on satellites presently achieve stray light levels in the 10^{-10} to $10^{-12}\bar{B}_\odot$ range and hence enable coronal observations out to at least 30 $R_\odot$ (Bruckner et al. 1995).

The values of polarization in the eclipse sky background range from 7.5% to 3070 for ground based observations.

9.4. *Visual brightness*

Observations of the F-coronal brightness are made during solar eclipses from ground, from rockets and from balloons in the visible and near infrared regime. Data were taken as well from space borne coronagraphs. An early review of

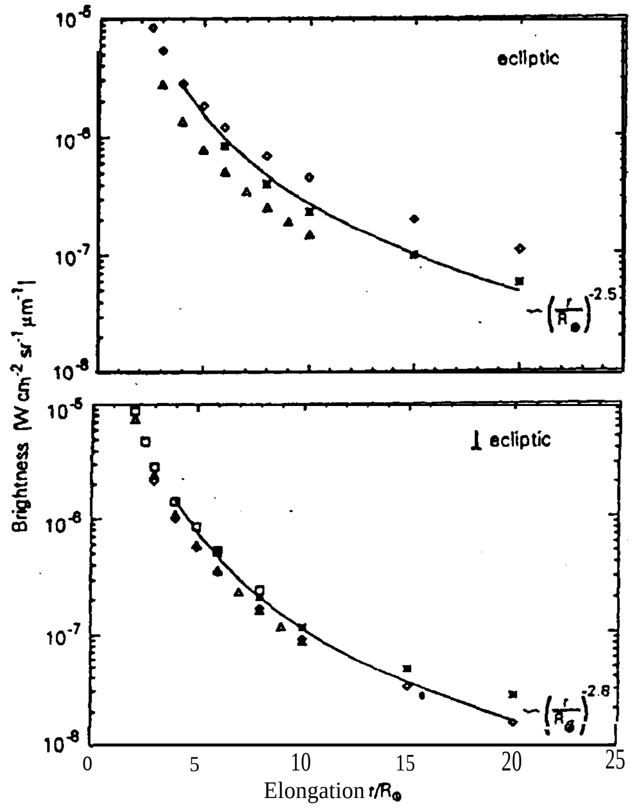

Fig. 57. The visible F-corona brightness, as measured along the ecliptic and the polar meridian. Asterisks: Blackwell 1995 (1954 eclipse); diamonds: Michard 1954 (1952 eclipse); triangles Dürst 1982; squares Maihara et al. 1985. The power laws best representing these data are shown as solid lines.

the visible coronal observations was given by Blackwell et al. (1967). They gave a description of the F-corona data as the continuation of the zodiacal light. A more recent review was given by Koutchmy and Lamy (1985) including already infrared observations. They describe the visible F-corona brightness at wavelength 400 nm < λ < 600 nm as proportional to $r^{-2.25}$ at the equator and $r^{-2.47}$ at the solar poles, based on a continuation of the zodiacal light data.

A measurement of the 1980 eclipse (Dürst 1982) yields a radial slope proportional to $r^{-2.44}$ in the equator and $r^{-2.76}$ at the poles when only fitting the slope to the eclipse

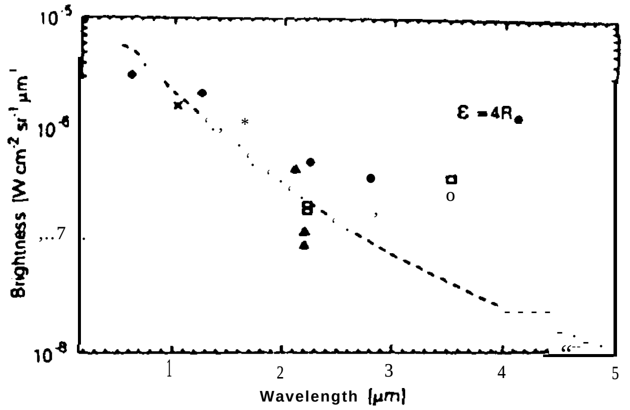

Fig. 58. The equatorial F-corona brightness at 4 $R_\odot$. Diamonds: Maihara *et* al. 1985, cross: Smartt 1973, triangles: MacQueen 1968 (lower values), MacQueen and Greeley 1995 (upper value); squares: Peterson 1967. The dashed line gives the solar spectrum normalized to wavelength 0.55 pm.

observations in the range from 2 to 10 $R_\odot$. Observations by Michard (1954) of the 1952 eclipse are fairly close to the model corona suggested by Koutchmy and Lamy (1985), whereas the Blackwell data and the more recent observations by Dürst are a little lower. Observations from the Apollo 16 spacecraft describe the equatorial brightness beyond 20 $R_\odot$ as $\sim r^{-1.93}$ (MacQueen et al. 1973).

Table 23. Proposed approximations to the F-coronal brightness distribution

< A > (pm)	region	I(λ) at 4 $R_\odot$ (W/m² sr μm)	radial slope
0.5	equatorial	2.8 .10-2	$r^{-2.5}$
	polar	2.2 .10-2	$r^{-2.8}$
2.12	equatorial	≈ 5 .10-3	$r^{-1.9}$
	polar	≈ 4 .10-3	$r^{-2.3}$

“For comparison: at 500 nm, 1 10^{-9} B/B_0 = 2.84×10^{-2} W/m² sr mum.

We suggest to use for the visual spectral region a radial slope of the brightness as $r^{-2.5}$ in the equator and $r^{-2.8}$ at the pole (see Table ??). This takes the recent measurements into account as well as the fact that the scattering properties change due to the increasing diffraction peak at small scattering angles.

9.5. Polarization and colour

Due to the difficulties of K-corona separation, mentioned above, the polarization of the F-corona brightness is not the polarization of the total visible F-coronal brightness together with two models of F-corona polarization. The

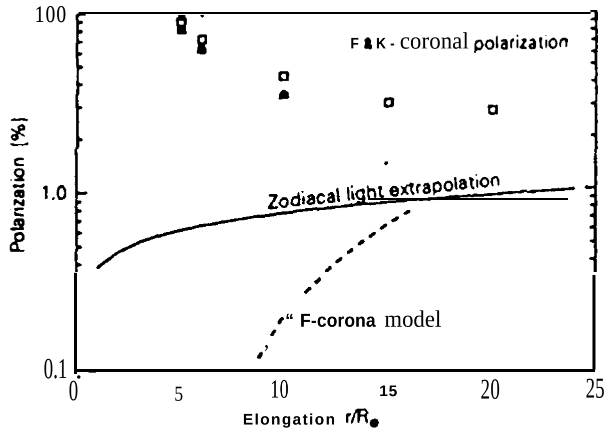

Fig. 59. The polarization of the total coronal brightness compared to the extrapolated zodiacal light model and the F-corona polarization according to Blackwell et al. (1967).

first case is the polarization curve extrapolated from the Zodiacal light polarization according to equation (16), the second case is the polarization derived by Blackwell et al. (1967). The classical coronal model suggested in Blackwell et al. gives almost no F-corona polarization within 10 $R_\odot$. Furthermore, it has been suggested, that an irregular slope of the F-corona polarization could either result from the beginning of the dust free zone around the Sun or reflect the existence of a dust ring. Observations of the 1991 eclipse show no hump in the polarization between 3 and 6.4 $R_\odot$ and give an upper limit of 10% for the polarization.

Similar to the uncertainties in the determination of absolute brightness levels, the colour of the coronal brightness is not well defined. Since both, thermal emission of dust as well as a spectral change of scattering properties cause a reddening of the F-corona (Mann 1993), we can expect reddening to vary within the corona. .4s far as the visible F-corona is concerned, several estimates of the colour are either describing only the inner corona or may be biased from uncertain calibrations. However it seems to be proven, that the reddening is stronger than in the Zodiacal light and is also stronger than the reddening of the inner Zodiacal light extrapolated to smaller elongations (Koutchmy and Lamy 1985).

9.6. *Infrared*

9.6.1. Near-infrared brightness

Different values of the F-corona brightness at 4 $R_\odot$ in the near infrared are shown in Figure 5S in comparison to the solar spectral slope from Allen (1985), normalized to the F-coronal brightness at 0.5 μm. Although the differences between data sets are still large, the majority of data at longer wavelengths is above the extrapolated solar spectrum, indicating a contribution from the thermal emission of dust near the Sun.

Only the early infrared observations do not follow this trend.

The radial slope of the near infrared F-corona brightness can be derived from observations of the 1991 eclipse (Hodapp et al. 1992, Kuhn et al. 1992, MacQueen et al. 1992), however the sky conditions were mediocre, as mentioned above, and no accurate photometry was possible. The equatorial brightness was described as $B \sim r^{-l.9}$ and the polar brightness as $B \sim r^{-2.3}$, for regions inside 8 $R_\odot$. Observations of the 1973 eclipse by Smartt(1973) in the near-infrared (λ = 1.03 pm) show a similar radial slope of $r^{-1.9}$ between 3$R_\odot$ and 5$R_\odot$ and of $r^{-2.2}$ in the outer corona.

9.6.2. Mid-infrared brightness

An important constituent of interplanetary dust particles is silicate, which exhibits a pronounced reststrahlen band in the 10 μm wavelength region. An enhanced brightness of the mid infrared corona could reveal for instance the presence of small silicate particles near the Sun (cf. Kaiser 1970). Unfortunately, data in the mid infrared regime are biased, either by scatterd light components from a window in case of aircraft measurements (Lena et al. 1974), or by strong atmospheric emission and fluctuations in the case of observations from ground (Mankin et al. 1974).

9.6.3. IR - humps and dust rings

First measurement of the near infrared coronal brightness showed a deviation of the slope from a continuous increase within the corona, with brightness enhancements by a factor of 3 – 3.5. Several of these humps were seen by Peterson (1967) and MacQueen (1968), and later checked by Isobe et al. (1985), Mizutani et al. (1985), and Tollestrup et af. (1994). Model calculations by Mukai and Yamamoto (1979) showed that these humps could be explained by a dynamical effect that produces dust rings around the Sun. It is also possible, that a hump of the infrared brightness is produced when the line of sight crosses the beginning of a dust free zone (Mann 1992). A model calculation by Kimura et al. (1997) shows that this effect may depend on the material composition of dust near the Sun. However, there have been several unpublished observations which could not detect a dust ring, and observers of the 1991 eclipse could not confirm the existence of humps in the near infrared brightness (Hodapp et al. 1992, Kuhn et al. 1992, Tollestrup et al. 1994). In this context we should mention, that the presently available data do not allow for a study of temporal effects in the F-coronal brightness, such as the appearance of dust clouds from sun-grazing comets or temporal dust rings.

10. Integrated starlight

10.1. Model predictions based on star counts

The combined light from unresolved stars contributes to the sky brightness from the ultraviolet through the mid-infrared, with the contribution being dominated by hot stars and white dwarfs at the shortest wavelengths, main sequence stars at visual wavelengths, and red giants in the infrared (Mathis, Mezger, and Panagia 1982). The integrated starlight contribution to the sky brightness depends on the ability of an experiment to resolve out the brightest stars, which in turn depends on the Galactic latitude. If we suppose that stars brighter than flux F_0 are resolved and excluded from the diffuse sky brightness, then the integrated starlight contribution is the integral over the line of sight of the brightness contributions from stars fainter than F_0,

$$I_{ISL} = \int_0^{F_0} dF \frac{dN(l,b)}{dF} F, \tag{28}$$

where $\frac{dN(l,b)}{dF}$ is the number of stars in the flux range F to F + dF, for a line of sight towards galactic coordinates l, b. In principle, we must also integrate the counts over the beam and divide by the beam size, but in practice, the variation in the number of sources over a beam is often small except for large beams at low galactic latitude. (In those cases, equation 28 is replaced by

$$I_{ISL} = \frac{1}{\Omega_b} \int_{\rm beam} d\Omega \int_0^{F_0} dF \frac{dN(l,b)}{dF} F, \tag{29}$$

where Ω_b is the beam solid angle.) The cumulative number of sources increases less steeply than l/F for the fainter stars, so that the integral converges; in the near-infrared at 2.2 μm, the peak contribution to the sky brightness occurs for stars in the range $0 < K < 6$. For reference, $K = 0$ corresponds to F. = 670 Jy (Campins, Rieke, and Lebofsky 1985), and there is of *order* 1 star per square degree brighter than K = 6, and (extrapolating) there is one star per square arcminute brighter than K = 15. Thus, for comparison, the DIRBE survey (42' beam, K = 4 detection limit) resolves about 50% of the starlight in the K band, while the DENIS survey (limiting magnitude K = 14) should resolve some 97%. Similarly, in the far-ultraviolet, the FAUST survey resolves some 96% of starlight (Cohen et al. 1994). And at visible wavelengths, star counts near the North Galactic Pole (Bahcall and Soneira 1984) also show that the visible surface brightness for low-resolution observations is strongly dominated by the brightest stars (≈6-13 mag). It is for deep surveys with low angular resolution that we address the remainder of this discussion of integrated starlight.

To estimate the contribution of integrated starlight to a deep observation, one must sum the contribution from each type of star along the line of sight. One may recast the integral in equation 28 more intuitively by integrating over the line of sight for each class of object (which has a fixed luminosity):

$$I_{ISL} = \sum_i \int_{s_i}^{\infty} ds\, s^2 n_i(s) \frac{L_i}{4\pi s^2}, \tag{30}$$

where n_i is the number density and L_i the luminosity of sources of type i. The integral extends outward from a given inner cutoff s_i that depends on the source type" through $s_i^2 = L_i/4\pi F_0$. Bahcall and Soneira (1984) constructed such a model, with the Galaxy consisting of an exponential disk and a power-law, spheroidal bulge. The shape parameters (vertical scale height and radial scale length of the disk, and bulge-to-disk density ratio) of the Galactic star distribution were optimised to match the star counts. A more detailed model (SKY), both in terms of Galactic shape and the list of sources, has been constructed by M. Cohen and collaborators (Wainscoat et al. 1992, Cohen 1993, 1994, Cohen et al. 1994, Cohen 1995).

Examples of the surface brightness predicted by the SKY model for two lines of sight and four wavebands, from the ultraviolet to the mid-infrared, are shown in Fig. 60. Of these, the basis for the ultraviolet part is discussed in more detail in section 10.2.2 below. Each curve in Figure 60 gives the fractional contribution to the surface brightness due to stars brighter than a given magnitude. The total surface brightness for each wavelength and line of sight is given in Table 24. The sky brightness due to unresolved starlight can be estimated for any experiment given the magnitude limit to which it can resolve stars. First, determine the fraction, f, of brightness due to stars brighter than the limit using Fig. 60. Then, using the total brightness of starlight, I_{ISL} from Table 24, the surface brightness due to *unresolved* stars is $I_{ISL} \times (1 - f)$.

Table 24. Surface Brightness due to Integrated Starlight (given as λI_λ, respectively νI_ν)

wavelength (μm)	surface brightness (10^{-9} W m^{-2} sr^{-1})	
	b = 30°	North Gal. Pole
0.1565	62	24
0.55	577	250
2.2	205	105
12	6.1	3.0

The old compilations of integrated starlight in the visual by Roach and Megill (1961) and Sharov and Lipaeva (1973) do not have have high (≈ 1°) spatial resolution and are not calibrated to better than ≈15%. However, they still give useful information, are conveniently available in tabulated form, and have been used, e.g. in work to be discussed below in sections 11.2 and 12.2.1.

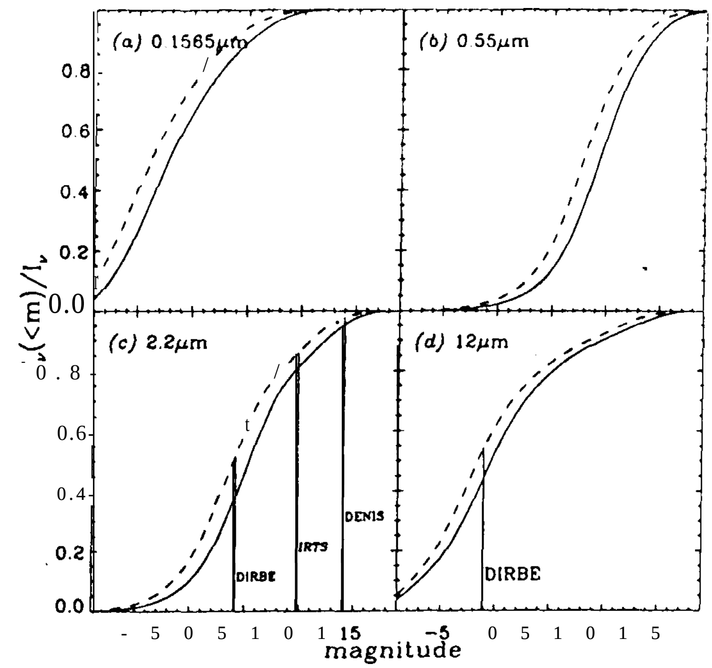

Fig. 60. Fraction of integrated starlight due to stars brighter than a given magnitude, for two lines of sight: the NGP (dashed curves) and a region at 30° galactic latitude (solid curves). Each panel is for a different wavelength: (a) 1565 A, (b) 55oO A, (c) 2.2 pm, and (d) 12 pm. In panel (c), the vertical lines indicate the magnitude limits adopted in analysis of DIRBE (Arendt et al. 1997), IRTS (Matsumoto et al. 1997), and DENIS (Epchtein 1994,1997) observations are shown.

10.2. *Ultraviolet*

10.2.1. Near ultraviolet (180 nm -300 nm)

The UV astronomy experiment S2/68 (Boksenberg et al. 1973) provided catalogs of stellar UV brightness over the sky in one photometric channel at 274 nm ($\Delta\lambda$ = 30 nm) and three spectroscopic channels around 156.5 nm ($\Delta\lambda$ = 33 rim), 196.5 nm ($\Delta\lambda$ = 33 rim), and 236.5 nm ($\Delta\lambda$ = 33 nm). Gondhalekar (1990) integrated over the spectroscopic channels to provide photometric information at all of the four UV wavelengths. The photometric accuracy is $\approx$ 10%. Only the 47039 stars with UV flux larger than 1.0×10^{-12} erg cm^{-1} s^{-1} sr^{-1} Å^{-1} ($m_{UV} \approx$ 8 mag) in at least one of the four passbands were kept for calculating the integrated starlight brightness over the sky. The resulting brightnesses are given in Tables 25 to 28.

Brosch (1991) also attempted to produce a galaxy model for the UV. He adapted the Bahcall and Soneira (1980) galaxy model by suitable colour relations to the 150-250 nm sky, and added Gould's belt and white dwarfs. He compared in his Figure 3 the model with the limited results available from a wide field UV imager flown on Apollo 16 (Page et al. 1982) and found reasonable agreement between his model and these data, but otherwise does not give an explicit description of the model.

10.2.2. FUV (91.2 nm -180 nm)

Table 25 discussed in the last subsection actually belongs to the FUV range.

As far as modelling is concerned, the stellar contributions to the FUV sky brightness have been well characterized. The optical and infrared SKY model of Cohen (1994) has been expanded into the FUV by fitting it to observations on the FUV sky obtained with the FAUST FUV telescope (Bowyer et al. 1993). The FAUST camera had obtained observational data on 5000 sources in 21 separate fields in the 140- 180 nm bandpass. These data covered FUV magnitudes from 5 to 12. The model resulting from the comparison to these data (Cohen et al. 1994) provides an excellent fit to the available FUV observations. The extrapolated flux for magnitudes greater than 12 is less than 4% of the total point source flux and is less than l% of the FUV diffuse sky brightness.

.4s is the case for other wavelength bands, the integrated starlight in the FUV (and also the near ultraviolet) is concentrated toward the plane of the Galaxy. In Figure 61 we display two examples of how the model accounts for the stellar contribution in the ultraviolet (kindly provided by Martin Cohen). The figure shows differential star counts as a function of a FUV magnitude centered at 166 nm, both for a position in the galactic plane at 1 = 90° and

Table 25. The intensity of stellar UV radiation at 156.5 nm in bins of 10°×10° in units of 10^{-10} W m^{-2} sr^{-1} μm^{-1}, respectively 10^{-11} erg cm^{-1} s^{-1} sr^{-1} Å^{-1}. Only stars brighter than a certain flux limit (see text) were included. From Gondhalekar (1990).

GALACTIC LATITUDE \ GALACTIC LONGITUDE	0–10	10–20	20–30	30–40	40–50	50–60	60–70	70–80	80–90	90–100	100–110	110–120	120–130	130–140	140–150	150–160	160–170	170–180
80 to 90	0	21	0	0	0	6	21	49	0	3	328	53	0	17	0	6	0	37
70 to 80	5	83	0	5	29	48	0	5	16	9	16	16	6	40	0	21	6	0
60 to 70	12	219	178	32	59	120	40	148	218	84	31437	457	2529	6	1631	71	10	602
50 to 60	23	203	191	257	5296	432	28	32	271	284	14	1067	63	287	1802	169	163	367
40 to 50	19	174	560	451	375	116	686	4992	381	363	525	260	2578	28	348	88	884	1160
30 to 40	1854	749	1604	599	680	3384	335	6088	332	3817	784	259	58	731	370	135	372	605
20 to 30	11518	1032	516	844	2007	1448	1281	763	1898	1093	1257	1668	1181	472	2487	389	1195	476
10 to 20	1418	1030	3499	4139	7251	3681	28071	7508	5931	2646	16979	1633	1922	1404	2429	2297	3043	1517
0 to 10	15909	1724	430	2684	3827	8123	10117	13728	10125	5398	6992	3558	9871	3542	2371	2231	13169	3820
−10 to 0	8569	7007	2239	5118	3961	6474	10371	7188	14751	11097	7060	7346	42327	5341	9645	10941	1816	21090
−20 to −10	37299	4028	2347	3716	2504	5086	5607	2397	4999	13788	10819	4954	8103	7110	11346	24350	15089	2645
−30 to −20	6283	983	1258	1607	1440	901	921	1544	2816	1160	1912	3302	2943	2071	1302	5977	8228	6502
−40 to −30	768	674	529	2178	608	212	1273	3018	398	536	305	9688	346	252	590	1234	1860	4238
−50 to −40	379	1029	73	3038	2187	1749	5431	3565	2768	172	20176	853	257	309	178	1271	1461	651
−60 to −50	3855	848	1685	885	416	819	308	67	350	304	338	447	38	204	22	373	122	6967
−70 to −60	8	484	2228	43	331	281	3168	0	0	987	19	13	5	7	15	69	0	44
−80 to −70	23	167	392	13	196	403	398	860	14	255	9	42	30	3	0	0	46	11
−90 to −80	0	0	0	0	0	0	121	7	0	124	3	196	0	14	0	4	0	0

GALACTIC LATITUDE \ GALACTIC LONGITUDE	180–190	190–200	200–210	210–220	220–230	230–240	240–250	250–260	260–270	270–280	280–290	290–300	300–310	310–320	320–330	330–340	340–350	350–360
80 to 90	0	4	11	36	83	53	77	0	225	0	20	0	0	0	0	0	13	0
70 to 80	20	4	23	0	13	106	0	493	102	22	0	173	65	0	8	25	0	0
60 to 70	570	282	20	166	264	1287	67	42	174	166	282	216	0	22	331	30	63	25
50 to 60	78	30	188	1656	73	4625	61	922	461	33	33	312	90	106916	278	93	697	836
40 to 50	333	164	76	216	16676	166	1921	93	37	644	2130	7479	102	199	340	180	372	21
30 to 40	287	246	631	639	1164	290	546	1264	376	581	148	164	303	331	685	402	2182	5121
20 to 30	3365	716	984	1112	6320	1276	1474	2114	630	1046	1497	2845	2231	696	11357	1652	35553	37753
10 to 20	1672	1664	6413	2859	2163	1557	721	1399	1302	1363	2366	15072	11637	88106	117263	58921	16750	49932
0 to 10	4819	5663	13009	7162	5091	10457	4842	17631	10247	17072	9510	37745	105723	161704	12339	7920	29225	6668
−10 to 0	20305	18057	8174	9534	72818	50109	28184	91693	37846	49445	28298	19445	46922	11441	8031	7380	20306	130928
−20 to −10	2082	78886	167335	47670	58440	80884	28658	9476	41031	16664	9862	8291	4927	3883	4581	16021	15895	10572
−30 to −20	4632	14493	62868	28471	2376	15051	7161	6088	7945	2355	1084	2779	833	1149	846	4460	1875	2850
−40 to −30	3074	9881	3591	2021	1084	953	573	659	649	1534	714	461	1056	165	1789	1014	34189	209
−50 to −40	728	1987	98	2508	1657	2575	298	2558	2340	284	1946	428	610	43	725	256	37	257
−60 to −50	129	23	890	1503	248	2793	66	32	171	38	166	82285	553	1229	88	171	9	18504
−70 to −60	284	1606	13	189	600	133	141	207	1673	3002	201	2137	68	282	1575	269	77	130
−80 to −70	125	128	101	22	1053	0	0	89	283	15	41	28	73	198	0	37	5	929
−90 to −80	0	0	0	0	0	0	0	0	1601	31	3	0	6	0	0	0	0	122

Table 26. The intensity of stellar UV radiation at 196.5 nm in bins of 10°x10° in units of 10^{-10} W m^{-2} sr^{-1} μm^{-1}, respectively 10^{-11} erg cm^{-2} s^{-1} sr^{-1} Å^{-1}. Only stars brighter than a certain flux limit (see text) were included. From Gondhalekar (1990).

GALACTIC LATITUDE (80, 60, 40, 20, 0, -20, -40, -60, -80)

0	66	5	21	10	9	67	51	34	38	281	61	4	61	7	27	4	77
46	103	60	106	115	69	64	106	123	67	134	69	66	83	65	122	20	39
73	474	173	159	192	144	484	348	380	248	19536	614	2937	176	1784	230	174	673
67	278	249	443	4651	458	269	262	611	510	265	1220	402	851	2248	400	454	824
199	466	844	610	488	318	870	3710	667	721	1029	528	2133	378	700	457	1528	1687
1844	766	1599	678	1118	2777	652	4285	933	3331	1167	887	754	1189	830	853	971	716
7024	816	560	1886	1778	1728	1442	1346	2535	1869	2102	2236	1840	1322	2614	1333	2148	912
2058	963	2723	2954	4668	3059	23470	6700	5901	3503	12495	2508	2519	2319	2813	2926	4577	2281
9974	1688	683	2372	3502	5780	7678	10428	9791	5584	5670	3369	7856	3528	3003	2977	9311	4329
6276	4984	1776	4160	5800	4943	7844	5689	11045	8961	6816	6846	29429	5468	8012	8299	1987	15113
24356	3189	2074	2436	2309	4265	4440	2240	3966	9074	8281	4840	6767	5386	9214	14407	8161	2294
3763	1170	1231	1370	1244	1123	904	1546	2366	1516	1646	2908	2873	2049	1977	4574	6132	4592
875	871	838	2091	669	405	1320	2290	441	809	501	7547	532	410	1433	1178	1388	3138
624	1159	301	2319	1818	1482	3811	2620	2842	332	12086	647	379	336	286	1045	1544	644
3012	989	1318	731	367	799	329	199	327	472	428	409	136	326	69	683	235	4283
66	547	4380	165	621	280	2322	21	38	718	64	66	77	107	107	123	60	153
54	141	376	93	275	396	403	686	55	217	48	48	90	48	25	65	130	58
0	23	11	20	0	9	162	14	48	120	52	189	8	45	9	18	3	41

0 10 20 . 3 0 4 0 6 0 6 0 7 0 8 0 90 100 110 120 130 140 150 160 170 180

GALACTIC LONGITUDE

GALACTIC LATITUDE (60, 60, 40, 20, 0, -20, -40, -60, -80)

14	39	89	151	250	66	157	18	276	18	23	11	7	13	9	36	17	4
78	84	104	28	54	158	33	1560	189	42	10	289	136	7	34	43	40	29
477	285	112	285	964	1208	144	92	176	327	468	466	29	72	759	100	145	69
367	208	261	1392	137	3251	236	915	336	99	130	397	204	66053	237	246	761	903
715	396	240	306	12364	220	1610	219	211	736	1394	6660	248	413	351	363	643	179
666	545	806	920	1136	617	744	1273	678	962	333	664	643	688	676	661	1847	4130
4423	1186	1196	1193	4074	1411	1328	1938	1242	1474	1810	2676	2264	1202	7816	1482	20214	20145
2265	1976	6608	3332	2379	1809	1077	1830	1834	2113	2878	10179	9363	51130	71532	35739	10912	26100
4118	5984	9198	5486	4179	7367	4658	12044	8346	12558	8043	24094	69117	96254	9369	6530	17294	5167
11983	12380	6266	7519	70802	31871	19438	57425	25242	34431	18527	13365	28565	8314	7297	6409	14822	78499
2130	49160	113627	32748	35036	50036	17642	7619	26005	11403	8333	6678	3624	2935	3853	11081	11076	8444
4077	9407	46824	18028	2921	10515	5486	5151	9324	2466	1270	2369	948	1095	1039	3432	2141	2456
2276	6384	2806	1514	1179	934	768	1117	981	1499	836	768	1247	551	2109	1415	21177	778
699	1602	247	2096	1364	2166	660	1832	2334	516	2077	685	703	241	848	627	445	683
297	149	824	1346	391	2032	322	203	226	291	612	51762	786	1364	436	587	268	12512
322	1172	127	350	625	282	190	335	1280	2202	438	1627	249	377	1054	426	297	186
191	106	136	81	939	45	38	159	297	75	108	116	114	450	46	91	96	740
11	23	19	18	6	7	3	0	1220	64	27	3	7	0	29	4	19	97

180 190 200 210 220 230 240 2s0 2$0 270 280 290 300 310 320 330 340 350 360

GALACTIC LONGITUDE

Table 27. The intensity of stellar UV radiation at 236.5 nm in bins of $10^\circ \times 10^\circ$ in units of $10^{-10}\,W\,m^{-2}\,sr^{-1}\,\mu m^{-1}$, respectively $10^{-11}\,erg\,cm^{-1}\,s^{-1}\,sr^{-1}$.4-1. Only stars brighter than a certain flux limit (see text) were included. From Gondhalekar (1990).

Galactic latitude \ Galactic longitude	0–10	10–20	20–30	30–40	40–50	50–60	60–70	70–80	80–90	90–100	100–110	110–120	120–130	130–140	140–150	150–160	160–170	170–180
90 to 80	0	62	11	6	51	0	39	14	35	23	160	52	0	36	10	18	3	60
80 to 70	208	87	50	101	88	61	34	105	124	23	166	22	69	118	33	106	16	54
70 to 60	117	678	142	127	191	116	518	214	281	158	9683	447	2096	56	1247	103	130	627
60 to 50	63	234	208	347	3171	295	293	190	378	366	137	740	281	604	1640	286	246	606
50 to 40	281	499	800	551	314	430	564	2040	473	486	733	229	1206	128	374	439	1167	1341
40 to 30	1201	610	999	477	894	1615	376	2196	496	1902	656	498	316	549	384	570	465	343
30 to 20	4804	599	433	1722	1135	1243	813	717	1105	899	1310	1219	1093	586	1182	602	1042	482
20 to 10	1554	833	2206	1972	2761	1891	16403	3737	2957	1627	5446	1444	1468	1215	1614	1549	2828	1117
10 to 0	4843	1279	672	1642	2493	3821	4661	7105	6728	2825	4445	2028	4666	1970	1865	1447	5684	2755
0 to −10	3756	3628	1222	2797	5170	3071	4564	3249	6398	5218	3890	3700	15065	2814	5416	5034	1339	8429
−10 to −20	12013	2112	1538	1640	1488	2728	2737	1361	2333	4674	4890	2531	3808	2957	5204	7315	6377	1826
−20 to −30	2080	692	792	904	767	955	669	1160	1411	961	1021	1676	1518	1256	1481	2878	5047	2863
−30 to −40	500	522	665	1438	542	298	935	1346	285	685	344	4373	405	374	1383	826	878	1848
−40 to −50	488	758	238	1863	1144	1059	2326	1620	1938	288	5133	358	333	274	255	720	1150	433
−50 to −60	1694	704	760	466	295	540	262	203	300	457	398	284	117	260	66	493	201	2046
−60 to −70	43	358	3336	125	521	194	1362	46	30	427	44	103	56	105	138	90	113	121
−70 to −80	30	100	272	83	236	254	269	445	84	158	18	61	77	169	28	67	113	114
−80 to −90	6	9	27	10	6	22	121	8	43	69	57	199	9	34	0	10	0	27

Galactic latitude \ Galactic longitude	180–190	190–200	200–210	210–220	220–230	230–240	240–250	250–260	260–270	270–280	280–290	290–300	300–310	310–320	320–330	330–340	340–350	350–360
90 to 80	10	50	74	156	215	44	122	16	192	16	18	0	17	18	3	47	19	0
80 to 70	72	80	84	21	56	133	38	1315	145	38	13	289	111	46	33	70	46	84
70 to 60	218	272	121	217	896	813	209	94	102	394	353	666	39	79	643	62	124	56
60 to 50	300	217	185	1144	122	2220	253	648	223	84	123	286	200	34737	153	297	645	695
50 to 40	606	303	258	216	6937	186	1009	166	140	600	789	3467	187	267	285	338	475	196
40 to 30	369	427	654	704	793	493	492	984	432	620	203	495	316	393	466	356	1169	2396
30 to 20	3119	980	738	740	2288	867	798	1181	638	942	1161	1596	1322	848	4004	868	9606	10684
20 to 10	1252	1376	3371	4399	1319	1107	774	995	992	1091	1704	10698	5361	21882	33153	15639	5344	10863
10 to 0	2736	3933	4812	3237	2298	4038	2700	6191	5068	6989	4754	11631	34732	50365	4670	3400	9218	3392
0 to −10	7286	6697	4197	4427	48567	17675	9963	27510	14347	20412	18332	8067	13096	6890	4781	3404	8712	38060
−10 to −20	1671	25494	57801	18338	19033	29396	9103	4051	12510	6395	6334	3249	2061	1810	2410	6796	5965	4648
−20 to −30	3818	5567	34237	8415	1734	5399	3054	2876	6687	1443	824	1418	664	694	694	1897	1094	1411
−30 to −40	1602	3410	1623	848	688	544	407	713	542	902	478	435	928	335	1480	866	9822	454
−40 to −50	496	1013	170	1205	751	1289	412	939	1353	397	1216	436	388	200	597	411	304	274
−50 to −60	289	177	515	877	409	1091	214	156	128	268	534	30119	574	819	358	465	144	6259
−60 to −70	282	716	162	313	373	211	147	236	676	1204	356	812	190	280	513	275	179	113
−70 to −80	155	53	110	54	579	15	18	98	179	54	80	168	95	342	65	51	86	444
−80 to −90	16	32	0	8	3	0	0	10	687	60	14	0	3	0	24	0	8	52

Table 28. The intensity of stellar UV radiation at 274 nm in bins of $10° \times 10°$ in units of 10^{-10} W m^{-2} sr^{-1} μm^{-1}, respectively 10^{-11} erg cm^{-1} s^{-1} sr^{-1} Å^{-1}. Only stars brighter than a certain flux limit (see text) were included. From Gondhalekar (1990).

GALACTIC LATITUDE

	8	50	8	3	13	0	60	31	32	10	173	54	0	41	6	18	0	57
80	52	80	41	74	82	67	20	76	96	36	103	37	51	72	41	90	9	41
	87	364	116	118	159	109	406	245	286	147	12969	416	2097	39	1261	129	106	489
60	45	202	193	311	3343	310	198	168	346	332	130	760	242	527	1459	239	240	638
	168	339	639	460	333	250	588	2576	474	413	677	250	1417	151	393	307	1034	1234
40	1142	547	1078	495	827	1922	406	2772	622	2148	681	460	295	575	380	454	495	439
	4669	485	364	1440	1198	1222	999	842	1370	960	1290	1347	1025	627	1399	647	1199	652
20	1365	622	1854	1941	3157	2005	16957	4509	3591	1960	8143	1510	1537	1289	1586	1629	2882	1367
	6823	987	451	1494	2293	3754	4994	7084	6211	3143	3672	1938	5213	2088	1686	1423	5959	2836
0	3559	3068	1037	2899	4181	3225	5277	3706	7266	5774	3870	3784	19816	2854	4754	5178	1138	10283
	16132	2079	1387	1591	1501	2893	2993	1466	2728	5803	5422	2918	4136	3625	5990	9658	5548	1581
-20	2423	727	774	877	830	773	691	1104	1603	1019	1135	1937	1788	1379	1421	3043	4047	3168
	585	802	627	1445	514	295	932	1547	290	545	373	5440	390	297	1073	825	930	2057
-40	457	803	201	1838	1247	1042	2650	1831	1904	240	8081	417	265	239	206	721	1097	441
	1996	681	913	538	314	525	248	142	244	381	348	279	86	234	50	441	142	2901
-60	39	347	3088	131	456	215	1673	27	23	480	39	57	54	58	83	76	71	108
	29	108	270	88	267	266	290	483	37	161	40	45	51	47	18	49	83	48
-80	0	9	16	13	6	10	112	9	26	80	46	136	0	24	10	13	0	15

0 10 20 30 40 50 60 70 80 90 100 110 120 130 140 150 160 170 180

GALACTIC LONGITUDE

GALACTIC LATITUDE

	4	33	66	120	175	53	127	9	190	8	14	10	8	13	4	38	18	0
80	55	60	73	15	54	117	22	1146	134	29	4	229	94	3	49	41	38	43
	320	200	104	207	750	828	140	68	117	273	314	451	29	60	575	52	112	61
60	257	179	182	969	90	2908	182	649	261	62	98	280	177	47457	165	200	529	670
	540	301	183	222	8673	178	1107	136	144	539	1018	4018	172	216	287	268	398	139
40	455	403	687	661	804	382	483	949	392	662	254	408	363	481	502	437	1287	2825
	3107	833	801	806	2750	1000	884	1358	629	1142	1237	1839	1486	778	5190	879	12717	12515
20	1514	1406	3900	3036	1556	1283	775	1193	1167	1237	1777	6682	6186	33063	49170	23585	7047	15286
	2835	4140	5958	3733	2657	4908	2948	8092	5311	8378	6242	16851	47224	70128	5669	3798	11068	3058
0	8421	8092	4236	4994	49181	22730	12759	35291	17005	22987	12729	8858	18449	5481	4464	3512	9722	53058
	1446	33830	76954	23842	25375	38722	12082	4980	16881	7813	5904	3855	2380	2015	2589	8104	7853	5548
-20	2822	7064	36818	11573	1761	6994	3769	3408	7168	1534	785	1549	618	692	667	2328	1333	1535
	1518	4598	1994	1014	773	599	483	683	557	1009	529	410	748	278	1448	876	13955	488
-40	438	1074	189	1388	912	1448	423	1191	1487	319	1304	420	416	128	553	358	250	276
	230	140	539	963	282	1336	212	125	124	190	385	36658	534	859	281	389	115	8312
-60	245	827	87	285	421	182	98	226	819	1435	314	985	169	246	672	290	146	124
	151	67	119	51	644	26	16	104	191	55	68	82	77	331	23	51	66	505
-80	10	35	8	3	0	0	3	0	836	54	10	4	0	0	21	8	10	66

180 190 200 210 220 230 240 250 260 270 280 290 300 310 320 330 340 350 360

GALACTIC LONGITUDE

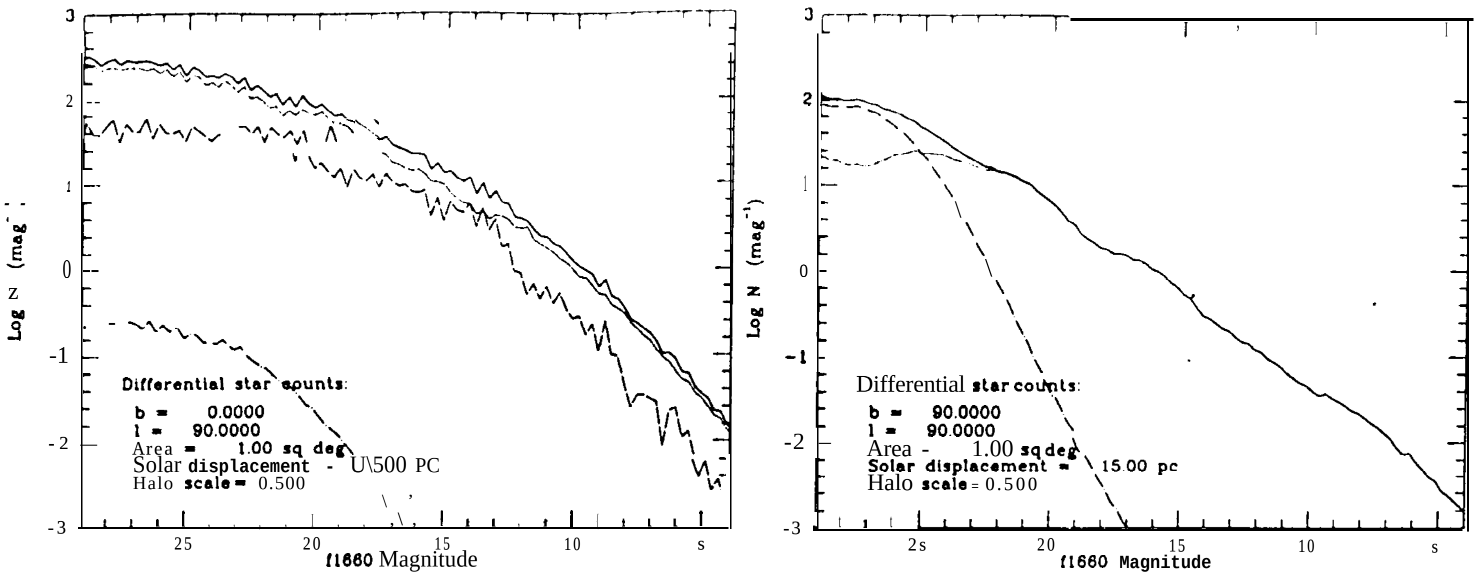

Fig. 61. Differential star counts as a function of FUV magnitude for a position in the galactic plane at l = 90° (left) and for the galactic pole (right). Solid line: total contribution! faint dotted line: disk component, dash-dot line: halo contribution, long-dashed line: spiral arms plus local spur (shown only for the field in the galactic plane).

Table 29. Total integrated surface brightness in the range 140 nm -180 nm due to point sources, as given by the SKY models at a galactic longitude of 90° as predicted by the SKY model.

Galactic latitude	I_ν mJy/□°	I_λ W/m^2 sr μm	I photons/cm^{2}s sr Å
90°	26.6 ± 0.01	102×10^{-10}	82.5
80°	40.6 ± 0.02	156×10^{-10}	125.8
70°	49.7 ± 0.03	191×10^{-10}	153.8
60°	58.2 ± 0.03	224×10^{-10}	180.4
50°	70.9 ± 0.05	273×10^{-10}	219.5
40°	89.8 ± 0.19	345×10^{-10}	278.0
30°	122.1 ± 0.3	469×10^{-10}	378.2
20°	185.0 ± 0.6	709×10^{-10}	571.1
10°	483.0 ±12.9	1860×10^{-10}	1496
0°	429.7 ± 7.8	1650×10^{-10}	1330

[a] Since this model was primarily constructed for the infrared, it cannot be expected to be accurate in the ultraviolet at low galactic latitudes ($|b| \leq 10°$), where the effects of clumsiness of the interstellar medium get dominating (Caplan and Grec 1979).

for the galactic pole. In both parts of the figure, the solid line is the total number of stars per square degree per magnitude interval, the disk component is shown by the faint dotted line, and the dash-dot line is the halo contribution. For the galactic plane (left diagram), the halo component is of lesser importance, but the spiral arms plus local spur contribution have to be taken into account (long-dashed curve). Table 29 gives the total stellar surface brightness in the 140-180 nm band as a function of galactic latitude. The brightness varies with galactic longitude; in this case we show the values for l = 90°.

In an attempt to unify the above information on ultraviolet integrated starlight, at present we suggest to rely on Tables 25 to 28 for the absolute and total brightness level, and to use the models demonstrated above for purposes like extrapolation to the contribution of faint stars or breakdown of the total brightness into the contribution of different components or brightness intervals.

10.3. *Ground-based UBVR photometries*

Besides airglow and zodiacal light, the Milky Way is the third major contributor to the diffuse night sky brightness in the visual spectral domain. In this part of the electromagnetic spectrum, the light of our Galaxy is the only constituent of the night sky which is fixed with respect to an inertial system of reference and also is constant over large time scales. For absolute brightness determinations, space experiments, free of disturbance by the earth's atmosphere, are best suited, for studies of structures, ground-based surveys are preferable because of their greater flexibility.

Efforts to describe the distribution of the Milky Way's brightness are numerous and can be traced back far into the past (Ptolemy's Almagest). Difficulties to get rid of atmospheric disturbances still are present in the classical paper by Elsässer and Haug in 1960, which otherwise, for the first time, presented photoelectric measurements of our Galaxy with a reasonable resolution in well defined passbands (see Tables 30 and 31).

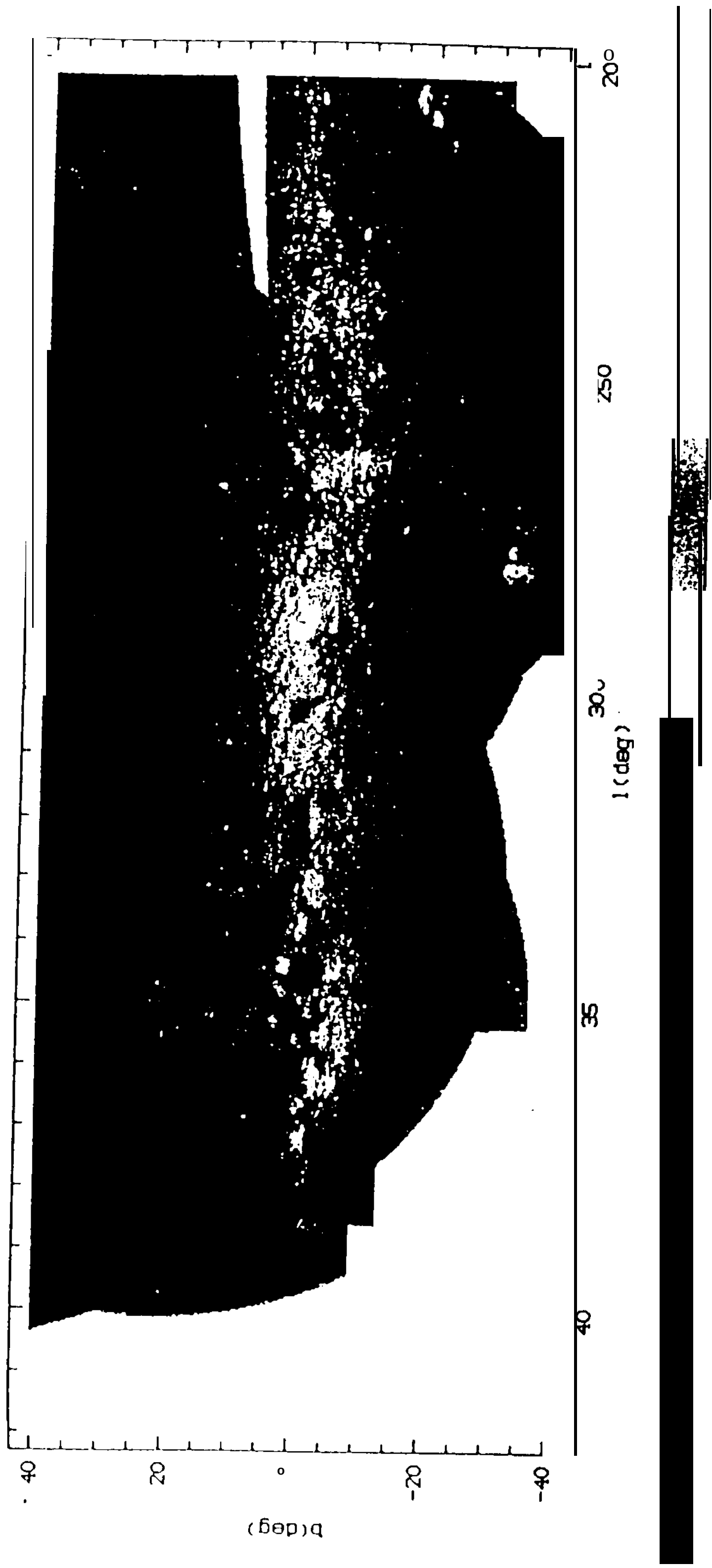

Fig. 62. U photometry of the Southern Milky Way. The photometry is accompanied by a colour bar. Its left end corresponds to -100 S_{10}. The brightness at the right end of the bar is 150 S_{10} units (U). The scale is linear. White areas denote non-valid data.

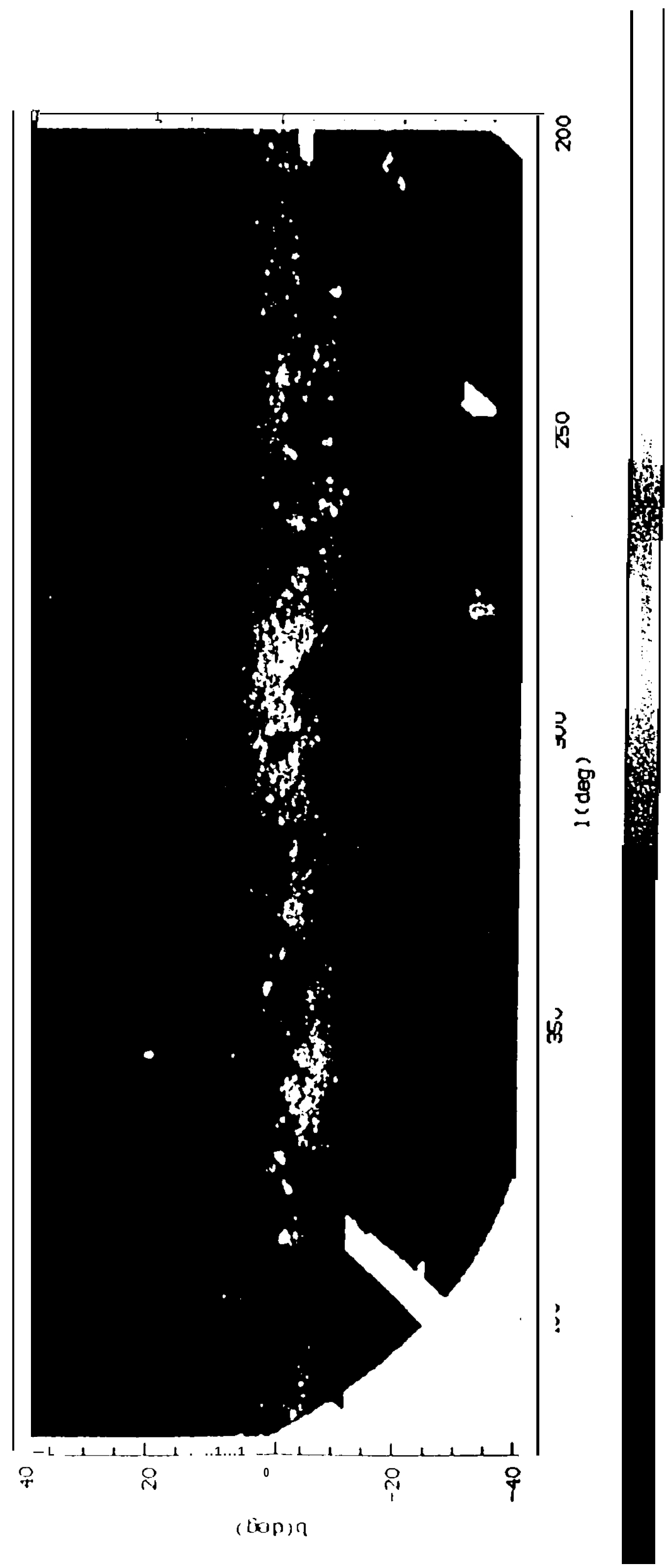

Fig. 63. B photometry of the Southern Milky Way. The photometry is accompanied by a colour bar. Its left end corresponds to -100 S_{10}. The brightness at the right end of the bar is 550 S_{10} units (B). The scale is linear. White areas denote non-valid data.

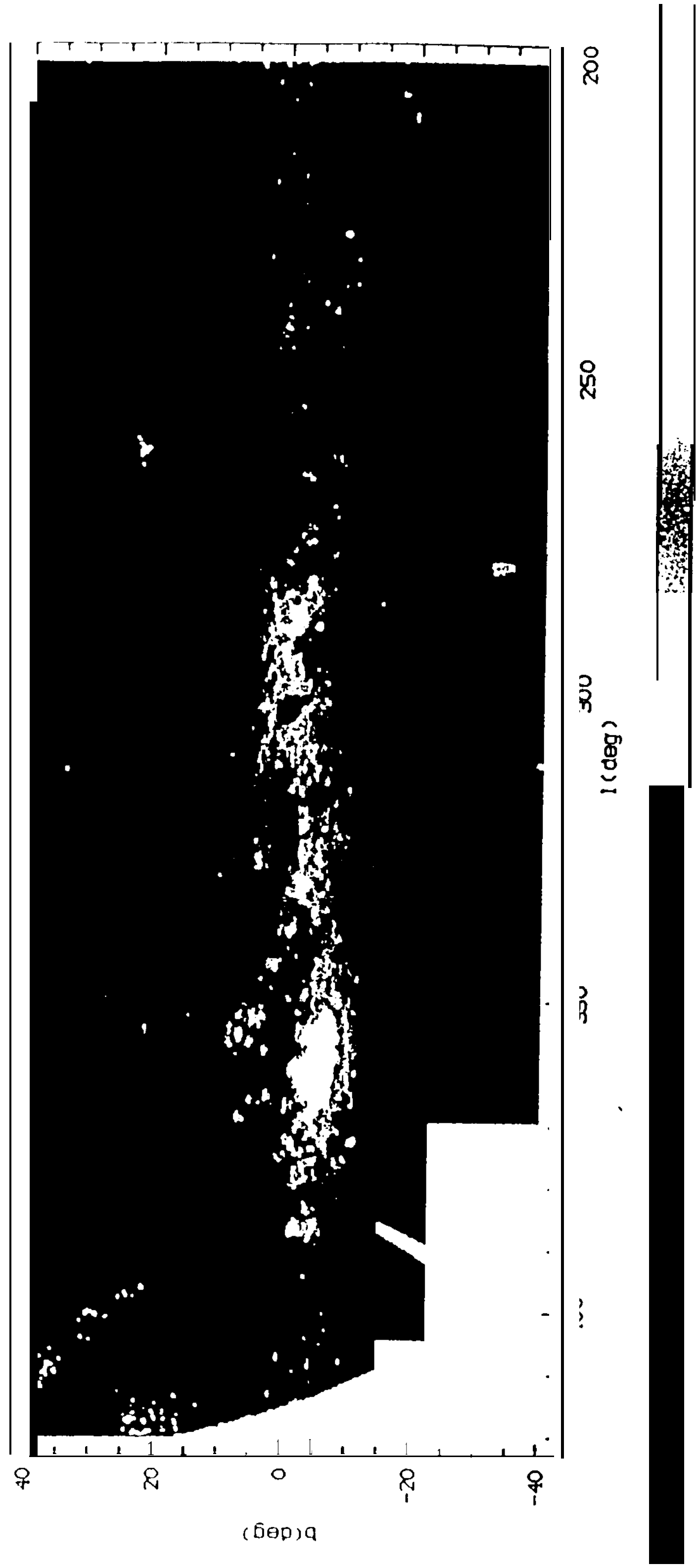

Fig. 64. V photometry of the Southern Milky Way. The photometry is accompanied by a colour bar. Its left end corresponds to -100 S_{10}. The brightness at the right end of the bar is [illegible] S_{10} units (-). The scale is linear. White areas denote non-valid data.

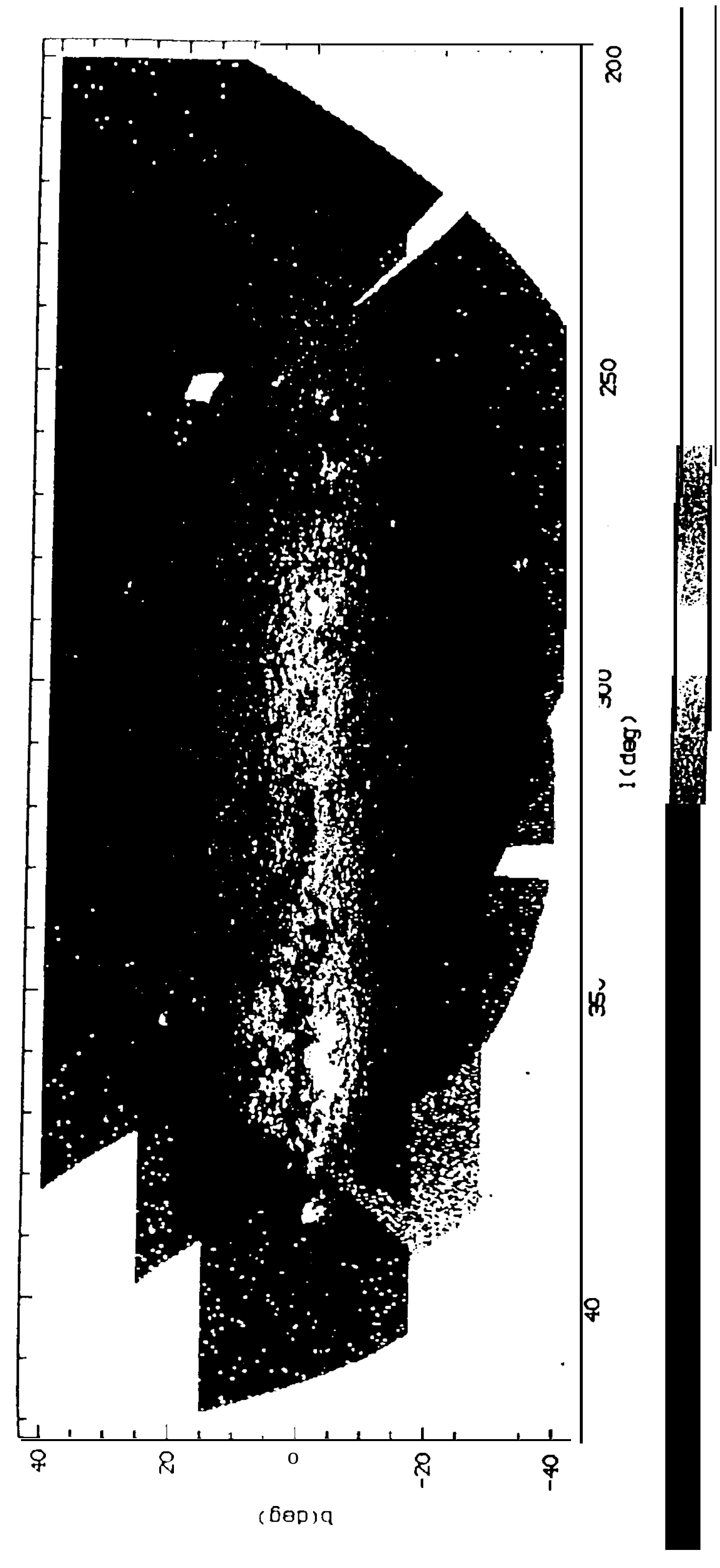

Fig. 65. R photometry of the Southern Milky Way The photometry is accompanied by a colour bar. Its left end corresponds to -100 S_{10}. The brightness at the right end of the bar is 2600 S_{10} units (R.) The scale is linear. White areas denote non-valid data.

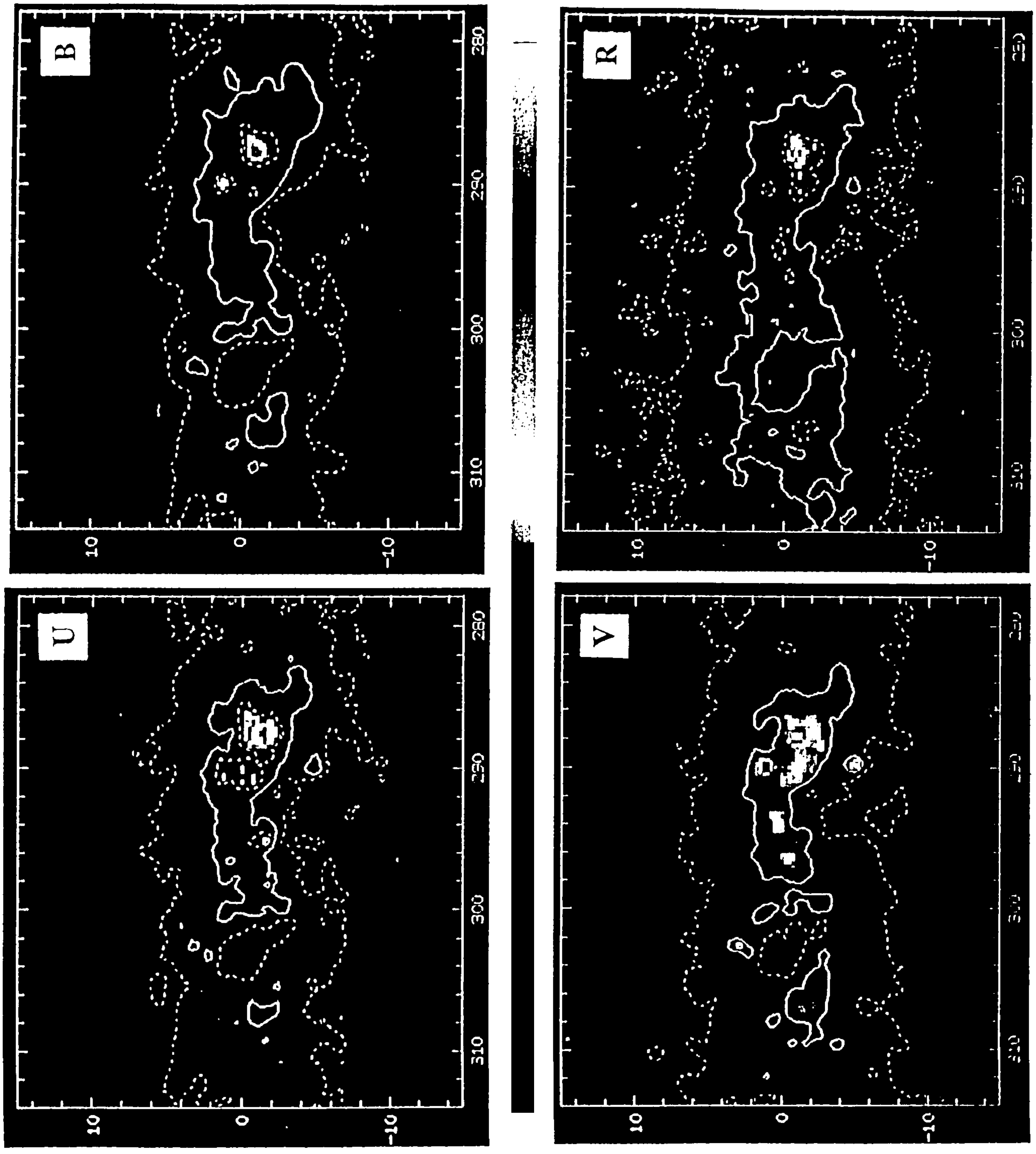

Fig. 66. Synopsis of the Carina-Coalsack region in U, B, V, R. To facilitate comparison, the levels are adjusted for an optimal visualization. The S_{10}-isophotes in the sense of "outer broken line, continuous line and inner broken line" are (150, 250, 380) for U, (150,230, 400) for B, (250, 500, 800) for V, and (1000, 1400, 1900) for R. The linear scale of the colour coding may be used for interpolation.

Table 30. Large scale surface photometries of the Milky Way in the visual/near visual spectral domain(in addition to those displayed as Figures 62- 66).

Spectral range	Approximate interval of galactic longitudes	latitudes	Reference
P, v	0...360°	-90 . . . +90°	Elsässer und Haug (1960)
530 * 15 nm	0...360°	-20 . . . +20°	Smith et al. (1970)
u	0...360°"	-50... +50°*	Pfleiderer and Mayer (1971) .
B	0...360°"	-90... +90°*	Classen (1971)
710 ±100 nm	Northern Milky Way		Zavarzin (1978)
440 * 45 nm	0...360°	-90...-55"	Weinberg (1981)+
640 ± 50 nm	0...360°	-90...-55°	Weinberg (1981)+
356 ± 53 nm	41 . ..210°	-41 . . . +41°	Winkler et al (1981)
B-R = 440nm -640nm	0...360°	-15 . . . +15°	Toiler (1990)+
B, V	0...360°	-90 . . . +90°	Wicenec(1995)+, Wicenec and van Leeuwen+

*as far as visible from about 30° southern geographical latitude
'space experiments, included here for comparison, see a detailed presentation of Pioneer 10 results in section 10.4
Note: The earlier photometries by Elsässer and Haug and Smith et al. rue included here only for comparison. It is recommended to refer to the space-based photometries, to the Bochum photometries shown in Figures 62-66 and to the later photometries of this table.

Table 31. Surface photometries covering *smaller areas* of the Milky Way.

Spectral range	Approximate interval of galactic longitudes	latitudes	Reference
B	295...310°	-6 . . . +5°	Mattila (1973)
u	-63 . . . +30"	-30 . . . +30°	Pröll (1980)
U, B, V	Scorpius		Hanner et al. (1978)"
U, B, V	selected scans		Leinert and Richter (1981)[a]
U, B, V, R	289...316°	-15 . . . +14°	Seidensticker et al. (1982)

[a] space experiment, included here for comparison, since well-calibrated

The four photometries of the Southern Milky Way presented here in colour as Figures 62-66 profit from the now more effective correction for the atmospheric effects. They cover the whole range in longitudes and galactic latitudes from -40° to +40°. They have a high angular resolution (0.25 x 0.25 square degrees). Moreover, all wavelength bands are processed in the same way, and so the colours U-B, B-V, V-R should be quite coherent. The Figures presented here only give an overview, although the linear scale of the colour bar will allow coarse interpolation. The data are accessible in digital form at the astronomical data center *Centre de Donnés* Stef/sires (CDS) in Strasbourg under

http: //cdsweb.u-strasbg.fr/htbin/myqcat3?VII/199/

It is planned to make accessible to the public under this address step by step all major ground-based photometries of the Milky Way contained in Table 30, in particular also the B photometry by Classen (1976), which has the advantage of large sky coverage and which fits quite well to the Helios and Pioneer space probe data (see Figure 69 below). For further information with respect to the four photometries discussed, see the papers by Kimeswenger et al. (1993) and Hoffmann et al. (1997). .4s an example for the kind of spatial detail to be expected, Figure 66 shows on an enlarged scale the UBVR photometry for the Coalsack region.

The UBVR photometries shown in Figures 62-66 are breed on photographic exposures, calibrated in situ by photoelectric measurements of the night sky. The raw data were obtained in 1971 by Schlosser and Schmidt- Kaler at La Silla (Schlosser, 1972). The well known disadvantages of photographic plates (their relatively low inherent accuracy, for instance) do not count so much if one considers the often rapid variations of the night sky in total. Such changes especially affect scanning photometers and reduce their inherent accuracy. A posteriori, it is vir-

Table 32. comparison of the Bochum UBVR photometries (denoted as 'X') with other photometries.

U passband		λ_{bi} =352 nm, W_λ = 51 nm, $\Delta\lambda$ = 97 nm)
	Leinert and Richter (1976)	= (0.97 ± 0.18)·X - (12 ± 4)
	Pröll (1980)	= (1.11 * 0.12)·X
	Pfleiderer and Meyer (1971)	= (0.84 ± 0.02)·X - (10 ± 3)
	Seidensticker et al. (1982)	= (1.19 ± 0.03)·X - (28 ± 5)
B passband		λ_{bi} = 421 nm, WA = 80 nm, $\Delta\lambda$ = 141 nm)
	Classen (1976)	= (0.83 ± 0.04)·X + (23+5)
	Leinert and Richter (1981)	= (0.93 ± 0.08)·X
	Mattila (1973)	= (0.82 ± 0.12)·X + (31 ± 23)
	Seidensticker et al. (1982)	= (1.18 ± 0.03)·X + (16 ± 3)
	Toiler (1989)	= (0.90)·X - 25
V passband		λ_{bi} = 530 nm, W_λ = 94nm, $\Delta\lambda$ = 159 nm)
	Dachs (1970)	= (1.03)·X
	Elsässer and Haug (1960)	= (0.64 ± 0.13)·X - (36 ± 8)
	Leinert and Richter (1981)	= (0.94
	Seidensticker et al. (1982)	= (1.13 * 0.091:- (88* 14)
R passband		λ_{bi} = 678 nm, W_λ = 24 nm, $\Delta\lambda$ = 53 nm)
	Seidensticker et al. (1982)	= (1.09 ± 0.04)·X - (464 ± 36)

λ_{bi} is the wavelength which bisects the recorded energy for this filter
Please note: 10 mean errors given only if data permit (multiplicative term)
and/or mean differs by more than 1 σ from zero (additive term)
The Bochum UBVR photometries are stored at the Strasbourg *Centre de Données Stellaires* (CDS) under http: //cdsweb.u-strasbg.fr/htbin/myqcat3?VII/199/

tually impossible to discriminate between temporal and spatial variations. For Figures 62-66, a wide angle camera (FOV 135°) was employed, which integrated the night sky at the same time, thus avoiding the above mentioned unwanted effects. Tables 30-32 contain supporting information. Table 30 gives a synopsis of photometries in the visual and near-visual spectral spectral domain. This list contains only photometries covering the whole Galaxy or a major part of it (for more details, see Scheffler, 1982). Some photometries of smaller galactic areas are contained in Table 31. In Table 32, the four Bochum photometries shown here are compared to those of other authors. Because the Helios data (Hanner et al. (1978), Leinert and Richter (1981)) are considered a well calibrated reference, these space probe measurements are also included here for comparison. The same is true for the south polar region subset of Pioneer data shown by Weinberg (1981) and the subset presented by Toiler (1989), while a much more complete overview on the Pioneer measurements of integrated starlight will be given in the following subsection.

10.4. Pioneer 10/11 spaceborne visual photometry

Small imaging photopolarimeters (IPP's) on the Pioneer 10 and 11 deep space probes were used during cruise phases (between and beyond the planets) to periodically measure and map over the sky brightness and polarisation in blue (395 nm - 495 nm) and red (590 nm - 690 nm) bands. This was done at heliocentric distances beyond 1.015 AU (Weinberg et al. 1974, Hanner et al. 1974). Early results suggested that observations of the same sky regions decreased in brightness with heliocentric distance R to ≈ 3.3 AU (Weinberg et al. 1974, Hanner et al. 1976), beyond which there was no observable change; i.e., the zodiacal light became vanishingly small compared to the background galactic light (i.e. was less than 2 SIOO). Subsequent analysis (Schuerman et al. 1977) found this detectability limit to be 2.8 AU. Thus, for sky maps made between 1 AU and 2.8 AU, the observations give the sum of zodiacal light and background starlight, while beyond 2.8 AU the background starlight, including some diffuse galactic light, could be observed directly. We summarise here those observations from beyond 2.8 AU.

Approximately 80 sky maps were obtained with the Pioneer 10 IPP, starting in March 1972, of which 50 maps fall into the year 1972 (see Table 33). The FOV'S covered most of the sky (see Figure 67) except for a region near the spin axis of the spacecraft (within 30° of the sun). Table 33 presents a log of observations with the Pioneer 10 IPP. A similar schedule was performed with the IPP on Pioneer 11, starting in April 1973. The combined data provide a

Table 33. Log of cruise phase observations with the Pioneer 10 Imaging Photopolarimeter.

Year	Calendar Date	Sun-S/C Distance (Au)	S/C Distance from ecliptic" (AU)	Heliocentric $\beta_{S/C}$	$\lambda_{S/C}$ (deg)	Usable LA* Range · (deg)	Signal/ Noise
1972	Mar 10	1.002	-.0065	-0.37	172.85	152-168	8.70
	11	1.004	-.0073	-0.41	174.12	135-167	4.15
	12	1.006	-.00805	-0.46	175.36	136-169	7.68
	14	1.011 "	-.0095	-0.54	177.63	128-169	7.00
	15	1.014	-.0103	-0.58	178.87	128-168	5.65
	16	1.017	-.01107	-0.62	180.07	128-169	4.93
	20	1.032	-.01428	-0.79	185.03	128-150	5.62
	22	1.040	-.01581	-0.87	187.37	128-168	5.00
	23	1.046	-.01677	-0.92	188.84	128-170	4.56
	29	1.075	-.02117	-1.13	195.47	128-169	6.43
	31	1.087	-.0227	-1.20	197.78	110-146	5.87
	Apr 4	1.110	-.02554	-1.32	201.95	110-170	4.93
	10	1.150	-.02971	-1.48	207.98	91-159	4.12
	13	1.171	-.03165	-1.55	210.76	91-170	3.78
	17	1.201	-.03424	-1.63	214.39	91-166	3.15
	20	1.224	-.03613	-1.69	217.02	91-168	4.71
	27	1.281	-.04027	-1.80	222.68	86-103	4.09
	28	1.289	-.04086	-1.82	223.48	91-158	3.75
	May 5	1.349	-.04474	-1.90	228.64	46-168 ,	11.46
	8	1.376	-.04632	-1.93	230.73	46-156	14.43
	17	1.453	-.05058	-1.99	236.23	46-170	13,87
	30	1.586	-.05694	-2.06	244.26	46-169	10.34
	June 7	1.652	-.05972	-2.07	247.70	46-169	8.90
	13	1.709	-.06196	-2.08	250.46	49-130	7.75
	20	1.774	-.06436	-2.08	253.40	42-067	7.96
	22	1.788	-.06485	-2.08	254.00	44-170	7.31
	27	1.841	-.06666	-2.08	256.21	91-130 141-168	4.21
	29	1.861	-.0673	-2.07	257.00	68-169	5.21
	July 21	2.062	-.07326	-2.04	264.32	128	3.87
	24	2.090	-.07399	-2.03	265.22	128	6.40
	27	2.117	-.07469	-2.02	266.11	128	4.34
	31	2.152	-.07557	-2.01	267.21	128	7.75
	Aug 3	2.179	-.07622	-2.00	268.04	104-137 160-170	4.81
	10	2.241	-.07766	-1.99	269.87	128	5.00
	11	2.249 "	-.07784	-1.98	270.11	91-140 158-170	4.43
	16	2.294	-.07880	-1.97	271.36	91-168	6.31
	23	2.354	-.08005	-1.95	273.01	74-145 167-170	5.90
	30	2.413	-.08121	-1.93	274.58	76-158	4.03
	Sept 5	2.467	-.08219	-1.91	275.94	76-166	5.09
	8	2.492	-.08263	-1.90	276.56	128-169	4.59
	26	2.640	-.085005	-1.85	280.07	76-105	
	27	2.641	-.08502	-1.84	280.09	76-150	7.34
	Ott 10	2.750	-.08652	-1.80	282.50	49-79	5.15
	Ott 18	2.812	-.08728	-1.78	283.81	(42- 68)" (77-163)'	4.78
	19	2.821	-.08739	-1.78	283.99	(91-157)"	4.71
	Nov 4	2,939	-.08865	-1.73	286.37	42-161	4.93
	19	3.056	-.08969	-1.68	288.63	43-173	2.62
	Dec 4	3.163	-.09046	-1.64	290.61	42-170	2.90
	19	3.269	-.09104	-1.60	292.47	40-170	5.15

Log of Pioneer 10 cruise phase observations - continued.

Year	Calendar Date	Sun-S/C Distance (Au)	S/C Distance from ecliptic[a] (AU)	Heliocentric $\beta_{S/C}$	$\lambda_{S/C}$ (deg)	Usable LA[b] Range (deg)	Signal/ Noise
1973	Jan 5	3.38-t	-.09150	-1.55	294.44	38-115	3.50
	8	3.404	-.09155	-1.54	294.77	109-163	2.71
	Feb 1	3.560	-.09180	-1.48	297.32	67-144	4.96
	13	3.805	-.09146	-1.38	301.10	(152-170)”	5.59
	Mar 3	3.927	-.09095	-1.33	302.92	128-137	4.21
						148-170	
	28	4.065	-.09009	-1.27	304.92	91-128	6.68
						154-170	
	May 29	4.226	-.08868	-1.20	307.21	38-170	6.71
	June 7	4.273	-.08818	-1.18	307.88	91-121	6.59
	Aug 4	4.545	-.08449	-1.07	311.66	91-170	5.53
	6	4.553	-.08434	-1.06	311.78	38-94	4.96
	25	4.636	-.08289	-1.02	312.92	38-145	6.31
	Ott 6	4.812	-.07924	-0.94	315.34	38-148	5.12
						164-169	
	2 6	4.892	-.07730	-0.91	316.41	38-115	5.53
						128-170	
1974	Jan 21	5.084	-.03264	-0.36	325.43	38-170	4.18
	Mar 9	5.152	-.00128	0.00	332.08	38-170	4.15
	Apr 21	5.253	+.03021	+0.33	338.05	38-109	4.06
	22	5.254	+.03033	+0.33	338.07	111-170	4.46
	June 25	5.466	+.07531	+0.79	346.36	40-152	4.34
			+			168-170	
	Aug 31	5.748	+.12004	+1.20	354.15	38-170	5.18
	Ott 28	6.042	+.15838	+1.50	0.31	38-168	12.40
1975	Jan 28	6.576	+.21749	+1.90	8.83	47-77	3.90
						100	
						147-167	
	Mar 28	6.953	+.25429	+2.10	13.57	42-91	3.09
						103-170	
	May 21	7.137	+.28729	+2.25	17.47	109-170	4.81
	30	7.378	+.29265	+2.27	18.07	37-114	4.46
						124-132	
						143-170	
	July 27	7.787	+.32721	+2.41	21.77	46152	4.21
	Sept 30	8.261	+.36524	+2.53	25.49	35-168	5.25
	Nov 28	8.704	+.39919	+2.63	28.53	35-68	3.06
						94-109	
						122-126	
						135-169	
1976	Jan 30	9.182	+.43440	+2.71	31.41	42-127	2.40
						135-170	

“positive values mean a location of the spacecraft north of the ecliptic plane.
[b]LA = look angle = angle measured from the spin axis.
‘approximately 1/2 of the data are lost due to low data rate and other factors

higher spatial resolution than would have been possible to obtain with a single map or with observations from a single spacecraft (S/C). Further, Pioneer 11 obtained 12 additional maps between November 1981 and December 1982 to “fill in” the aforementioned sky gap regions.

The instantaneous field of view of each IPP was approximately 2.3° square. Brightness was integrated for $1/64^{th}$ (one sector) of the 12.5 s spacecraft spin period, giving a maximum effective FOV of 2.3° $\times$ 7.9° when the telescope was perpendicular to the spin axis (LA=90°). The spin axis was directed more or less toward the sun. By moving the IPP telescope in steps of 1.8” in look angle, the entire sky between 29° and 170° from the spin axis could be scanned. The spinning, sectoring and stepping resulted in a two-dimensional overlapping pattern of FOV’S on the sky for each map (see Figure 67). Since the spin axis moved slowly on the celestial sphere according to the moving spacecraft position, most of the sky was

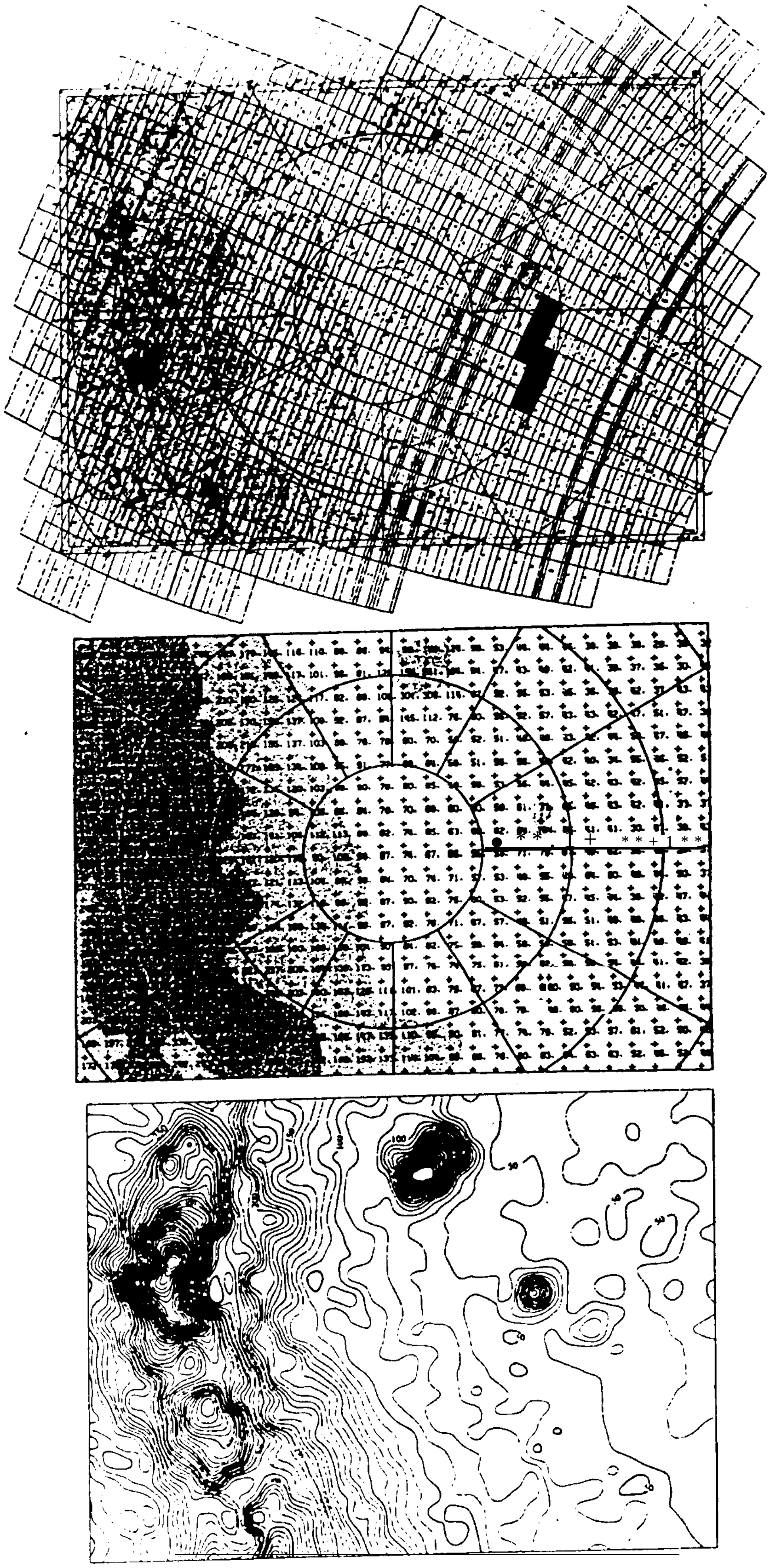

Fig. 67. Example for Pioneer data in the blue (440 nm), from a sky map observed beyond 3 AU. Upper panel: Map of the Becvar atlas showing part of the southern Milky Way and the Magellanic clouds, with the sectored field-of-view of Pioneer 10 overlaid. Middle panel: Brightness values in $S10_\odot$ units interpolated from the individual sector brightnesses to a rectangular coordinate grid. Lower panel: Isocontour map constricted from this set of brightnesses.

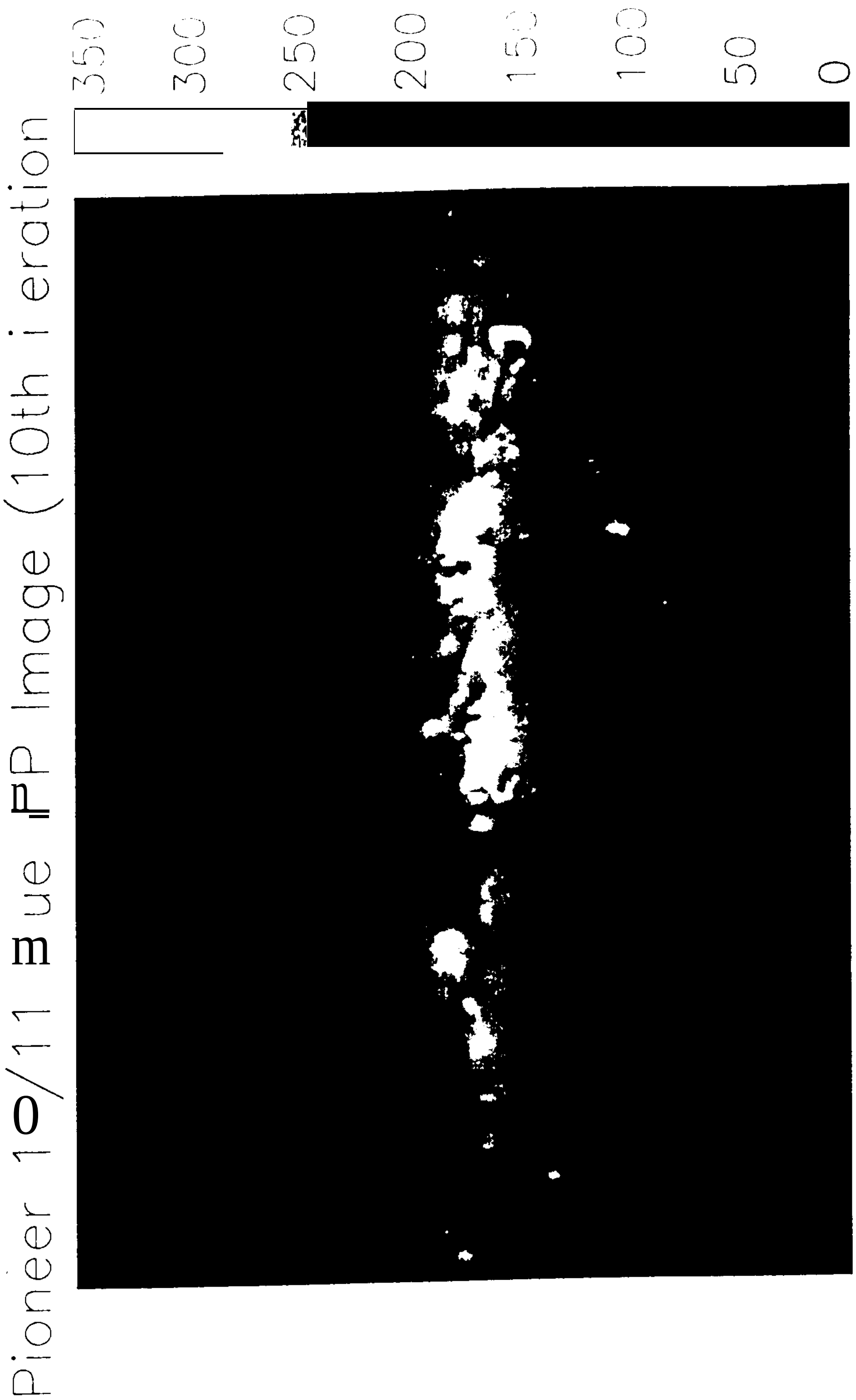

Fig. 68. Pioneer 10/11 blue sky map at 440 nm at 0.5° resolution, constructed from Pioneer 10 and Pioneer 11 maps taken at 3.26 AU to 5.15 AU heliocentric distance. The map is in Aitoff projection. The galactic center is at the center. From Gordon 1997

Table 34. Brightnesses of background starlight and integrated starlight at the north and south celestial, ecliptic, and galactic poles (in $S10_\odot$ units). Stars with $m_V < 6.5$ excluded. Adapted from Toller et al. 1987.

Effective Wavelength (Å)	U	V	4407	B	4280	4300	B	Pg 4250	B 4400	Palomar Blue 4150	Palomar Red 6440	64
Investigation (Year)	Hoffmann et al. 1997		Pioneer 10 (1978)	Elsässer and Haug (1960)	Lillie (1968)	Classen (1976)	Kimeswenger et al 1993	Roach and Megill (1961)	Sharov and Lipaeva (1973)	Tanabe (1973)	Tanabe (1973)	Pio (1)'
Method	Photometries							Starcounts				Photo
NCP			56	<95	56			48	37	48	76	..
NEP			66	<95	98			52	50	66	76	82
NGP			29		27	22		24	2[illegible]	26	41	3.
SCP	52	86	74	<95		58	55	56	41			94
SEP	61	106	128	124		87	67	50	39			12
SGP	26		33	27	28	23	53	79	36			

eventually covered with a resolution better than the 1.8° roll-to-roll separation of FOV's in a single map.

The data reduction methodology is described in a User's Guide (Weinberg and Schuerman 1981) for the Pioneer 10 and Pioneer 11 IPP data archived at the National Space Science Data Center (NSSDC). Signals of bright stars were used to calibrate the decaying sensitivity of the IPP channels. Individually resolved stars, typically those brighter than 6.5 mag, were removed from the measured brightnesses on the basis of a custom made catalog containing 12457 stars. The absolute calibration was based on the instrument's response to Vega. Finally, the Pioneer 10 and 11 blue and red data were represented in $S10_\odot$ units. The result is a background sky tape, which, for the data beyond 2.S AU, contains the integrated starlight, including the contribution from the diffuse galactic light. A more complete description of the reduction and use of the data is being prepared (Weinberg et al. 1997).

The background sky data set can be addressed in a variety of ways, including overlaying the data on a sky atlas such as Becvar's Atlas Coeli (1962), interpolating the posted data on an evenly spaced coordinate grid, and contouring the data. Each of these is shown in the three panels of Figure 67, all covering the south celestial pole region, which includes low galactic latitude regions and both the Small and Large Magellanic Clouds. The map scale and magnitude limit of the Atlas Coeli make this atlas convenient for illustrating and manipulating Pioneer background sky data. The upper panel in Figure 67 shows a single Pioneer 10 map's pattern of FOV's overlaid to the corresponding region of the Becvar atlas. The map shows the overlap in both look angle and sector (day 68 of year 1974, observed at R=5. 1.5 AU). The middle panel shows the result of interpolating the data for six map days of observations in blue on an evenly spaced coordinate grid for the same region of sky. We estimate that the random error in the numbers shown in the middle panel is 2 to 3 $S10_\odot$ units, and perhaps 5 units in the Milky Way and the Magellanic clouds. An isophote representation of the data (lower panel) is perhaps the most convenient way to present the data. The interval between isophotes is 5 $S10_\odot$ units. The spatial resolution was found to be approximately 2°. Regularly celestial spaced grid values of Pioneer 10 blue and red brightnesses were determined in this manner for the entire sky, from which data were derived every two degrees both in galactic and equatorial coordinates. Part of these data are used in Tables 35 to 38 to depict Pioneer 10 blue and red data at 10° intervals in both coordinate systems. Pioneer 11 data showed no significant differences to Pioneer 10 data, so only Pioneer 10 data are discussed and shown here.

More recently, Gordon (1997) further analyzed Pioneer 10 and 11 data from beyond the asteroid belt. He found no significant differences between the Pioneer 10 and 11 data. His grey scale presentation of the combined data with 0.5° spatial resolution is shown in an Aitoff projection in Figure 68. The gap in this figure corresponds to that discussed earlier. Gordon did not have available those special data sets closing the gap.

From the Pioneer data, blue and red brightnesses at the celestial, ecliptic and galactic poles *were* derived from isophote maps of the polar regions like the one shown for the south celestial pole in Figure 67. They are compared with other photometric data and with star counts in Table 34. There is fair agreement among the photometries. However, because of the lack of atmospheric and interplanetary signals in the Pioneer data, these data should be preferred over the other photometries when determining the level of galactic light in a certain region. Generally che photometries are at higher levels than the star counts, as one would expect. since the photometries contain the contributions of diffuse galactic light (section 11) and extragalactic background light (section 12). Equal numbers for the brightnesses in the blue and the red shown in Table 34 would mean that the galactic component of the night sky brightness has solar colour. The Pioneer data show a reddening at the poles, and this reddening appears all over

Table 37. Pioneer 10 background starlight in blue (440 nm), in equatorial coordinates and $S10_{\odot}$ units. From Toller(1981).

α	declination β																								
(°)	-80	-70	-60	-50	-40	-30	-24	-20	-16	-12	-8	-4	0	4	8	12	16	20	24	30	40	50	60	70	80
0	53	49	44	38	36	32	28	30	25	34	34	33	36	43	39	41	41	49	51	67	93	166	234	112	96
10	55	61	36	33	30	29	30	26	25	26	34	32	32	33	36	36	39	44	46	58	94	145	208	121	92
20	61	56	47	39	30	26	30	29	35	35	35	34	34	37	38	39	43	46	49	60	88	140	192	121	90
30	62	42	47	42	32	27	34	28	33	34	32	39	37	37	43	40	45	46	54	64	85	153	202	98	88
40	57	48	39	36	31	31	33	35	34	36	36	41	43	41	40	44	47	51	52	67	113	145	167	101	82
50	54	49	44	36	35	35	34	35	38	40	43	43	51	44	44	51	55	58	67	67	115	128	143	98	87
60	58	59	42	42	38	40	41	46	40	49	53	54	60	59	58	71	64	73	82	83	96	136	122	96	92
70	68	108	56	49	47	46	54	52	50	62	72	69	76	83	76	73	67	72	65	66	131	108	104	102	88
80	73	319	60	61	50	52	68	71	86	94	126	134	117	115	111	116	113	124	87	121	195	134	84	94	76
90	75	204	77	94	76	84	96	112	119	114	125	126	132	139	167	200	192	185	196	184	143	116	82	82	68
100	79	79	96	110	121	150	164	240	241	221	194	227	223	240	217	213	190	192	174	165	118	91	87	75	65
110	85	86	120	143	159	277	286	299	261	254	262	247	208	180	160	139	129	116	111	97	76	80	66	60	61
120	94	124	161	233	239	320	290	245	206	170	144	146	145	143	131	-	-	-	-	75	62	48	54	60	58
130	93	160	209	263	226	211	146	123	120	-	-	-	-	-	-	-	-	-	-	-	53	50	45	56	57
140	99	192	313	214	183	125	102	84	86	71	69	-	-	-	-	-	-	-	-	-	-	45	40	51	57
150	110	194	433	255	141	91	73	72	75	59	56	59	63	61	67	-	-	-	-	-	-	48	42	48	51
160	109	205	718	197	121	75	60	56	53	57	47	51	51	55	59	68	66	57	50	45	46	39	43	39	46
170	108	226	573	176	102	65	63	56	44	46	46	45	52	55	53	49	50	44	40	36	36	33	44	40	50
180	114	269	459	173	91	61	52	52	44	46	44	46	41	42	36	41	39	29	32	30	30	36	33	40	51
190	116	264	252	163	88	61	53	47	45	43	41	40	28	36	37	35	32	32	32	25	30	26	36	43	50
200	115	286	385	184	101	58	56	51	53	56	48	39	34	37	31	29	34	31	26	27	31	28	33	39	46
210	121	243	384	182	115	76	56	54	49	47	45	36	36	36	35	33	37	36	30	28	33	42	33	41	45
220	126	241	331	189	136	86	73	63	54	49	50	42	42	36	39	40	29	36	34	28	31	34	36	41	49
230	122	245	321	295	161	88	83	70	71	60	51	48	49	43	42	42	39	34	40	31	36	35	42	43	50
240	114	217	350	211	143	148	140	110	75	71	65	61	56	52	48	54	44	44	41	37	40	41	42	51	48
250	101	182	278	312	247	204	142	88	84	74	72	68	73	70	63	59	58	59	52	45	53	42	50	55	52
260	95	140	216	321	291	248	145	180	165	98	76	65	78	84	88	82	81	71	68	63	58	56	53	62	57
270	90	125	158	217	438	641	330	235	214	122	88	85	133	160	129	121	114	114	97	97	80	72	63	76	61
280	85	95	115	159	195	274	241	287	269	220	215	136	103	142	217	209	159	152	147	139	122	81	83	71	67
290	81	91	89	100	102	143	164	192	187	171	166	147	184	199	190	145	143	136	186	270	194	134	94	77	76
300	79	80	72	79	80	94	86	92	102	99	113	99	125	158	188	228	248	269	198	264	307	191	126	83	80
310	73	80	69	59	60	71	66	74	79	71	84	82	86	103	116	122	135	168	188	202	214	189	130	93	79
320	70	63	56	55	46	55	58	56	59	63	63	61	66	74	78	78	93	91	104	141	212	213	151	116	82
330	63	62	49	48	41	45	49	44	47	42	52	54	60	53	57	63	66	73	82	102	144	301	171	126	89
340	55	55	41	39	39	38	39	37	43	43	43	39	47	54	48	47	55	57	64	86	130	233	162	131	92
350	55	46	44	32	34	32	38	35	38	39	37	42	40	43	42	38	52	54	61	67	95	169	174	114	95

Table 34. Brightnesses of background starlight and integrated starlight at the north and south celestial, ecliptic, and galactic poles (in $S10_{\odot}$ units). Stars with $m_V < 6.5$ excluded. Adapted from Toller et al. 1987.

Effective Wavelength (A)	U	v	4407	B	4280	4300	B	P.g. 4250	B 4400	Palomar Blue '41s0	Palomar Red 6440	641
Investigation (Year)	Hoffmann et al. 1997		Pioneer 10 (1978)	Elsässer and Haug (1960)	Lillie (1968)	Classen (1976)	Kimeswenger et al. 1993	Roach and Megill (1961)	Sharov and Lipaeva (1973)	Tanabe (1973)	Tanabe (1973)	Pion. 10 (197
Method	Photometries							Star counts				Photon
NCP			56	<95	56			48	37	48	76	77
NEP			66	<95	98			52	50	66	76	82
NGP			29		27	22		24	21	26	41	31
SCP	52	86	74	<95		58	.55	56	41			94
SEP	61	106	128	124		87	67	50	39			125
SGP	26		33	27	28	23	53	79	36			

eventually covered with a resolution better than the 1.8° roll-to-roll separation of FOV's in a single map.

The data reduction methodology is described in a User's Guide (Weinberg and Schuerman 1981) for the Pioneer 10 and Pioneer 11 IPP data archived at the National Space Science Data Center (NSSDC). Signals of bright stars were used to calibrate the decaying sensitivity of the IPP channels. Individually resolved stars, typically those brighter than 6.5 mag, were removed from the measured brightnesses on the basis of a custom made catalog containing 12457 stars. The absolute calibration was based on the instrument's response to Vega. Finally, the Pioneer 10 and 11 blue and red data were represented in $S10_{\odot}$ units. The result is a background sky tape, which, for the data beyond 2.8 AU, contains the integrated starlight, including the contribution from the diffuse galactic light. A more complete description of the reduction and use of the data is being prepared (Weinberg et al. 1997).

The background sky data set can be addressed in a variety of ways, including overlaying the data on a sky atlas such as Becvar's Atlas Coeli (1962), interpolating the posted data on an evenly spaced coordinate grid, and contouring the data. Each of these is shown in the three panels of Figure 67, all covering the south celestial pole region, which includes low galactic latitude regions and both the Small and Large Magellanic Clouds. The map scale and magnitude limit of the Atlas Coeli make this atlas convenient for illustrating and manipulating Pioneer background sky data. The upper panel in Figure 67 shows a single Pioneer 10 map's pattern of FOV's overlaid to the corresponding region of the Becvar atlas. The map shows the overlap in both look angle and sector (day 68 of year 1974, observed at R=5.15 AU). The middle panel shows the result of interpolating the data for six map days of observations in blue on an evenly spaced coordinate grid for the same region of sky. We estimate that the random error in the numbers shown in the middle panel is 2 to 3 $S10_{\odot}$ units, and perhaps 5 units in the Milky Way and the Magellanic clouds. An isophote representation of the data (lower panel) is perhaps the most convenient way to present the data. The interval between isophotes is 5 $S10_{\odot}$ units. The spatial resolution was found to be approximately 2°. Regularly celestial spaced grid values of Pioneer 10 blue and red brightnesses were determined in this manner for the entire sky, from which data were derived every two degrees both in galactic and equatorial coordinates. Part of these data are used in Tables 35 to 38 to depict Pioneer 10 blue and red data at 10° intervals in both coordinate systems. Pioneer 11 data showed no significant differences to Pioneer 10 data, so only Pioneer 10 data are discussed and shown here.

More recently, Gordon (1997) further analyzed Pioneer 10 and 11 data from beyond the asteroid belt. He found no significant differences between the Pioneer 10 and 11 data. His grey scale presentation of the combined data with 0.5° spatial resolution is shown in an Aitoff projection in Figure 68. The gap in this figure corresponds to that discussed earlier. Gordon did not have available those special data sets closing the gap.

From the Pioneer data, blue and red brightnesses at the celestial, ecliptic and galactic poles were derived from isophote maps of the polar regions like the one shown for the south celestial pole in Figure 67. They are compared with other photometric data and with star counts in Table 34. There is fair agreement among the photometries. However, because of the lack of atmospheric and interplanetary signals in the Pioneer data, these data should be preferred over the other photometries when determining the level of galactic light in a certain region. Generally the photometries are at higher levels than the star counts, as one would expect, since the photometries contain the contributions of diffuse galactic light (section 11) and extragalactic background light (section 12). Equal numbers for the brightnesses in the blue and the red shown in Table 34 would mean that the galactic component of the night sky brightness has solar colour. The Pioneer data show a reddening at the poles, and this reddening appears all over

Table 37. Pioneer 10 background starlight in blue (440 rim), in equatorial coordinates and $S10_{\odot}$ units. horn Toller(1981).

α (°)	declination β .0	-70	-60	-50	-40	-30	-24	-20	-16	-12	-8	-4	0	4	8	12	16	20	24	30	40	50	60	70	80
0	3	49	44	38	36	32	28	30	25	34	34	33	36	43	39	41	41	49	51	67	93	166	234	112	96
10	5	61	36	33	30	29	30	26	25	26	34	32	32	33	36	36	39	44	46	58	94	145	208	121	92
20	1	56.	47	39	30	26	30	29	35	35	35	34	34	37	38	39	43	46	49	60	88	140	192	121	90
30	2	42	47	42	32	27	34	28	33	34	32	39	37	37	43	40	45	46	54	64	85	153	202	98	88
40	7	48	39	36	31	31	33	35	34	36	36	41	43	41	40	44	47	51	52	67	113	145	167	101	82
50	4	49	44	36	35	35	34	35	38	40	43	43	51	44	44	51	55	58	67	67	115	128	143	98	87
60	.8	59	42	42	38	40	41	46	40	49	53	54	60	59	58	71	64	73	8“	83	96	136	122	96	92
70	18	108	56	49	47	46	54	52	50	62	72	69	76	83	76	73	67	72	65	66	131	108	104”	102	88
80	‘3	319	60	61	50	52	68	71	86	94	126	134	117	115	111	116	113	124	87	121	195	134	84	94	76
90	‘5	204	77	94	76	84	96	112	119	114	125	126	132	139	167	200	192	185	196	184	143	116	82	82	68
1 00	‘9	79	96	110	121	150	164	240	241	221	194	227	223	240	217	213	190	192	174	165	118	91	87	75	65
110	35	86	120	143	159	277	286	299	261	254	262	247	208	180	160	,139	129	116	111	97	76	80	66	60	61
1 20	)4	1’24	161	233	239	320	290	245	206	170	144	146	145	143	131	-	-	-	-	75	62	48	54	60	58
130	)3	160	209	263	226	211	146	123	120	-	-	–	–	–		--		--	--	53	50	45	56		57
140	)9	192	313	214	183	125	102	84	86	71	69	-	-	-	-	-	-	-	-	-	-	45	40	51	57
150	10	194	433	255	141	91	73	72	75	59	56	59	63	61	67	-’-	-	-	-	-	48	42	48		51
160	09	2U5	718	197	121	75	60	56	53	57	47	51	51	55	59	68	66	57	50	45	46	39	43	39	46
170	08	226	573	176	102	65	63	56	44	46	46	45	52	55	53	49	50	44	40	36	36	33	44	40	50
180	14	269	459	173	91	61	52	52	44	46	44	46	41	42	36	41	39	29	32	30	30	36	33	40	51
190	16	264	252	163	88	61	53	47	45	43	41	40	28	36	37	35	32	32	32	25	30	26	36	43	50
200	115	286	385	184	101	58	56	51	53	56	48	39	34	37	31	29	34	31	26	27	31	28	33	39	46
210	121	243	384	182	115	76	56	54	49	47	45	36	36	36	35	33	37	36	30	28	33	42	33	41	45
220	126	241	331	189	136	86	73	63	54	49	50	42	42	36	39	40	29	36	34	28	31	34	36	41	49
230	122	245	321	295	161	88	83	70	71	60	51	48	49	43	42	4’2	39	34	40	31	36	35	42	43	50
240	114	217	35U	211	143	148	140	110	75	71	65	61	56	52	48	54	44	44	41	37	40	41	42	51	48
250	104	182	278	312	247	204	142	88	84	74	72	68	73	70	63	59	58	59	52	45	53	42	50	55	52
260	95	140	216	321	291	248	145	180	165	98	76	65	78	84	88	82	81	71	68	63	58	56	53	62	57
270	90	125	158	217	438	641	330	235	214	122	88	85	133	160	129	121	114	114	97	97	80	72	63	76	61
280	85	95	115	159	195	274	241	287	269	220	215	136	103	142	217	209	159	152	147	139	122	81	83	71	67
290	81	91	89	100	102	143	164	192	187	171	166	147	184	199	190	145	143	136	186	270	194	134	94	77	76
300	79	80	72	79	80	94	86	92	102	99	113	99	125	158	188	228	248	269	198	264	307	191	126	83	80
310	73	80	69	59	60	71	66	74	79	71	84	82	86	103	116	122	135	168	188	202	214	189	130	93	79
320	70	63	56	55	46	55	’58	56	59	63	63	61	66	74	78	78	93	91	104	141	212	213	151	116	82
330	63	62	49	48	41	45	49	44	47	42	52	54	60	53	57	63	66	73	82	102	144	301	171	126	89
340	55	55	41	3(J	39	38	39	37	43	43	43	39	47	54	48	47	55	57	64	86	130	233	162	131	92
350	55	46	44	32	34	32	38	35	38	39	37	42	40	43	42	38	52	54	61	67	95	169	174	114	95

Table 36. Pioneer 10 background starlight in red (640 urn), given in galactic coordinates and SIO_o units. From Toller(1981).

l (°)	-80	-70	-60	-50	-40	-30	-24	-20	-16	-12	-8	-4	0	4	8	12	16	20	24	30	40	50	60	70	80
	galactic latitude b																								
0	12	48	52	57	67	106	143	152	245	461	801	1306	593	442	375	310	153	125	130	96	65	52	44	56	37
10	18	40	62	63	78	99	153	181	233	337	563	734	537	508	444	246	148	135 .	110	79	81	56	44	44	3-t
20	15	56	53	57	73	110	133	181	230	328	404	556	342	264	182	159	150	121	95	91	69	51	47	49	33
30	10	40	42	59	65	94	128	152	191	244	288	395	258	165	191	226	190	148	116	8 6	6 4	4 7	4 0	4 9	3 5
40	11	51	48	52	76	88	130	148	165	224	307	359	200	333	339	242	185	139	123	85	58	48	42	44	34
50	13	39	49	59	70	118	126	156	185	243	307	419	287	349	278	211	176	139	106	93	60	47	44	37	33
60	10	38	54	51	79	109	1'23	138	176	249	335	411	338	361	306	221	166	128	116	84	60	47	41	32	36
70	37	42	50	54	70	96	116	123	166	223	290	292	403	488	319	218	183	135	107	85	69	51	35	43	36
80	39	42	44	63	55	86	108	133	158	215	310	323	284	309	296	2X6	172	118	103	76	53	42'	44	38	37
90	17	45	45	59	56	78	90	123	147	186	259	343	330	240	265	206	151	113	98	78	56	52	44	39	38
100	16	45	52	42	65	83	97	118	164	188	280	394	342	270	212	165	138	98	82	79	58	47	45	42	38
110	41	50	45	46	57	79	88	118	146	182	244	289	248	216	189	166	122	99	94	75	58	49	51	33	37
120	40	41	44	50	60	73	101	134	149	192	219	248	'276	202	154	157	120	113	100	77	49	43	42	36	33
130	38	44	35	50	53	81	92	107	134	172	217	273	250	205	146	132	123	114	94	72	55	41	40	34	30
140	35	45	33	51	57	81	93	104	139	160	186	172	197	198	149	119	132	104	88	62	62	60	43	36	33
150	35	40	42	63	58	64	97	109	142	165	189	169	188	165	154	1'26	128	108	84	77	58	55	40	35	33
160	41	42	51	47	64	73	83	99	88	142	135	162	200	214	181	135	109	126	93	81	57	58	37	39	34
170	40	41	38	53	79	75	92	99	90	114	122	170	"238	213	176	156	127	113	109	69	54	59	51	48	36
180	37	45	46	53	70	88	85	105	120	138	112	143	219	230	191	157	135	103	97	73	71	-	52	50	36
190	34	46	43	47	70	83	90	92	123	145	187	214	225	254	216	179	127	113	106	-	-	-	56	52	36
200	34	40	37	50	60	76	105	124	154	176	211	254	271	238	203	179	129	127					56	50	36
210	36	40	48	59	61	101	129	147	169	163	225	234	293	254	202	169	148	-		–	–	–	57	50	35
220	36	36	41	49	60	81	100	130	146	158	210	259	309	283	204	176	-	-					60	51	41
230	35	37	39	43	58	77	96	131	156	230	276	285	296	282	220	157	-	-		–	–	66	58	51	41
240	30	38	42	46	58	72	106	104	163	210	279	329	355	310	246	160	-	-			66	70	68	54	36
250	33	36	39	48	57	75	94	115	160	205	267	314	344	339	252	159	139	119	114	73	63	72	65	53	34
260	38	40	4"	58	58	101	124	123	185	239	314	302	283	253	207	194	142	105	107	71	65	67	58	43	34
270	37	36	4-t	59	69	86	115	143	171	210	268	331	256	248	227	190	146	108	95	77	64	52	50	45	32
280	37	32	48	49	70	230	113	124	149	212	329	445	427	383	261	191	162	119	105	90	61	53	50	43	34
290	38	41	47	50	68	88	109	141	161	256	319	464	760	516	301	210	152	124	108	83	60	48	46	47	39
300	41	42	44	48	69	90	123	132	152	223	312	481	493	436	319	236	154	127	116	86	64	55	42	46	39
310	44	35	44	59	67	107	123	151	208	251	348	535	584	505	324	271	204	149	117	91	70	60	46	41	35
320	45	41	49	58	75	95	124	164	207	309	420	517	479	401	304	2"6	189	156	118	94	68	63	45	38	36
330	43	39	47	55	78	96	127	164	231	307	448	736	530	440	359	286	231	159	126	102	64	61	45	37	39
340	41	43	47	55	75	106	143	178	240	329	487	478	526	331	219	241	190	131	124	102	78	54	49	43	42
350	38	41	53	68	88	105	151	189	'260	366	575	617	460	526	382	415	283	161	145	108	68	55	43	45	41

Table **37.** Pioneer 10 background **starlight** in **blue** (440 mu), in equatorial coordinates and $S10_0$ **units. From Toller(1981)**

α (°)	declination β 80	-70	-60	-50	-40	-30	-24	-20	-16	-12	-8	-4	0	4	8	12	16	20	24	30	40	50	60	70	80
0	53	49	44	38	36	32	28	30	25	34	34	33	36	43	39	41	41	49	51	67	93	166	234	112	96
10	55	61	36	33	30	29	30	26	25	26	34	32	32	33	36	36	39	44	46	58	94	145	208	121	92
20	51	56	47	39	30	26	30	29	35	35	35	34	34	37	38	39	43	46	49	60	88	140	192	1'21	90
30	52	42	47	42	32	27	34	28	33	34	32	39	37	37	43	40	45	46	54	64	85	153	202	98	88
40	57	48	39	36	31	31	33	35	34	36	36	41	43	41	40	44	47	51	52	67	113	145	167	101	82
50	54	49	44	36	35	35	34	35	38	40	43	43	51	44	44	51	55	58	67	67	115	128	143	98	87
60	58	59	42	42	38	40	41	46	40	49	53	54	60	59	58	71	64	73	82	83	96	136	122	96	92
70	58	108	56	49	47	46	54	52	50	62	72	69	76	83	76	73	67	72	65	66	131	108	104	102	88
80	73	319	60	61	50	52	68	71	86	94	126	134	117	115	111	116	113	124	87	121	195	134	84	94	76
90	75	204	77	94	76	84	96	112	119	114	125	126	132	139	167	200	192	185	196	184	143	116	82	82	68
100	79	79	96	110	121	150	164	240	241	221	194	227	223	240	217	213	190	192	174	165	118	91	87	75	65
110	85	86	120	143	159	277	286	299	261	254	262	247	208	180	160	139	129	116	111	97	76	8(I	66	60	61
120	94	124	161	233	239	320	290	245	206	170	144	146	145	143	131	-	-	-	-	-	75	62	48	54	60	58
130	93	160	209	263	226	211	146	123	120	-	-	-	-	-	-	-	-	-	-	-	53	50	45	56	57
140	99	192	313	214	183	125	102	84	86	71	69	-	-	-	-	-	-	-	-	-	-	45	40	51	57
15U	110	194	433	255	141	91	73	72	75	59	56	59	63	61	67	-	-	-	-	-	-	48	42	48	51
160	109	205	718	197	121	75	60	56	53	57	47	51	51	55	59	68	66	57	50	45	46	39	43	39	46
17U	108	2'26	573	176	102	65	63	56	44	46	46	45	52	55	53	49	50	44	40	36	36	33	44	40	50
181	114	269	459	173	91	61	52	52	44	46	44	46	41	42	36	41	39	29	32	30	30	36	33	40	51
19(	116	264	252	163	88	61	53	47	45	43	41	40	28	36	37	35	32	32	32	25	30	26	36	43	50
20(	115	286	385	184	101	58	56	51	53	56	48	39	34	37	31	29	34	31	26	27	31	28	33	39	46
21(	121	243	384	182	115	76	56	54	49	47	45	36	36	36	35	33	37	36	30	28	33	42	33	41	45
22(	126	241	331	189	136	86	73	63	54	49	50	42	42	36	39	40	29	36	34	28	31	34	36	41	49
23(	122	'245	321	295	161	88	83	70	71	60	51	48	49	43	42	42	39	34	40	31	36	35	42	43	50
24(	114	217	350	211	143	148	140	110	75	71	65	61	56	52	48	54	44	44	41	37	40	41	42	51	48
25(	1(J4	182	278	312	247	204	142	88	84	74	72	68	73	70	63	59	58	59	52	45	53	42	50	55	52
26(	95	140	216	321	291	248	145	180	165	98	76	65	78	84	88	82	81	71	68	63	58	56	53	62	57
27(	90	125	158	217	438	641	330	235	214	122	88	85	133	160	129	121	114	114	97	97	80	72	63	76	61
28(	85	95	115	159	195	274	241	287	269	220	215	136	103	142	217	209	159	152	147	139	122	81	83	71	67
29(	81	91	89	100	102	143	164	192	187	171	166	147	184	199	190	145	143	136	186	270	194	134	94	77	76
30(	7(J	80	72	79	80	94	86	92	102	99	113	99	125	158	188	228	248	269	198	264	307	191	126	83	80
31(	73	80	69	5(J	60	71	66	74	79	71	84	82	86	103	116	122	135	168	188	202	214	189	130	93	79
32(	70	63	56	55	46	55	58	56	59	63	63	61	66	74	78	78	93	91	104	141	212	213	151	116	82
33	63	62	49	48	41	45	49	44	47	42	52	54	60	53	57	63	66	73	82	102	144	301	171	126	89
34	55	55	41	39	39	38	39	37	43	43	43	39	47	54	48	47	55	57	64	86	130	233	162	131	92
35	55	46	44	32	34	32	38	35	38	39	37	42	40	43	42	38	52	54	61	67	95	169	174	114	95

G-1

Table S8. Pioneer 10 background **starlight** in red (640 rim), in equatorial **coordinates** and $S10_\odot$ **units. From Toller(1981).**

α (°)	80	-70	-60	-50	-40	-30	-24	-20	-16	-12	-8	-4	0	4	8	12	16	20	24	30	40	50	60	70	80
0	58	55	55	56	49	35	39	40	38	42,	49	46	50	56	43	51	59	56	61	71	116	192	284	162	124
10	74	74	42	38	36	35	34	43	39	34	44	45	35	48	47	51	55	52	63	64 79	108 99	158	250	185	121
20	78	67	51	44	40	31	36	40,	39	39	43	38	32	53	45	40	56	58	67	82	97	187	265	176	106
30	?8	53	48	44	39	38	34	46	45	41	40	51	-43	47	64	.56	61	56	66					157	110
40	73	69	49	42	36	36	45	42	40	44.	45	48	53	49	59	54	61	62	60	74	116	177	240	150	109
50	72	63	56	41	48	50	44	41	44	51	49,	56	60	59	61	70	74	79	78	65	141	166	205	140	111
60	77	71	53	52	48	50	51	52	52	57	60	68	68	73	88	65	82	90	103	108	133	183	175	128	117
70	81	90	72	62	54	58	66	64	64	74	76.	75	87	82	93	95	112	122	102	104	189	164	161	137	103
80	81	341	64	72	64	63	80	84	98	115	134	131	-i36	135	135	125	146	143	130	179	.214	164	125	115	85
90	88	226	88	93	83	90	117	123	138	147	155	158	174	174	220	238	258	218	246	227	169	137	112	91	83
100	98	107	114	116	135	.176	193	248	240	248	225	253	273	280..	284	263	229	233	.207	210	145	119	108	77	84
110	102	111	141	182	218	315	331	321	297	312	295	267	.225,	206	182.	184	165	135	138	105	108	93	81	73	77
120	110	141	176	275	308	385	327	288	249	200	166-	178	173,	167’	“’	155	-	-	-	105.	,75	63	75	79	73
130	113	142	224	337	278	274	201		156		137	-	-	-	-	-	-	-	-	-	77	52	57	74	70
140	119	205	372	294	239	175	114		116		126		109	101	-	-	-	-	-	-	-	53,	57	80	65
150	116	244	490	334	193	120	104	85	72	68	65	65	66	67		68	-	-	-	-	-	52	55	57	55
160	116	265	846	250	156	100	75	74	62	65	57	68	71	71	65	62	59	60	58	55	52	46	52	46	49
170	141	308	744	229	116	88	76	59	63	61	66	52	55	60	68	66	58	52	52	50	60	36	51	54	52
180	145	340	632	230	99	78	61	61	57	58	54	56	54	54	41	47	50	31	45	38	37	43	45	38	52
190	137	335-	450	214	120	72	67	59	63	54	51	42	43’	55	45	41	‘41’”	36”	41’		3X37	35	42	50	51
200	145	410	565	262	115	91	77	59	53	58	51	49	44	48	40	34	39	42	38	36	34	37	45	50	58
210	154	351	516	256	144	95	73	68	66	.“71	58	52	47	50	49	44	57	44	40	40	40	43	43	48	59
220	153	337	559	284	173	102	87	81	80	77’-	54”	53	58	48	53	47	42.’.	47	54	38	35	44	40	54	61
230	156	310	538	481	249	134	110	88	97	79	77	62	,71	69	54	50	52	43	46	41	55	44	49	61	69
240	146	262	537	357	242	200	152	137	106	101	82	83	77	77	64	64	54	54	55	53	47	51	53	60	68
250	128	213	373	571	485	366	217	145	141	145	108	110	101	89	87	79	75	68	67	59	57	59	56	65	71
260	127	190	284	494	550	571	344	356	301	172	144	119	136	120.	123	119	116	90	85	89	81	66	64	78	75
270	115	155	205	284	626	1393	649	498	474	261	199	162	204	225	“201	166	157	148	132	120	94	96	73	82	76
280	101	106	150	191	262	461	481	534	542	515	509	343	.210	254	382	341	237..	’218	206	176	145	111	96	91	81
290	103	113	129	135	141	183	211	246	272	274	260	257	331	366	374	271	283	250	327	387	228	168	117	90	89
300	102	107	93	99	112	112	117	134	144	143.	162	149	178	215	237	323	366.,	407	316	421	403	245	163	102	93
310	93	88	78	80	77	81	89	85	89	91	91	109	128	138	145,	174	168	227	240	288	280	292	187	133	94
320	87	81	72	65	64	73	70	73	,72	77	100	75	85	93	.109	107	131	119	153	192	279	286	225	136	105
330	75	76	56	54	60	42	66	60	56”	67	67	63	81	78:	78	103	85	93	105	142	168	364	259	167	119
340	66	69	57	52	51	53	43	48	56	64	57	47	49	67	65	58	63	76	76	97	171	268	241	178	122
350	64	66	59	43	46	56	48	49	43”	50’	44”	47	62	48	55	59	61	69	72	84	104	203	256	“166	119

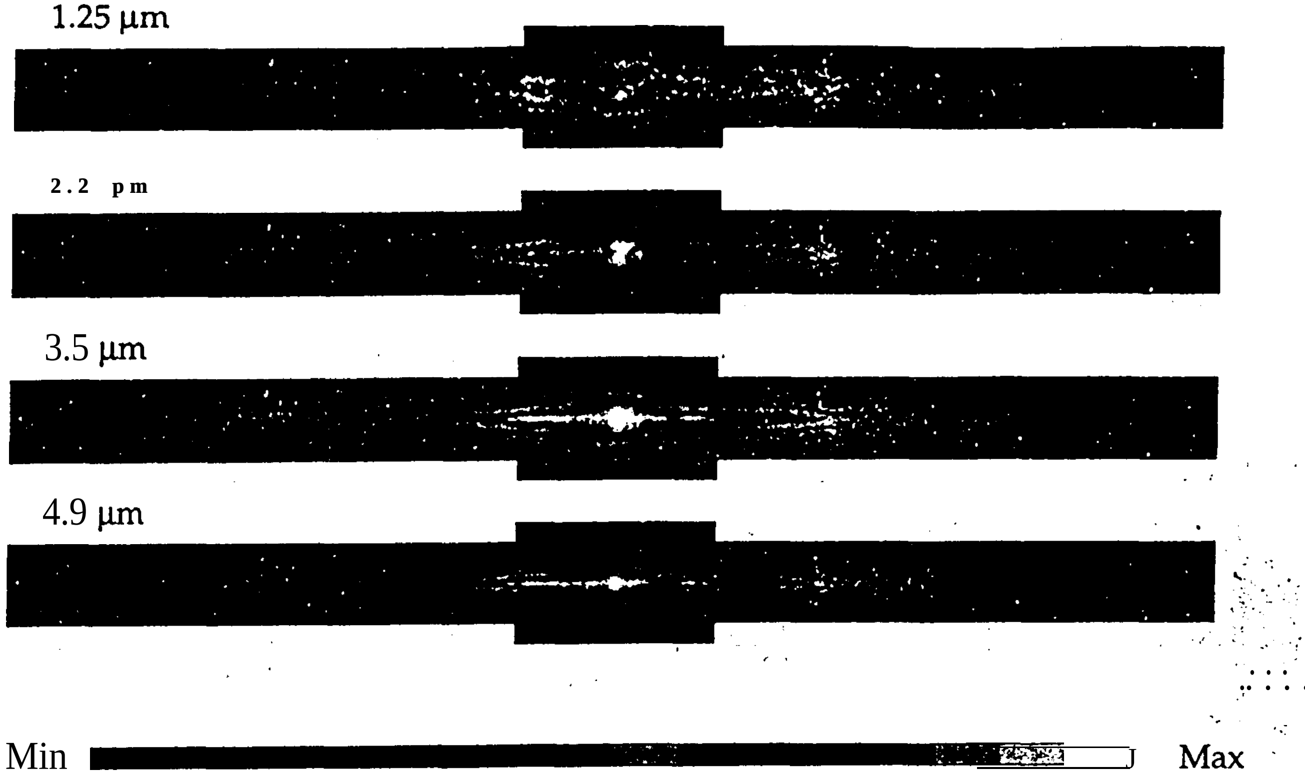

Fig. **71.** DIRBE maps of sky brightness at 1.25, 2.2, 3.5, and 4.9pm at low Galactic latitudes ($|b| \leq 15$ deg within 30 degrees of Galactic center, and $|b| \leq 10$ deg elsewhere). Zodiacal light has been removed. North is up, and galactic longitude is increasing from right to left. These maps are generally dominated by Galactic starlight. No extinction correction has been made. Intensities are provided at 16 levels on logarithmic scales ranging from 0.6 to 25 MJy/sr (1.25 μm and 2.2 μm), 0.4 to 16 MJy/sr (3.5 um), and 0.3 to 12.5 MJy/sr (4.9 urn). In detail these levels are: 0.63, 0.81, 1.03, 1.32, 1.69, 2.15, 2.75, 3.52, 4.50, 5.75, 7.36, 9.40, 12.02, 15.37, 19.65, and 25.12 MJy/sr at 1.25 μ and 2.2 μm; 0.40, 0.51, 0.65, 0.83, 1.06, 1.36, 1.74, 2.22, 2.84, 3.63, 4.64,'5.93, 7.59, 9.70, 12.40, and 15.85 MJy/sr at 3.5 pm; 0.32, 0.40, 0.52, 0.66, 0.84, 1.08, 1.38, 1.76, 2.26, 2.88, 3.69, 4.71, 6.03, 7.70,9.85, and 12.59 MJy/sr at 4.9 pm.

with the zodiacal light removed using the DIRBE zodiacal light model. Since starlight is the dominant source at low latitudes over this spectral range, these maps are a good approximation to the inbred stellar light, with extinction of course decreasing as wavelength increases. Corresponding maps at 12 microns and longer are not shown, because at these wavelengths interplanetary dust emission becomes the dominant contributor to sky brightness, and artifacts from imperfect removal of the zodiacal emission become more serious, as does the contribution from cirrus cloud emission. More elaborate modeling would be required to extract the stellar component of the sky brightness at these wavelengths. Figure 72 shows two sets of repesentative intensity profiles taken from the 1.25 μm - 4.9 μm approximate "starlight" maps: the first set on a constant-latitude line near the Galactic plane and the second along the zero-longitude meridian. FM-sky DIRBE maps at 1.25 μm, 2.2 μm, 3.5 μm, 4.9 pm, 12 μm, 25 pm, 60 μm, 100 μm, 140 μm, and 240 μm with the zodiacal light removed, from which these approximate starlight maps have been selected, are available as the 'Zodi-Subtracted Mission Average (ZSMA)' COBE data product, available from the NSSDC through the COBE homepage website at http://www.gsfc.nasa.gov/astro/cobe/cobe_home.html.

Model predictions for the integrated starlight, based on the galaxy model of Bahcall and Soneira(1980), were given for the near- and mid-infrared as function of the brightness of the individually excluded stars by Franceschini et al. (1991 b). Figures 73 and 74 show these results for wavelengths of 1.2 μm, 2.2 μm, 3.6 μm, and 12μm.

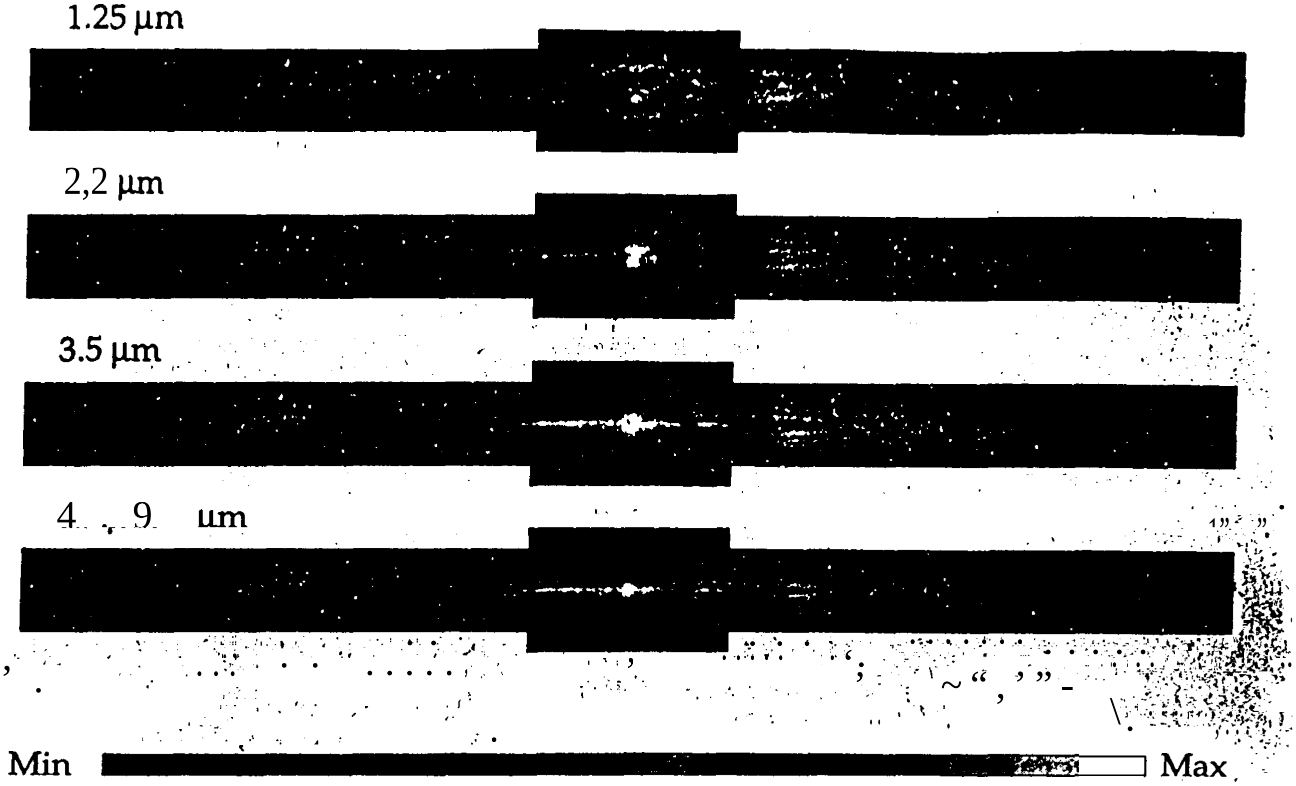

Fig. 71. DIRBE maps of sky brightness at 1.25, 2.2, 3.5, and 4.9pm at low Galactic latitudes ($|b| \leq$ 15 deg within 30 degrees of Galactic center, and $|b| \leq$ 10 deg elsewhere). Zodiacal light has been removed. North is up, and galactic longitude is increasing from right to left. These maps are generally dominated by Galactic starlight. No extinction correction has been made. Intensities are provided at 16 levels on logarithmic scales ranging from 0.6 to 25 MJy/sr (1.25 μm and 2.2 pm), 0.4 to 16 MJy/sr (3.5 urn), and 0.3 to 12.5 MJy/sr (4.9 urn). In detail these levels are: 0.63, 0.81, 1.03, 1.32, 1.69, 2.15, 2.75, 3.52, 4.50, 5.75, 7.36, 9.40, 12.02, 15.37, 19.65,and 25.12 MJy/sr at 1.25 μ and 2.2 μm; 0.40, 0.51, 0.65, 0.83, 1.06, 1.36, 1.74, 2.22, 2.84, 3.63, 4.64, 5.93, 7.59, 9.70, 12.40, and 15.85 MJy/sr at 3.5 μm; 0.32, 0.40, 0.52, 0.66, 0.84, 1.08, 1.38, 1.76, 2.26, 2.88, 3.69, 4.71, 6.03, 7.70, 9.85, and 12.59 MJy/sr at 4.9 pm.

with the zodiacal light removed using the DIRBE zodiacal light model. Since starlight is the dominant source at low latitudes over this spectral range, these maps are a good approximation to the infrared stellar light, with extinction of course decreasing as wavelength increases. Corresponding maps at 12 microns and longer are not shown, because at these wavelengths interplanetary dust emission becomes the dominant contributor to sky brightness, and artifacts from imperfect removal of the zodiacal emission become more serious, as does the contribution from cirrus cloud emission. More elaborate modeling would be required to extract the stellar component of the sky brightness at these wavelengths. Figure 72 shows two sets of repesentative intensity profiles taken from the 1.25 μm - 4.9 μm approximate "starlight" maps: the first set on a constant-latitude line near the Galactic plane and the second along the zero-longitude meridian. Full-sky DIRBE maps at 1.25 μm, 2.2 μm, 3.5 μm, 4.9 μm, 12 μm, 25 μm, 60 μm, 100 μm, 140 pm, and 240 μm with the zodiacal light removed, from which these approximate starlight maps have been selected, are available as the 'Zodi-Subtracted Mission Average (ZSMA)' COBE data product, available from the NSSDC through the COBE homepage website at http: //www.gsfc.nasa.gov/astro/cobe/cobe_home. html.

Model predictions for the integrated starlight, based on the galaxy model of Bahcall and Soneira(1980), were given for the near- and mid-infrared as function of the brightness of the individually excluded stars by Franceschini et al. (1991 b). Figures 73 and 74 show these results for wavelengths of 1.2 μm, 2.2 μm, 3.6 μm, and 12μm.

2.2 μm

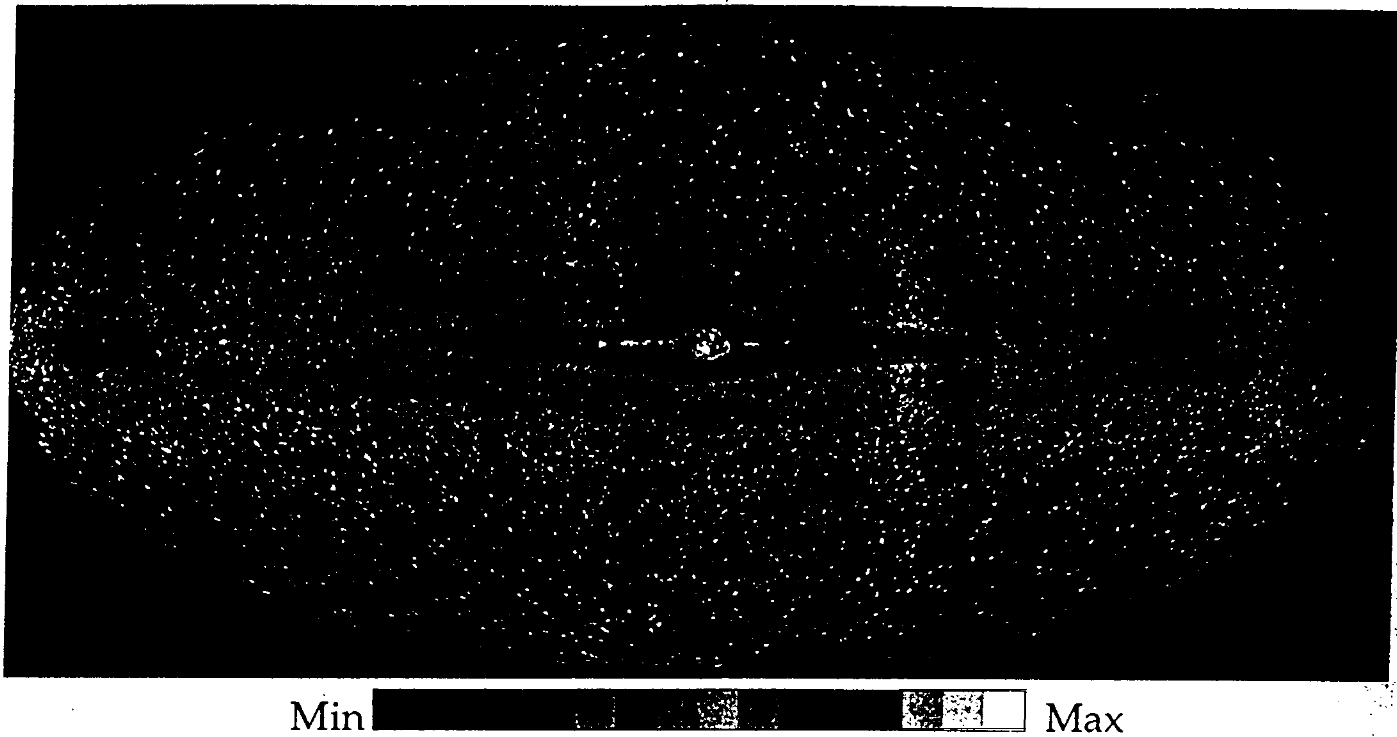

Fig. **70.** DIRBE map of sky brightness at 2.2 microns in galactic coordinates, with zodiacal light removed. North is up, the galactic center in the middle, and galctic longitude increasing from right to left. This map is dominated by galactic starlight. No extinction correction has been made. Intensities are provided at 16 levels on a logarithmic scale ranging from 0.04 to 32 MJy/sr. In detail these levels are: 0.040, 0.062, 0.097, 0.15, 0.24, 0.37, 0.57, 0.90, 1.40, 2.19, 3.41, 5.33, 8.32, 12.98, 20.26, and 31.62 MJy/sr.

10.5. Near- and mid-infrared

Maps of the starlight distribution in the infrared are difficult to obtain. There are currently no sensitive, all-sky, surveys of stars in the infrared, though the ground-based 2MASS and DENIS programs will provide that in the next several years. Extracting starlight maps from diffuse sky brightness measurements is challenging because of the need to separate the various contributions to the measured light. The COBE/DIRBE team has developed a detailed zodiacal light model which allows such a separation, at least in the near-infrared.

An all-sky image dominated by the stellar light of the Galaxy is presented in Figure 70. The map was prepared by averaging 10 months of DIRBE data at 2.2 μmwavelength after removal of the time-dependent signal from solar-system dust via a zodiacal light model. The remaining sky brightness at this wavelength is dominated by the cumulative light from K and M giants (Arendt et al. 1994), though individual bright sources can be detected at a level of about 15 Jy above the local background in unconfused regions. Although this map also contains small contributions from starlight scattered by interstellar dust (cirrus) and any extragalactic emission, these contributions are much smaller than that from stars. No extinction correction has been applied to the map in Figure 70; Arendt et al. (1994) found 2.2 μm optical depths greater than 1 within ≈3° of the Galactic plane for directions toward the inner Galaxy and bulge (—l—< 700). Arendt et al. used the multi-wavelength DIRBE maps to construct an extinction-corrected map over the central part of the Milky Way.

The typical appearance of the galactic stellar emission in the infrared the Milky Way is apparent in Fig. 70: because the interstellar extinction is much reduced in the infrared, this internal view of our Galaxy looks like a galaxy seen edge-on from the outside. Bulge and disk are clearly visible and separated. This appearance shows at all near-infrared wavelengths (see Fig. 71).

To look at the starlight distribution over a broader spectral range it is useful to Concentrate on the low Galactic-latitude region. Figure 71 presents DIRBE maps of this region at 1.25 μm, 2.2 pm, 3.5 μm and 4.9 urn, each

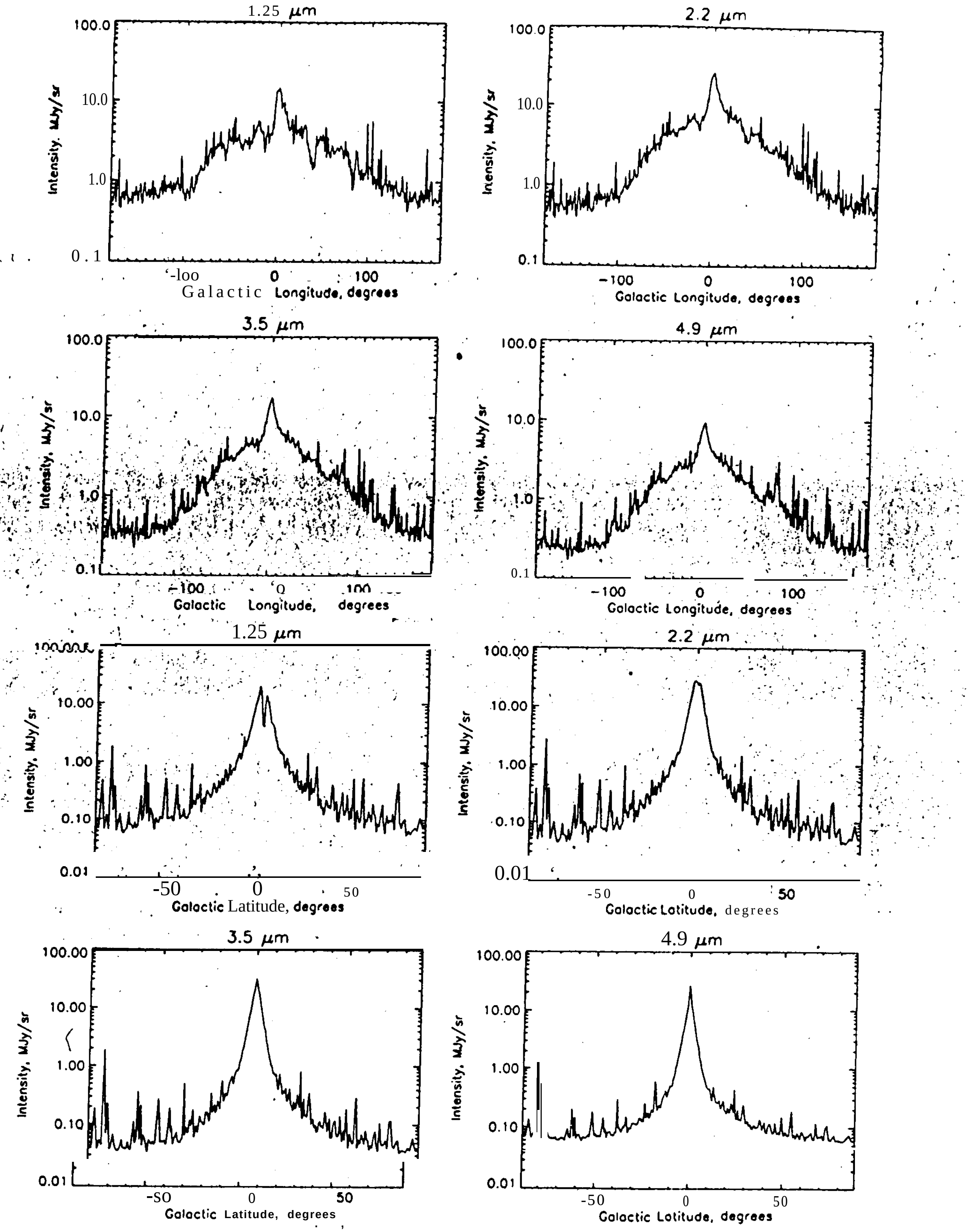

Fig. 72. **Intensity profiles of "Galactic starlight" as** measured from the **DIRBE maps at** 1.25 μ, 2.2pm, 3.5 μm and 4.9pm **after** subtraction **of zodiacal** light. **Upper half**: longitudinal profile sat **a fixed Galactic latitude of $b = 1.6$ deg ($b = 0$ deg is not** shown **as** representative **because** extinction insignificant at some wavelengths). Lower **half**: latitudinal profiles at fixed Galactic longitude off = O deg.

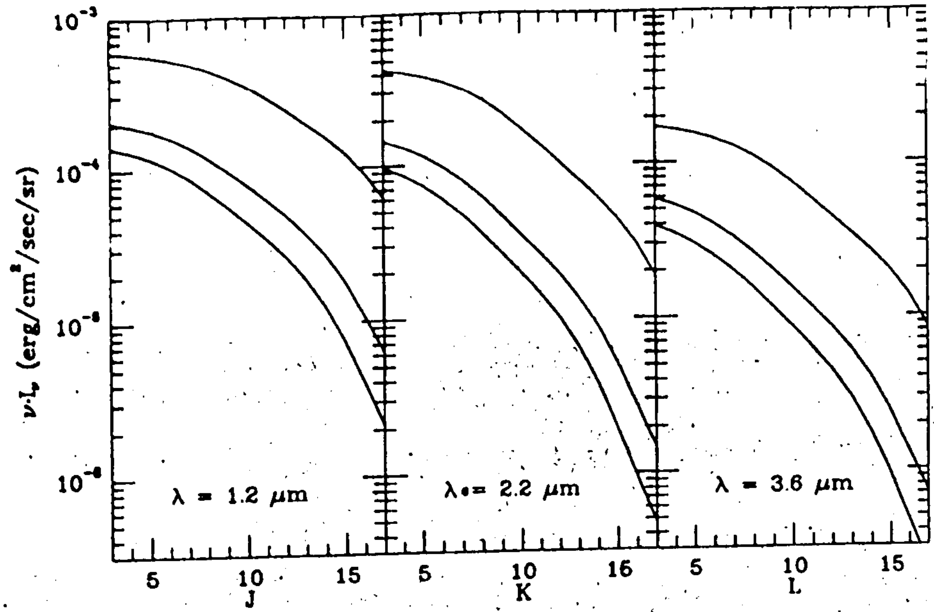

Fig. 73. Residual contributions to the near-infrared background radiation of stars fainter than a given apparent magnitude, for galactic latitudes of 20°, 50°, and 90° (from top to bottom, respectively). The values at the galactic pole at the intersection with the ordinate axis (cutoff magnitude = 3 mag) corresponds to 0.063 MJy/sr for J, to 0.081 MJy/sr for K, and to 0.053 MJy/sr for the L waveband.

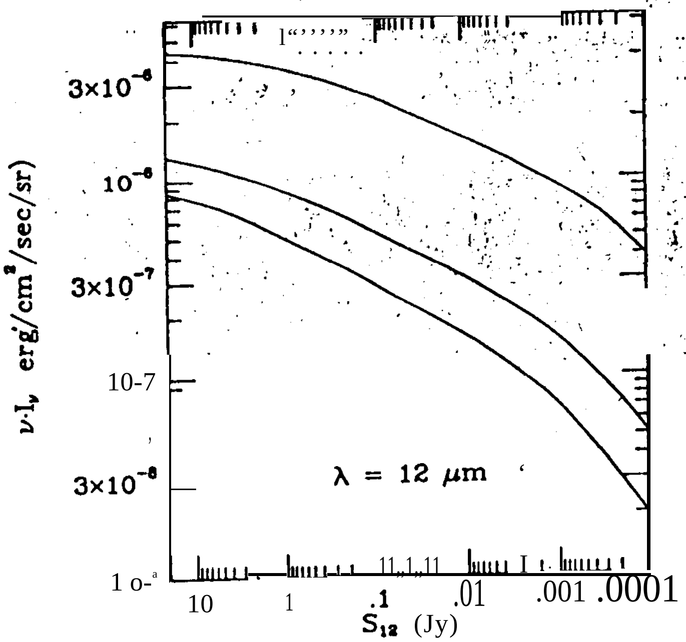

Fig. 74. **Residual contributions** to the **12 μm** background radiation of stare fainter than a given flux limit, for galactic **latitudes** of 20°, 50°, and 90° (from top to bottom, respectively). The values at the galactic pole at the intersection with the ordinate axis (cutoff flux = 20 Jy) correspond to 0.002 **MJy/sr,** which is much less than the contribution due to diffuse emission from the **interstellar** medium.

11. Diffuse galactic light

11.1. Overview

Historically, the term Diffuse Galactic Light (DGL) denotes the diffuse component of the galactic background radiation which is produced by scattering of stellar photons by dust grains in interstellar space (Elvey and Roach 1937; Roach and Gordon 1973). This scattering process is the dominant contributor to the general interstellar extinction of starlight; thus, the DGL is most intense in directions where the dust "column density and the integrated stellar emissivity are both high. This is generally the case at the lowest galactic latitudes, in all spectral regions extending from the far-ultraviolet into the near-infrared. Typically, the DGL contributes between 20% to 30% of the total integrated light from the Milky Way.

However, for the purpose of this reference we are also interested in other sources of diffuse galactic background radiation, and they will be" mentioned in the following where appropriate.

11.2. *Visual*

No comprehensive map of the DGL for the entire sky or even a significant fraction of the sky exists at this time. Groundbased observations in the visual face" the difficult requirement that airglow, zodiacal light, and integrated starlight all need to be known to very high precision (*Mo(V)) if the DGL is to be derived by subtraction of the above components from the total sky brightness. In addition, the problems of atmospheric extinction and atmospheric scat tering (Staude 1975) need to be solved.

Observations of the DGL at visual wavelengths carried out with rocket- or satellite-borne photometers still have the same major sources of uncertainty, i.e. the integrated starlight and the zodiacal light, remain principal contributors to the measured intensity.

The best prospect for a comprehensive measurement of, the DGL in the visual was offered by the Pioneer 10 probe' (see the more detailed description in section 10.4), which carried out an all-sky photometric mapping in two wavebands centered near 440 nm and 640 nm from beyond the asteroid belt (R > 3 AU), where the contributions from zodiacal light are negligible (Hanner et al. 1974). The instantaneous field of view of the Pioneer 10 photometer was 2.28° square, which due to spacecraft spin (12.5 sec period) and finite integration time (0.2 see) was drawn into elongated effective fields-of-view of variable size depending on the look angle. Contributions due to unresolved stars begin to enter the Pioneer 10 data at m $\geq$ 6.5 for an average galactic latitude; thus, stars dominate the measured fluxes.

Toiler (1981) derived DGL intensities from the Pioneer 10 blue data (440 nm) by subtracting integrated starlight intensities of Roach & Megill (1961) and Sharov & Lipaeva (1973) at the positions of 194 Selected Areas (Blaauw & Elvius 1965). The residuals, interpreted as the sum of DGL and extragalactic background light, are most representative in terms of sky coverage.

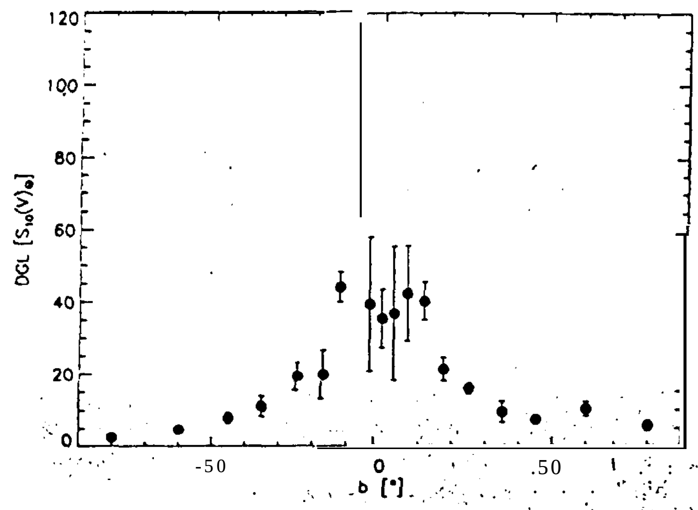

Fig. 75.' The average intensity of the DGL as a function of' galactic latitude based on' the analysis by Toiler (1981) of Pi-'. oneer 10 photometry of 194 Selected Areas 'at λ_{eff} = 440 nm. Error bars denoting one standard deviation of the means are a measure of the longitudinal variation of the DGL intensity.,

For reference purposes, several directions may be taken to estimate the intensity of the DGL at $\lambda \approx$ 440 nm:
In Fig. 75 we present, the mean galactic latitude dependence of Toiler's (1981) values of "the sum of DGL and extragalact ic background, averaged over all galactic longitudes. The error bars, representing one standard deviation of the mean, reflect in part the real variations of the DGL intensity with galactic longitude, especially at lower latitudes.

A second avenue toward a DGL estimate can be found in ratios of DGL to total line-of-sight starlight (LOS.) intensities. In Table 39 we list the average ratios of DGL/LOS. for $\lambda \approx$ 440 nm based on Toiler's data. The use of the values in Table 39 may be advisable, if one wants to estimate the variation of DGL with galactic longitude, where large differences in LOS. may occur. Due to the strongly forward scattering nature of interstellar grains the DGL intensity generally tracks the LOS. intensity at constant latitude.

A third approach toward a DGL estimate might rely on the mean correlation between DGL intensities found in Selected Areas by Toiler (1981) and corresponding column densities of atomic hydrogen. Toiler finds:

$$DGL(S_{10}(V)_\odot) = N_{HI} / (2.4\times10^{20}\,[\text{atoms cm-2}]). \qquad (31)$$

A good source for N_{HI} values is the Bell Lab HI survey by Stark et al. (1992). This approach is based on the fact

Table 39. Ratio of DGL to line-of-sight starlight

b [°]	N	[SA] (DGL/LOS.)
0-151	19	0.21 * 0.05
151-1101	11	0.34 ± 0.07
|10| - |15|	28	0.31 ± 0.03
1151-1201	15	0.19 * 0.04
1201-1301	29	0.25 ± 0.04
1301-1401	22	0.17 ± 0.04
|40| -1601	41	0.17 * 0.02
1601-1901	29	0.12 ± 0.02

that the dust and HI column densities are well-correlated (Bohlin et al. 1978) and that the DGL intensity is determined in part by the dust column density, as long as the line-of-sight is not optically thick. This third approach is therefore recommended mostly for higher galactic latitudes, or $N_{HI} < 2x10^{21}$ atoms cm-?." Estimates based on eqn. 31 rue at best good to within a factor of two, because eqn. 31 reflects only the dependence of the DGL intensity on the dust column density and ignores the dependence on the intensity of the illuminating radiation field.

The red band (λ = 640 run) data from Pioneer 10 have not been subjected to a DGL analysis so far for lack of suitable star count data.

The U-B and B-V colours of the DGL have been measured and have been found to be bluer than the colour of the integrated starlight, as expected from scattering by interstellar grains with scattering cross sections varying as λ^{-1} in the visible region (Witt 1968, Mattila 1970). Table 40, to give an example, 'contains UBV colours of the DGL and of the integrated starlight in Cygnus (upper panel), respectively in Crux (lower panel).

Table 40. Colour of the DGL

	DGL		Integrated	Starlight	Reference
l,|b|	U-B	B-V	U-B	B-V	
70°,0°	-0.05	+0.57	+0.07	+0.73	Witt
75°,250	-0.10	+0.44	+0.00	+0.68	(1968)
300°,0°	-0.10	+0.50	-0.01	+0.71	Mattila (1970)

Recently, Gordon (1997) reported the detection of extended red emission (ERE) on a galaxy-wide scale in the diffuse interstellar medium of the Milky Way Galaxy (see also Gordon, Witt, & Friedmann 1997; Gordon & Witt 1997). The ERE consists of a broad emission band (FWHM 800Å) with a peak wavelength found in the 6500Å to 8000Å range, depending on environment, with a long-wavelength tail extending well into the I-band. The ERE is believed to result from a photoluminescence process in hydrogenated carbonaceous grain mantles, and it has been previously detected photometrically and spectroscopically in numerous reflection nebulae (Witt & Schild 1988; Witt & Boroson 1990), in carbon-rich planetary nebulae (Furton & Witt 1990,1992), in HII regions (Perrin & Sivan 1992, Sivan & Perrin 1993), and in the scattered light halo of the starburst galaxy M82 (Perrin et al. 1995). Gordon (1997) derived the galactic ERE intensity from Pioneer 10 and 11 sky photometry obtained at heliocentric distances greater than 3.3 AU, where the contribution from zodiacal light is no longer detectable (see Sect. 10.4). The integrated star light due to stars of m >6.5 was determined by integrating recent starcount data from the APS Catalog (Pennington et al. 1993), the HST Guide Star Catalog, and photometric catalogs on brighter stars and was subtracted from the Pioneer 10 and 11,@" both the blue and red bands. The diffuse residuals consist of DGL in the blue band, and of a sum of DGL and ERE in the red band. As a result, the B - R colour of the diffuse galactic background radiation is substantially redder than that of the DGL alone. The excess ERE in the R - band can be estimated to be about equal in intensity to the "R. . - band DGL. This ERE intensity is consistent with the measured B-R and B-I colour excesses of individual galactic cirrus filaments (Guhathakurta & Tyson 1989), found to be 0.5 -.1.0 msg. and 1.5 -2.0 msg. redder, respectively, than expected for scattered disk starlight.

Quantitatively, Gordon (1997) finds the galactic ERE and the atomic hydrogen column density at intermediate and high latitudes ($|b|$ > 20") to be well-correlated, yielding an average ERE intensity of (1.43 ±0.31)x10-2? erg." s^{-1} $Å^{-1}$ sr^{-1} l-I-atom-l. This correlation may therefore be used to estimate the expected ERE intensity in the R - band in different portions of the sky.

Partial linear polarization of the DGL at a level of 1-2% is expected, and some tentative detections of this polarization have been reported by Schmidt & Leinert (1966), Weinberg (1969), Sparrow & Ney (1972), and Bandermann & Wolstencroft (1976). Both the scattering by grains partially aligned with their short axes parallel to the galactic plane and the scattering of the non-isotropic galactic radiation field by dust in the galactic plane should produce partially polarized scattered light with the electric vector perpendicular to the galactic plane when observed near b = 0°. A review of existing polarization measurements is given by Leinert (1990).

11.3. Near-Infrared

The diffuse galactic background radiation in the near-infrared (near-IR) is composed of several components, each produced by different constituents of the diffuse interstellar medium by different physical processes. The most

The observational results presented here are summarised for each wavelength range in a separate table in the corresponding subsection, They are also put together in overview in Figure 77 at the end of this section, where in the visual and near-infrared region some model predictions are added for comparison with the data, which stretch over a wide range of brightnesses at these wavelengths. Otherwise, model prediction of EBL brightness are not the topic of this reference. For this matter see, e.g., the conference proceedings by Bowyer and Leinert (1990) and Rocca-Volmerange et al. (1991) or the work of Franceschini et al. (1991 b).

12.1. *Ultraviolet*

An extragalactic component is certainly present in the UV/FUV since the summed flux of galaxies is present at some level. Early in the Space Age it was realized "that searches in the FUV had substantial advantages" *over searches* in the UV, because the zodiacal light component is not present at a measurable level and contributions from stellar sources were expected to be small. In particular, it was hoped that emission from a very hot (10^8 K) or hot (10^5 K) intergalactic medium might be detected. These measurements were far more difficult to carry out than was originally anticipated, and a wide range of conflicting results were reported.

At this point, the most cited argument that some of the Far UV diffuse background is extragalactic in origin is that most measurements of this flux show a correlation with galactic neutral hydrogen column density, and the extrapolation to zero hydrogen columns yields fluxes that are in the *range* of 50 to 300 photon units. These results are only upper limits to an extragalactic background, however, since there is no guarantee that galactic components are not producing this flux.

While the total picture is far from clear, some aspects of a possible extragalactic flux have been established. Quasar absorption line studies definitely constrain' emission from a diffuse intergalactic medium to a marginal role (Jakobsen 1991). Paresce and Jacobsen (1980) had shown before that integrated light from QSOS and AGNs will not produce a significant contribution to the diffuse FUV background. However, Armand et al. (1994) have used data on galaxy counts, obtained at 2000 Å with a limiting magnitude of 18.5, to calculate the ultraviolet flux due to the integrated FUV light of all galaxies. The extrapolation is small and leads to an expected flux of 40 to 130 photon $cm^{-2} s^{-1} sr^{-}$ 1A-1. Hence it seems certain that there is at least some extragalactic *flux* present in the diffuse FUV background. It is interesting to note that the flux predicted by Armand et *al.* is consistent with the (uncertain and controversial) observational results for a possible extragalactic diffuse FUV background.

Table 43. Possible Components of a Diffuse Extragalactic Far Ultraviolet Background with their Estimated Intensities"

Summed from all galaxies	40 to 200
QSOs/AGNs	<lo
Intergalactic medium	<lo
observed upper limit	50 to 300

[a] Intensities are given in units of photons cm-o S-l sr^{-1} A-l.

12.2. Visual

A selection of upper limits from photometric measuremerits as well as lower limits obtained from galaxy counts are summarised in Table 44. In the table, the author(s) and date of publication are given in column (1). The wavelength of observation and the I_{EBL} value (or its upper limit) as given in the original publication are listed in columns (2) and (3). In column (4) we give our critical revision (upper limit) of each I_{EBL} value; in deriving these 'revised values' we, have tried to consider the effects 'of some additional uncertainties or corrections which" in our opinion *were not* sufficiently discussed in the original paper. In column (5) we give $\lambda I_\lambda = \nu I_\nu$ for the revised EBL values. The last column (6) gives the method used.

12.2.1. Photometric upper limits

Three surface photometric measurements are included in Table 44:

(1) *Dube,* With *and Wilkinson (1979)* observed the total night sky brightness from the ground in eleven high-' latitude fields. As a mean, value of the 11 fields Dube et" al. gave an EBL+DGL value of $1.0\pm1.2\, S_{10}$. Because it was not possible to estimate the DGL contribution the result was interpreted as a 2σ upper limit to the EBL of 3.4 S_{10} or 5.110-9 ergs $cm^{-2}\, s^{-1}\, sterad^{-1}\, Å^{-1}$. A basic problem with this method is that it starts with the total night-sky brightness which is a factor of $\approx$ 100 brighter than the EBL. Thus, very accurate measurements of the *absolute* intensities of ZL and airglow are required. The most critical point in the data analysis of Dube et al. was the way they corrected for the airglow. They assumed that airglow is a linear function of sec z and used *linear* extrapolation to sec z = O to eliminate airglow. This method is doubtful since the sec z - dependence of the airglow is not strictly linear but follows the so-called van Rhijn's (1921) law. Mattila, Leinert and Schnur (1991) have reanalyses the airglow problem using, as far as possible, the observational values given in Dube et al. (1979) and in Dube (1976). They have thus found that Dube et al. probably have overestimated the airglow intensity by $\approx 3\, S_{10}$. Thus the residuaf value for EBL + DGL should be *increased* by this amount, resulting in $I_{EBL+DGL} = 4.0 \pm 1.2\, S_{10}$ or an 1σ upper limit of 5.2 S_{10}.

important ones are the DGL, caused by scattering of star light on larger interstellar grains; the near-IR continuum emission, caused by a non-equilibrium emission process probably associated with small carbonaceous grains; and the set of so-called unidentified infrared bands which have been attributed to emission from interstellar aromatic hydrocarbon molecules, such as polycyclic aromatic hydrocarbons (PA H). We will refer to them as aromatic hydrocarbon bands,

No separate detection of the DGL at near-IR wavelengths has been accomplished so far, although the galactic component of the near-IR background at 1.25 μm and 2.2 μm observed by the DIRBE experiment (Silverberg et al. 1993; Hauser 1996) undoubtedly contains a scattered light contribution. Recent evidence (Witt et al. 1994; Lehtinen & Mattila 1996) provides a strong indication that the dust albedo remains as high as it is in the visible out through the K-band (2.2 μm). The K-optical depth is about 10% of that at V; hence, only at quite low galactic latitudes ($|b| < 5°$) can one find, the required dust column densities which will give rise to substantial (scattered) DGL. At the galactic equator, however, the ratio of DGL/LOS$_*$ should be similar to the values listed in Table 39. At higher galactic latitudes, the ratio DGL/LOS$_*$ will be substantially lower than the, values listed in Table 39.

The near-IR continuum emission was first recognized in reflection nebulae whose surface brightnesses in the 1 μm - 10pm wavelength range exceeded that expected from scattering by factors of several (Sellgren, Werner, & Dinerstein 1983; Sellgren 1984). Absence of polarization provided additional confirmation of the non-scattering origin of this radiation. The non-equilibrium nature of the radiation process was recognized from the fact' that the colour temperature of the emerging radiation was independent of distance from the 'exciting star and thus independent of the density of the exciting radiation. This leaves as the cause of this radiation non-equilibrium processes which depend upon excitation by single photons, e.g. photoluminescence of grain mantles or, alternatively, non-equilibrium heating of tiny grains resulting in large temperature fluctuations. The galactic distribution of this radiation component has yet to be studied; it depends on a very accurate assessment of the near-IR integrated starlight (see Sect. 10.5) and the near-IR zodiacal light (see Sect. 8.5), which need to be subtracted from photometries of the near-IR sky background.

The aromatic hydrocarbon bands centered at wavelengths 3.3 μm, 6.2 μm, 7.7 μm, 8.6 μm, and 11.3 μm, with widths in the range of 0.03 to 0.5 μm, were first observed in bright nebulous regions by Gillett, Forrest, and Merrill(1973). Thanks to the successful AROME balloon-borne experiment (Giard et al. 1988) and the more recent missions of the Infrared Telescope in Space (IRTS, Onaka et al. 1996) and the Infrared Space Observatory (1S0, Mattila et al. 1996, Lemke et al. 1997), they have now been observed in the diffuse interstellar medium at low galactic latitudes. The relative bandstrengths and widths are very similar to those observed in reflection nebulae, planetary nebulae, and HII regions, pointing toward a common emission mechanism. Onaka et al. (1996) show that the band intensities at 3.3 μm and 7.7 μm and the far-IR background intensities at 100pm along identical lines of sight are correlated very tightly, suggesting that the respective emitters, presumably PAH molecules in the case of the aromatic hydrocarbon bands and classical sub-micron, grains for the 100-pm thermal continuum, are* well-mixed spatially and are excited by the same interstellar radiation field. The correlation of the band intensities with the atomic hydrogen column density is also excellent, reflected in the dust emission spectrum per hydrogen atom given in Table 41.

11.4. *Thermal infrared*

The infrared emission from the diffuse galactic ISM is dominated by thermal and other emissions by dust, with some additional contributions from interstellar cooling lines, mainly from CII and NIL At wavelengths < 100 μm the galactic diffuse emission is weaker than the infrared emission from the zodiacal dust cloud (see Fig. 1); at wavelengths > 400 pm” the cosmic background radiation dominates over the galactic thermal radiation. Only in the 100-400 μm band is the galactic emission” the primary background component. However, as the composite spectrum of all night sky components in Fig. 1 schematically indicates, the thermal IR spectrum of galactic dust is” complex in structure, suggesting significant contributions from grains covering a wide range of temperatures. In par-” titular, there is substantial excess emission in the 5 to 50 μm spectral range. This excess is generally attributed to stochastically heated very small grains with mean temperatures in the range 100- 500K (Draine and Anderson 1985; Weiland et al. 1986), while the main thermal emission peak near 150 μm is attributed to classical-sized dust grains in equilibrium with the galactic interstellar radiation field, resulting in temperatures around 20K.

The exploration of the infrared background has been greatly advanced by the highly successful missions of the Infrared Astronomical Satellite (IRAS; Neugebauer et al. 1984), the Diffuse Infrared Background Experiment (DIRBE; Boggess et al. 1992) and the Far-Infrared Absolute Spectrophotometer (FIRAS; Fixsen et al. 1994) on board of the COBE satellite, the Infrared Telescope in Space (IRTS; Murakami et al. 1994,1996), and the AROME balloon-borne experiment (Giard et al. 1988).

Interstellar dust appears to be well-mixed with all phases of the interstellar gas (Sodroski et al. 1997); however, to obtain a first-order representation of the emissions from galactic dust, the well-established correlations with N(HI) provide the best guide, The average dust emission spectrum per H-atom is given in Table 41., as derived from

The observational results presented here are summarised for each wavelength range in a separate table in the corresponding subsection, They are also put together in overview in Figure 77 at the end of this section, where in the visual and near-infrared region some model predictions are added for comparison with the data, which stretch over a wide range of brightnesses at these wavelengths. Otherwise, model prediction of EBL brightness are not the topic of this reference. For this matter see, e.g., the conference proceedings by Bowyer and Leinert (1990) and Rocca-Volmerange et al. (1991) or the work of Franceschini et al. (1991 b).

12.1, Ultraviolet

An extragalactic component is certainly present in the UV/FUV since the summed flux of galaxies is 'present at some level. Early in the Space Age it was realized that searches in the FUV had substantial advantages over searches in the UV, because the zodiacal light component is not present at a measurable level and contributions from stellar sources were expected to be small. In particular, it was hoped that emission from a very hot (10^6 K) or hot (10^5 K) intergalactic medium might be detected. These measurements were far more difficult to carry out than was originally anticipated, and a wide range of conflicting results were reported.

At this "point, the most cited argument that some of the Far UV diffuse background is extragalactic in origin is that most measurements of this flux show a correlation with galactic neutral hydrogen column density, and the extrapolation to zero hydrogen columns yields fluxes that are in the range of 50 to 300 photon units. These results are only upper limits to an extragalact ic background, however, since there is no guarantee that galactic components are not producing this flux.

While the total picture is far from clear, some aspects of a possible extragalactic flux have been established. Quasar absorption line studies definitely constrain emission from a diffuse intergalactic medium to a marginal role (Jakobsen 1991). Paresce and Jacobsen (1980) had shown before that integrated light from QSOS and AGNs will not produce a significant contribution to the diffuse FUV background, However, Armand et al. (1994) have used data on galaxy counts obtained at 2000 Å with a limiting magnitude of 18.5, to calculate the ultraviolet flux due to the integrated FUV light of all galaxies. The extrapolation is small and leads to an expected flux of 40 to 130 photon $cm^{-2}\,s^{-1}\,sr^{-1}\,Å^{-1}$. Hence it seems certain that there is at least some extragalactic flux present in the diffuse FUV background. It is interesting to note that the flux predicted by Armand et al. is consistent with the (uncertain and controversial) observational results for a possible extragalactic diffuse FUV background.

Table 43. Possible Components of a Diffuse Extragalactic Far Ultraviolet Background with their Estimated Intensities[a]

Summed from all galaxies	40 to 200
QSOs/AGNs	<lo
Intergalactic medium	<lo
observed upper limit	50 to 300

[a] Intensities are given in units of photons $cm^{-2}\,s^{-1}\,sr^{-1}$ A-l. ,

12.2. Visual

A selection of upper limits from photometric measurements as well as lower limits obtained from galaxy counts are summarised in Table 44. In the table, the author(s) and date of publication are given in column (1). The wavelength of observation and the I_{EBL} value (or its upper limit) as given in the original publication are listed in columns (2) and (3). In. column (4) we give our critical revision (upper limit) of each I_{EBL} value; in deriving these 'revised values' we have tried to consider the effects of some additional uncertainties or corrections which in our opinion were not sufficiently discussed in the original paper. In column (5) we give $\lambda I_\lambda = \nu I_\nu$ for the revised EBL values. The last column (6) gives the method used.

12.2.1. Photometric upper limits

Three surface photometric measurements are included in" Table 44:

(1) Dube, Wickes and Wilkinson (1979) observed the total night sky brightness from the ground in eleven high-latitude fields. As a mean value of the 11 fields Dube et al. gave an EBL+DGL value of $1.0 \pm 1.2\ S_{10}$. Because it was not possible to estimate the DGL contribution the result was interpreted as a 2σ upper limit to the EBL of 3.4 S_{10} or 5.110-9 ergs $cm^{-2}\,s^{-1}\,sterad^{-1}\,Å^{-1}$. A basic problem with this method is that it starts with the total night-sky brightness which is a factor of $\approx$ 100 brighter than the EBL. Thus, very accurate measurements of the *absolute* intensities of ZL and airglow are required. The most critical point in the data analysis of Dube et al. was the way they corrected for the airglow. They assumed that airglow is a linear function of sec z and used *linear* extrapolation to sec z = O to eliminate airglow. This method is doubtful since the sec z - dependence of the airglow is not strictly linear but follows the so-called van Rhijn's (1921) law. Mattila, Leinert and Schnur (1991) have reanalyses the airglow problem using, as far as possible, the observational values given in Dube et al. (1979) and in Dube (1976). They have thus found that Dube et al. probably have overestimated the airglow intensity by $\approx 3\ S_{10}$. Thus the residual value for EBL + DGL should be *increased* by this amount, resulting in $I_{EBL+DGL} = 4.0 \pm 1.2\ S_{10}$ or an 1σ upper limit of 5.2 S_{10}.

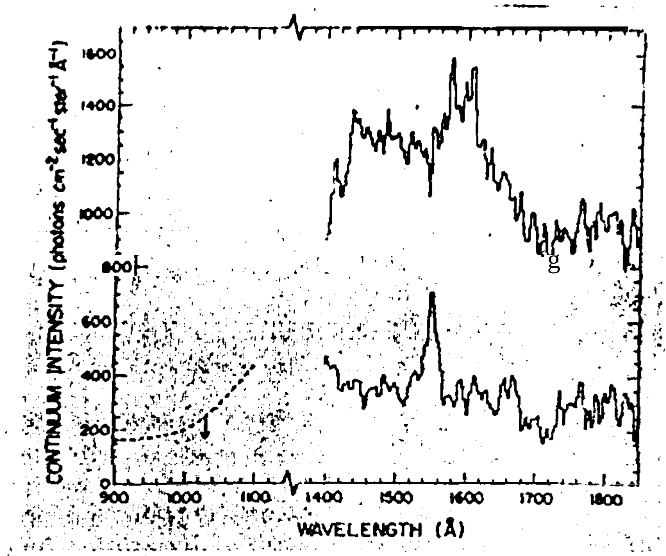

Fig. 76. **Summary** data on the'diffuse cosmic far ultraviolet **background**. The data from 902 to **1200** A **are** from **Holberg (1986)** **and are** upper limits **to the flux from** a high, **Galactic** latitude "view **direction**. Two data sets are shown for the 1400 to, **1850** A band. **The** upper line is from **Hurwitz, Bowyer** and Martin (1991) and **shows** typical data obtained **in** view **directions with** $\tau_{dust} \geq 1$. The lower line **is** from Martin **and Bowyer** '(1990) **and** shows data obtained **at** a high Galactic **latitude; the CIV** 1550' A line is clearly evident **in emission** and the 1663 A line of 0111] **is** also apparent, though at lower signal-t-noise **ratio. The** **extragalactic** contribution to **these** data probably is small (see table 42).

evident as an additional component "at wavelengths from 1550 to 1650 Angstrom., The lower line **is** from Martin and **Bowyer** (1990) **and** "shows data obtained at a high galactic latitude and a low-total galactic neutral hydrogen column. The **CIV** 1550 Angstrom line is clearly evident in emission, and the **1663** Angstrom. line of forbidden O III is also apparent though at a *lower* **signal-to-noise.**

As already, mentioned, **the** major components of the cosmic far ultraviolet background are summarized in Table 42 above.

11.5.2. Near-ultraviolet (180 **nm** -300 nm)

The **diffuse** radiation in this band is the sum of zodiacal light and starlight scattered by **interstellar** dust. A few first studies of the zodiacal light in this band have been carried out, which suggest this component exhibits characteristics similar to that observed in the visible (see section 8.6). A few studies of scattering by dust by early type stars have been carried out. The results obtained differ, and independent of these differences, the scattering varies tremendously from place to place in the galaxy. We refer the reader to Dring et al. (1996) and references therein for a discussion of these results.

12. **Extragalactic** background light

For **the** extragalactic background radiation no **generally-accepted** measured values exist **in** the UV, optical or infrared **wavebands**. However, upper limits from surface photometry and lower limits from galaxy counts are **available**. We present a critical evaluation **and** tabulation of the available results.

Extragalactic background light **(EBL)** in **UV,** optical and **near-IR ($\lambda \lesssim 5\mu m$)** is thought to **consist mainly** of redshifted starlight from unresolved **galaxies;** more **hypothetical** contributions would" be, e.g., from **stars** or **gas** in the intergalactic space, and from decaying elementary particles (e.g. neutrinos). In the mid- and far-infrared the main contribution is thought to be redshifted emission from dust particles, heated by starlight in galaxies.

Observations of the EBL are hampered by the much stronger foreground components of the night sky brightness described in the other sections. Unlike the other components the EBL is isotropic which, in combination with its weakness, complicates its separation. Recent reviews of the observational and" theoretical status of the EBL have been given by **Mattila** (1990), **Tyson(1990,** 1995), **Mattila,** Leinert and **Schnur(1991)** for the optical; by **Bowyer(1991),** Henry (1991), Henry and **Murthy** (1995) and **Jakobsen(1995)** for the ultraviolet; by **Matsumoto(** 1990), Franceschini, **Mazzei** and De **Zotti** (1991), **Hauser(1995a, 1995b,** 1996) and **Lonsdale(1995)** for the infrared; **Longair(** 1995) has given a general review covering all wavelengths.

Table 44, Observational upper and *lower* limits to the EBL intensity as determined from surface photometry or galaxy counts

Author(s)	λ (A)	I_{EBL}	I_{EBL} revised, 1σ	λI_λ(revised) limits erg $s^{-1}cm^{-2}sr^{-1}$	Method
Dube, Wickes and Wilkinson (1979)	5115	1.0 * 1.2 S_{10} $\leqq$ 3.4 S_{10}	4.0 * 1.2 S_{10} $\leqq$ 5.2 S_{10}	$\leqq$ 4.0 10-^{s}	photometry
Toiler (1983)	4400	1.3 * 1.3 $S10_\odot$ $\leqq$ 3.9 $S10_\odot$	2.2 ± 4.8 $S1O_o$ $\leqq$ 7. OS1OQ	$\leqq$ 3.7 10^{-5}	photometry
Mattila and Schnur (1990)	4000	6.5 ± 2.5 cgs*	$\leqq$ 9.0 Cgs"	$\leqq$ 3.6 10^{-5}	photometry
Cowie et al. (1994)	3400 (U')			1.310-6	galaxy counts (K $\leqq$ 22^m)
	4470 (B)			1.810-0	
	5425 (V)			3.1 10-*	
	8340 (I)			4.710-6	
	22000 (K)			5.2 10^{-6}	
Tyson (1995)	3600 (U)			2.5(+.07 -.04) 10^{-6}	galaxy counts ($B_j \leqq 29^m/\square''$)
	4500 (B)			2.9(+.09 -.05) 10^{-6}	
	6500 (R)			2.9(+.09 -.05) 10^{-6}	
	9000 (I)			2.6(+.3 -.2) 10^{-6}	
	22000 (K)			7.2(+1 -1) 10^{-6}	
Morgan and Driver (1995)	4500 (B)			1.910-6	galaxy counts (B $\leqq$ 26^m)
	5500 (v)			1.310-6	
	6500 (R)			3.210-6	
	9000 (I)			3.510-6	
	'4500(B)			4.710-6 '	galaxy counts ($m_{Filter} \leqq 38^m$)
	5500 (V)			6.410-6	
	6500 (R)			8.210-6	
	9000 (I)			10.010-6.	

* cgs = 1 0^{-9} ergs $cm^{-2}s^{-1}sterad^{-1}$ A-'

(2) *Toiler (1983)* utilized measurements of a photometer aboard Pioneer 10 as it moved out of the zodiacal dust cloud ($R \geqq$ 3.3AU). From these he subtracted integrated starlight and gave a value for the average brightness of the diffuse background light of $I_{DGL+EBL}$ = 3.3 ± 1.2 $S10_\odot$ He estimated I_{DGL} to be 2.0 ± 0.4 SIO_o. As a final result Toiler thus obtained an EBL intensity of 1.3 ± 1.3 SIO_o which he expressed as a 2σ upper limit of $I_{EBL} \leqq$ 3 . 9 $S10_\odot$.

Since Toiler's EBL value has been frequently cited as the EBL reference value, it deserves a detailed discussion of errors. The basic problem for his EBL determination is the large field of view (2.3 x 2.3 deg) of the photometer. Thus, the starlight entered with full weight into the measured sky brightness, and in order to derive the small residual EBL one must know the ISL very accurately *in the Pioneer 10 photometric system*. This was not fully the case. The ISL values of Roach and Megill (RM, 1961) and Sharov and Lipaeva (SL,1973) are based on the Harvard-Groningen (Pickering et al. 1918, 1923,1924; van Rhijn 1929) and Mount Wilson starcounts (Scares et al. 1930) the magnitudes of which were calibrated by using photographic techniques. Sharov and Polyakova(1972) have shown that the Harvard-Groningen photographic magnitude scales are in need of positive corrections of as much as 0.4 mag to 0.5 mag in order to reduce stars of 7 to 16 mag from m_{pg} to the B system. In their ISL summation SL tried to take these photometric corrections into account and thus their ISL values should be given the preference over the RM values. Then an average $I_{DGL+EBL}$ of 4.2 SIO_o, instead of 3.3 SIO_o, is obtained. There is. a the remaining *systematic* error of the Sharov and Lipaeva ISL values due to the scale errors which is at least 15 %. With an average ISL value of 25 $S10_\odot$ this amounts to 3.8 $S10_\odot$. The systematic error of the Pioneer 10 photometry itself (e.g. due to calibration) has been given as 8 % (Schuerman et al. 1981), which for 25 SIO_o corresponds to 2.0 $S10_\odot$. A further uncertainty of 1.6 SIO_o results from variations in the cutoff for bright stars. The total error resulting from quadratically adding the systematic and statistical errors then is 4.8 SIO_o.

Thus we end up with a revised EBL value of I_{EBL} = 3.2 ± 4.8 SIO_o, which corresponds to 2.6 ± 5.7.10^{-9} ergs $cm^{-2} s^{-1} sterad^{-1} Å^{-1}$ or to a one σ upper limit of 8.3.10^{-9} ergs $cm^{-2} s^{-1} sterad^{-1} Å^{-1}$.

(3) *Mattila and Schnur(1990)*, on the basis of their observations in the dark cloud area L1642, have presented a preliminary estimate for the EBL of 6.5 ± 2.5 10^{-9} ergs

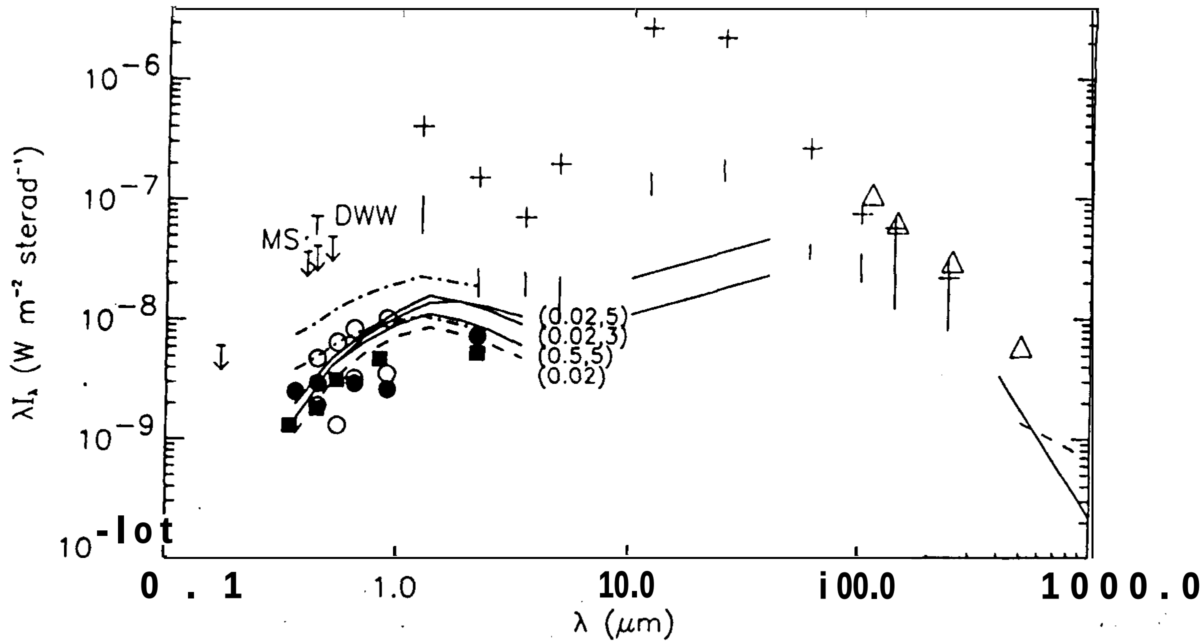

Fig. 77. Summary of present observational **limits** and model **predictions** for the EBL. The photometric upper limits by Dube et al. **(DWW),** Toiler (T) and **Mattila** and **Schnur** (MS) in optical and the **UV** upper limit of 300 photon units at 170 nru (see text) are shown as downward pointing arrows. The **COBE/DIRBE and COBE/FIRAS** dark sky (total) **brightnesses** between 1.25 **μmand** 500 **μm are** shown **as** crosses and open triangles, respectively. The **ranges** of isotropic residuals after foreground subtraction are shown by vertical bars for the **DIRBE** 1.25 **μm** -240 **μm** bands **(Hauser** 1996). The Mather et al. (1994) estimate for **an** upper limit of possible **sub-mm** excess above the CMB spectrum **is** shown"& a **dashed** line between 500pm and 100,0 **μm.** The claimed tentative detection of **CIBR** by **Puget** et al. (1996) is shown **as** a solid line between 400pm and 1000 **μm.** Solid lines at 10 **μm** -40 **μm are** the possible detections from Dwek & **Slavin** (1994); the upper line is for H_0= 100 km $s^{-1}Mpc^{-1}$ "and the lower one for 50 kms-^{1} Mpc^{-1}. The results from galaxy counts **are** are shown with different symbols: Cowie et al.: black squares; Tyson: solid **circles;** Morgan and Driver: open circles (two **values** at each wavelength band, see Table 44 and text). In the visual *range*, some model **calculat** ion results are shown **as** well for comparison: solid lines are after Yoehii and **Takahara** (1988) for evolving galaxy models, **labeled** with q_0 and z_F, where z_F means the epoch (measured by **redshift)** of galaxy formation; the dashed line is for a non-evolving galaxy model with q_0 = 0.02. The two **dash-dotted** lines are after **Väisänen (1996)** for models which include the estimated effect of low-surface-brightness and faint blue **galaxy** populations: the upper line is with **Ferguson** and **McGaugh** (1995) luminosity function and with luminosity evolution (model labeled' **FMB-LE** in **Väisänen** 1996) ; the lower line is with a luminosity function evolution in accordance with the findings of Lilly et al. (1995), i.e. extra brightening of the blue **galaxies** over the **passive** luminosity evolution, and **an** excess of a non-evolving blue population of faint galaxies (model labeled BBG in **Väisänen** 1996).

Table 45. Upper limits and claims of tentative detections of the *cosmic* **infrared** background radiation

λ μm	νI_ν nW m^{-2} sr^{-1}	Reference	νI_ν nW m^{-2} sr^{-1}	Reference	Ref.
1.25	393 *13	DIRBE dark sky	50-104	DIRBE residual	1
2.2	150 *5	"	15-26	"	1
3.5	63 ±3	"	15-24	"	1
4.9	192 ±7	"	9-22	"	1
12	2660 ±310	"	102-164	"	1
25	2160 ±330	"	136-210	"	1
60	261 ±22	"	31-42	"	1
100	74 ±10	"	20-35	"	1
140	57 ±6	"	12-63	"	1
240	22 ● 2	"	8-33	"	1
111	108	FIRAS dark sky			1
143	63	"			1
250	30	"			1
500	6	"			1
500-5000			$680/\lambda(\mu m)$	FIRAS residual	2
400-1000			3.4 $(\lambda/400\,\mu m)^{-3}$	FIRAS residual	3
10-40			6 h $(\lambda/\mu m)^{0.55}$	γ-ray method	4

[1] Hauser (1996)
[2] Mather et al. (1994)
[3] Puget et al. (1996)
[4] Dwek & Slavin (1994) ; $h = H_0/100$ km s^{-1} Mpc^{-1}

Puget et al. (1996) have claimed a tentative detection of far-IR CIBR using COBE/FIRAS data. They have modelled and removed the foreground components above 140 μm. For estimating the interstellar cirrus emission they used its correlation with HI 21-cm data, and for zodiacal emission its spectral and spatial distribution as determined at shorter wavelengths, $\lambda \leq 100$ μm. The residual isotropic component claimed for the 400 μm - 1000 μm range can be represented by $\nu B_\nu \approx$ 3.410-9 $(\lambda/400\mu m)^{-3}$ W m^{-2} sr^{-1}.

An indirect method for measurement of the mid-IR CIBR is based on the spectra of γ-ray sources, since γ-rays interact with intergalactic IR-photons by pair production, giving rise to energy-dependent extinction. A recent application gives, for $\lambda \approx 10 - 40\mu m$, the result $\nu B_\nu \approx 6\ h\ 10^{-9}(\lambda/\mu m)^{0.55}$ W m^{-2} sr^{-1} (Dwek & Slavin 1994). The result depends on the Hubble constant $h = H_0/100$ km s^{-1} Mpc^{-1}. This estimate is by a factor of $\approx$ 10 lower that the DIRBE isotropic residuals at 10 and 25 μm, but fits nicely to the DIRBE isotropic residuals at shorter and longer wavelengths (see Fig. 77). Again, there are uncertainties in this method, since the intrinsic high energy gamma ray spectra before attenuation by interaction with the cosmic infrared radiation field are not really known.

12.4. Overview On EBL observations

Figure 77 summarises the current observational limits to the extragalactic background light in the wavelength range from 0.1 μm to 1000 μm. In the visual and near-infrared range, where discrepancies between different methods of determination are particularly large, we also plot a few selected model predictions for comparison, without the intent to discuss them here. Compared to the situation ten years ago, the gap between upper limits from direct measurements, lower limits from galaxy counts, and model predictions is getting smaller, being mostly less than a factor of ten by now. A comparison with the tots! sky brightness values shown in Figure 1, which are typically brighter by two orders of magnitude, is informative. In this comparison please note that νI_ν and λI_λ are identical units of brightness.

Acknowledgements. We thank Martin Cohen for providing results of his SKY model tailored to the purposus of this reference paper, and we thank Paul Feldman, Robert MacQueen, H. Kimura and Hans Lauche for helpful advice and discussions. We are grateful to Petri Väisänen, who contributed the first and the last figure of this paper, and we very much thank Doris Anders, Karin Dorn, and in particular Martina Weckauf for the careful and patient work in producing or making computer-readable most of the numerous figures of this paper.

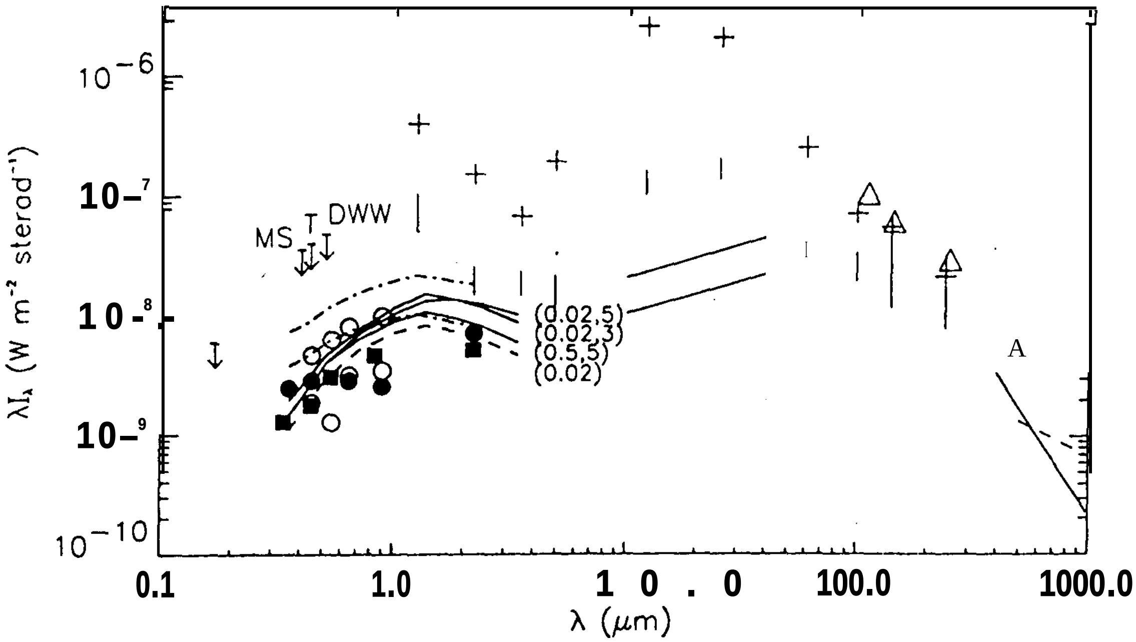

Fig. 77. Summary of present observational limits and model predictions for the EBL. The photometric upper limits by Dube et al. (DWW), Toller (T) and Mattila and Schnur (MS) in optical and the W upper limit of 300 photon units at 170 nm (see text) are shown as downward pointing arrows. The COBE/DIRBE and COBE/FIRAS dark sky (total) brightnesses between 1.25' μm and 500 μm are shown as crosses and open triangles, respectively. The ranges of isotropic residuals after foreground subtraction are shown by vertical bars for the DIRBE 1.25 μm -240 μm bands (Hauser 1996). The Mather et al. (1994) estimate for an upper limit of possible sub-mm excess above the 'CMB spectrum is shown as a dashed line between 500 μm and 1000 pm. The claimed tentative detection of CIBR by Puget et al. (1996) is shown ss a solid line between 400 μm and 1000 pm. Solid lines at 10 μm -40 μm are the possible detections from Dwek & Slavin (1994); the upper Line is for H_0 = 100 km S-* Mpc^{-1} and the lower one for 50 km s 1 Mpc^{-1}. The results from galaxy counts are are shown with different symbols: Cowie et al.: black squarea; Tyson: solid circles; Morgan and Driver: open circles (two values at each wavelength band, see Table 44 and text). In the visual range, some model calculation results are" shown as well for comparison: solid lines are "after Yoshii and Takahara (1988). for evolving galaxy models, labeled with q_0 and z_F, where z_F means the epoch (measured by redshift) of galaxy formation; the dashed line is for a non-evolving galaxy model with q_0 = 0.02. The *two* dash-dotted lines are after Väisänen (1996) for models which include the estimated effect of low-surface-brightness and faint blue galaxy populations: the upper line is with Ferguson and McGaugh (1995) luminosity function and with luminosity evolution (model labeled FMB-LE in Väisänen 1996) ; the lower line is with a luminosity function evolution in accordance with the findings of Lilly et al. (1995), i.e. extra brightening of the blue galaxies over the passive luminosity evolution, and an excess of a non-evolving blue population of faint galaxies (model labeled BBG in Väisänen 1996).

References

Ábráham P., Leinert Ch., and Lemke D. 1997, A& A,,in press

Allen C. W., 1985, Astrophysical Quantities, third, reprinted edition. The Athlone Press, London, p.162

Alonso A., Arribas S. and Martínez-Roger C., 1995, A&A 297, 197

Angel J.R.P and Woolf N.J. 1997, ApJ 475, 373

Arendt R. G., Berriman G. B., Boggess N., Dwek E., Hariser M. G., Kelsall T., Moseley S. H., Murdock T. L., Odegard N., Silverberg R. F., Sodroski T.J., and Weiland J.L. 1994, ApJ 425, L85

Arendt R. G. et al. 1997, in preparation

Armand C., Milliard B., and Deharveng J.M. 1994, A&A 284, 12

Ashley M. C. B., Burton M. G., Storey J.W.V., Lloyd, J. P., Bally J., Briggs J.W., and Harper D.A. 1996, PASP 108, 721

Bahcall J. N. and Soneira R. M. 1980, ApJ Suppl. 44, 73

Bandermann, L.W. & Wolstencroft, R.D. 1976, Mere. R. Astron. Sot. 81, pt. 2, 37

Barbier D. 1956, The Airglow and the AUrorae, Special Suppl. No. 5 to the J. Atm. Terr. Phys., p.38

Barth C.A. and Schaffner S. 1970, JGR 75, 4299

Becklin E.E. et al., 1973, AJ 78,1063

BeckWith S.V.W. 1994, in "Star Formation and Technique in Infrared and mm-Wave Astronomy", T. R.Ray and S.V.W. BeckWith, eds., Lecture Notes in Physics. 431, Springer-Verlag Berlin/Heidelberg/New York, p.157

Becvar A. 1962, Atlas Coeli 1950.0, Atlas of the Heavens, Sky Publishing Company, Cambridge, Massachuset ts

Beichman, C.A. 1987, ARAA 25, 521

Bennett C.L. et al. 1994, ApJ 434, 587

Bernard, J.-P., Boulanger, F., Desert, F. X., Giard, M., Helou, G., and Puget, J.L. 1994, A&A, 291, L5

Berriman G. B., Boggess N. W., Hauser M. G., Kelsall T., Lisse C. M., Moseley S. H., Reach W.T. and Silverberg R. F., 1994, ApJ Letters 431, L63

Berry, R. L., 1976, J.R.A.S. Canada 70, 97

Bertiau, F. C., de Greve, E., Treanor, P. J., 1973, Publ. Vatican Ohs. Vol. 1, 159

Bessell M. S., 1979, PASP 91, 589

Bessell M.S. and Brett J. M., 1988, PASP 100, 1134

Blaauw, A., & Elvius, T. 1965, in Galactic Structure, Stars & Stellar Systems V, ed. by A. Blaauw & M. Schmidt, Chicago: University of Chicago Press, p. 589

Blackwell D.E. 1955, Mon. Not. R. Astron. Sot. 112, 625

Blackwell D. E., Dewhirst D. W., and Ingham M.F. 1967, Adv. Astron. Astrophys. 5, 1

Blackwell D. E., and Petford, A.D. 1963, Mon. Not. R. Astron. Soc. 131, 383

Boggess, N. W., et al. 1992, ApJ 397, 420.

Bohlin, R. C., Savage, B. D., & Drake, J.F. 1978, ApJ 224, 132

Boksenberg A. et al. 1973, MNRAS 163, 291

Boulanger, F. and Perault, M. 1988, ApJ 330, 964

Boulanger, F., Abergel, .4., Bernard, J.-P., Burton, W. B., Desert, F.-X., Hartmann, D., Lagache, G., and Puget, J.-L. 1996, A&A, 3i2, 256

Bowyer S. and Leinert Ch., eds.1991, The galactic and extragalactic background radiation, IAU SYmposium No. 139, Kluwer, Dordrecht

Bowyer S., Sasseen T., Lampton M., and WU, X. 1993, Ap.J., 415

Bowyer, S., 1991, ARA&A 29, 59

Brecher K., Brecher A., Morrison P., and Wasserman 1. 1979, Nature 282, 502

Broadfoot, A.L., Kendall, K. R. 1968, J. Geoph.Res. 73, 426

Broadfoot, A.L., Kumar S. 1978, ApJ 222, 1054

Brosch N. 1991, MNRAS, 250, 780

Bruckner G., Howard R. A., Koomen M. J., Corendyke C. M., Michels D. J., Moses J. D., Socker D.G., Dere K. P., Lamy P. L., Llebaria A., Bout M. V., Schwenn R., Simmnet G. M., Bedford D.K., and Eyles C.J. 1995, Phys. 162, 357

Campins H., Rieke G. H. and Lebofsky M. J. 1985, AJ 90,896

J. Caplan and G.Grec 1979, A&A 78, 335

Caulet, A., Hook, R. N., Fosbury, R.A.E, 1994, A&AS 108, 271

Cebula R.P. and Feldman P.D. 1982, ApJ 263, 987

Cebula R. P., and Feldman P.D. 1984, JGR 89, 9080

Chamberlain J.W. 1961, Physics of the Aurora and the Airglow. Academic Press, New York

Classen, C. 1976, PhD Diss., University of Bonn

COBE Diffuse Infrared Background Experiment (DIRBE) Explanatory Supplement, Version 1.2, ed. M.G. Hauser, T. Kelsall, D. Leisawitz, and J. Weiland, COBE Ref. Pub. No. 97-A (Greenbelt,MD: NASA/GSFC), available in electronic form from the NSSDC

Cohen M. 1993, AJ 105, 1860

Cohen M. 1994, AJ 107, 582

Cohen M., Sasseen T. P. and Bowyer S. 1994, ApJ 427, 848

Cohen M. 1995, ApJ 444, 874

Cowie, L.L. et al., 1994, APJ 434, 114

Dachs, J. 1970, A&A 6, 155

Dave J.V. 1964, J. Opt. Soc.America 54, 307

Davidson W. C., MacQueen R. M., Mann 1.1995, Planet. Space Sci. 43, 1395

Davies J. K., Sykes M. V., Reach W. T., Boulanger F., Sibille F, and C.J. Cesarsky 1997, Icarus 127, 251

de Bary E. 1964, Appl. Optics 3, 1293

de Bary E., Bullrich K. 1964, J. Opt. Soc.America 54, 1413

Dermott S. F., Nicholson P. D., Burns J.A. and Houck J.R., 1984 Nature 312, 505

Dermott S. F., Nicholson P. D., Kim Y., Wolven B. and Tedesco E. F., 1988, in "Comets to Cosmology", ed. A. Lawrence, Lecture Notes in Physics 297, Springer-Verlag Berlin/Heidelberg/New York, p. 3

Dermott S. F., Jayaraman S., Xu Y. L., Gustafson B.Å.S. and Lieu J. C., 1994, Nature 369, 719

Dermott S. F., Jayaraman S., Xu Y. L., *Grogan* K. and B.Å.S. Gustafson, 1996a, *in* "Unveiling the cosmic infrared background, E. Dwek, cd., AIP Conf. Proc. 348, Woodbury, New York, p. 25

Dermott S. F., Grogan K., B.Å.S. Gustafson, Jayaraman S., Kortenkamp S.J. and Xu Y. L., 1996b, in 'Physics, chemistry, and dynamics of interplanetary dust", B.Å.S. Gustafson and M.S. Hanrrer, eds., ASP Conf.Ser. 104, San Francisco, p. 143

Désert F.-X., Abergel A., Bernard J.-P. et al. 1996, Limits on the far infrared CIBR from DIRBE, FIRAS and HI surveys, in E. Dwek (cd.) Unveiling the cosmic infrared background, AIP Conf. Proc. 348, 96

Désert F.-X., Boulanger F., Puget J.-L. 1990, A&A 237, 215

Deul and Wolstencroft 1988, A&A 196, 277

Draine D. T., and Anderson N. 1985, ApJ 292, 494
Dring A., Murthy J., Henry R., Walker H. 1996, Ap.J. 457, 764
Dube, R. R., 1976, Ph.D. Thesis, Princeton University
Dube, R. R., Wickes, W. C., Wilkinson, D. T., 1979, ApJ 232, 333
Dumont R. 1965, Astron. Astrophys. 28, 265
Dumont R. and Levasseur-Regourd A.-Ch., 1978, A&A 64, 9
Dumont R. and Levaaseur-Regourd A.-Ch. 1985, Planet. Space Sci. 33, 1
Dumont R., and Sanchez Martinez F. 1966, A&A 29, 113
Dumont R. and Sanchéz F., 1976, A&A 51, 393
Dürst J. 1982, Astron. Astrophys. 112, 241
Dwek, E., Slavin, J., 1994, ApJ 436, 696
Dwek, E. et al. 1997, ApJ, 475, 565
Elias J. H. 1978, AJ 83, 791
Elsässer H., Haug U. 1960, ZfA 50, 121
Elvey, C. T., & Roach, F.E. 1937, ApJ 85, 213
Epchtein N. et al. 1994, in "Science with astronomical near-infrared sky surveys", N. Epchtein, A. Omont, B. Burton, and P. Persi, eda., Kulwer, Dordrecht, p.3
Epchtein N. et al. 1997, ESO Messenger No. 87, March 1997, p.27
Fechtig H., Leinert C., Grün E. 1981, in: Landolt-Börnstein, New Series 2a (K. Schaifers and H.H. Voigt, eds,), Springer. Berlin, p. 228
Feldman P.D. 1977, A&A 61, 635
Feldman P.D. and eight co-authors 1992, Geophys.Res.Letters 19, 453
Ferguson, H.C., McGaugh, S. S., 1995, ApJ 440, 470 ,
Fixsen, D. J., et al. 1994, ApJ, 420, 457
Franceschini,A., Mazzei,P., De Zotti, G. , 1991a, In: Rocca-Volmerange, B., Deharveng, J. M., Tran Thanh Van, J. (eds.) The Early Observable Universe from Diffuse Backgrounds, , Editions Frontieres, p. 249
Franceschini A., Toffolatti L., Mazzei P., Danese L., and De Zotti G. 1991b, A&AS 89, 285
Frank L. A., Craven J. D., and Rairden R.L. 1985, Adv. Space Res. 5, No.4, 53
Frey A., Hofmann W., Lemke D.'and Thum C., 1974, A&A 36, 447
Frey A., Ho fmann W. and Lemke D. 1977, A&A 54, 853
Furton D. G., and Witt A.N. 1990, ApJ "364, L45
Furton D. G., and Witt A.N. 1992, ApJ 386, 587
Gardner, J. P., Cowie, L. L., Wainscoat, R. J., 1993, ApJ, L9
Garstang, R. H., 1986, PASP 98, 364
Garstang, R. H., 1988, Observatory 108, 159
Garstang, R. H., 1989a, Ann. Rev. A&A 27, 19
Garstang, R. H., 1989b, PASP 101, 306
Garstang, R. H., 1991, PASP 103, 1109
Giard, M., Pajot, F., Lamarre, J. M., Serra, G., Caux, E., Gispert, R., Leger, A., and Rouan, D. 1988, A&A, 201, L1
Giard, M., Pajot, F., Lamarre, J. M., Serra, G., and Caux, E. 1989, A&A, 215, 92
Giese R.H. 1979, A&A 77, 223
Giese R. H., Kneissel B., Rittich U. 1986, Icarus 68, 395
Giard M., Pajot F., Lamarre J. M., Serra G., Caux E., Gispert R., Léger A., and Rouan D. 1988, A&A 201, L1
Giard M., Pajot F., Lamarre J. M., Serra G., and Caux E. 1989, A&A 215, 92
Gillett, F.C. and Stein W.A., 1971, ApJ 164, 77
Gillet F. C., Forrest W. J., and Merrill K.M. 1973, ApJ 183, 87
Gondhalekar, P.M., 1990, in: S. Bowyer and Ch. Leinert (eds.) Galactic and Extragalactic Background Radiation, Proc. of IAU symposium No. 139, Kluwer, Dordrecht, p. 49
Gordon, K.D. 1997, PhD Thesis, The University of Toledo
Gordon, K. D., Witt, A.N., and Friedmann, B.C. 1997, ApJ (submitted)
Gordon, K. D., & Witt, A.N. 1997, ApJL (Submitted)
Guhathakurta, P., & Tyson, J.A. 1989, APJ 346, 773
Haikala, L. K., Mattila, K., Bowyer, S., Sasseen P., Lampton M. 1995, ApJ 443, L33
Hanner, M. S., Weinberg, J. L., De Shields 11, L. M., Green, B. A., & Toiler, G.N. 1974, J. Geophys. Res. 79, 3671
Hanner M. S., Sparrow J. G., Weinberg J.L. and Beeson D. E., 1976, in:'Interplanetary Dust and Zodiacal Light', H. Elsässer and H. Fechtig, eds., Lecture Notes in Physics 48, Springer-Verlag Berlin/Heidelberg/New York, p. 29
Hanner M., Leinert Ch., and Pitz E. 1978, A&A 65, 245
Hanner M.S. 1991, in "Origin and evolution of interplanetary dust", A.C. Levasseur-Regourd and H. Hasegawa, eds., IAU Colloquium 126, Kluwer, Dordrecht, p. 171
Harrison A.W. and Kendall D.J.W. 1973, Planet.Space Sci. 21, 1731
Hauser, M. G., et al. 1984, ApJ 278, L15
Hauser M. G., 1988, in "Comets to cosmology", A. Lawrence, cd., Lecture Notes in Physics 297, Springer-Verlag Berlin/Heidelberg/New York, p.27
Hauser M. G., 1995b, in "Examining the Big Bang' and Diffuse Background Radiations", IAU symposium N0.168, M. Kafatos, Y. Kondo, and S. Bowyer, eda., Kluwer Academic Publishers, Dordrecht, p. 99
Hauser, *M. G.*, 1995a, in D. Cazetti, M. Livio and P. Madau (eds.) Extragalactic Background Radiation, Cambridge University Press, p. 135 .
Hauser, M. G., 1996, in "Unveiling the cosmic infrared background", E. Dwek, cd., AIP Conf. Proc. 348, Woodbury, New York, p. 11
Hayes D.S. in "Calibration of fundamental stellar quantities",, D.S. Hayes, L.E. Pasinetti and A.G.D. Philip, eds., Reidel Publishing Company, Dordrecht 1985, p.225
Hayes D.S. and Latham D. W., 1975, ApJ 197, 593
Henry, R. C., 1990, ARA&A 29, 89
Henry, R. C., Murthy, J., 1995, in D. Cazetti, M. Livio and P. Madau (eds.) Extragalactic Background Radiation, Cambridge University Press, p. 51
Henry, T. J., McCarthy Jr., D.W. 1990, ApJ, 350, 334
Henry R. 1991, ARA&A 29, 89
Hodapp K.-W., MacQueen R. M., Hall D. N. B.: 1992, Nature 355, 707
Hoffmann B., Tappert C., Schlosser W., Schmidt-Kaler T., Kimeswenger S., Seidensticker, K., and Schmidtobreick, L. 1997, A&A, in print
Hofmann W., Lemke D., Thum C. and Fahrbach U. 1973, Nature 243, 140
Hofmann W.. Frev A.. and Lemke D. 1974, Nature 250, 636
Hofmann W., Lemke D., and Thum C 1977, Applied Opt. 16, 3125
Holberg J. 1986, ApJ 311, 969
Hovenier J.W. and Bosma P. B., 1991, in: 'Origin and Evolution of Interplanetary Dust', A.C. Levasseur-Regourd and H. Hasegawa, eds., Kluwer Academic Publishers, Dordrecht, p.155

Maihara T., Mizutani K., Hiromoto N., Takami H., Hasegawa, H. 1985, in: Properties and Interactions of Interplanetary Dust (R.H. Giese and P.L. Lamy, eds.), Reidel, Dordrecht, p.63

Mampaso A., Sánchez-Magro C., Buitrago J.: 1982, in: Sun and Planetary System (W. Fricke and C. Teleki, eds.), p.257

Mampaso A., Sánchez-Magro C., Selby M. J., MacGregor A. D.: 1983, Rev. Mexicana Astron. Astrof. 8, 3

Mankin W. G., MacQueen R. M., Lee R.H. 1974, Astron. Astrophys. 31, 17

Mann I. 1990, Dissertation, Universität Bochum

Mann 1.1992, Astron. Astrophys. 261, 329

Mann I. 1993, Planet. Space Sci. 41, 301

Mann 1. 1996, in: Physics, Chemistry and Dynamics of Interplanetary Dust (B.A.S. Gustafson und M.S. Hanner eds.) PASP conf. Ser. 104, p. 315

Mann I., MacQueen R.M. 1993, Astron. Astrophys., 275, 293-297

Martin C. and Bowyer S. 1990, ApJ 350, 242

Massey, P., Gronwall, Pilachowski, 1990, PASP 102, 1046,

Mather J. C., et rd., 1994, ApJ, 420, 439

Matsumoto, T., 1990, in: S. Bowyer and Ch. Leinert (eds.) Galactic and Extragalactic Background Radiation, Proc. of IAU Symposium No. 139, Kluwer, Dordrecht, p. 317

Matsumoto T., et al. 1996, PASJ 48, L47

Matsumoto S., Matsuura S., and Noda M. 1994, PASP 106, 1217

Matsumoto T., Kawada M., Murakami H., Noda M., Matsuura S., Tanaka M., and Narita K. 1996, PASJ 48, L47

Matsuura S., Matsumoto T., Matsuhara H. and Noda M. 1995, Icarus 115, 199

Mattila K. 1973, Sterne und Weltraum 12, 246

Mattila, K. 1970, A&A 8, 273

Mattila, K. 1971, A&A 15, 292

Mattila, K., 1979, A&AS 39, 53

Mattila, K., 1980, A&A 78, 253

Mattila, K., 1990, in: S. Bowyer and Ch. Leinert (eds.) Galactic and Extragalactic Background Radiation, Proc. of IAU Symposium No. 139, Kluwer, Dordrecht, p. 257

Mattila, K., Schnur, G., 1990, see Mattila, 1990

Mat tila, K., Leinert, Ch., Schnur, G., 1991, In: Rocca-Volmerange, B., Deharveng, J. M., Tran Thanh Van, J. (eds.) The Early Observable Universe from Diffuse Backgrounds, , Editions Frontiers, p. 133

Mattila K., Väisänen P., and v. Appen-Schnur G.F.O. 1996, A&A Suppl. 119, 153

Mattila K., Lemke D., Haikala L. K., Laureijs R. J., Léger A., Lehtinen K., Leinert Ch., and Mezger P.G. 1996, A&A 315, L353

Maucherat-Joubert M., Cruvellier P. and Deharveng J.M. 1979, A&A 74, 218

Meier R.R. 1991, Space Sci. Rev. 58, 1

Meier R. R., Carruthers G. R., Page T. L., and Levasseur-Regourd A.-Ch. 1977, JGR 82, 737

Milford N., 1950, Ann.d'Astrophys. 13, 243

Misconi N.Y. 1977, A&A 61, 497

Mizutani K., Maihara T., Hiromoto N., Takarni H.: 1984, Nature 312, 134-136

Morgan D.H. 1978, A&A 70,543

Morgan, I., Driver, S. P., 1995, in D. Cazetti, M. Livio and P. Madau (eds.) Extragalactic Background Radiation, Cambridge University Press, p. 285

Morgan D, H., Nandy K. and Thompson G.I. 1976, M.N. 177, 531

Morrison D., Feldman P. D., and Henry R.C. 1992, JGR 97, 1633

Mukai T., Yamamoto T. 1979, Publ. Astron. Sot. Japan 31, 585

Murakami, H., et al. 1994, ApJ, 428, 354

Murakami H., et al. 1996, PASJ 48, L41

Murdock T.L. and Price S. D., 1985, AJ 90, 375

Murthy J., Henry R. C., Feldman P.D. and Tennyson P.D. 1990, A&A 231, 187

Neckel H. and Labs D. 1984, Solar Physics 90, 205

Neugebauer G., et al. 1984, ApJ 278, L1

Neugebauer G., Wheelock S., Gillett F., Aumann H. H., Gautier T. N., Low F. J., Hacking P., Hauser M., Harris S., Clegg P. 1988, IRAS catalogs and atlases, Volume 1: Explanatory Supplement, C.A. Becihman et al., eds, NASA RP-1190, Washington, VI-21

Nguyen H.T., Rausche B. J., Severson S. A., Hereld M., Harper D. A., Loewenstein R. F., Mrozek F., and Pernic R.J. 1996, PASP 108, 718

Nishimura T. 1973, Publ.Astr.Soc.Japan 25,375

Oliva E. and Origlia L. 1992, A&A 254, 466

Onaka, T., Yamamura, I., Tanabe, T., Roellig, T.L., and Yuen, L. 1996, PASJ, 48, L59

Osterbrock, D. E., Walker, M. F., Koski, T. A., 1976, PASP 88, 349

Osterbrock, D. E., Martel, A., 1992, PASP 104, 76

Page T., Carruthers G., and Heckathorn H. 1982, NRL Report 8487

Paresce F. and Jakobsen P. 1980, Nature, 288, 119

Pennington R. L., Humphreys R. M., Odewahn S. C., Zumach W., and Thurmes P.M. 1993, PASP 105,"521

Pepin T.J. 1970, Astrophys. J. 159, 1067..',

Perrin, J.-M., Darbon, S., & Sivan, J.-P. 1995, A&A 304, L21

Perrin J.-M., and Sivan J.-P. 1995, A&A 255, 271

Peterson A.W. 1963, Astrophys. J. 138, 1218

Peterson A.W. 1967, Astrophys. J. 148, L37

Peterson A.W. 1969, Astrophys. J. 155, 1009

Pfleiderer J., and Mayer U. 1971, AJ 76, 692,

Pickering, E. C., Kapteyn, J. C., vanRhijn, P. J., 1918, Ann. Harvard College Oba. 101

Pickering, E. C., Kapteyn, J. C., vanRhijn, P. J., 1923, Ann. Harvard College Ohs. 102

Pickering, E. C., Kapteyn, J. C., vanRhijn, P. J., 1924, Ann. Harvard College Ohs. 103

Pilachowski C., Afriano J., Goodrich B., and Binkert W., 1989, PASP 101, 707

Pitz E., Leinert Ch., Schulz A. and Link H. 1979, A&A 74, 15

Pröll J. 1980, Diploma Thesis, Ruhr-University Bochum

Puget, J.-L. et al., 1996, A&A 308, L5

Ramsay S. K., Mountain C. M., and Geballe T.R. 1992, MNRAS 259, 751

Raurden R., Frank L., and Craven J. 1986, JGR 91, 13613

Reach W.T. 1988, ApJ 335, 468

Reach W.T. 1991, ApJ 369, 529

Reach W.T. 1992, ApJ 392, 289

Reach, W.T. et al. 1995a, ApJ, 451, 188

Hurwitz M., Bowyer S., and Martin C. 1991, Ap.J. 372, 167

Isobe S., Tanabe H., Hirayama T., Korea Y., Soegijo J., Baba N. 1985, in: Properties and interactions of interplanetary dust (R.H. Giese and P.L. Lamy, eds.), Reidel, Dordrecht, p. 49

Isobe S., Sateesh-Kumar A. 1993, in: Meteoroids and their Parent Bodies (J. Stohl und I.P. Williams, eds.), published by the Astronomical Inst., Slovak Acad. Sci., Bratislava, p. 381

Jakobsen P. 1991, *in* "*The* Early Observable Universe from Diffuse Backgrounds", Rocca-Volmerange B., Deharveng J. M., and Tran Thanh Van J. (eds.), Edition Frontières, p. 115

Jakobsen, P.,1995, in D. Cazetti, M. Livio and P. Madau (eds.) Extragalactic Background Radiation, Cambridge University Press, p. 75

Johnson H. L., 1966 ARA&A 4,193

Kaiser C.B. 1970, Astrophys. J. 159, 77

Kalinowski K. J., Roosen R. G., and Brandt J. C., 1975, PASP 87, 869

Kashlinsky, A., Mather, J. C., Odenwald, S., 1996, ApJ 473, L9

Kessler M., et al. 1996, A&A 315, L27.

Kimeswenger S., Hoffmann B., Schlosser W., and Schmidt-Kaler T. 1993, A&A Suppl. 95, 517.

Knude, J., 1996, Reddening at the North Galactic Pole: cosecant variation, $A_B = 0.0$ or $A_B = 0.2$?, A&A (in press)

Korneef J., 1983, A&AS 51, 489

Koutchmy S., Dzubenko N. J., Nesmjanovich A.T., Vsekhsvjatsky S.K. 1974, Sol. Phys. 35, 369

Koutchmy S., Lamy P.L. 1985, in: Properties and Interactions of Interplanetary Dust (R.H. Giese and P.L. Lamy, eds.), Reidel, Dordrecht, p.'63

Krisciunas K., 1990, PASP 102, 1052

Kuhn J. R., Lin H., Lamy P., Koutchmy S., Smartt R. N.: 1994, in: Infrared Solar Physics (D. M. Rabin et rd., eds.), IAU 1994, The Netherlands, p. 185 .

Kwon S. M., Hong S. S., and J.L. Weinberg 1991,in "Origin and evolution of interplanetary dust", A.C. Levasseur-Regourd and H. Hasegawa, eds., IAU Colloquium 126, Kluwer, Dordrecht, p. 179

Lamy P., Kuhn J.R., Lin H., Koutchmy S., Smartt, R.N.: 1992, Science 257, 1377-1380

Laureijs, R., Mattila, K., Schnur, G., 1987, A&A 184, 269

Léger A., Mariotti J.-M., Mennesson B., Ollivier M., Puget J.-L., Rouan D., and Schneider J. 1996, Icarus 123,249

Lehtinen, K. & Mattila, K. 1996, A&A 309, 570

Leinert Ch. 1975, Space Sci. Rev. 18, 281

Leinert, C. 1990 in The Galactic and Extragalactic Background Radiation, S. Bowyer and C. Leinert (eds.) (Dordrecht: Kluwer), p. 75

Leinert Ch., Link H., Pitz E. and Giese R. H., 1976, A&A 47, 221

Leinert Ch., Richter I., Pitz E. and Hanner M., 1980, in:'Solid particles in the solar system', I. Halliday and B. A. McIntosh, eds., D. Reidel Publishing Company, Dordrecht, p.15

Leinert Ch., Hanner M., Richter I. and Pitz E., 1980b, A&A 82, 328

Leinert Ch., Pitz E., Link H. and Salm N., 1981, Space Sci. Instrumentation 5, 257

Leinert Ch., arrd Richter I. 1981, A&A Suppl. 46, 115

Leinert Ch., Richter 1., Pitz E. and Hanner M., 1982, A&A 110,355

Leinert Ch. and Pitz E., 1989, A&A 210, 399

Leinert Ch 1990, in "The Galactic and Extragalactic Background Radiation", S. Bowyer and Ch. Leinert, eds., Kluwer, Dordrecht, p. 75

Leinert, Ch., Grün, E., 1990, Interplanetary Dust, in R. Schwenn and E. Marsch (eds.) Physics and Chemistry in Space - Space and Solar Physics, Vol. 20, Springer, Berlin - Heidelberg, p. 207

Leinert Ch., Väisanen P., Mattila K. and Lehtinen K, 1995, A&AS 112, 99

Lemke D. et al. 1997, A&A submitted

Léna P., Viala Y., Hall D., Soufflot A.: 1974, Astron. Astrophys. 37, 81

Levasseur A.-Ch. and Blamont J. E., 1973, Nature 246, 26

Levasseur A.-Ch. and Blamont J. E., 1975, Space Res. XV, 573

Levasseur A.-Ch., Meier R. R., and Tinsley B.A. 1976, JGR 81, 5587

Levasseur-Regourd, A.-Ch. and Dumont, R., 1980, A&A 84, 277

Levasseur-Regourd A.-Ch. 1996, *in* "Physics, chemistry, and dynamics of interplanetary dust", Bo A. S. Gustafson and M.S. Hanner, eds., Astr.Soc.Pac.Conf.Ser. 104, San Francisco, p.301

Lillie C.F. 1968, Ph.D. Thesis, University of Wisconsin

Lillie C.F. 1972, in 'The scientific results from OAO-2', ed. A.O. Code, NASA SP-31O, Washington, p.95 ."

Lilly, S. J., LeFevre, O., Crampton, D., Hammer, F., Tresse, L., 1995, ApJ 455; 50

Lockman F. J., Jahoda K. and McCammon D., 1986, ApJ 302, 432

Longair, M. S., 1995, In A.R. Sandage, R.G. Kron and M. S. Longair The Deep Universe, Springer, Berlin/Heidelberg/New York, p. 317

Lonsdale, C. J., 1995, in D. Cazetti, M. Livio and P. Madau (eds.) Extragalactic Background Radiation, Cambridge University Press, p. 145

Louistisserand, S., Bücher, A., Koutchmy, S., Lamy, Ph., 1987, A&A S 68, 539

Low F.J. and Rieke G. H., 1974, Methods of Exper. Phys. 12, 415

Low F.J. et al. 1984, ApJ Letters 278, L19

LyutyiV.M., and Sharov A. S., 1982, AZh 59,174

Lyot M. B.: 1939 *Mon.* Not. R. Astron. Sot. 11, 580

MacQueen R.M. 1968, Astrophys. J. 154, 1059

MacQueen R. M., Davidson W. C., Mann I.: 1996, in: Physics, Chemistry and Dynamics of Interplanetary Dust (B.A.S. Gustafson und MS. Hanner eds.) PASP Conf. Ser.104, p. 349

MacQueen R. M., Greeley B.W. 1995, Astrophys. J. 154, 1059

MacQueen R. M., Hodapp K.-H., Hall D. N. B.: 1994, Infrared Solar Physics (D. M. Rabin et al., eds.), IAU 1994, The Netherlands, p. 199

MacQueen R. M., Ross C. L., Mattingly T.: 1973, Planet. Space Sci. 21, 2173-2179

McCaughrean M.J. 1988, "The astronomical application of infrared array detectors", Ph. D. Thesis, University of Edinbourgh

McNally (cd.), D., 1994, The Vanishing *Universe,* Adverse Environmental Impacts on Astronomy, Cambridge University Press

Reach W. T., Franz B. A., Weiland J. L., Hauser M.G., Kelsall T.N., Wright E. L., Rawley G., Stemwedel S.W. and Spiesman W. J., 1995b, Nature 374, 521

Reach W. T., Franz, B. A., Kelsall, T. and Weiland, J.L. 1996a, in "Unveiling the cosmic infrared background", E. Dwek, cd., AIP Con f. Proc. 348, Woodbury, p. 37

Reach W.T. et al. 1996b, A&A 315, L381

Reed E.I. and Blamont J.E. 1967, Space Res. VII, 337

Richter I., Leinert Ch. and Planck B., 1982, A&A 110, 115

Rieke G. H., Lebofsky M.J. and Low F. J., 1985, AJ 90, 900

Roach F.E. 1964, Space Sci. Rev. 3, 512

Roach, F. E., & Gordon, J.L. 1973, The Light of the Night Sky D. Reidel Publ. Company, Dordrecht

Roach F.E. and Meinel A.B. 1955, ApJ 122, 530

Roach, F. E. and Megill, L. R, 1961, ApJ 133, 228

Rocca-Vomerange B., Deharveng J. M., and Tran Thanh Van J., eds. 1991, The early observable universe from diffuse backgrounds, Éditions Frontières, Gif-sur-Yvette

Röser S. and Staude H.J. 1978, A&A 67, 381

Rowan-Robinson M., Hughes J., Vedi K and Walker D. W. 1990, MN 246, 273

Sandage, A., 1983, 'in W. L. H. Shuter (ed.) Kinematics, Dynamics and the Structure of the Milky Way, D. Reidel, Dordrecht, p. 320

Scheffler H. 1982, Landolt-Börnstein VI/2c, 176,

Schlosser W. 1972, Habilitationsschrift, Ruhr-Univeraity Bochum

Schmidt, T. & Leinert, C. 1966, Z.f.Ap. 64, 110

Schmidtobreick L. 1997, Ph.D. Thesis, Universität Bochum

Schnur G., and Mattila K., 19?9, "Mitt. Astron.Ges. 45,196"

Schuerman D.W., Weinberg J.L., and Beeson D.E. 1977, BAAS 9, 313

Schuerman D. W., Tanabe H., Weinberg J. L., Toiler G. N., and Beeson D.E. 1977, 'Abstract, COSPAR, Tel Aviv

Schuerman D. W., and Weinberg J.L. 1981, User's 'manual for the Pioneer 10/11 data, available at the NSSDC

Schuerman, D. W., Weinberg, J. L., Giovane, F., 1981, see ' reference in Toiler, 1981

Scares. F. H., Kapteyn, J. C., van Rhijn, P. J., 1930, Mount Wilson Catalogue of Photographic Magnitudes in Selected Areas 1-139, Carnegie Inst. Washington Publ. No. 402

Seidensticker K., Schmidt-Kaler T., and Schlosser W. 1982, A&.4 114, 60

Sellgren K. 1984, ApJ 277,623

Sellgren K., Werner M. W., and Dinerstein H.L. 1983, APJ 271, L13

SharoV, A. S., & Lipaeva, N.A. 1973, Soviet Astr. 17, 69

Sharov, A. S., Polyakova, G. I., 1972, Soobshch. Gos. Astron. Inst. Shternberga, No. 177, 3

Shcheglov P. V., Shestakova L. I., Ajmanov A.K. 1987, Astron. Astrophys. 173, 383

Silverberg, R. F., et rd. 1993, Proc. SPIE Conf. 2019, Infrared Spaceborne Remote Sensing, ed. M.S. Scholl (Bellingham: SPIE), p. 180

Simon T., Morrison D.D. and Cruikshank D. P., 1972, ApJ (Letters) 177, L17

Sivan J.-P., and Perrin J.-M. 1993, ApJ 404, 258

Smith L. L., Roach F.E., and Owen R.W. 1970, Batelle Institute Report BNWL-1419-UC-2

Sodroski, T. J., Odegard, N., Arendt, R. G., Dwek, E., Weiland, J. L., Hauser, M. G., and Kelsall, T. 1997, ApJ, 480, 173

Sparrow J.G. and Ney E. P., 1968, Ap.J. 154, 783

Sparrow J.G. and Ney E. P., 1972, Ap.J. 174, 705

Sparrow, J.G. k Ney, E.P. 1972, APJ 174, 717

Sparrow J.G. and Weinberg J. L., 1976, in:'Interplanetary Dust and Zodiacal Light', H. Elsässer and H. Fechtig, eds., Lecture Notes in Physics 48, Springer-Verlag Berlin/Heidelberg/New York, p. 41

Spiesman W.J. et al. 1995, ApJ 442, 662

Stark, A. A., Gammie, C. F., Wilson, R, W., Bally, J. Linke, R. A., Heiles, C., & Hurwitz, M. 1992, ApJS 79, 77

Staude, H.J. 1975, A&A 39, 325

Stebbins, J., Whitford, A. E., Johnson, H. L., 1950, ApJ 112, 469

Strecker D. W., Erickson E.F. and Witteborn F. C., 1979, ApJS 41, 501

Sykes M. V., 1985, Icarus 85, 267

Sykes M.V., Lebofsky L. A., Hunten D.M. and Low F., 1986, Science 232, 1115

Sykes M. V., 1988, ApJ Letters 334, L55

Sykes M. V., Lien D.J. and Walker R. G., 1990, Icarus 86," 236

Sykes M.V. and Walker R. G., 1992, Icarus 95, 180

Tanabe H. 1973, in "Papers on the night sky and airglow continuum at Chichijima", World data center C2 (Airglow), Tokyo Astron. Ohs. 45 '.

Tanabe T., Tsumuraya F., Baba N., Alvarez M., Noguchi M., Isobe S. 1992, Publ. Astron. Sot. Japan 44, L221 ,.'. .

Taylor, B. J., 1992, PASP 104, 500

Tennyson P. D., Henry R. C., Feldman P.D. and Hartig G.F. 1988, Ap.J. 330, 435

Thomas G.E. 1978, Ann.Rev.Earth Planet.Sci. 6, 173

Toiler, G. N., 1981, Ph.D. Thesis, State University of New York at Stony Brook

Toiler, G. N., 1983, ApJ 266, L79

Toiler G. N., Tanabe H., and Weinberg J.L. 1987, A&A 188, 24

Toiler G.N. 1990, in: S. Bowyer and Ch. Leinert (eds.) Galactic and Extragalactic Background Radiation, Proc. of IAU Symposium No. 139, Kluwer, Dordrecht, p. 21

Toiler, G.N. and Weinberg, J. L., 1985, in: 'Properties and Intractions of Interplanetary Dust', R. H. Giese and Ph. Lamy, eds., D. Reidel Publishing Company, Dordrecht, p.21

Tollestrup E. V., Fazio G. G., Woolaway J., Blackwell J., Brecher K. 1994, in: Infrared Solar Physics (D.M. Rabin et al., eds.), L4U 1994, The Netherlands; 179

Torr M. R., Torr D. G., and Eun J.W. 1985, JGR 90:4427

Treanor, P. J., 1973, Observatory 93, 117

Tug H. and Schmidt-Kaler Th., 1982, A&A 105, 400

Turnrose B. E., 1974 PASP 86, 512

Tyson, J. A., 1990, in: S. Bowyer and Ch. Leinert (eds.) Galactic and Extragalactic Background Radiation, Proc. of IAU Symposium No. 139, Kluwer, Dordrecht, p. 245

Tyson, J. .4., 1995, in D. Cazetti, M. Livio and P. Madau (eds.) Extragalactic Background Radiation, Cambridge University Press, p. 103

Väisänen, P., 1996, A&A 315, 21

Van de Hulst H.C. 1947, Astrophys. J. 105, 471-488

Van de Hulst H.C. 1962, in: The Sun (G.D. Kuiper, cd.), University of Chicago Press, Chicago

Vande Noord E.L. 1970, Ap.J. 161, 309

van Dijk M.H.H., Bosma, P.B. and Hovenier, J. W., 1988, A&A 201, 373

van Rhijn, P. J., 1921, Publ. Astr. Lab. Groningen no. 31, 1

van Rhijn, P. J., 1929, Publ. Astr. Lab. Groningen No. 43
Vrtilek J., and Hauser M.G. 1995, ApJ 455, 677.
Wainscoat R. J., and Cowie L.L. 1992, AJ 103, 332
Wainscoat R. J., Cohen M., Volk K., Walker H. J., and Schwartz D. E. 1992, ApJ Suppl. 83,111
Waldmeier M. 1965, in: Landolt-Bernstein Zahlenwerte und Funktionen in Naturwissenschaft und Technik, Gruppe IV: Astronomic, Astrophysik und Weltraumforschung, Band I: Astronomic und Astrophysik, Springer, Berlin, p. 115
Walker M. F., 1988, PASP 100, 496
Walker M.F., 1977, PASP 89, 405
Walker M. F., 1970, PASP 82,674
Weiland J. L., Blitz L., Dwek E., Hauser M. G., Magnani L., and Rickard L.J. 1986, ApJ 306, L101
Weiland J. L., Arendt R. G., Berriman G. B., Dwek E., Freudenreich H. T., Hauser M. G., Kelsall T., Lime C. M., Mitra M., Moseley S. H., Odegard N. P., Silverberg R. F., Sodorski T.J., Spiesman W. J., and Stemwedel S.W. 1994, ApJ 425, L81
Weinberg J.L. 1964, Ann. Astrophys. 27, 718
Weinberg J.L. and Mann H.M. 1967, in "The zodiacal light and the interplanetary medium", J.L. Weinberg, cd., NASA SP-150, Washington D. C., P.1
Weinberg J. L., 1969, BAAS 1, 368
Weinberg J. L., Hanner M. S., Beeson D. E., De Shields L.M. III, and Green B.A. 1974, JGR 79, 3664
Weinberg J.L. 1981, Sky and Telescope 61, 114
Weinberg J.L. and Schuerman D.W. 1981, User's Guide forthe Pioneer 10/11 background sky tape, NSSDC
Weinberg J.L. and Hahn R. C., 1980, in: 'Solid particles in the solar system', I. Halliday and B. A. McIntosh, eds. D Reidel Publishing Company, Dordrecht, p.19
Wheelock S. L., et al. 1994 "IRAS Sky Survey Atlas Explanatory Supplement", JPL Publication 9411 (Pasadena:JPL)
Wicenec A.J. 1995, Ph.D. Thesis, Universität Tübingen
Wicenec A. J., and van Leeuwen F. 1995, A&A 304, 160
Winkler C., Schmidt-Kaler T., and Schlosser W. 1981, Mitt. Astr. Ges. 52, 163
Witt, A.N. 1968, ApJ 152, 59,
Witt. A.N. & Schild, R. E., 1988, ApJ 325, 837
Witt, A.N. & Boroson, T.A. 1990, APJ 355, 182
Witt, A. N., Lindell, R. S., Block, D. L., & Evans, Rh. 1994, ApJ 427, 227
Wright, E. L., et al. 1991, ApJ, 381, 200
Wolstencroft R.D. and Brandt J. C., 1967, in "The zodiacal light and the interplanetary medium", J.L. Weinberg, cd., NASA SP-150, Washington, P.57
Yoshii Y., Ishida K. and Stobie R. S. 1987, AJ 92, 323
Yoshii, Y., Takahara, F., 1988, ApJ 326, 1
Zavarzin M.Yu. 1978, Astrophysics (Engl. Transl.) 14, 168

This article was processed by the author using Springer-Verlag LaTeX A&A style file *L-AA* version 3.